Doctoral Dissertation
Doctoral Program in Energetics (33.rd cycle)

Modelling liquid metals for nuclear fusion and fission reactors

Giuseppe Francesco Nallo

* * * * * *

Supervisors
Prof. Piero Ravetto
Prof. Roberto Zanino

Doctoral Examination Committee:
Prof. Roberto Bonifetto, Politecnico di Torino
Dr. Giacomo Grasso, ENEA
Dr. Matteo Iafrati, ENEA
Dr. Thomas Morgan, DIFFER
Prof. Fabio Subba, Politecnico di Torino
Dr. Mariano Tarantino, ENEA

Politecnico di Torino
10 September, 2021

I hereby declare that, the contents and organisation of this dissertation constitute my own original work and does not compromise in any way the rights of third parties, including those relating to the security of personal data.

Disclaimer for part I of the thesis: this work has been carried out within the framework of the EUROfusion Consortium and has received funding from the Euratom research and training programme 2014–2018 and 2019-2020 under grant agreement No 633053. The views and opinions expressed herein do not necessarily reflect those of the European Commission.

. . . . . .

Giuseppe Francesco Nallo

Turin, 10 September, 2021

Summary

Liquid metals (LMs) are used in both fusion and fission nuclear systems: in advanced divertor solutions and in breeding blankets for fusion reactors, and as coolants for fission fast reactors. The present thesis reports the research work carried out by the candidate along two main lines:

I. the modelling of **Liquid Metal Divertors (LMDs)** for future nuclear fusion reactors, including the interactions of the LM with the Scrape-Off Layer (SOL) plasma;
II. the multi-physics (neutronics and thermal-hydraulic) modelling of the full core of **Liquid Metal-cooled Fast Reactors (LMFRs)**.

I. Liquid metal divertors LMDs are currently being considered as an alternative solution to the power exhaust problem in future fusion reactors, because of their self-healing features, among others. In the first part of the thesis, the development and application of computational tools to model LMDs, with specific focus on the interactions of the LM with the SOL plasma, are reported. Two different LMD designs are considered: the first, having an ITER-like shape of the plasma-facing components, is based on the Capillary-Porous Structure (CPS) concept, while the second is based on the "vapor-box" divertor concept.

First, the results of simulations aimed at assessing the effect of installing a **CPS-based, ITER-like LMD** in the EU DEMO tokamak, within the same envelope of the reference solid divertor, are presented. The SOLPS-ITER code was used to model the SOL plasma and neutral species (both fuel neutrals and metal eroded from the target), with the latter treated by means of a fluid model, for the sake of simplicity. SOLPS-ITER was coupled to an ad-hoc developed model for the target temperature distribution, to allow for the self-consistent evaluation of temperature-dependent erosion phenomena such as evaporation. In this way, a fair comparison between Li and Sn as materials for an LMD target could be performed. First simulations considering only D and Li (or Sn) suggested that the margin for operating an ITER-like LMD in the EU DEMO without any additional impurity seeding could be narrow, if existing. For this reason, further simulations assessing the effect of seeding Ar in the SOL to further reduce the target heat load, and thus the metal erosion rate, were performed. Results show a noticeable and promising

widening of the operational window in terms of both core plasma compatibility and tolerable target heat flux.

Second, a simplified but self-consistent model for an **LM vapor-box divertor** is presented, together with its application to the Divertor Tokamak Test (DTT) facility, which is under construction in Italy. Given the upstream plasma conditions, the model evaluates the plasma heat and particle flux on the LM surface, the thermodynamic state of the metal (liquid and vapor) in the divertor boxes and the temperature distribution in the solid walls. Also for this design, the model is used to compare Li and Sn as possible LMs, in terms of operating temperatures and of metal vapor flux from the divertor box system towards the main plasma chamber. The results indicate that, for both Li and Sn, this design allows to reduce the impurity flux towards the main plasma by ~ 2 orders of magnitude. However, only for Li the evaporation and radiation cooling are effective in reducing the target heat load, thanks to the relatively large Li concentration inside the boxes.

II. Liquid Metal-cooled Fast Reactors The development of LMFRs is currently under way within the Generation-IV program. In particular, Italy is involved in the development of the design of the Advanced Lead-cooled Fast Reactor European Demonstrator (ALFRED). In the second part of the thesis, the development, validation and application of computational tools to model the full-core, coupled neutronic and thermal-hydraulic behavior of LFRs is reported.

First, the design, development and preliminary validation of **a Design-Oriented Code, TIFONE**, aimed at evaluating the effect of the inter-subassembly heat transfer in the core of an LMFR, is presented. The code is based on the sub-channel method and the development was carried out in compliance with the ENEA software quality assurance requirements. TIFONE computes the axial and perimetrical coolant temperature profiles in the inter-subassembly gaps throughout the whole core, as well as the axial and perimetrical wrapper temperature profiles, and notably the (possibly) different values of each side of the wrapper itself. The code results allow the core designers to assess the presence of cold by-passes and of excessive thermal gradients among opposite faces of the wrapper of each subassembly, as well as the effectiveness of possible gagging schemes in mitigating these undesired phenomena. The code was compared with experimental data from the KALLA inter-wrapper flow and heat transfer experiment, confirming its ability in reproducing the measured data in its anticipated validity domain.

Second, the application of **FRENETIC, a multiphysics (neutronic/thermal-hydraulic) code** recently developed at Politecnico di Torino, to the full-core analysis of the ALFRED design is presented, together with results of the benchmarking activity against high-fidelity single-physics codes (Serpent for Monte Carlo neutron transport and OpenFOAM for CFD). The satisfactory results obtained for these benchmarks confirm the suitability of FRENETIC for the characterization of the ALFRED core in both steady-state and time-dependent conditions.

Acknowledgements

It is necessary for me to acknowledge the invaluable support I have received from researchers and professors outside PoliTo during this thesis work, in terms of useful discussions, knowledge sharing, smart questions, technical support and much more: Giuseppe Mazzitelli, Matteo Iafrati, Selanna Roccella, Giacomo Dose and Riccardo De Luca (ENEA Frascati), Giacomo Grasso and Francesco Lodi (ENEA Bologna), Mariano Tarantino (ENEA Brasimone), Thomas Morgan and Peter Rindt (DIFFER), Robert Goldston, Jacob Schwartz and Eric Emdee (PPPL), Lefteris Benos (University of Thessaly), David Horsley (CCFE), Francisco Tabarès and Joao Loureiro (CIEMAT), Yoshi Hirooka (CHUBU University), David Ruzic (University of Illinois at Urbana-Champaign), Michele Sala (PoliMi), Michal Poradzinski (IPPiLM), David Coster (IPP Garching), Xavier Bonnin (ITER IO), Stefano Carli (KU Leuven). I also wish to thank the reviewers of the thesis for their comments: I believe that their suggestions have stimulated a significant improvement of the final product.

I must also sincerely thank my supervisors for the opportunities they gave me in terms of personal and professional growth, and all the researchers and professors at Dipartimento Energia that have generously devoted some of their time to discuss with me and support this work in many ways.

Thanks to all the fellows that I had the honour and pleasure to meet during this journey. It would take a separate book to describe the invaluable help I received by each of them. Indeed, as a dear friend and colleague of mine used to say: *"Research is like music. There is only one way to do it: together."*.

Ai miei nonni,
ed a Lino.
Il vostro sorriso mi
ricorda la straordinaria
bellezza di ogni giorno.

Contents

List of Tables

List of Figures

Chapter 1

Introduction

> *Οὐδεὶς δύναται δυσὶ κυρίοις δουλεύειν· ἢ γὰρ τὸν ἕνα μισήσει, καὶ τὸν ἕτερον ἀγαπήσει· ἢ ἑνὸς ἀνθέξεται, καὶ τοῦ ἑτέρου καταφρονήσει.*
>
> *No man can serve two masters: for either he will hate the one, and love the other; or else he will hold to the one, and despise the other.*
>
> – Mt. 6:24

The present thesis deals with applications of Liquid Metals (LMs) for both fusion and next-generation fission nuclear reactors. The overall nature of the work can be described as the *development, verification, validation and application of computational tools for the design and analysis of intrinsically multi-physics nuclear systems based on liquid metals.*

Two lines of activity are presented: the modelling of Liquid Metal Divertors (LMDs) for future fusion reactors, including the interactions of the eroded metal with the plasma; and the modelling of the core of Heavy Liquid Metal Cooled Reactors (HLMCRs). These two lines of activity are addressed separately in the respective parts of the thesis.

To guide the reader through this two-headed work, this introductory chapter has been added with the purpose of briefly providing introduction and motivation for each line of activity, together with a clarification of the aim of the work and an outlook of the key results obtained.

1.1 Liquid Metal Divertors for nuclear fusion reactors

1.1.1 Background and motivation

Nuclear fusion has the potential to provide almost unlimited, carbon-free energy without producing long-lived radioactive waste [42]. The most promising fusion reactor concept is the *tokamak*, involving the confinement of a hot, ionized gas (the *plasma*) away from the tokamak chamber walls by means of magnetic fields.

The arrangement of magnetic field lines in a tokamak defines two regions: the central *core plasma*, hotter than the Sun ($\sim$ 100 MK) where fusion reactions occur, and the external, *edge plasma* or Scrape-Off Layer (SOL) [209, 190]. In the SOL, the magnetic field lines intersect suitably designed solid surfaces called *divertor targets*. The anisotropy of plasma transport, which preferentially occurs *along* the field lines, determines a relatively small wetted area for energetic plasma particles to strike on the divertor targets. The resulting heat fluxes are of the order of tens of MW/m^2, comparable with conditions at the surface of the sun or to a rocket exhaust. In a reactor, these harsh conditions must be withstood 24/7 without the need for frequent component replacement, which would hinder the economic feasibility of nuclear fusion electricity production. This requires to minimize not only the probability of component failure, but also the target erosion arising from the plasma impact. The design of a reliable solution to this challenging Power EXhaust (PEX) problem is among the milestones indicated in the European Research Roadmap to the Realization of Fusion Energy [42].

The strategy adopted for current fusion devices, including the ITER experiment (under construction in Cadarache, France) is based on using actively cooled tungsten (W) *monoblocks* as Plasma-Facing Components (PFCs), while relying on seeded impurities to operate in a condition of partial or full *detachment*, thus minimizing target erosion. The latter would not only pose concerns in terms of divertor lifetime, but also threaten the purity of the core plasma, possibly leading to radiation losses which are incompatible with the fusion performance requirements. Additionally, complete suppression or, at least, mitigation of Edge-Localised Modes (ELMs) is required. ITER operation should prove the feasibility of this scenario in terms of detachment control, high radiation fractions and ELM suppression [220].

However, even if this *baseline* or *ITER-like* strategy will be successfully tested in ITER, this does not guarantee extrapolation to future fusion reactors such as the EU DEMO, whose pre-conceptual design is ongoing within the EUROfusion consortium, for the following reasons:

- the more significant neutron fluence, due to the larger fusion power and foreseen operational time, will lead to component embrittlement over time;
- the fraction of the power entering the SOL which must be radiated in the EU DEMO will be larger, in view of the larger unmitigated heat flux;

- also the fraction of power to be radiated in the core plasma will be larger;
- the larger energy stored in the EU DEMO plasma implies that ELM must be suppressed completely to avoid component damage.

For this reason, alongside with the refinement of this baseline strategy, alternative solutions are being developed within EUROfusion, and even a dedicated experiment, the Divertor Tokamak Test (DTT), is being built at ENEA Frascati, Italy [52, 3, 53].

One possible alternative solution involves the use of Liquid Metal (LM) "shields" to protect the divertor targets. The key strength of this idea is the self-healing nature of a liquid surface, as opposed to a solid one. LM erosion, which is caused by evaporation and sputtering associated to the plasma impact on the target, can indeed be compensated by replenishing the exposed surface with "fresh" LM. By coating the divertor target with a LM-wetted Capillary-Porous Structure (CPS), capillary forces can be exploited to passively "pump" the LM from a reservoir (which could be embedded in the divertor target) to the eroded surface, thus providing the required replenishment – the same working principle as for a candle wick. Using a CPS also prevents undesired droplet ejection by counteracting electromagnetic forces which would otherwise tear the LM layer apart. Moreover, the eroded metal, hereafter called *vapor* for simplicity, is responsible for the *vapor shielding* effect, leading to the radiation of part of the plasma energy before it is deposited on the Plasma-Facing Surface (PFS) [201]. The combined effect of passive replenishment capabilities and vapor shielding might lead to a divertor target featuring a longer lifetime and a superior resilience to transient events. Lithium (Li) and Tin (Sn) are currently regarded as the most promising metals to be used in a Liquid Metal Divertor (LMD).

Among the downsides of LMDs, there is the fact that target erosion can be significant due to evaporation and thermal sputtering acting on top of physical sputtering [7, 2]. This might lead to unacceptable core plasma dilution (in the case of Li) or to intolerable power losses from the core plasma (in the case of Sn) [132]. For this reason, while designing LMD targets, it is of paramount importance to assess their compatibility with an EU DEMO-relevant plasma scenario. This requires to *self-consistently* model the edge plasma and the divertor target erosion, as well as the impact of impurities on the core plasma performance. The problem of simulating an LMD target, considering the interactions of the eroded metal with the plasma, was addressed in the past by means of simplified models [67, 66, 139, 118]. More recently, simulations of the eroded metal transport in the SOL, with a detailed account of its interactions with the plasma, have been performed by means of 2D edge plasma codes, namely UEDGE [169, 164] and SOLPS-ITER [119, 51]. 2D self-consistent simulations were also performed using TECXY [154, 153], and integrated target-edge-core simulations were performed using COREDIV [156].

From this very brief overview on the state of the art of SOL plasma modelling in the presence of an LMD, it can be seen that the problem of self-consistency

has only marginally been addressed. Although self-consistent calculations using TECXY and COREDIV allowed to perform early and extensive parametric scans over reactor operating conditions, some known code limitations, including the simplified treatment of neutrals and the consequent impossibility to deal with detached plasma regimes, limit the applicability range of these codes.

1.1.2 Aim of the first part of the thesis

The discussion above points out the need for **self-consistent** simulations to assess the performance of LMDs in future fusion reactors such as the EU DEMO, comparing the performance of different LMs and LMD designs in terms of:

- peak heat flux to the target;
- impurity transport in the SOL and core contamination.

This work aims at addressing this need in two ways:

1. by adapting existing state of the art modelling tools (SOLPS-ITER);
2. by purposely developing fast-running tools to support the divertor design process.

1.1.3 Summary of key results

SOLPS-ITER simulations of an LM divertor for the EU DEMO

The simplest way to integrate an LMD in the EU DEMO design is to coat the divertor target by means of a CPS while keeping the same shape of the PFC (an *open*, or *ITER-like* LM divertor, schmematically indicated in Figure 1.1).

In this work, the compatibility of an LMD using Li or Sn with an EU DEMO plasma scenario is studied by simulating the transport of the eroded metal and its interactions with the plasma, evaluating the target erosion in a self-consistent way. The SOLPS-ITER code, which is currently the reference code for SOL plasma simulations in support of divertor design within EUROfusion, was employed [211]. SOLPS-ITER provides a 2D multi-fluid description of the charged plasma species (e.g. H^+, Li^+, Li^{2+}, Li^{3+}) and either a fluid or a kinetic description of neutral species (e.g. H^0, Li^0). The outboard midplane electron density at the separatrix was varied from $\sim 40\%$ to $\sim 52\%$ of the Greenwald density, to assess the robustness of the proposed solution to different reactor operating conditions. An external target erosion model was developed and coupled to SOLPS-ITER, to self-consistently account for plasma-vapor interactions. For Li, the study considered a design consisting in a thin (2 mm) W plate covered by a Li-filled CPS, 0.5 mm thick, and actively cooled via a water-gas spray impinging on the back of the plate – the side not exposed to the plasma heat flux [202]. The maximum tolerable heat flux of this design is ~ 20 MW/m^2, the limiting factor being the mechanical stresses on the actively cooled W substrate on which the plasma-facing CPS is placed. For

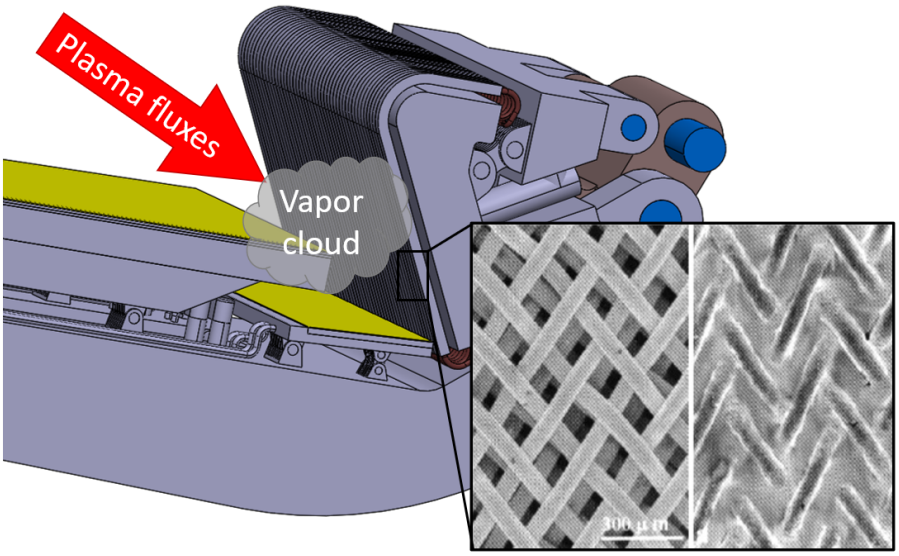

Figure 1.1: Sketch of the EU DEMO baseline divertor (CAD from [126]), with a picture of a CPS from [124].

Sn, a design proposed by ENEA was instead considered [167]. In the present work, this figure is taken as a reference, although it is recognized that the problem could be circumvented by reducing the size of the units, if this is compatible with the adopted cooling strategy. For this design, a 2 mm-thick CPS, intended to continuously resupply the Plasma-Facing Surface (PFS) with liquid Sn passively pumped from an LM reservoir, is placed on top of a CuCrZr heat sink, which is actively cooled by pressurized water (50 bar) flowing in cooling channels. According to design calculations, heat fluxes as large as ~ 40 MW/m^2 can be tolerated, the limiting factor being the Critical Heat Flux (CHF) to the coolant. In the present work, this figure is taken as a reference, although it is recognized that the temperature range of the copper alloy can represent the limiting factor, leading to a lower tolerable heat flux.

A first set of calculations considering only D and Li (or Sn) showed a significant reduction of the target heat load with respect to reference simulations considering only D, thanks to the vapor shielding effect. Nevertheless, the computed peak heat flux to the target (~ 31 MW/m^2 for Li and ~ 44 MW/m^2 for Sn, respectively) was still larger than the power handling limit of the above-mentioned LMD concepts. Moreover, the Li concentration in the pedestal region, which was regarded as a proxy for the core plasma dilution, was computed to be approximately three times larger than the tolerability limit suggested by previous COREDIV simulations [157], even at the largest separatrix density considered in this study. For Sn, the concentration in the pedestal was instead found to be acceptable only at the largest values of the outboard midplane electron density at the separatrix here

considered. These results suggest that the operational window of an LMD using Li or Sn for the EU DEMO without any additional impurity seeding might be too narrow, if it exists, with Sn being more promising than Li.

These results motivated a second set of calculations to assess the effect of seeding Ar in the SOL, aimed at further reducing the target heat load, and consequently the metal erosion rate - a technique adopted in conventional divertors. Increasing levels of Ar seeding were considered. The results indicate that Ar radiation in the SOL effectively replaces Li/Sn radiation in the proximity of the target, thus allowing to operate the LMD in a regime of low target erosion. The resulting operational window for the EU DEMO equipped with an LMD using either Li or Sn in combination with Ar seeding was found to be significantly wider, both in terms of acceptable core plasma contamination and of tolerable peak target heat flux.

Numerical modelling of an LM vapor box divertor for the DTT

A second possible LMD design, inspired by Goldston's *vapor-box divertor*, was also considered [65, 67]. This design involves an Evaporation Chamber (EC) containing an LM pool, corresponding to the plasma strike point. To reduce the flux of metal arising from the evaporation of the pool, a second chamber (called Differential Chamber (DC)) is added. This design, as suggested by Goldston, allows to concentrate strong plasma-vapor interactions, leading to a beneficial strong plasma cooling, within the "boxes", limiting the amount of vapor threatening the core plasma purity, as schematically indicated in Figure 1.2. The reduction of the vapor flux towards the Main plasma Chamber (MC) is achieved by means of the passive pumping provided by condensation. This design, albeit more difficult to integrate in a fusion reactor, could be effective in preventing the vapor leakage towards the plasma core, with the additional benefit of reducing the amount of LM to be recollected from the reactor internal walls.

To study such a system, a new, self-consistent model was developed, and applied to a possible vapor-box divertor for the DTT, which is schematically represented in Figure 1.2. The choice of developing a new, simplified model was motivated by two main facts:

- it is difficult to set up a SOLPS-ITER simulation in a configuration featuring baffles;
- during the pre-conceptual design phase of the system, simplified and fast-running models are required.

The model includes the most relevant aspects of the physics of a vapor-box divertor, as well as some engineering elements. Given the upstream plasma conditions and for a fixed divertor geometry, the code implementing the model computed the plasma heat and particle flux on the LM surface, the thermodynamic state of the metal (liquid and vapor) in the divertor boxes and the temperature distribution in

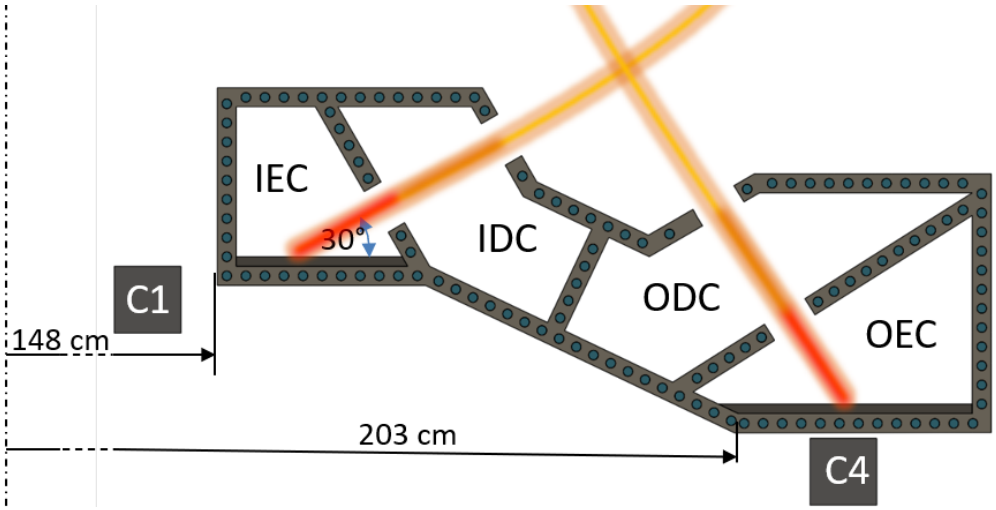

Figure 1.2: Cross section of the DTT closed vapor box divertor geometry. Radial coordinates start from the symmetry axis of the torus. The interaction region between SOL plasma and metal vapor is schematically indicated.

the solid walls. Also for this design, the model is used to compare Li and Sn as possible LM choices, in terms of operating temperatures and of metal vapor flux from the divertor box system towards the main plasma chamber. The results indicate that, for both Li and Sn, this design allows to reduce the impurity flux towards the main plasma by ~ 2 orders of magnitude. However, only for Li the evaporation and radiation cooling are effective in reducing the target heat load, thanks to the relatively large Li concentration inside the boxes.

In perspective, opportunities for validating the modelling strategies described above will arise from the planned implementation of an LM divertor module in the COMPASS and ASDEX Upgrade fusion experiments, as well as from the testing of LM target prototypes in linear plasma devices.

1.2 Liquid Metal-cooled Fast Reactors

1.2.1 Background and motivation

The development of Liquid Metal Cooled Reactors (LMCRs) is currently being pursued within the Generation IV International Forum (GIF) program. GIF promotes the development of sustainable, safe and cost-effective nuclear reactors which minimize the production of long-lived radioactive waste and reduce the risk of proliferation. Among the six selected design, three are characterized by a fast neutron spectrum, which allows to reduce the long-term radiotoxicity of nuclear waste and to improve the fuel utilization efficiency [144, 145]. The second part of the present thesis specifically focuses on Heavy Liquid Metal Cooled Reactors (HLMCRs), which are additionally characterized, among other features, by enhanced intrinsic safety features, do not require coolant pressurization and increase the thermodynamic efficiency of the plant thanks to the large coolant temperatures. Among the currently ongoing European projects in this framework, the Advanced Lead-cooled Fast Reactor European Demonstrator (ALFRED) is being designed by the Fostering ALfred CONsortium (FALCON) international consortium [69]. ALFRED is a 300MW_{th} pool-type prototype aimed at proving the maturity of the Lead-cooled Fast Reactor (LFR) technology, as well as assessing the feasibility of Small Modular Reactors (SMRs) based on this concept.

The design of the core of LFRs is a multidisciplinary task which deals with a large number of tightly interconnected physical/engineering parameters. It can be logically subdivided into Thermal-Hydraulic (TH), NEutronic (NE) and Thermo-Mechanic (TM) design, based on the three most relevant physics involved. The LFR core design procedure involves: deriving guidelines from technological constraints, including safety principles and criteria from the early stages; managing interfaces between the core and other reactor systems; designing individual components, optimizing performance by working on the available margins with respect to the above-mentioned constraints. This process is supported by Design-Oriented Codes (DOCs), i.e. fast-running codes with a clear application domain which can effectively inform design decisions by highlighting the relations between the parameters entering the specific problem. The successive phase consists in *verifying* the design using more detailed codes, the so-called Verification-Oriented Codes (VOCs), which sacrifice computational time and clarity of the relationship between the parameters in favour of accuracy. The design-verification process is then iterated.

Examples of DOCs are ANTEO+ [114, 112], a TH code based on the subchannel (SC) for the analysis of a single sub-assembly (SA), and TEMIDE [111], a TM code for the single fuel pin. A review of the landscape of available and operational DOCs performed at ENEA Bologna pointed out the need to develop a tool for the full-core TH analysis of an LFR [70]. This tool should account for the Inter-Wrapper (IW) flow and heat transfer, eventually coupling multiple instances of a SA code such as

ANTEO+ to simulate the TH behavior of the full core.

Examples of VOCs are the Monte Carlo NE code Serpent [109] and Computational Fluid Dynamics (CFD) codes such as OpenFOAM [206]. Alongside with the native application of VOCs, i.e. design verification, they can also serve as benchmark tools to assess the capability of simplified codes such as e.g. DOCs to correctly simulate the corresponding problem within the anticipated validity domain. However, due to the different structure, level of detail and coupling of these two families of codes, suitable strategies must be developed to successfully carry out such benchmark activities.

1.2.2 Aim of the second part of the thesis

The present work aims at addressing the above-mentioned need for a DOC for the full-core TH analysis of LFRs by developing, verifying and validating such a code. Specific care has been devoted to perform the code design in compliance with Software Quality Assurance Plan (SQAP) procedures. This approach allows to thoroughly document the fact that the tools employed to obtain a given core design have been developed following best practices and validated against experimental data and/or benchmarked against reference codes. This documentation should in turn promote the acceptance of a given design by the safety authorities during the design phase.

Moreover, in view of the above-mentioned need for structured benchmarking procedures to compare simpler codes with VOCs, this thesis aims at identifying a viable benchmark strategy between a multi-physics (NE-TH) code relying on simplified model and corresponding VOCs.

1.2.3 Summary of key results

Design and validation of the TIFONE code

Among the goals of the core TH design of LFRs exploiting the closed SA option, cold by-passes must be avoided and excessive thermal gradients among opposite faces of the assembly ducts prevented. To achieve these goals, a suitable coolant flow outside the assemblies themselves must be guaranteed, compatibly with the Inter-Wrapper (IW) gap, which is established by the core TM design. Moreover, for wrapped assemblies, the possibility of gagging arises, giving an extra degree of freedom to the designer for leveling thermal gradients at the assemblies' outlet. Therefore, the design process requires knowledge of the axial and radial coolant temperature profiles in the inter-wrapper gaps throughout the whole core (i.e., including all core SAs), as well as the axial and perimetrical wrapper temperature profiles, and notably the (possibly) different values of each side of the wrapper itself which could induce SA bowing. In view of the above-mentioned requirements, a

DOC, TIFONE, was developed and verified in compliance with the ENEA software quality assurance requirements. The subchannel (SC) approach was chosen, since it allows to achieve a sufficient level of spatial resolution while retaining the key features of a DOC, namely equilibrium, a low computational time and a clear application domain. The current version of TIFONE solves, for an LFR exploiting the closed SAs option in hexagonal geometry, the inter-SAs coolant mass, energy and momentum equations, as well as the convection equations between the coolant and the wrapper. The calculation domain extends radially over the IW region of the entire core, and axially between the dividing and the merging points of the inter- and intra-SAs coolant flows, see Figure 1.3. Among the perspective applications of TIFONE is the coupling with codes for the thermal-hydraulic analysis of the single SA, such as ANTEO+, so to allow for a full-core simulation. The code has been preliminarily validated against experimental data from the KALLA IW flow and heat transfer experiment. This first application of TIFONE confirmed its ability in reproducing the measured data in its anticipated validity domain.

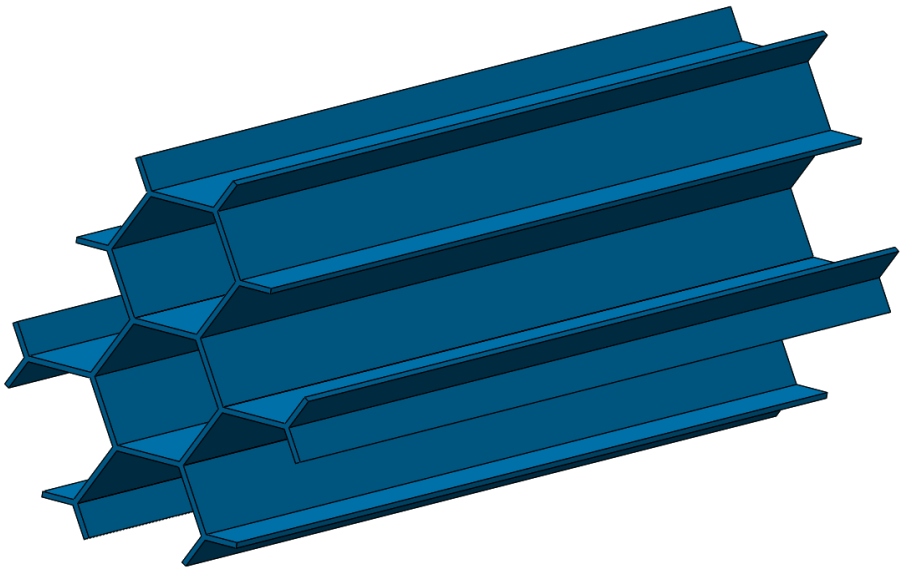

Figure 1.3: Sketch of the inter-wrapper flow domain considered in TIFONE.

Benchmark of the FRENETIC code

The neutron kinetics in an LFR core is generally faster with respect to an Light Water Reactor (LWR) core, due to the relevant presence of plutonium in the nuclear fuel. This fact calls for the correct simulation of the NE/TH coupling in order to reliably assess the core performances. In view of this necessity, within the framework of Italian activities aimed at deploying the LFR technology, during the last years

Politecnico di Torino has been developing the Fast REactor NEutronics/Thermal-hydraulICs (FRENETIC) code for the multiphysics analysis of liquid-metal cooled cores. The code aims at the NE and TH coupled simulation of the steady state and transient behavior of the full core of LMCRs adopting a closed SA design. To achieve this ambitious goal while keeping the simulation time reasonably low, FRENETIC adopts simplified physical models, namely:

- a multigroup neutron diffusion model, spatially discretized with a coarse mesh nodal method at the SA level;
- a 1D advection/diffusion model for the coolant flowing within each SA, accounting for the inter-SA heat transfer via a thermal resistance model to achieve a quasi-3D solution.

In the past years, the individual modules of the FRENETIC code have been benchmarked against other computational tools and validated against experimental data (e.g. TH validation against RELAP). More recently, the multi-physics capabilities of the code have been validated against experimental data from the EBR-II SHRT-45R test in the frame of a Coordinated Research Project of the International Atomic Energy Agency [25]. That activity allowed to identify some necessary developments to be carried out in FRENETIC, such as the inclusion of a model for the photon and decay heat.

Although FRENETIC is not strictly speaking a DOC, since it is a multi-physics tool aimed at full-core transient simulations, it is based on simplified models, and therefore its benchmark falls within the above-mentioned area of research - to compare simplified codes with reference VOCs. For this reason, in view of the continuous testing and validation of FRENETIC, in this work a steady-state benchmark has been performed against more detailed numerical codes that allow to obtain accurate solutions at the fuel pin level, and can therefore be regarded as a reference. Specifically, the following two codes have been selected:

- a full-core neutron transport code based on the Monte Carlo (MC) method (Serpent-2) [109];
- a Computational Fluid Dynamics (CFD) code (OpenFOAM) [206].

Due to the significant computational cost associated to a full-core simulation performed by coupling Serpent-2 and OpenFOAM, a direct comparison of the FRENETIC results with a full-core solution from the detailed model remains prohibitive, even in steady state. For this reason, a benchmark strategy that circumvents this problem has been devised and implemented, showing satisfactory results for what concerns both the NE and TH calculations.

Part I

Liquid metal divertors for nuclear fusion reactors

Chapter 2

Nuclear fusion reactors and the problem of power exhaust

Nuclear fusion has the potential to provide almost unlimited, carbon-free electricity without producing long-lived radioactive waste. The most promising fusion reactor concept is the *tokamak*, involving the confinement of a hot, ionized gas (the *plasma*) by means of magnetic fields. Due to the anisotropy of plasma transport, which occurs preferentially *along* magnetic field lines, the wetted area available for the plasma to strike on specifically designed surfaces, the *divertor targets*, is relatively small, resulting in significant heat and particle fluxes. This can lead to melting and erosion, threatening both the integrity of the Plasma-Facing Surface (PFS) and the core plasma performance, since eroded particles cause harmful core plasma radiation which could hinder the fusion process. The extrapolation of the currently available solutions to this Power EXhaust (PEX) problem to future fusion reactors such as the EU DEMO is subject to considerable uncertainties, mainly due to the larger amount of energy stored in the core plasma and to the presence of significant neutron irradiation. For this reason, alternative strategies are being considered, including self-healing liquid metal divertors.

This chapter aims at providing a very brief introduction to the problem of power exhaust in future fusion reactors, to motivate the development of advanced solutions such as liquid metal divertors. An introductory description of nuclear fusion reactors, including the most favourable fusion reaction and the arrangement of the confining magnetic fields, is provided in section 2.1. In the same section, the role of the ITER experiment and of the EU DEMO reactor along the path towards the realization of fusion electricity is described. The terminology for describing the problem of the power exhaust, which shall be employed throughout part I of the thesis, is introduced in section 2.2. In the same section, the problem associated to plasma heat and particle fluxes impinging on the divertor is described, together with the role of impurities. The present-day solutions are briefly reviewed, and the need for alternative strategies is pointed out.

2.1 Nuclear fusion reactors

2.1.1 The most favourable fusion reaction

Nuclear fusion has the potential to provide almost unlimited, carbon-free and intrinsically safe energy without producing long-lived radioactive waste.

Nuclear fusion reactions involve the merging of light elements, typically hydrogen (H) isotopes, which occurs with an energy release, essentially due to the shape of the binding energy per nucleon curve, reported in Figure 2.1 (left). The stars, including our sun, are powered by fusion reactions, the most favourable of which, in terms of reaction rate at viable plasma temperatures, is the one involving deuterium (D) and tritium (T):

$$ {}^{2}_{1}\mathrm{D} + {}^{3}_{1}\mathrm{T} \longrightarrow {}^{4}_{2}\mathrm{He}\,(3.5\,\mathrm{MeV}) + n\,(14.1\,\mathrm{MeV}) \tag{2.1} $$

The D-T reaction is the one targeted in present and near-future fusion devices. As shown in Figure 2.1 (right), the temperatures required to achieve a large D-T fusion reaction rate are in the order of $\sim 100 \cdot 10^6 K$, larger than those found at centre of the sun. At these temperatures, the reactants are in the *plasma* state, i.e. they are:

- ionized;
- electrically neutral;
- dominated by collective effects.

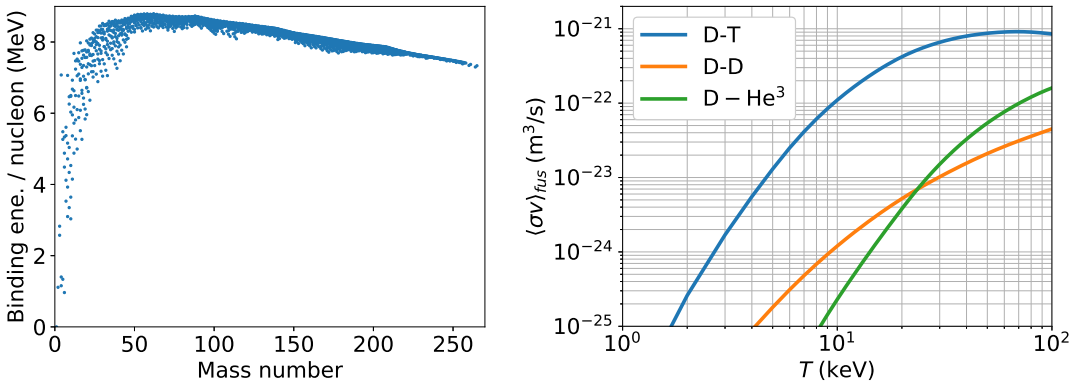

Figure 2.1: Binding energy per nucleon vs. mass number (left) and reaction rates for three fusion reactions (right). Data from [13] and [85], respectively.

2.1.2 Magnetic confinement of plasmas and the tokamak

The first part of the present thesis work deals with magnetically confined fusion reactors. The most promising fusion reactor concept is the tokamak, involving the

confinement of a hot, ionized gas (the *plasma*) away from the tokamak chamber walls by means of magnetic fields. The tokamak concept currently represents the main focus of nuclear fusion research efforts in the EU [42]. The word *tokamak* derives from the russian ***to****roidalnaya* ***ka****mera s* ***ma****gnitymi* ***ka****tushkami*, meaning "toroidal chamber with magnetic coils" [209]. Indeed, in a tokamak, the plasma is confined in a toroidally-shaped device by means of magnetic fields.

It can be shown that various magnetic field components are required to properly confine the plasma [62]. The components devoted to the production of each field component are as follows:

- the toroidal field coils produce a relatively large toroidal field;
- the ohmic transformer, or central solenoid, induces the toroidal plasma current, which in the tokamak concept is used to generate the required poloidal field component;
- the vertical field coils produce a vertical field required for the toroidal force balance;
- additional shaping coils allow to achieve a non-circular plasma cross-section, which is beneficial in terms of improved MagnetoHydroDynamic (MHD) stability limits.

A conceptual schematic of the magnet system required for a tokamak is shown in Figure 2.2.

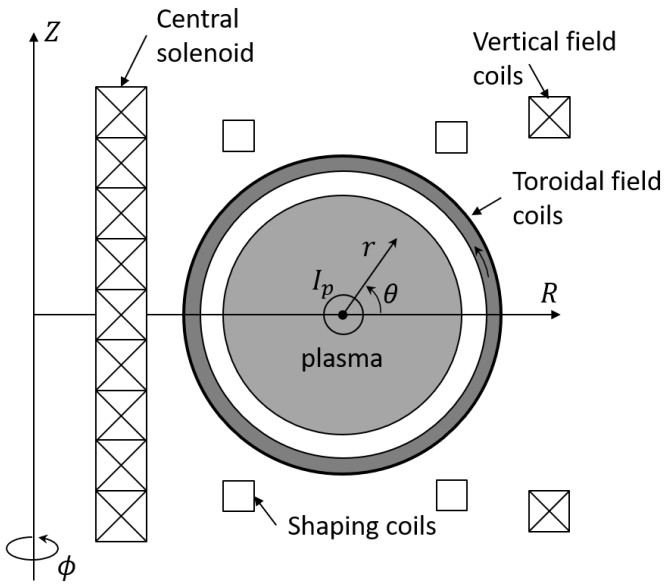

Figure 2.2: Schematic of the magnet system of a tokamak.

In a tokamak, ions and electrons are mostly constrained to spiral around magnetic field lines, whereas neutrons escape the plasma as soon as they are produced. Therefore, neutrons do not participate in sustaining the fusion reaction, but rather

are only employed in the energy production (they are stopped in the *blanket*, where they release their kinetic energy) and in the breeding of T. The fusion reaction is instead sustained *thermally* by the alpha particles which are confined and release their energy within the plasma, thereby contributing to its heating, together with some level of auxiliary heating or current-drive power. These power sources are necessary to maintain the temperature, and hence the fusion reaction rate, sufficiently large.

2.1.3 The role of ITER and of the EU DEMO

The next-step fusion machine, ITER, is currently being built in France. Its role is to bridge the knowledge gap - in terms of both physics and engineering - between current fusion experiments and the first demonstration power plant - the EU DEMO, see Figure 2.3. ITER should address issues related to plasma confinement and transport, MHD stability, operational limits and disruptions, power and particle control, physics of energetic ions, plasma auxiliary heating and current drive, measurement of plasma parameters, plasma operation and control.

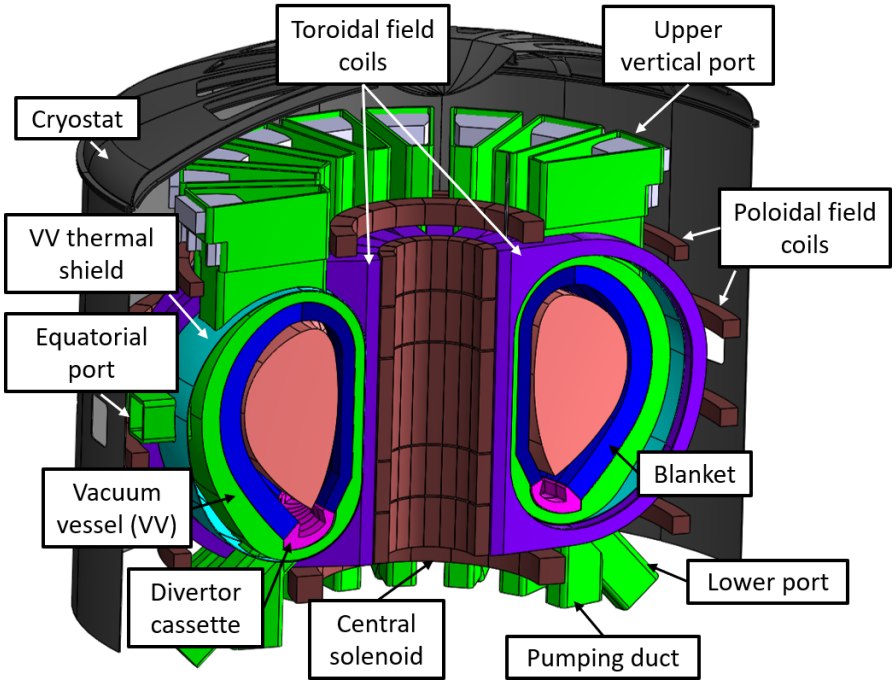

Figure 2.3: CAD model of the EU DEMO from [126], with the main components indicated.

2.2 The problem of power exhaust

2.2.1 Terminology

The edge or boundary plasma can be defined as the region in which the plasma (dynamics, composition, ...) and the vessel components are directly and strongly mutually affected [163]. The edge plasma is separated from the core plasma by the *separatrix*, i.e. the Last Closed Magnetic Surface (LCMS). Indeed, outside the separatrix, magnetic field lines intersect solid walls, and are therefore usually called "open" field lines. The plasma crossing the separatrix enters the edge region, also called Scrape-Off Layer (SOL), where it is preferentially transported *along* field lines, leading to a relatively small plasma-wetted area of the PFCs, which in turn determines strong Plasma-Wall Interactions (PWI).

In present-day experiments, two different strategies are employed to identify the LCMS. The first is the *limiter*: a metallic surface protruding inside the plasma chamber defines the boundary between closed and open field lines, thus generating the separatrix mechanically. One example of a tokamak using a limiter is Frascati Tokamak Upgrade (FTU). The second strategy is the *divertor*, which relies on an additional coil to divert the poloidal magnetic field, thus creating an *X-point* or *null* where $B_\theta = 0$. The divertor configuration is more suitable for tokamaks such as ITER and the EU DEMO, as it allows to confine plasma-wall interactions relatively far from the plasma core, thus reducing the consequent plasma contamination. Moreover, the open field lines are forced to intersect the physical wall of the tokamak in a specific region, that can be equipped with suitably designed Plasma-Facing Components (PFCs) to withstand the resulting heat and particle loads for a sufficiently long time. A schematic representation of a diverted plasma is reported in Figure 2.4.

2.2.2 Heat and particle fluxes to the target

The radial extension of the SOL in a fusion reactor is expected to be of several cm, with a power fall-off length measured at the OMP of a few mm for the EU DEMO [48]. With such a limited radial extension, even accounting for various strategies focused at increasing the plasma-wetted area (e.g. carefully shaping the target plates at a shallow angle with respect to the magnetic field [155], or flaring the field itself near the plates [4]), it can be estimated that the total surface available for power exhaust will not exceed a few square metres. On the other hand, the power crossing the separatrix, which is then anisotropically transported along the edge plasma region via plasma advection/conduction, must be kept above the level necessary to sustain the H-mode operating regime [120]. This plasma operating regime is characterized by favourable temperature and density profiles in the core,

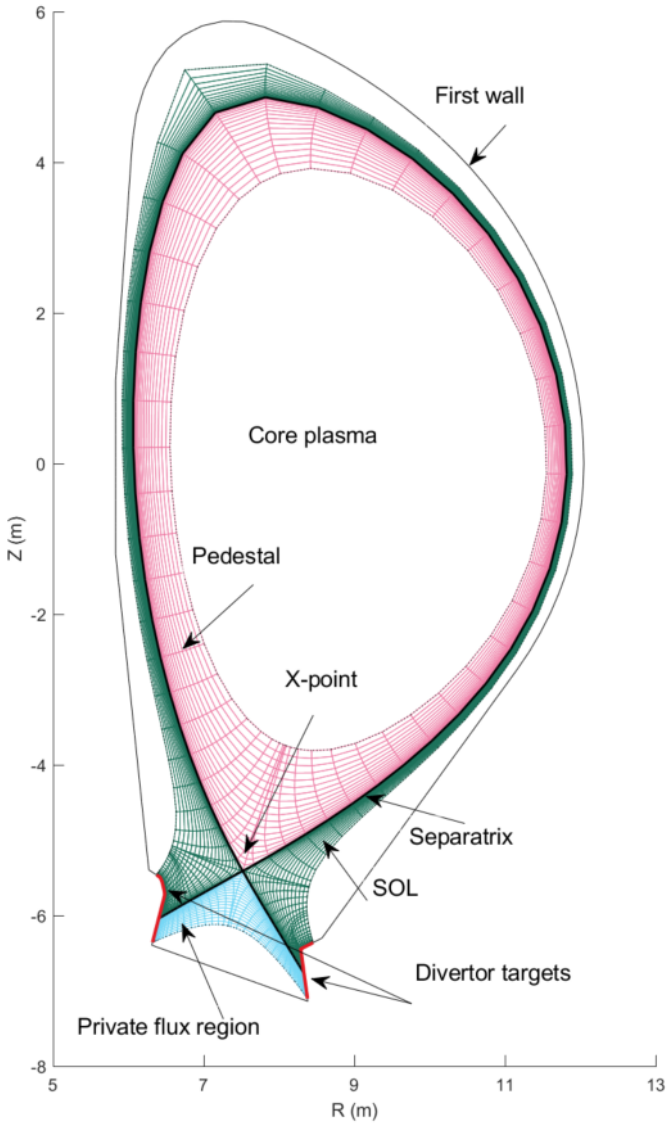

Figure 2.4: Sketch of a diverted SOL with the most relevant plasma regions indicated. The drawing refers to the cross section of the EU DEMO 2017 design, and to the corresponding magnetic equilibrium [208].

which promote high-performance tokamak operation. Typical estimates for the L-H transition threshold are of about 100 MW (ITER) or 150 MW (EU DEMO), possibly leading to peak heat fluxes of several tens of MW/m^2 to be exhausted at the divertor plates in steady state. On top of these large heat fluxes, if the plasma in contact with the solid wall is too hot, impinging ions cause significant *sputtering* of the divertor targets. The upper bound for the plasma temperature at the target has been estimated to be $\sim$ 5 eV [207] if the wall is made of W, as is expected

for, e.g. the ITER and EU DEMO divertors. The concern associated to sputtered wall atoms arises from the possibility that they enter the *core plasma* - i.e. the region of closed magnetic field surfaces, see again Figure 2.4 - where they can cause radiation losses, thus cooling the plasma and hindering the thermally sustained fusion process.

2.2.3 The role of impurities

Impurities, i.e. atoms other than the fusion reactants (D and T), are always present in a fusion plasma. Indeed, α particles represent *intrinsic* impurities, meaning that they are inherent to the fusion process. Moreover, additional impurities arise due to the interactions of the plasma with the wall (both in limiter and divertor configurations). It is convenient to provide here a very brief overview of the beneficial and detrimental effects of impurities, distinguishing between the light ones (low-Z), and the heavy ones (high-Z). This topic will be discussed in greater detail in section 3.5.

Impurities interact with the plasma via a number of processes which will be described in section 3.5. Here it shall be sufficient to mention the fact that impurities cause *plasma cooling*, e.g. by radiating the plasma power via *line radiation* and *bremsstrahlung*. Plasma cooling is desirable if it occurs in the SOL, since it contributes to radiating plasma energy, possibly leading to plasma detachment. On the other hand, should it occur in the core plasma, this would negatively affect the plasma energy balance, possibly hindering the fusion process. Moreover, if present in sufficiently large densities, impurities can cause core *plasma dilution*, determining an intolerable reduction of the fusion power density.

With respect to the above-mentioned phenomenology, low-Z and high-Z impurities behave differently:

- Most light (i.e. low-Z) impurities in the core plasma are fully stripped of electrons. Therefore, they no longer produce line radiation in the core plasma of e.g. ITER, and *bremsstrahlung* represents the only contribution to plasma cooling. Since the bremsstrahlung radiated power density in a given plasma region is proportional to Z_{eff}, the effective charge, tolerable core concentrations of low-Z impurities are relatively large, the limiting factor being core plasma dilution rather than excessive radiation losses.
- On the other hand, heavy (i.e. high-Z) impurities such as W are typically not fully stripped of electrons before entering the core plasma. For this reason, line radiation occurs even at core-relevant temperatures, on top of the ubiquitous bremsstrahlung losses, which are more significant for high-Z impurities due to the above-mentioned dependence on Z_{eff}. This leads to very low tolerable core concentrations, limited by excessive radiation.

2.2.4 Present-day solutions

The above mentioned constraints, together with the significant neutron fluence expected in a fusion reactor, make the task of selecting a satisfactory material combination and engineering design for the PFCs very challenging if one relies on the currently available technologies. For this reason, the identification of a strategy to solve the Power EXhaust (PEX) problem in future fusion devices is among the milestones indicated in the recently updated European Research Roadmap to the Realisation of Fusion Energy [42]. The envisaged strategy for ITER foresees the use of actively cooled W *monoblocks* (with enhanced heat transfer via swirl tapes) as divertor plates, in combination with impurity injection in the edge plasma to enhance radiation in the SOL while keeping it as low as possible in the core. The physics basis of this strategy consists in the fact that radiated energy propagates isotropically and is therefore, in principle, spread over the entire chamber surface. Therefore, if the plasma power is transferred from the strongly anisotropic "advection/diffusion channel" to the "radiation channel", the peak heat flux is expected to be reduced. Additionally, plasma cooling (together with momentum exhaust) should allow to access *partially detached* plasma operation [220], which guarantees low plasma temperatures at the target and consequently a reduced sputtering.

However, there is currently no certainty that it is possible to radiate a sufficient fraction of the power crossing the separatrix before it is conducted to the solid walls (it can be estimated that at least 85% of the power entering the edge would need to be dissipated isotropically [207]). Moreover, massive impurity injection may lead to radiation clustering, giving rise to near X-point instabilities such as Multifaceted Asymmetric Radiation From the Edges (MARFEs) [190]. For the EU DEMO, this baseline strategy should allow to reduce the heat load on the PFCs below 20 MW/m^2 during transient events and 10 MW/m^2 in steady state [220].

2.2.5 The need for alternative strategies

It is at present unclear whether the baseline solution will extrapolate to the even harsher environment of a future fusion reactor (such as the EU-DEMO, whose preconceptual design is ongoing within the EUROfusion consortium). In a DEMO-class reactor, W is subject to a high neutron fluence. Solid PFCs might fail due to macrocracking, exceeded Critical Heat Flux (CHF) leading to component melting, fatigue failure, net material erosion. Moreover, the energy associated to any large unmitigated Edge-Localised Mode (ELM) or Vertical Displacement Event (VDE) would likely lead to component failure. In this case, replacing the component could take $\sim$ 6 months.

For this reason, alongside with the refinement of the baseline approach, alternative solutions are being investigated, including LMDs [143, 102]. Furthermore, the cited roadmap foresees the constuction of a dedicated Divertor Tokamak Test

(DTT) facility to reproduce DEMO-relevant scenarios in terms of heat exhaust. This experiment will shortly begin construction at ENEA Frascati, Italy [52, 53, 3]. This facility would cover a range of the DEMO parameter space which cannot be studied in ITER and therefore provide answers in time for DEMO operation startup, and assess alternative solutions for the power exhaust problem in future fusion reactors, including an LM divertor [52].

Chapter 3

The liquid metal path towards the solution of the power exhaust problem

LMDs are among the alternative solutions to the power exhaust problem in fusion reactors currently being developed alongside with the baseline strategy, which relies on solid (W) divertors, detached plasma via impurity seeding and ELM mitigation/suppression [220].

A liquid surface would avoid cracking/mechanical failure, thus promising a longer lifetime. Moreover, it could be more resilient to power excursions (e.g. ELMs). On the other hand, the erosion rate from a liquid surface can be significantly larger with respect to the one of a solid one, due to the presence of thermally activated processes such as evaporation. This would possibly lead to core plasma contamination, and to the necessity to devise a scheme to recollect and recirculate LM condensed on the FW. Moreover, liquid PFCs are globally less technologically mature with respect to solid ones.

This chapter aims at providing a brief introduction to the subject of LMDs, including their main advantages and disadvantages, as well as the relevant design criteria. The potential advantages and main drawbacks of LMDs, as compared to solid targets, are summarized in section 3.1. In the same section, the Capillary-Porous Structure (CPS) concept is described, and experimental activities carried out worldwide are mentioned. The characteristics and properties of the two most extensively studied LMs, Lithium (Li) and Tin (Sn), are reported in section 3.2. An overview of LMD concepts is presented in section 3.3. A list of design criteria and requirements driving the LMD development within EUROfusion and a brief description of a design recently developed by ENEA Frascati are provided in section 3.4. Finally, the phenomenology of interactions between the SOL plasma and an LM surface are summarized in section 3.5.

3.1 Introduction and state of the art

The use of LMs as PFCs was first proposed in the 90s [68, 55], in the form of a slow-flow LMD based on the CPS concept. From that point on, a series of fundamental physics studies [11, 91] and experiments [93, 105, 123, 130, 95] has been performed in a number of research institutions worldwide. The original motivation for implementing LMDs consisted in the beneficial effect of Li in plasma discharges, in terms of improved confinement, plasma purity, low recycling and consequently enhanced performance. Moreover, Mirnov et al. [129] showed that Li could be used as an impurity to cool the SOL plasma. This cooling could be very effective due to the presence of strong non-coronal effects.

3.1.1 Potential advantages

Availability of additional heat exhaust channels

For a solid divertor, the available paths to exhaust the power anisotropically advected/conducted along the SOL consist in radiation due to seeded impurities and heat conduction to the coolant - once the power has reached the divertor target. A liquid surface additionally allows to exploit the latent heat of vaporization (*evaporation cooling*). Moreover, evaporated metal interacts with the near-target plasma, leading to the *vapor shielding* effect, causing an additional amount of plasma power to be radiated before reaching the target [56, 201].

Passive replenishment of the surface

Both solid and liquid PFCs are eroded by the impact of plasma heat and particles. On the one hand, the erosion of a liquid surface is generally more significant due to the presence of, e.g., evaporation. On the other hand, a liquid surface can be continuously replenished, thus compensating for the erosion losses and preventing the need to frequently replace the PFC. In case a CPS is employed to constrain the LM, the replenishment can be performed *passively*.

Absence of thermo-mechanical stresses on the PFC and resistance to neutron damage

One of the main issues limiting the lifetime of a solid divertor is the presence of thermo-mechanical stresses, potentially leading to component failure. In the case of an LMD, the most loaded surface (i.e., the PFS) is liquid, and therefore immune to those stresses, which are also absent at the interface between the CPS and the solid substrate [204]. Of course, the solid substrate itself would instead be subject to those stresses. A similar reasoning suggests that, for an LMD, neutron loading effects would be less threatening to the component integrity.

Resilience to off-normal events

The combined characteristics of being self-healing and of vapor shielding can allow these components to be more forgiving in case of an unmitigated ELM, or even of a VDE [165].

3.1.2 Main disadvantages

Possible plasma contamination

As mentioned above, a liquid is more easily eroded with respect to a solid, since evaporation occurs, and sputtering itself could be enhanced. This could lead to unacceptable core plasma dilution (in the case of a low-Z LM such as Li) or to intolerable core radiation losses (in the case of a high-Z LM such as Sn). Therefore, an LMD should be operated at sufficiently low surface temperatures, so that evaporation is kept sufficiently low. This can be achieved by a combination of:

- exhausting most of the plasma heat via isotropic radiation before it reaches the liquid surface - via purposely seeding impurities such as Ar in the SOL;
- designing the target aiming at a low thermal resistance between the PFC and the coolant.

It is clear from the foregoing discussion that self-consistent modelling of the target evaporation and SOL plasma behavior is of paramount importance to support the design of LM PFCs, especially for what concerns the identification of a plasma scenario which is compliant with the requirement of low evaporation.

Material recollection

This issue is tightly related to the foregoing one: in case of exacerbated LM target evaporation, a significant amount of LM should be recollected from the FW, recirculated, purified and eventually made again available. The need to close the LM loop would represent a significant engineering challenge, in terms of integration with other components. This is an additional reason for designing an operational scenario where the LMD surface temperature is kept low.

Technological readiness

In view of their application to ITER and DEMO, solid (W) divertors have been extensively studied, designed and tested, both in Linear Plasma Devices (LPDs) and in tokamaks, during the last 30 years. LM targets are instead much less mature in this respect.

3.1.3 The CPS concept

Among the proposed LMD concepts, the one adopting an LM-filled CPS as the PFS is currently considered to be the most mature [143]. The effectiveness of capillary forces in preventing LM droplet ejection and splashing phenomena, as well as the capability of this concept to withstand large plasma heat fluxes (of several tens of MW/m^2), have indeed been demonstrated experimentally both in tokamaks and in linear plasma devices [128, 123, 124, 133]. The most attractive feature of a CPS-based LMD is its self-healing nature: the PFS is indeed passively replenished by capillary forces, thus compensating for the relatively large erosion rate of an LM target, which is caused by both sputtering and evaporation, as mentioned above. A CPS can thus be used in PFCs to form, confine and redistribute homogeneously LM film on surfaces (self-sustaining system). This fact, together with the absence of thermo-mechanical stresses in the CPS itself and at the interface between the CPS and the solid substrate, and to the presence of vapor shielding, have the potential to guarantee a longer divertor lifetime and a superior resilience to transient events with respect to the currently considered baseline solution [132]. Moreover, eroded metal could be condensed and captured on the CPS surface of a zone far from the strike point, thus reaching a regime of passive recirculation.

The porous matrix can be obtained by means of wire meshes, metal felt, sintered metal powder, sintered braid or other options. Two pictures of a CPS based on W wires, before and after being wetted by Sn, are reported in Figure 3.1.

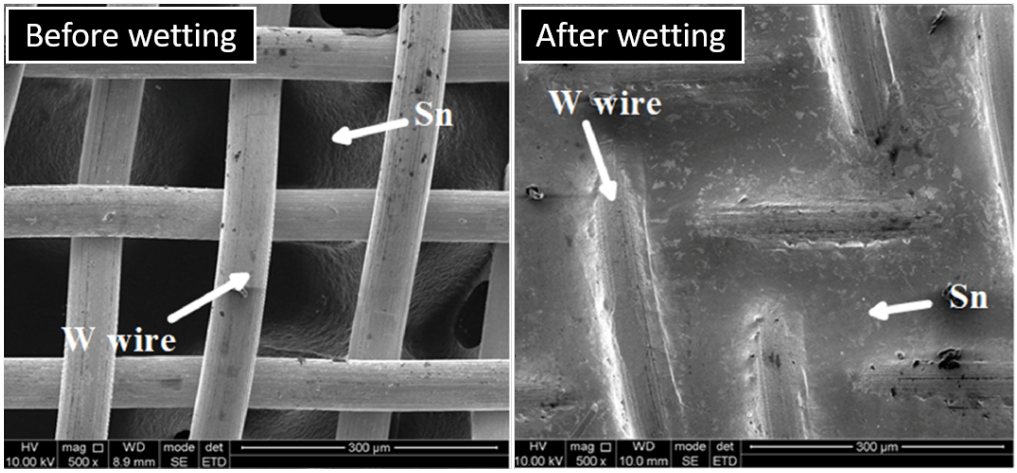

Figure 3.1: Picture showing a CPS based on W wires, before (left) and after (right) wetting. Adapted from [213].

The ability of a CPS to compensate LM consumption is determined by the pressur balance, which can be stated via the following inequality:

$$P_c \geq \Delta P_L + \Delta P_G + \Delta P_F + \Delta P_{MHD} \tag{3.1}$$

where:

- P_c is the capillary pressure
- ΔP_L is the hydraulic pressure drop in the CPS
- ΔP_G is the hydrostatic pressure drop
- ΔP_F is the pressure drop occurring at the evaporating surface due to the liquid - vapor phase transition
- ΔP_{MHD} is the pressure drop due to MHD effect on the flowing LM

The capillary force P_c is determined as: $P_c = \frac{2\sigma\cos(\theta)}{r_{eff}}$, where θ is the wetting angle, r_{eff} is the CPS pore radius and σ is the surface tension of the LM.

3.1.4 Liquid metal experiments

Experiments in linear plasma devices

Experiments in LPDs play a crucial role in the characterization of PWIs, allowing to expose targets to plasma conditions similar to those expected near the strike point of e.g. the EU DEMO while avoiding the complications associated to the tokamak environment. LM targets have been, and are being, exposed to linear plasmas to study plasma-vapor interactions [201], power handling capabilities of the concepts [132] and/or issues associated to D retention [36]. A schematic of a typical configuration of an LM target exposure in Pilot-PSI (DIFFER, Eindhoven) is shown in Figure 3.2.

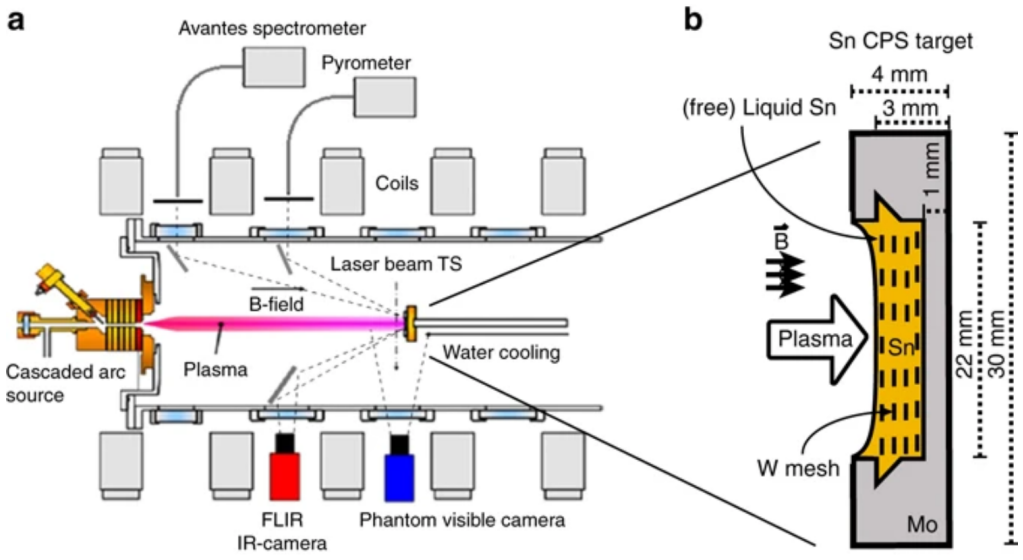

Figure 3.2: Schematic of the linear plasma generator Pilot-PSI (left) and liquid target design (right), reproduced from [201].

Experiments in tokamaks

In Italy, since 2006, pioneering work has been performed in Frascati Tokamak Upgrade (FTU) with a liquid Li limiter, pictured in Figure 3.3 (left). More recently, an improved (actively cooled) Li limiter has been installed and tested, see Figure 3.3 (right). Figure 3.5 (left) shows the green light associated to the Li^+ most intense line in the visible range, typically observed in the FTU experiments when a regime of high evaporation is entered.

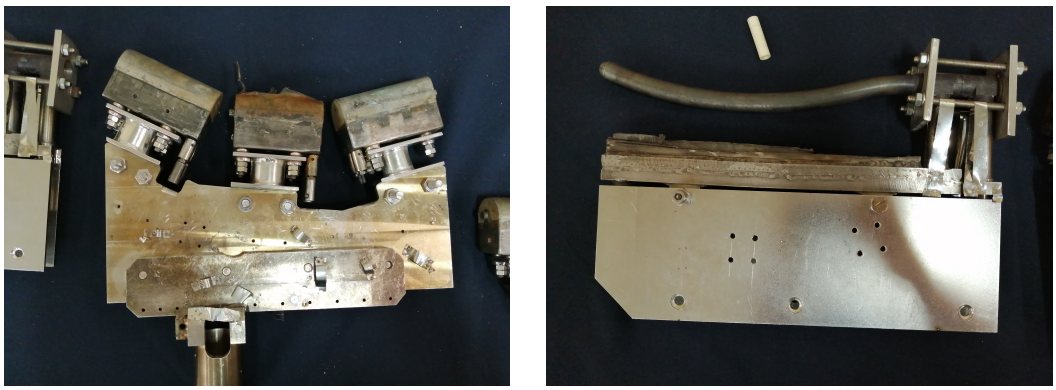

Figure 3.3: Photographs of the liquid lithium limiter (left) and of the cooled lithium limiter (right).

The National Spherical Tokamak Experiment (NSTX) at Princeton Plasma Physics Laboratory also has a long operating experience with lithium-coated plasma facing components [92].

Very recently, an LM CPS module has been installed in the COMPASS divertor. The experimental setup is shown in Figure 3.4 (left) and the CPS module is shown in Figure 3.4 (right). Figure 3.5 (right) shows instead a visible picture during a typical COMPASS discharge with the LM CPS module.

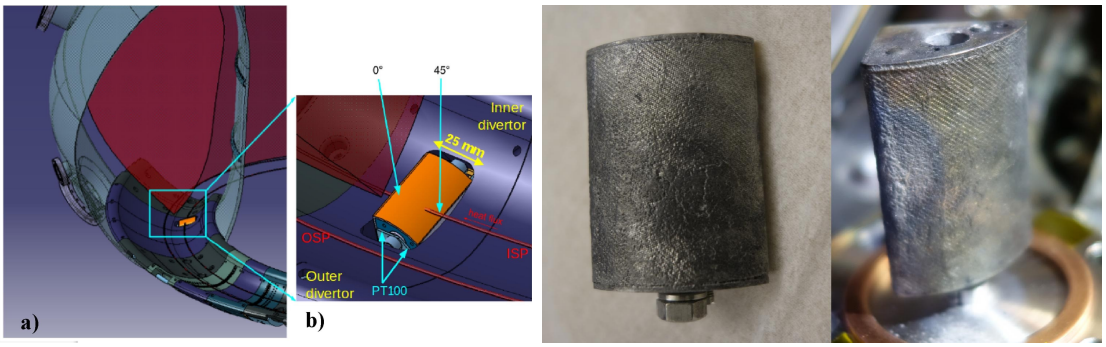

Figure 3.4: Experimental setup (left) and photos of the CPS target for the COMPASS experiment (right), reproduced from [38].

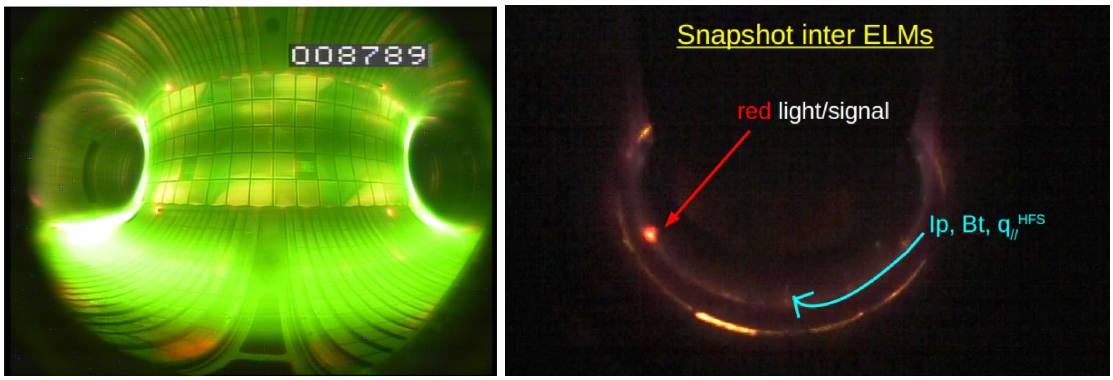

Figure 3.5: Visible picture of Li radiation in the FTU tokamak [86] (left) and visible picture of COMPASS experiment, reproduced from [38].

3.2 Choice of the liquid metal

In the following, the features of the most extensively studied LMs to be used for an LMD, Li and Sn, are compared. Their properties are compared in Table 3.1. It should be noticed that early experiments also considered gallium (Ga), see e.g. [127], and that this LM is still considered especially for applications involving flowing LMs. However, it has not been considered in the present thesis, mostly due to the fact that EUROfusion is currently oriented towards Li and Sn. This choice is mostly associated to compatibility issues with candidate materials for the CPS and substrate [86].

Quantity	Unit	Meaning	Li	Sn
Z		Charge	3	50
A	amu	Mass number	6.94	118.7
ρ	kg/m^3	Density at melting temperature	512	6990
T_m	°C	Melting temperature	180.5	231.9
T_b	°C	Boiling temperature	1347	2270
ΔH_{vap}	$\cdot 10^6$ kJ/kg	Latent heat of evaporation	1.02	35.15
k	W/(m K)	Thermal conductivity at melting temperature	45	30
E_{iz}	eV	First ionization potential	5.39	7.34

Table 3.1: Li and Sn properties.

3.2.1 Lithium

Li has first been proposed as a plasma-facing LM due to its low Z, which makes it more tolerable, should it reach the core plasma. Moreover, experiments carried out on several fusion devices have shown that the presence of Li in plasma discharges is responsible for an attractive improvement of the machine performance in terms of confinement and reduced presence of impurities (especially O), mostly associated to the capability of operating in low-recycling regime [148]. On the other hand, the straightforward issues associated to Li are the retention of T and the high evaporation rate (see Figure 3.6), which may lead to excessive plasma dilution. As for T retention, it has been shown that it becomes negligible at temperatures above $\sim$ 650 K, due to dissociation of LiD (or LiT) [54, 8]. Therefore, for slow-flow, high temperature LM concepts such as the ones relevant for the present thesis (as opposed to fast-flow, low temperature concepts, see section 3.3), hydrogen (and therefore T) retention are considered not to be relevant. Conversely, the potentially excessive evaporation rate of Li indeed represents a significant concern.

The current knowledge on the subject suggests that, for a slow-flow LM divertor employing Li, it is necessary to employ a confining structure for the vapor such as the Goldston's vapor box divertor [65] or to employ a concept such as the emitter-collector suggested in [130].

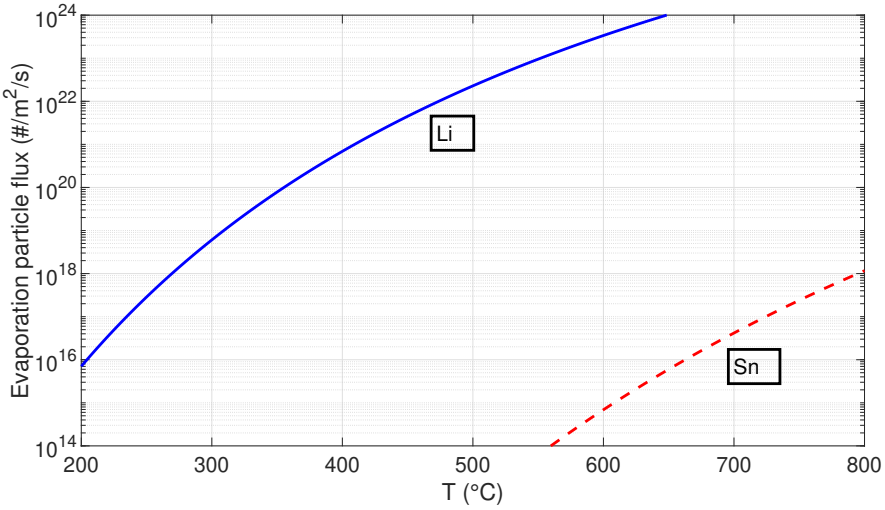

Figure 3.6: Evaporation flux for Li and Sn as a function of temperature, evaluated following the Hertz-Knudsen relation [174].

3.2.2 Tin

As mentioned above, the temperature range of Li for slow-flow LMD concepts such as the one of interest for the present thesis would likely be too large to allow for low recycling operation. Since that originally represented the main reason for choosing Li, other LMs have started to be considered, with particular emphasis on Sn. The matter of H (D/T) retention in liquid Sn is currently a debated topic. Indeed, very low D retention values were measured by Loureiro et al. [115] and by Cremona et al. [36], but the relatively narrow range of D energies and fluxes investigated in these works called for further studies. More recently, Manhard et al. exposed a liquid Sn-filled crucible - without a CPS - to a D plasma, observing the formation of gas bubbles deep inside the liquid layer [117]. The authors of that study suggested that, based on the equilibrium between formation and decay of metastable *stannane* (SnD_4) molecules, these phenomena could lead to enhanced D retention. However, the experimental setup adopted for that study is believed not to be directly relevant for a CPS-based liquid Sn divertor. Another study by Ou et al. recently measured D retention for a CPS-constrained liquid Sn layer exposed to D plasma [149], showing retention levels around two orders of magnitude larger with respect to pure tungsten, with D retained at the Sn-wall interface found to be the dominant contribution and very low retention in pure Sn itself. Further studies will be necessary, but it can be stated that the currently available knowledge on the subject does not discourage the use of Sn [167].

The lower evaporation rate of Sn (see again Figure 3.6) with respect to Li for a given surface temperature should lead to a lower flux towards the main plasma and could in principle be employed without a box-structure, resulting in an ITER-like LMD. Nevertheless, it cannot be excluded a priori that enough Sn can be evaporated to sustain a high-radiation regime in a closed divertor.

As a final remark, it is interesting to notice that Sn is a good radiator not only at core-relevant plasma temperatures, but also in the temperature range which is relevant for the plasma edge, see Figure 3.7. This might mean that a much lower Sn density would need confinement within a box structure to achieve plasma cooling comparable to the one obtained with Li. Again, since the balance between the various aspects hereby mentioned is not straightforward, dedicated modelling is strongly motivated.

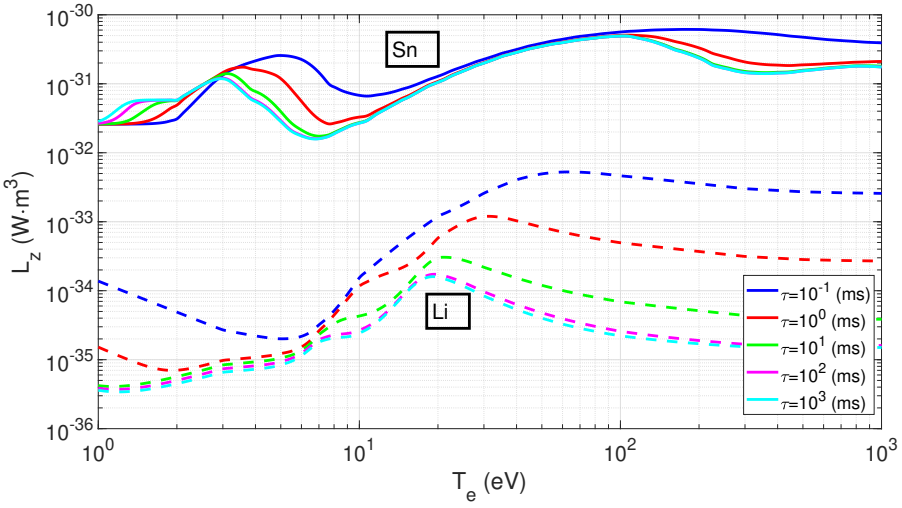

Figure 3.7: Plasma cooling functions for both Li and Sn, as a function of electron temperature and of the non-coronal parameter tau. Data for Li are from [193], whereas data for Sn are from [160].

3.2.3 Summary

Lithium:

- Low melting point (180 °C)
- Low Z
- Beneficial for plasma performance
- High vapor pressure $\longrightarrow$ large evaporation at $T > 600$ °C
- T retention up to ~ 400 °C
- Possible fuel dilution
- Safety risk in the case of water leak

Tin:

- Low melting point (230 °C)
- Low vapor pressure $\longrightarrow$ negligible evaporation up to $T \sim 1300$ °C
- Acceptable T retention in liquid state (to be confirmed)
- High Z (plasma compatibility to be assessed via modelling and experiments)

3.3 Overview of LMD concepts

3.3.1 Flowing LMDs: the LiMIt concept

The Lithium Metal Infused Trenches (LiMIT) design, proposed by Ruzic et al. [171, 172, 28], is based on exploiting ThermoElectric MagnetoHydroDynamic (TEMHD) effects to passively promote radial LM flow, which allows to exhaust the plasma heat flux while continuously providing "fresh" LM to the PFS. If Li is used as an LM, the high rate of surface renewal, combined with the capability of Li of retaining hydrogen ions and atoms, have the potential to allow for *low recycling* tokamak operation. This regime has been observed to be characterized by an improved energy confinement [143].

3.3.2 The Lithium Vapor Box divertor

The Li vapor box divertor, as proposed by Goldston et al. [135, 65, 67, 50, 176, 177, 51], is based on the idea that stable plasma detachment can be obtained by confining a dense cloud of Li vapor in the proximity of the target thanks to a series of *boxes*, see Figure 3.8. The necessary combination of large density close to the target and as low as possible density in the last box (which is directly connected to the plasma chamber) can be achieved by a suitable choice of the surface temperature to induce either evaporation or condensation.

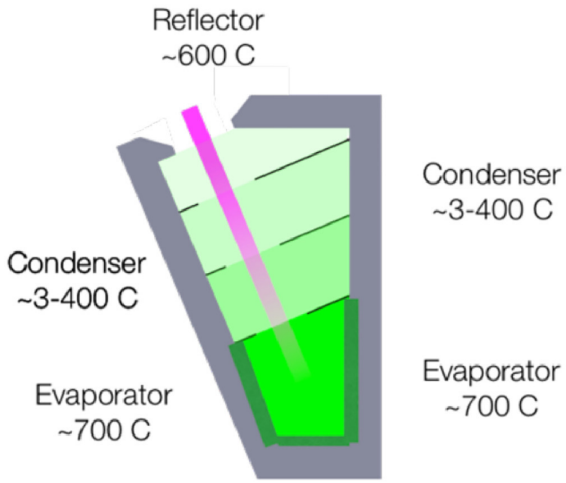

Figure 3.8: Schematic of a cross section of a vapor box divertor. Baffles separating the successive chambers are shown, as well as the role of the various surfaces: the bottom box has evaporating surfaces, whereas the other boxes are actively cooled to promote condensation. The last baffle is heated to 600 °C to achieve a reflecting surface. Reproduced from [50].

3.3.3 ITER-like liquid metal divertor using a CPS

This concept aims at replacing the baseline divertor with an LMD while minimizing the impact on the design of the machine. For this reason, the shape of the PFCs should be kept unchanged, and the LMD should operate in high recycling conditions with very limited evaporation. This is possible if the surface temperature is maintained sufficiently low, which can be achieved by carefully designing the PFCs to minimize the thermal resistance for heat transport to the coolant. To achieve the requirement of low evaporation during normal operation, seeding impurities in the SOL to partly radiate the plasma heat might be necessary.

3.4 LMD design criteria

3.4.1 Guidelines for LMD design

The design process starts from setting *operational requirements*. An LMD must successfully accomplish all the functions required for a conventional divertor in terms of, e.g., heat/particle handling, ash removal, compliance with the plasma scenario, remote handling - hence the cassette structure - while being compliant with in-vessel components, pumps, diagnostics. These requirements must be satisfied notwithstanding the presence of LM - and the consequent presence of vapor. Moreover, additional requirements that are specific to an LMD must be set:

- to constantly cool the CPS substrate;
- to constantly replenish the PFS to avoid CPS damage;
- to constantly heat the replenishing LM to avoid freezing.

The design must additionally be carried out carefully addressing *physical/chemical issues* which are specific to an LMD:

- possible exothermic reactions with water/air (for Li);
- material erosion, arising in case of imperfect replenishment;
- material corrosion due to contact with high-temperature liquid metal;
- plasma contamination due to emitted metal;
- compliance with activation limits and T inventory issues.

The design process must therefore be informed by SOL plasma calculations, as well as by safety assessments. In view of these considerations, within the EUROfusion program for the development of LMDs, the actively cooled CPS option has been selected [220]. The choice between Li and Sn must also be performed accounting for the above-mentioned considerations about design requirements and constraints. As mentioned above, Li could be compatible with a high recycling operation, if a sufficiently large temperature can be ensured at the strike point. On the other hand, a Li temperature exceeding ~ 700 °C would likely imply an intolerably large erosion rate. These considerations anticipate a narrow operational window for Li, therefore seeming to favour Sn.

3.4.2 Description of the ENEA Frascati LMD design

To provide an example of the application of the above-mentioned guidelines, this section describes the preliminary design of the LMD using Sn recently proposed by ENEA Frascati [167]. The main components of the proposed LMD are briefly described, distinguishing between those located inside and outside the Vacuum Vessel (VV). The design here described will also be among those considered for detailed SOL plasma modelling in chapter 5.

In-vessel components

The LMD design here considered is consistent with [167], and was complemented with suitable assumptions in case of missing information. The proposed design is highly modular. The divertor is subdivided into 48 *cassettes*, covering the entire toroidal extension of the tokamak, in compliance with remote handling requirements. In each cassette there are two Vertical Targets (VTs), i.e. the components directly exposed to the plasma heat and particle loads. Each VT is covered by 24 *modules*, each containing 3 *units*. The structure of each of these components is briefly described in the following.

The CAD of a single divertor cassette was presented in Figure 3.9 (left). In the current EU DEMO divertor design, the cooling water inlet to each cassette is connected to a Bottom Ring Collector (BRC), see Figure 3.9 (right). Correspondingly, the water outlet from each cassette is connected to a Top Ring Collector (TRC). BRC and TRC are in turn connected to an ex-vessel water circuit, which shall be briefly described in the next subsection. For the present study, it has been assumed that both inlet and outlet LM and heating gas pipes for each cassette are connected to a corresponding BRC and TRC, respectively, see again Figure 3.9 (right). LM and heating gas BRC and TRC are in turn connected to external circuits, to be described in the next subsection. The heating gas could be pressurized He, but other options such as CO_2 are viable.

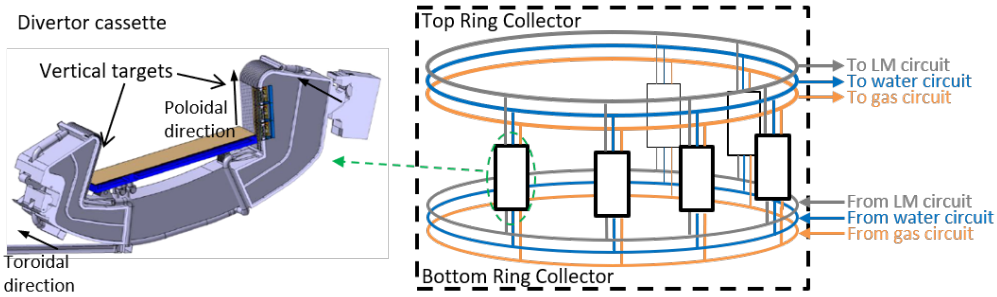

Figure 3.9: CAD of a single divertor cassette, adapted from [53] (left) and schematic representation of the hydraulic connections of the cassettes to the BRC and TRC (right). Note that, for the sake of simplicity, only 6 divertor cassettes out of the total 48 are shown.

In the single divertor cassette, the surface of each VT is covered by 8x3 divertor modules (8 in the toroidal direction and 3 in the poloidal direction). The three modules in the poloidal direction are connected in series, whereas all the eight series of three modules each are connected in parallel. The schematic of the hydraulic connections of the modules for a single VT is shown in Figure 3.10 (right). The CAD of a single module is shown in Figure 3.10 (left). Each module is connected to the cooling water inlet (in blue) and outlet (in orange) lines, to the heating gas

inlet and outlet lines (in yellow) and to the LM refill line (in grey). The PFS of each module is composed by three units, juxtaposed in the toroidal direction.

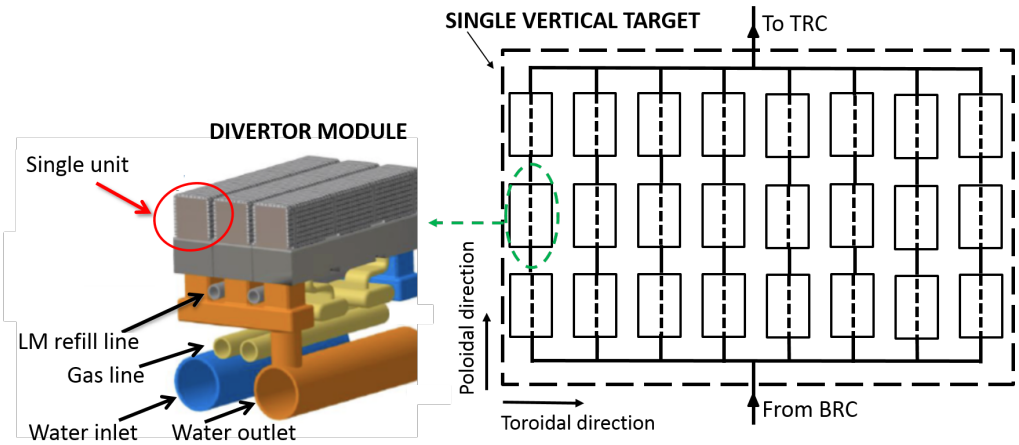

Figure 3.10: CAD of a single divertor module, adapted from [53] (left) and schematic representation of the hydraulic connections of the modules to the inlet and outlet collectors of the cassette (right). Note that, for the sake of simplicity, the water, LM and gas lines have not been explicitly indicated in the schematic. The dotted lines indicate that the pipes pass below the modules.

Figure 3.11 shows the cross section of one of the three units on top of each module. The CPS (in blue) is made of a W mesh or felt. It extends downwards to reach an LM reservoir (in green), so as to allow for capillary forces to passively replenish the PFS. The reservoir is connected to the LM refill line shown in Figure 3.10 (left). Being located away from the PFS, the reservoir is not reached by the plasma heat. The water cooling channels, connected to the water inlet and outlet lines shown in Figure 3.10, are located near the CPS to optimize the heat removal. The gas heating channels, connected to gas inlet and outlet lines shown in Figure 3.10 (left), are located in proximity of the reservoir to avoid LM freezing. The specific LMD design here considered is hence based on decoupling the functions of cooling the PFS (pressurized water) and heating the reservoir (gas).

It should be noticed that the one here analysed is not the only LMD design currently under investigation for EU DEMO. For instance, concepts where the heating and cooling fluids coincide, possibly characterized by a lower degree of modularity, are being considered [166].

Ex-vessel components

The ex-vessel circuits for the cooling water, the replenishing LM and the heating gas feeding the LM divertor are schematically indicated in Figure 3.12. For the purpose of the present thesis, and in the absence of a detailed design, only the

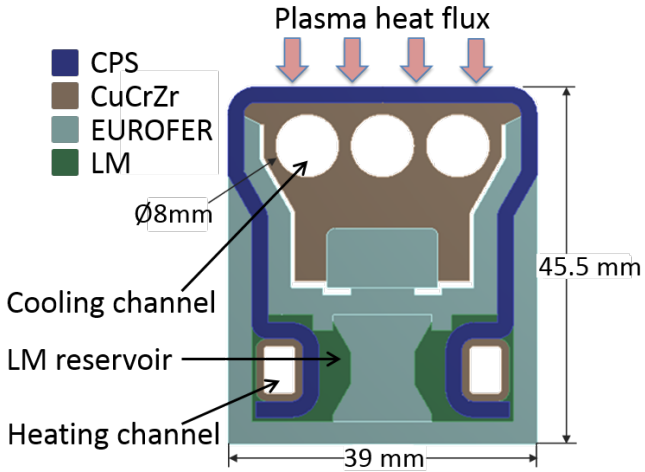

Figure 3.11: Cross section of a single module unit, adapted from [167].

Design choice	**Selected value**
Liquid metal	Sn
CPS type	Mesh/felt
CPS thickness	2 mm
Sn resupply	Capillary reservoir
Maximum CPS pore size	50 µm
Water temperature	120 °C
Water pressure	50 bar
Water flow speed	12 m/s
Requirement for liquid Sn	$q'' > 5$ MW/m^2
CHF	40 MW/m^2
CHF margin at $q'' = 20$ MW/m^2	1.6
Sn heating method	Gas in PFC

Table 3.2: Design choices for the ENEA CPS-based target [167]. Following the typical nomenclature of thermal-fluid dynamics, the symbol q'' indicates the surface heat flux [88].

essential subsystems to achieve the required functions for each circuit have been reported.

The LM flow from an LM tank towards the BRC is promoted by means of an

Electro-Magnetic (EM) pump. The LM flowing out of the VV from the TRC is treated by means of an LM purification system to remove impurities (e.g. due to the erosion/corrosion of piping materials), which could be activated, and Tritium, and subsequently heated by means of a heat exchanger to compensate for the heat losses from the pipes. The LM eventually flows into the above-mentioned LM tank. Although more detailed design information would be required to quantify the total LM inventory, it can be estimated that the total LM volume constrained by the CPS inside the VV will be $\sim$ 10 litres. The water circuit is composed by a pressurizer, a pump and a purification system, alongside with a heat exchanger to discharge the heat gained in the PFCs. The water circuit operational pressure is $\sim$ 50 bar and the inlet temperature to the cassette is $\sim$ 140 °C. The temperature increase induced by the plasma power is small ($\sim$ 10 °C) thanks to significant water flowrate (the velocity in the cooling channels is $\sim$ 12 m/s) [167]. The He flowrate in the gas circuit is promoted by a compressor and heated by means of a heat exchanger. A He tank is necessary to ensure pressure control (the He operating temperature is $\sim$ 350 °C [124]).

The LM eroded from the PFS due to the plasma heat and particle flux is, at least partially, recondensed on the FW and recollected. It is assumed that the recollected LM passes through a recollection line featuring a purification system (to remove impurities and codeposited Tritium) and an EM pump, and is connected to the LM tank.

The LM tank, the water pressurizer and the He tank are connected to external refill lines, which are however out of the scope of the present study.

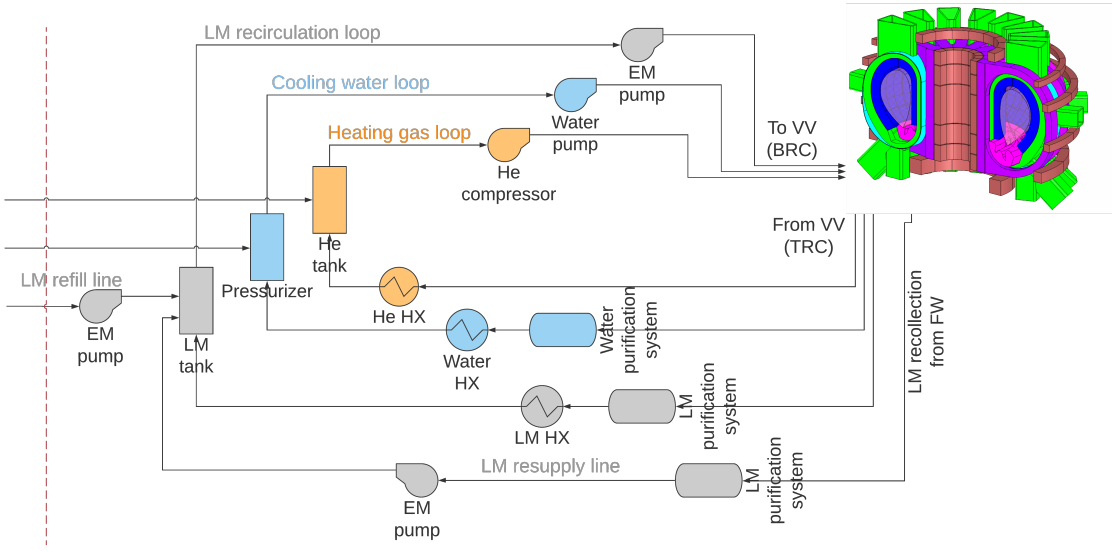

Figure 3.12: Schematic representation of the ex-vessel LMD circuits. CAD of the EU DEMO tokamak reproduced from [104].

3.5 Phenomenology

The SOL plasma behavior is strongly influenced by the presence of:

- D and/or T *neutrals* arising from recyling at walls.
- *Impurities* produced from the erosion of the PFCs (especially from target sputtering and evaporation) or intentionally introduced in the plasma chamber (via *impurity seeding*). Impurities can exist as neutrals or become ionized due to interactions with the main plasma electrons (e.g. Li can exist as Li^0, Li^+, Li^{2+}, Li^{3+}). As mentioned in section 2.2.3, interactions of the plasma with impurities determine, among other processes, radiation losses.

The resulting phenomenology, encompassing both surface processes and atomic physics processes, is schematically indicated in Figure 3.13. The most relevant aspects of this phenomenology are discussed in the following.

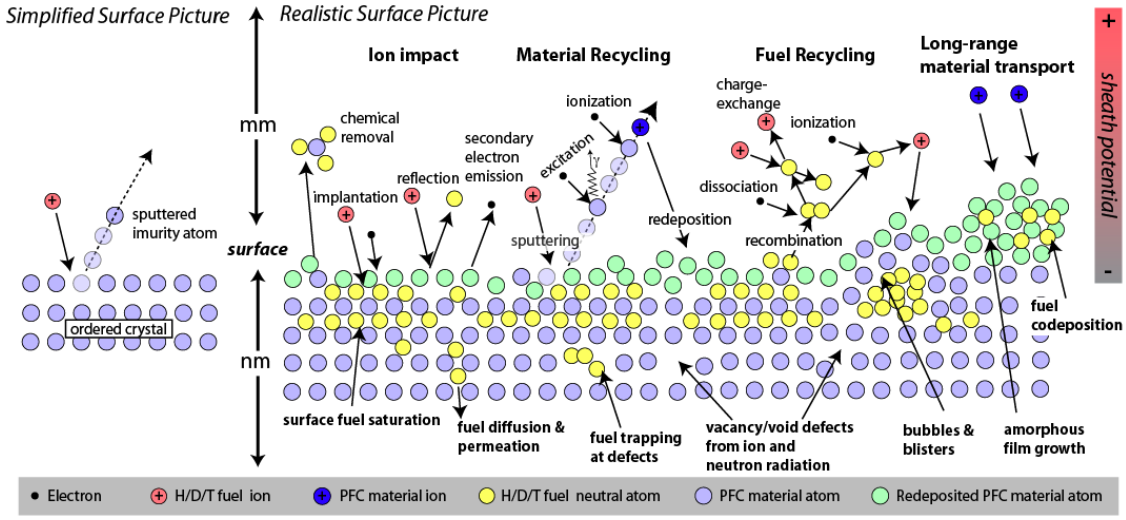

Figure 3.13: Overview of plasma-surface interactions with particular focus on the consequences of particle bombardment on the surface itself. Reproduced from [163].

3.5.1 Erosion processes

The plasma heat and particle loads impinging on the divertor target determine the erosion of the plasma-facing LM - which should be constantly compensated by capillary forces. In the following, the most relevant erosion mechanisms are summarized.

Physical sputtering

Physical (or *collisional*) sputtering is associated to momentum transfer from energetic ions to wall atoms. An energetic ion or neutral atom striking the wall causes

a collision cascade among the lattice atoms, which can cause sputtering of one or more surface atoms if they receive sufficient energy to overcome the surface binding energy [209]. This process is present also in the case of a solid target, for which it represents a major concern in terms of divertor lifetime. The physical sputtering yield for a solid material does not depend on surface temperature [21], and increases with the mass of the projectile, while decreasing with the target atomic mass, see figure 3.14. The sputtering yield increases with the energy of the impinging ions until it reaches a maximum, and then decreases monotonically. For ion energies above the one corresponding to the maximum sputtering yield, indeed, the collision cascade takes place deeper inside the surface, so that the sputtering rate is reduced.

Experiments have shown that, in the case of Li, only $\sim 1/3$ of the particles arising from physical sputtering are neutral, the rest being ions [7]. Due to the presence of the electrostatic sheath at the plasma-wall interface [190], it can be assumed that the sputtered ions are immediately redeposited on the surface (e.g. not contributing to volumetric loss processes in the near-target plasma).

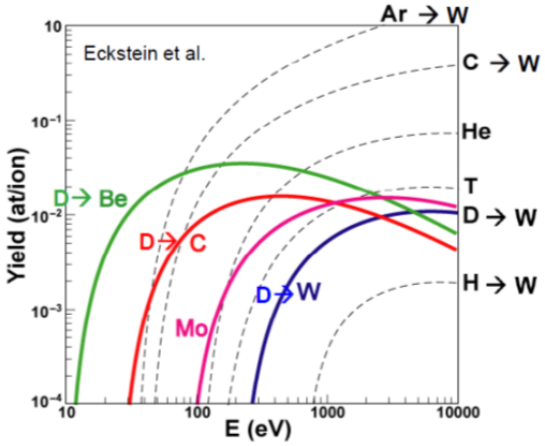

Figure 3.14: Physical sputtering yields for selected projectile-target combinations. Reproduced from [163].

Evaporation/condensation

Evaporation is an erosion process relevant for liquid (or molten) PFCs. The evaporation rate does not depend on the impinging particle flux, but increases with surface temperature (see e.g. Figure 3.6).

Thermal sputtering

There is experimental evidence, for some materials, of a temperature dependence of the sputtering yield, on top of the above-mentioned dependence on the impinging particle flux and energy. For solid graphite, for instance, this is associated to

chemical sputtering arising from the formations of hydrocarbons such as CH_4 [190]. For liquid Li, a temperature dependent component of the sputtering yield was observed by Doerner et al. [41] and Allain et al. [7]. Although the origin of this *thermal sputtering* is currently a debated topic, it is worth reporting here the explanation proposed in [41] that energetic particles impinging on a liquid surface create *adatoms*, which are loosely bound to the surface itself, and therefore evaporated/sublimated at lower temperatures with respect to the ones conventionally needed to observe significant evaporation/sublimation.

Other processes

In the foregoing discussion the erosion of the CPS material has been neglected, based on the assumption that the LM constantly wets the porous surface. Furthermore, macroscopic droplet ejection of the LM has been neglected, having assumed a stable confinement within the CPS against the effect of MHD forces.

3.5.2 Erosion suppression mechanisms

The *gross* erosion rate associated with the above-mentioned erosion mechanisms is reduced by *redeposition* processes, leading to a lower *net* erosion rate. Moreover, changes in surface composition can further contribute to reduce the erosion flux.

Prompt redeposition

Prompt redeposition is caused by the ionization of eroded neutral atoms within the *magnetic pre-sheath*, i.e. approximately within one gyro-radius from the surface, which results in the particles returning to the surface without participating to volumetric loss processes in the near-surface plasma [1, 197].

Non-prompt redeposition

As pointed out by [6], redeposition could also occur for particles not ionized within the first gyro-radius, since particles that are not promptly redeposited can still be ionized outside the pre-sheath region. In this case, essentially based on the balance between friction and thermal forces, they have a finite probability of being redeposited on the surface.

Effect of D retention

D retention can represent a mechanism of erosion supression, as explained in [1]. However, D retention is negligible for Sn [115], as it is for Li for surface temperatures above $\sim$ 650 K [8]. Low D retention has important consequences in terms of the plasma scenario, since it allows to operate in a high recycling operation, consistently

with the baseline strategy, avoiding a buildup of T inventory in the PFCs. It should be noticed that, based on the specific reactor design, the opposite (i.e. low recycling operation) could be desirable [96, 217].

3.5.3 Fuel (D) recycling

Once plasma ions and electrons impact on the divertor target, they are *retained* up to wall saturation. In a reactor, this condition is soon reached, and therefore after the impact plasma ions *recombine* on the wall (i.e. they are neutralized) and are successively emitted with an energy corresponding to the wall temperature (thermalized D^0 atoms). More complex phenomena, such as molecular emission and dissociation, can occur.

3.5.4 Plasma-vapor interactions

Both eroded metal (which will be referred to as *vapor* in the following) and *fuel neutrals* arising from recycling at the target interact with the plasma. In the following, a summary of the possible interactions is provided.

Ionization/recombination

Both *vapor* and *fuel neutrals* have a high probability of being ionized in the proximity of the target. Once ionized, they start behaving as further plasma components, that can in turn redeposit on the surface and cause sputtering. For D, the two processes can be described as:

- Electron-impact ionization:
  $e^- + D^0 \longrightarrow D^+ + 2\,e^-$
- Recombination:
  $e^- + D^+ \longrightarrow D^0$

The phenomenology for impurity atoms is similar, except that impurities can have multiple ionized states (e.g. Li has three).

Charge-exchange

Charge eXchange (CX) is responsible for ion-neutral friction. The process is the following:

$$D^0(\text{cold}) + D^+(\text{hot}) \longrightarrow D^+(\text{cold}) + D^0(\text{hot}) \tag{3.2}$$

CX processes are dominant for $T_e < 5$ eV, as shown in Figure 3.15. These processes are effective momentum sinks (hence the term ion-neutral friction). For this reason, if the plasma electron temperature can be decreased below 5 eV before it reaches the target, plasma momentum can be exhausted.

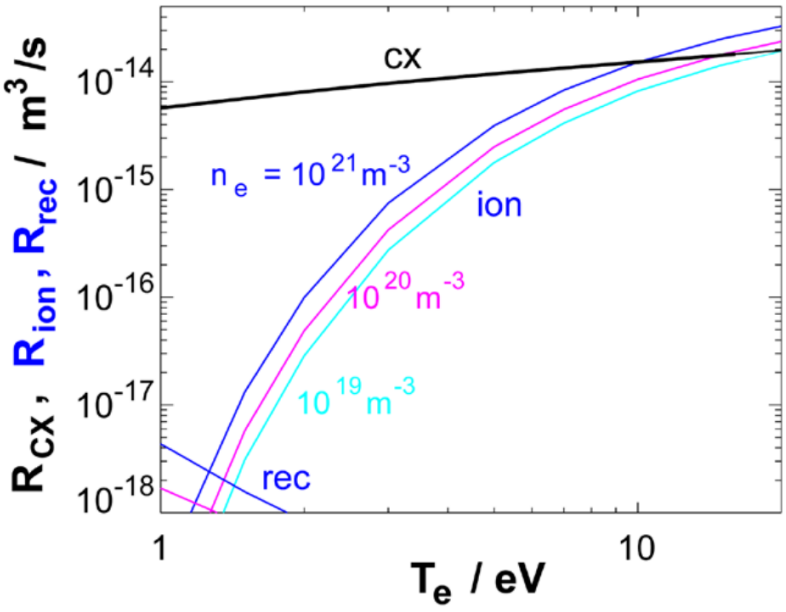

Figure 3.15: Deuterium reaction rates at low electron temperatures, reproduced from [97] with permission. Note the weak dependence of the rates on the electron density.

This momentum exhaust is part of the phenomenology encountered in a *detached plasma*. A schematic representation of the processes involved in plasma detachment is reported in Figure 3.16.

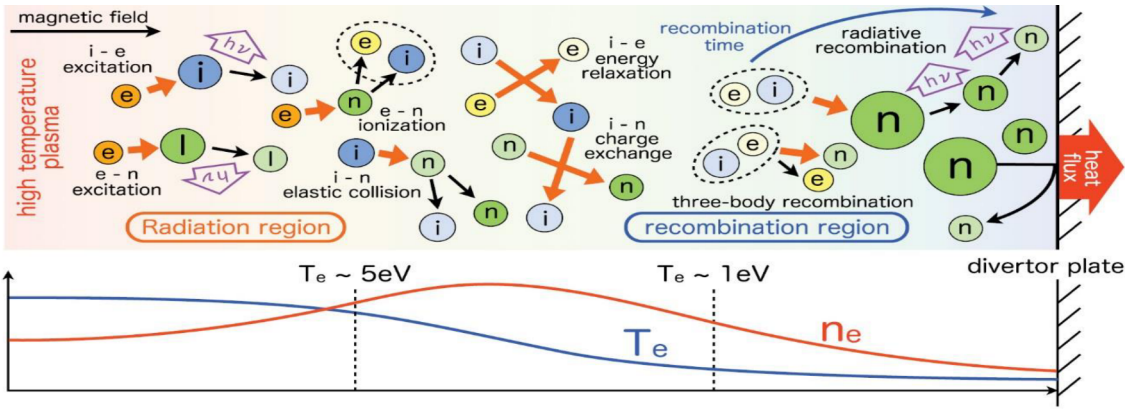

Figure 3.16: Schematic view of processes involved in plasma detachment. Reproduced from [163].

Radiation from impurities

Both impurities produced from target erosion (sputtering, evaporation) and those intentionally introduced in the plasma chamber (via *impurity seeding*) are responsible for two types of *radiation*:

- *Bremsstrahlung* is always present in a plasma, due to free electrons deflecting their trajectories following the passage close to an ion), but it becomes the dominant power loss process only at large temperatures, as $S^E_{e,Brem} \propto T_e^{\frac{1}{2}}$.
- *Line radiation* is associated to excitation/de-excitation of the electrons of impurity atoms/ions due to the impact of free electrons in the plasma. Lower charge states (e.g. Li^0, Li^+), for a given temperature, are responsible for more radiation than, e.g., Li^{2+}, since more electrons are available. The fully ionized state (e.g. Li^{3+} for Li) is not responsible for any line radiation due to the absence of bound electrons.

Figure 3.17 summarizes the most relevant interactions between the near-surface plasma and an LMD.

The overall effect of these plasma-vapor interactions (which occur on top of plasma-neutrals interactions) is the *vapor shielding* of the target [201, 124, 118], which results in a self-regulation of the heat flux reaching the LM target, and consequently of the erosion rate. The actual target operating conditions are therefore dependent on both the SOL plasma behavior and on the target response, which must be computed self-consistently. The local distribution of charge states depends on the local temperature and density, and on plasma transport, all of which are in turn dependent on plasma-vapor and plasma-neutrals interactions.

The plasma energy loss due to these effects is quantified by the *loss functions* $L_Z(T_e, n_e\tau)$, see Figure 3.7, where τ is a particle dwell time. Intuitively, as τ decreases, an impurity has fewer time to reach its coronal equilibrium charge-state distribution, and therefore it will have a lower $\langle Z \rangle$ (mean charge) for a given temperature. This fact explains the increase of L_Z, for a given T_e and for a given impurity, if τ decreases.

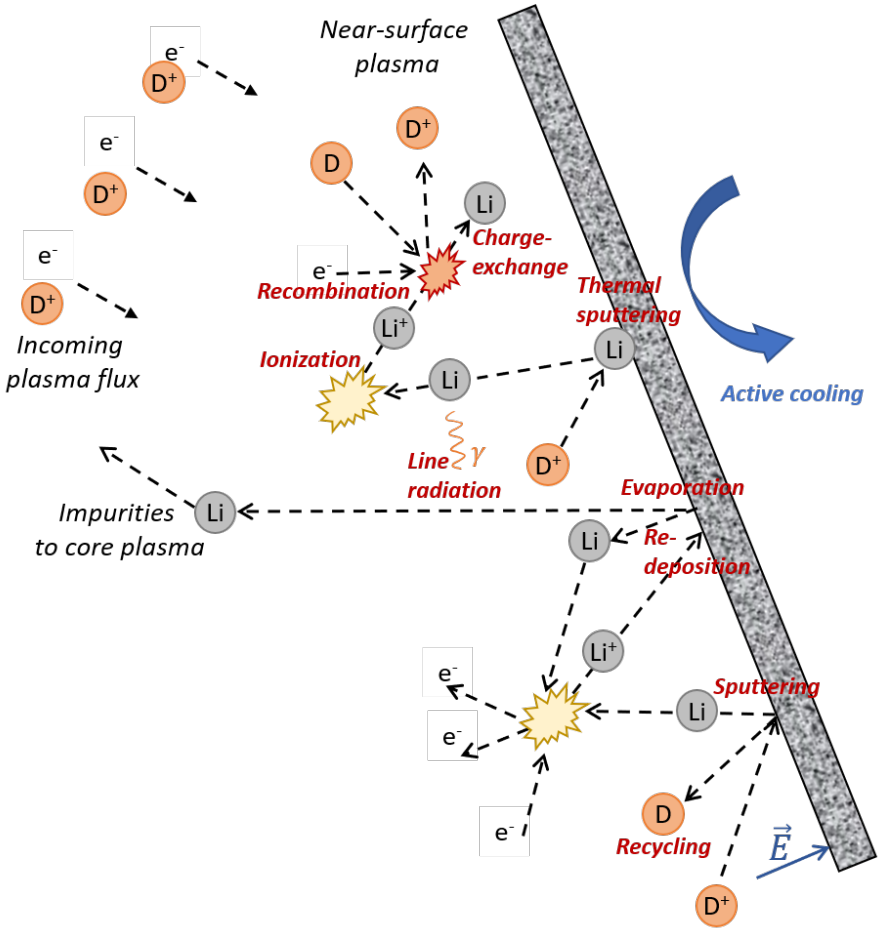

Figure 3.17: Sketch of the main plasma-vapor interactions.

3.6 The need for self-consistent modelling

The erosion of the LMD target can be significant due to evaporation and thermal sputtering acting on top of physical sputtering [7, 2], as discussed above. This might lead to unacceptable core plasma dilution (in the case of Li) or to intolerable power losses from the core plasma (in the case of Sn) [138]. For this reason, modelling the behavior of the plasma in the presence of an LMD, with the purpose of predicting whether an operating window for this system exists, is fundamental to support the LMD design. The following two chapters will be devoted to describe the modelling activities performed during this Ph.D. work.

Chapter 4

Scrape-Off layer plasma modelling

This chapter aims at introducing the basic concepts associated to SOL plasma modelling, as well as the main processes here occurring.

The SOL power balance is important for a tokamak, since it determines the power deposited onto the divertor plates. If P_{SOL} was only transported via plasma advection/conduction, which is strongly anisotropic due to the presence of the magnetic field, the peak heat flux to the divertor targets would be unacceptably large.

The strategy that will be adopted in ITER for reducing the peak heat flux to the divertor consists in radiating part of P_{SOL} *before* it reaches the divertor targets, thus reducing the power transported via the anisotropic channel.

This strategy can allow for detachment to take place, if the SOL plasmas temperature is reduced below $T_e \sim 5$ eV before it reaches the target plate. Below this temperature, charge-exchange reactions become dominant, and momentum losses take place.

To quantitatively assess the various terms involved in the SOL power balance, it is necessary to compute the distribution of SOL plasma temperature, density and velocity. It is also important to understand the role of *impurities* and *neutrals* in the SOL plasma power balance. These topics will be discussed in the following sections.

Specifically, the simplified geometry adopted in the present chapter for the sake of introducing the topic is reviewed in section 4.1; a discussion concerning the justification for a fluid modelling approach is provided in section 4.2; finally, a simplified set of fluid conservation equations suitable for the core plasma is presented in section 4.3, with the source/sink terms associated to plasma/neutral interactions highlighted.

4.1 Geometry

For the sake of clarity, the present discussion focuses on the outboard divertor leg, i.e. from *upstream* (i.e. OMP) to the outboard target. The scheme reported in figure 4.1 shows the poloidal projection of the path travelled by plasma particles. Indeed, particles follow the helical field lines, as shown in Figure 4.2. The target-to-target distance along the magnetic field can be estimated as $L_c \sim 2\pi R_0 q$, where L_c is the *connection length* and q is the *safety factor*, which can in turn be estimated as $q \sim \frac{aB_\phi}{RB_\theta}$, a and R being the minor and major radii of the plasma, respectively.

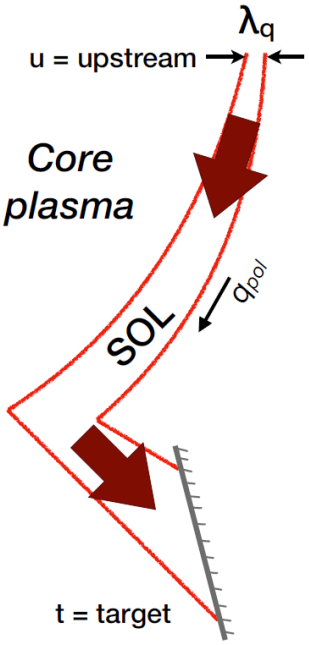

Figure 4.1: Sketch of a diverted SOL.

To clarify the directions involved in the present discussion, figure 4.3 shows two possible reference frames for the plasma description. $\parallel$: parallel to $\mathbf{B}$, $\perp$: perpendicular to $\mathbf{B}$.

4.2 Collisionality

Conservation equations are based on the continuum hypothesis: the mean-free path of a particle λ_{mfp} is assumed to be smaller than the characteristic length L of the system. In other words, a requirement on the Knudsen number $Kn = \frac{\lambda_{mfp}}{L} < 0.1$ is set. To justify a fluid description of the SOL plasma, its collisionality along the two relevant directions ($\parallel$ and $\perp$) must be discussed.

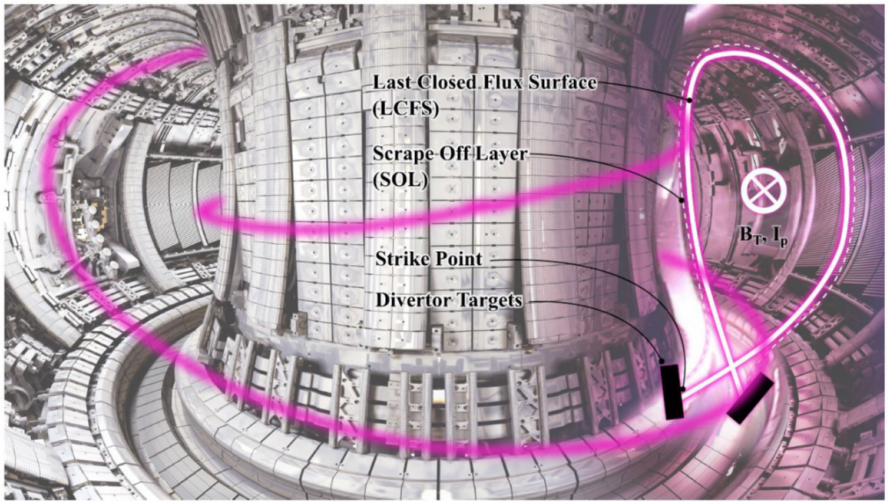

Figure 4.2: Representation of field lines, reproduced from [166].

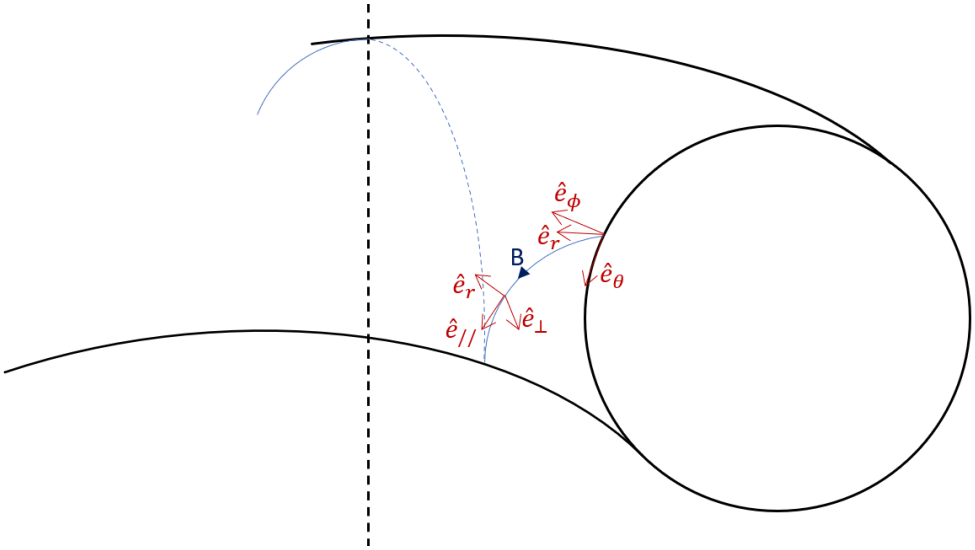

Figure 4.3: Schematic of the directions involved in the calculations.

Collisionality across B ($\perp$ direction)

The presence of the magnetic field makes the $\perp$ direction collisional (the $j \times \mathbf{B}$ force acts as a confinement mechanism). This can also be thought about differently, in terms of collision frequency vs. gyro-frequency.

Collisionality along B (∥ direction)

The Knudsen number for both ions and electrons can be computed. For both species, the characteristic distance can be estimated as half the target-to-target distance:

$$L \sim \frac{L_c}{2} = \frac{\pi a B_\phi}{B_\theta} \equiv L_\parallel \tag{4.1}$$

For ions, $Kn_i = \frac{\lambda_{mfp,i}}{L_\parallel}$. $\lambda_{mfp,i}$ can be estimated as the ratio of the ion velocity and a collision frequency: $\lambda_{mfp,i} = \frac{v_{th,i}}{\nu_{ii}}$, where $v_{th,i} = \sqrt{\frac{kT_i}{m_i}}$. The appropriate collision frequency ν_{ii} is the one associated to the slowing-down of a thermal ion in a background of ions, $\nu_{ii} \sim \hat{\nu}_{ii} = \mu^{1/2} \cdot 1.33 \cdot 10^5 \frac{n_{20}}{T_K^{3/2}}$, where in turn $\mu = \frac{m_e}{m_i}$. Here follows an estimate using ITER numbers: $\mu = 2.1784 \cdot 10^{-4}$, assuming a 50% D-T plasma, $T_i \sim 100$ eV (i.e. $T_K \sim 0.1$), $n_{SOL} \sim 10^{20}$ m^{-3} (i.e. $n_{20} \sim 1$), $q \sim 3$. These numbers yield $v_{th,i} \sim 10^5$ m/s and $\nu_{ii} \sim 6.2 \cdot 10^4$ s^{-1}, which in turn lead to $\lambda_{mfp} \sim 1.6$ m and $L_\parallel \sim 2\pi \cdot 6.2 \cdot 3 = 117$ m, thus confirming $Kn_i \ll 1$ for the ITER SOL plasma.

For electrons, the same approach can be adopted. The relevant collision frequency is now represented by the slowing-down collision frequency for a thermal electron in a background of ions, i.e. the electron-ion Coulomb collisions: $\lambda_{mfp,e} = \frac{v_{th,e}}{\nu_{ei}}$, where $v_{th,e} = \sqrt{\frac{kT_e}{m_e}}$ and $\nu_{ei} \sim \hat{\nu}_{ei} = 1.33 \cdot 10^5 \frac{n_{20}}{T_K^{3/2}}$. Estimating Kn_e for ITER: $v_{th,e} = 4.19 \cdot 10^6$ m/s, $\nu_{ei} \sim 4.2 \cdot 10^6$ s^{-1}, leading to $\lambda_{mfp,e} \sim 1$ m, again confirming $Kn_e \ll 1$ for the ITER SOL plasma.

It can be concluded from these estimates that a fluid model is adequate for describing the SOL plasma behavior. Specifically, if toroidal symmetry can be assumed, a 2D fluid model can be employed.

In concluding this section, it should be recalled that a fluid treatment would be completely inadequate in the sheath region, which is almost collisionless. Therefore, it is customary to consider the Sheath Edge (SE) as a boundary for the fluid domain, where boundary conditions arising from the Bohm criterion and the sheath heat transmission relation are imposed [190]. However, treating the electrostatic SE as a boundary condition for the fluid model may lead to unphysical values of the heat flux (since the SE is a transition region between a collisional and a nearly collisionless region). To ensure that heat conduction at the SE boundary of the fluid domain is maintained below physically allowable values, a limit heat flux can be defined as the maximum convection which could be provided by electrons, if they all had a directed velocity equal to the sound speed:

$$\vec{q}_e = \frac{\nabla T_e}{|\nabla T_e|} \frac{1}{|k^e_{\parallel,cl} \nabla T_e|^{-1} + q_{lim}^{-1}} \tag{4.2}$$

which results in a flux-limited electron conductivity:

$$k_{\parallel}^{e} = k_{\parallel,cl}^{e} \cdot \left(1 + \left|\frac{k_{\parallel,cl}^{e} \cdot \frac{\partial T_e}{\partial v}}{F n v_{th,e} T_e}\right|\right)^{-1} \tag{4.3}$$

where $q_{lim} = F n v_{th,e} T_e$ and $k_{\parallel,cl}^{e}$ is the classical (Spitzer-Härm) heat conductivity.

4.3 Fluid equations for the SOL plasma

4.3.1 Relation with kinetic theory

Fluid equations can be rigorously derived by taking moments of kinetic equations. This procedure is completed by the choice of a suitable *closure*. In the following, the kinetic equation from which the Braginskii equations are derived, as well as the nature of the Braginskii closure, are discussed in brief. The complete derivation can be found in [20]. A kinetic equation which is suitable for describing a plasma where collisions are present is the Fokker-Planck equation. For each plasma species α it reads:

$$\frac{\partial f_\alpha}{\partial t} + \vec{v} \cdot \nabla_{\vec{r}} f_\alpha + \frac{e_\alpha}{m_\alpha}\left(\vec{E} + \vec{v} \times \vec{B}\right) \nabla_{\vec{v}} f_\alpha = \left(\frac{\partial f_\alpha}{\partial t}\right)_{coll} + S_\alpha\left(\vec{r}, \vec{v}\right) \tag{4.4}$$

This equation coincides with the Boltzmann equation, with the exception of the collision term $\left(\frac{\partial f_\alpha}{\partial t}\right)_{coll}$. In the Boltzmann equation written for a neutral gas, the collision term accounts for binary collisions, whereas in the Fokker-Planck equation long-range, small-angle collisions, which are those relevant for a plasma, are considered, including the effects associated to all particle species. A synthetic but exhaustive discussion on this topic can be found in [209]. The closure problem involves evaluating unknown quantities (pressure tensor, heat flux, rate of change of momentum due to collisions, heat generated as a result of collisions) that arise when taking moments of the kinetic equations. The closure approach proposed by Braginskii consists in obtaining expressions for the unknown quantities by expanding the Fokker-Planck equation around an equilibrium (Maxwellian) distribution $f = f_0 + \delta f$.

4.3.2 Fluid (Braginskii) equations

Here, for the sake of simplicity, equations are written for a D plasma (i.e. the fluids considered are D^+ ions and e^- electrons. However, for a fusion reactor, this system must be generalized to include, as a minimum, also T^+, He^+ and He^{2+} ions. In practical applications, also equations for the seeded impurity ions (e.g. Ar^+, Ar^{2+}, ... Ar^{18+}) should be included, thus resulting in a larger system of coupled, nonlinear

Partial Differential Equations (PDEs). For the case where an LMD is employed, the plasma species resulting from Li/Sn emission and successive ionization(s) are also present. It should be noticed that the equations here reported are, for the sake of clarity, simpler with respect to the ones actually implemented in SOLPS-ITER.

Source and sink terms are associated to atomic processes, which are relevant for the SOL plasma and will be described in the following.

Continuity (particle conservation)

For ions:

$$\frac{\partial n_i}{\partial t} + \nabla \cdot (n_i \vec{u_i}) = S^P_{iz} + S^P_{rec} \tag{4.5}$$

where:

$$S^P_{iz} = n_e n_0 \langle \sigma v \rangle_{iz} \text{ is the particle source due to ionization of neutrals}$$
$$S^P_{rec} = -n_e n_0 \langle \sigma v \rangle_{rec} \text{ is the particle sink due to plasma recombination}$$

For electrons, the quasi-neutrality condition is used:

$$n_e = n_i \tag{4.6}$$

Momentum conservation

For ions:

$$\left(\frac{\partial}{\partial t} + \vec{u}_i \cdot \nabla \right) m_i n_i \vec{u}_i = -\nabla p_i - \nabla \cdot \overleftrightarrow{\Pi}_i + e n_i \left(\vec{E} + \vec{u}_i \times \vec{B} \right) + \vec{R}_i + \vec{S}^M_i \tag{4.7}$$

where:

$$\nabla \cdot \overleftrightarrow{\Pi}_i \text{ is the divergence of the stress tensor, responsible for the viscous stress}$$
$$e n_i \left(\vec{E} + \vec{u}_i \times \vec{B} \right) \text{ is the electro-magnetic force}$$
$$\vec{R}_i \text{ is the rate of change of momentum due to collsions}$$
$$\vec{S}^M_i \text{ is the rate of change of momentum due to atomic processes}$$

The $\vec{R}_i$ term arises from the closure procedure and is related to the specific nature of collisions in plasmas (i.e. this term is absent in a neutral gas). It can be written as:

$$\vec{R}_i = en_e\left(\eta_\parallel j_\parallel + \eta_\perp j_\perp\right) - 0.71 n_e \nabla_\parallel T_e - \frac{3}{2}\eta_\perp \frac{en_e^2}{B^2}\vec{B}\times\nabla T_e \tag{4.8}$$

where the terms on the right-hand side are the *ion-electron friction force*, the *parallel thermal force* and the *perpendicular thermal force*, respectively. The $\vec{S}_i^M$ term is instead associated to the momentum loss and sink processes, namely CX, ionization and recombination:

$$\begin{aligned}\vec{S}_i^M &= \vec{S}_{i,CX}^M + \vec{S}_{i,iz}^M + \vec{S}_{i,rec}^M \\ &= n_i n_0 \langle\sigma v\rangle_{cx} m_i\left(\vec{u}_0 - \vec{u}_i\right) + n_e n_0 \langle\sigma v\rangle_{iz} m_i \vec{u}_0 \\ &- n_i n_0 \langle\sigma v\rangle_{rec} m_0 \vec{u}_i\end{aligned}$$

For electrons:

$$\left(\frac{\partial}{\partial t} + \vec{u}_e\cdot\nabla\right) m_e n_e \vec{u}_e = -\nabla p_e - \nabla\cdot\overleftrightarrow{\Pi}_e - en_e\left(\vec{E} + \vec{u}_e\times\vec{B}\right) + \vec{R}_e + \vec{S}_e^M \tag{4.9}$$

where:

$$\vec{R}_i = \vec{R}_e$$

Energy conservation

For ions:

$$\begin{aligned}\left(\frac{\partial}{\partial t} + \vec{u}_i\cdot\nabla\right)\left(\frac{3}{2}n_i T_i\right) + p_i\nabla\vec{u}_i = -\nabla\vec{q}_i + \nabla\cdot\left(\vec{\Pi}_i\vec{u}_i\right) \\ + Q_{ei} + S_i^E - + en_i\vec{E}\vec{u}_i - \vec{R}\vec{u}_i\end{aligned} \tag{4.10}$$

where:

$p_i\nabla\vec{u}_i$ is the compression work
$-\nabla\vec{q}_i$ is the electron heat conduction
$\nabla\cdot\left(\overleftrightarrow{\Pi}_i\vec{u}_i\right)$ is the viscous dissipation
Q_{ei} is the heating due to collisions
S_i^E is the heating due to atomic physics processes
$\vec{R}_i\vec{u}_i$ is the ohmic heating term

The ion heat flux in a plasma, $\vec{q}_i$, can be written as:

$$\vec{q}_i = -\chi_{\parallel}^i \nabla_{\parallel} T_i - \chi_{\perp}^i \nabla_{\perp} T_i + \chi_{\wedge}^i \frac{\vec{B}}{B} \times \nabla_{\perp} T_i \tag{4.11}$$

$\chi_{\parallel}^i$ and $\chi_{\perp}^i$ are parallel and perpendicular heat conductivities, respectively. $\chi_{\parallel}^i = \kappa_{o,i} T_i^{\frac{5}{2}}$, with $\kappa_{o,i} \sim 60$, is the strongly nonlinear parallel heat conductivity according to the Spitzer-Härm conductivity formula. The ion-electron energy exchange can be written as: $Q_{e,i} = 3\frac{m_e}{m_i} n_e \nu_{ei} (T_e - T_i)$, and the ion energy source due to atomic physics processes is computed as $S_i^E = S_{i,cx}^E + S_{i,iz}^E + S_{i,cx}^E$, where:

$$\begin{aligned}
S_{i,cx}^E &= n_i n_0 \langle \sigma v \rangle_{cx} \frac{3}{2} (T_i - T_0) \text{ is the ion-neutral energy exchange} \\
S_{i,iz}^E &= n_e n_0 \langle \sigma v \rangle_{iz} \frac{3}{2} T_0 \text{ is the ion energy gain due to ionization} \\
S_{i,rec}^E &= n_e n_0 \langle \sigma v \rangle_{rec} \frac{3}{2} T_i \text{ is the ion energy loss due to recombination}
\end{aligned}$$

For electrons:

$$\begin{aligned}
\left(\frac{\partial}{\partial t} + \vec{u}_e \cdot \nabla\right) \left(\frac{3}{2} n_e T_e\right) + p_e \nabla \vec{u}_e = &-\nabla \vec{q}_e + \nabla \cdot \left(\vec{\Pi}_e \vec{u}_e\right) \\
&- Q_{ei} + S_e^E + e n_e \vec{E} \vec{u}_e + \vec{R}_e \vec{u}_e
\end{aligned} \tag{4.12}$$

where:

$$\begin{aligned}
p_e \nabla \vec{u}_e &\text{ is the compression work} \\
-\nabla \vec{q}_e &\text{ is the electron heat conduction} \\
\nabla \cdot \left(\overleftrightarrow{\Pi}_e \vec{u}_e\right) &\text{ is the viscous dissipation} \\
Q_{ei} &\text{ is the heating due to collisions} \\
S_e^E &\text{ is the heating due to atomic physics processes} \\
\vec{R}_e \vec{u}_e &\text{ is the ohmic heating term}
\end{aligned}$$

The electron heat flux in a plasma, $\vec{q}_e$, can be written as:

$$\vec{q}_e = -\chi_{\parallel}^e \nabla_{\parallel} T_e - \chi_{\perp}^e \nabla_{\perp} T_e + \chi_{\wedge}^e \frac{\vec{B}}{B} \times \nabla_{\perp} T_e - 0.71 \frac{T_e}{e} j_{\parallel} - \frac{3}{2} \frac{T_e}{e \omega_e \tau_e B} \vec{B} \times \vec{j}_{\perp} \tag{4.13}$$

$\chi_{\parallel}^{e}$ and $\chi_{\perp}^{e}$ are parallel and perpendicular heat conductivities, respectively. $\chi_{\parallel}^{e} = \kappa_{o,e} T_e^{\frac{5}{2}}$, with $\kappa_{o,e} \sim 2000$, is the strongly nonlinear parallel electron heat conductivity according to the Spitzer-Härm conductivity formula. The ion-electron energy exchange can be written as: $Q_{e,i} = 3\frac{m_e}{m_i} n_e \nu_{ei} (T_e - T_i)$. The ion energy source due to atomic physics processes $S_e^E = S_{e,iz}^E + S_{e,rad}^E$, where $S_{e,iz}^E$ is the electron volumetric power loss due to neutral ionization, written as:

$$S_{e,iz}^E = n_e n_0 \langle \sigma v \rangle_{iz} E_{iz} \tag{4.14}$$

and $S_{e,rad}^E$ is the ion volumetric power loss due to radiation, written as:

$$S_{e,rad}^E = n_e n_0 L_{z,rad}^D (T_e, n_e \tau_D) + \sum_{j=1}^{n_{imp}} n_e n_{z,j} L_{z,j}^{rad} (T_e, n_e \tau_z) \tag{4.15}$$

In the foregoing equation, the radiation contribution has been written separately for D and other impurities. The first part represents radiation (line radiation + Bremsstrahlung) caused by neutral D, and the second part represents radiation caused by impurities present in the plasma (e.g. Ar, Li, W, ...).

4.3.3 Edge plasma codes

The solution of the Braginskii equations for the plasma species, together with a set of conservation equations for the neutral particles, represents an important task to support divertor design. For this reason, a number of codes are currently used and actively developed worldwide. An edge plasma code is typically composed of at least two modules: a multi-fluid solver for the plasma, and a kinetic solver for neutral species, thus allowing to model the plasma-wall interactions in the edge region. The SOLPS-ITER code is the result of the coupling between B2.5 (a multi-fluid solver for ions) with EIRENE, a kinetic transport code [211]. Another example of multi-fluid solvers coupled to EIRENE are SOLEDGE2D-EIRENE [22], EDGE2D-EIRENE [185] and EMC3-EIRENE [60] (the latter featuring a 3D model for ions, i.e. it does not assume axial symmetry). It should be noticed that a kinetic treatment for neutral species is usually responsible for a significant increase of the time required to obtain an edge plasma solution. For this reason, codes such as UEDGE [170] have a fluid model for the neutral species, which allows for faster convergence times, albeit with some limitations, see section 5.3.2. Also B2.5 (the latter corresponding to the plasma solver of SOLPS-ITER) features a fluid model for neutral species. Finally, TECXY [215] features an even simpler, analytical model for neutral species, which allows for very fast calculations at the cost of even more severe approximations.

Chapter 5

SOLPS-ITER simulations of an LM divertor for the EU DEMO

As discussed in the previous chapter, one of the possible shortcomings of LMDs is the core plasma dilution/contamination caused by eroded liquid metal. On the other hand, the erosion itself can lead to beneficial vapor shielding of the target. To assess the balance of these effects and their impact on the performance of a fusion reactor such as the EU DEMO, self-consistent models are required.

In this chapter, simulations to investigate the effect of installing an LMD using a CPS on the EU DEMO tokamak within the same envelope of the baseline solid divertor are presented. The SOLPS-ITER code is used to model the SOL plasma and neutral species (both fuel neutrals and metal eroded from the target). A fluid neutral model was adopted, for the sake of simplicity. SOLPS-ITER was coupled to a model for the target temperature distribution, thus enabling the self-consistent calculation of the LM target erosion rate. This allowed to fairly compare Li and Sn used as materials for an LMD target, and to assess the effectiveness of seeding Ar in the SOL to reduce the target heat flux and, consequently, the erosion rate.

This chapter is organized as follows: first, an introduction is provided, mentioning previous studies on which the present work is based (section 5.1). The specific EU DEMO configuration and LMD designs here considered are described in section 5.2. The model and the simulation strategy are described in section 5.3. Results of simulations without and with Ar seeding are finally presented and discussed in section 5.4.1 and 5.4.2, respectively, comparing the behavior of Li and Sn. The chapter is concluded by section 5.5, which provides a recap of the most relevant results and future perspective of the present work

5.1 Background and motivation

The study here presented is motivated by the currently ongoing research efforts to develop an LMD design which complies with the EU DEMO divertor requirements (e.g. in terms of PEX, He removal, engineering integration and core plasma performance). As mentioned in the foregoing chapters, Li and Sn are currently regarded as the most promising candidates for an LMD [143]. For a given plasma heat and particle flux impinging on the target, a larger mass flux is eroded from a Li target with respect to a Sn target, due to the larger sputtering yield and vapour pressure. Conversely, for a given amount of eroded metal, Sn produces a more significant plasma cooling rate, mostly associated to line radiation [138]. For both Li and Sn, the vapor shielding effect has been experimentally observed [201, 166]. However, the resulting self-mitigation of the target heat load might still fail to prevent an excessive erosion rate, leading to unacceptable core plasma dilution (in the case of Li) or to intolerable radiative energy losses in the core plasma (in the case of Sn). Moreover, albeit partially self-mitigated, the peak target heat flux might still overcome the power handling capability of the CPS-based LMD target, which is limited by e.g. the maximum tolerable thermo-mechanical stresses on the solid substrate supporting the CPS [202], the Critical Heat Flux (CHF) to the coolant [167], or the maximum PFS replenishment rate allowed by the CPS [165]. Therefore, the strategy of seeding external impurities such as Ar to increase the SOL plasma radiation and, consequently, further mitigate the target heat load – a strategy that is strictly necessary for a conventional solid divertor – may be considered also for an LMD [192].

Modelling the SOL behavior in the presence of an LMD is essential to predict whether an operating window for this system exists, both in terms of core plasma compatibility and of target heat load. This challenge has been addressed in the past by means of simplified models [138, 67, 140, 118]. Recently, more detailed simulations, including the transport of the eroded metal in the SOL and a detailed account of its interactions with the plasma, have been performed by means of 2D edge plasma codes. Notably, the UEDGE, SOLPS4.3 and SOLPS-ITER codes were used to study the NSTX-U tokamak equipped with a liquid Li divertor, the T15-MD tokamak equipped with a liquid Li divertor and the FSNS facility equipped with a Li vapor box divertor, respectively [164, 119, 51]. The TECXY code was instead used to study a CPS-based LMD for both the EU DEMO and the DTT, also including a 1D thermal model of the LM target to self-consistently account for target evaporation [153, 154]. First integrated target-edge-core simulations for the EU DEMO with an LMD were also performed using COREDIV [156].

In the present work, the SOLPS-ITER code was used, for the first time, to simulate the edge plasma of the EU DEMO equipped with a CPS-based LMD, comparing Li and Sn used as LMs. The target response was considered self-consistently by coupling SOLPS-ITER to a thermal model to determine the surface temperature

distribution, in order to correctly describe the feedback on the SOL plasma. This approach enables to fairly compare Li and Sn as target materials, in terms of core plasma dilution/contamination and target heat flux and erosion. The effect of the eroded metal in terms of the core plasma dilution/contamination was also studied, although it is noticed that a more detailed evaluation of the impurity accumulation in the core plasma would require coupling SOLPS-ITER to a core transport code, which is beyond the scope of the present study. Finally, the effectiveness of seeding Ar to mitigate the target heat flux, thereby reducing the erosion rate, is assessed via further, dedicated simulations.

5.2 System description

5.2.1 Vessel shape and magnetic equilibrium

The EU DEMO wall geometry considered in this work is consistent with [192], which referred to the 2017 EU DEMO design [208], and is shown in Figure 5.1. Consistently with the EUROfusion strategy for the development of the LMD concept, the vessel shape and magnetic equilibrium were not modified with respect to the baseline scenario, whereas the divertor target material (originally W) was replaced with liquid Li/Sn.

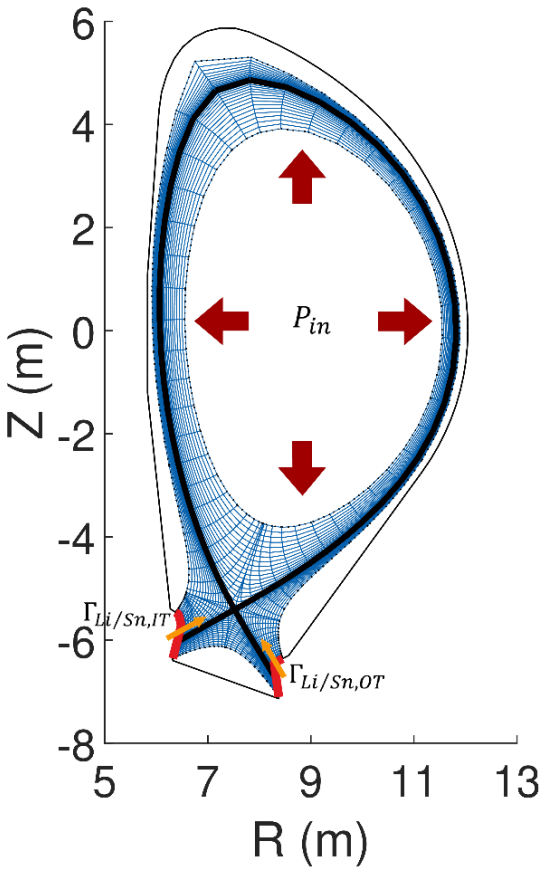

Figure 5.1: Sketch of the EU DEMO FW geometry, with the divertor targets highlighted in red. The Li/Sn net emission from the inboard and outboard targets ($\Gamma_{Li/Sn,IT}$ and $\Gamma_{Li/Sn,OT}$, respectively) is schematically indicated. The separatrix is represented by the thick black line. The power entering the computational domain from the plasma core (P_{in}) is also schematically indicated.

5.2.2 Liquid metal target

For Li, the design proposed by Vertkov et al. [202] is considered, consisting in a thin (2 mm) W plate covered by a Li-filled CPS (0.5 mm thick), see Figure 5.2. The W plate is cooled on the side not exposed to the plasma via an impinging water-gas spray, with a water temperature of 20 °C. It has been shown experimentally that this technique allows to achieve heat transfer coefficients as large as 70-100 kW/(m^2 K). This an important feature for an LMD, since it allows to withstand large heat loads while keeping the PFS temperature as low as possible, thus promoting a reduced evaporation. The maximum tolerable heat flux for this specific LMD target design is claimed to be $\sim$ 20 MW/m^2 and limited by mechanical stresses on the actively cooled W plate, i.e. the substrate on which the plasma-facing CPS is placed. This figure has been taken as a reference in the present work, although it is recognized that this could be improved by reducing the size of the units, if this is compatible with the adopted cooling strategy.

For Sn, the design developed at ENEA Frascati, which was described in some detail in section 3.4.2, is considered [167]. The cooling water temperature is 120 °C and the heat transfer coefficient can be computed according to the formulation proposed in [167]. For this design, a heat flux handling capability up to $\sim$ 40 MW/m^2 is claimed, which is limited by the critical heat flux to the coolant. This figure has been used as a term of reference in this study, even though the upper temperature limit for CuCrZr might be achieved at lower heat fluxes. For this reason, an alternative PFC using W-Cu as a heat sink has been developed at ENEA Frascati, and a prototype is foreseen to be tested soon in a linear plasma device.

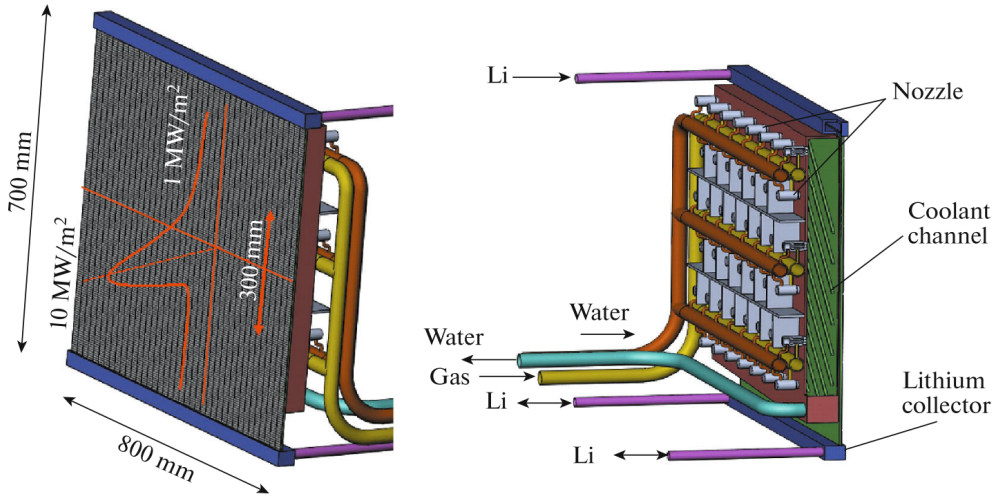

Figure 5.2: Schematic of the Li target considered for the simulations. Reproduced from [202] with permission.

5.3 Simulation setup

Steady-state calculations are performed considering the 2D domain shown in figure 5.1 for both plasma and neutral species, assuming toroidal symmetry. The SOL plasma and pedestal are described via multi-fluid, Braginskii-like equations, and also the neutrals are assumed to behave as a fluid. The target erosion is computed self-consistently with the plasma and neutral distributions.

A self-consistent approach is achieved by coupling two models:

1. A 2D SOL plasma model (SOLPS-ITER), computing: the SOL plasma temperature and density profile; the advection/conduction load on the divertor targets; the radiated power in the SOL due to plasma-vapor interactions; the impurity flux to core plasma.
2. A thermal model computing the wall temperature distribution, and consequently the LM evaporation and sputtering rates.

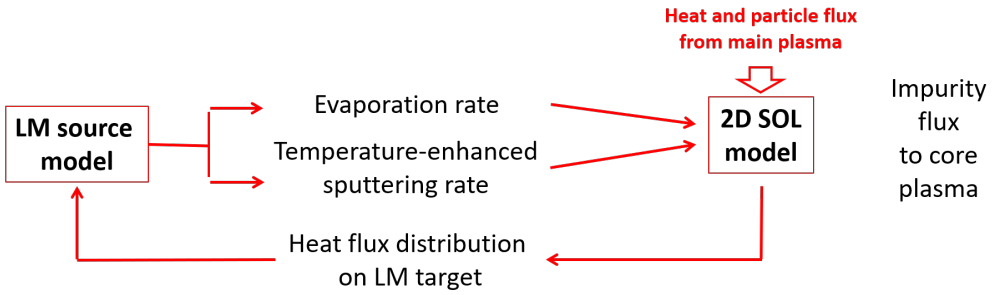

Figure 5.3: Schematic of the coupling strategy.

5.3.1 SOL plasma

The SOLPS-ITER code is employed in the present stydy [211]. For each element included in the simulation, the full set of charge states is considered, each treated as a separate fluid. This approach is computationally expensive, but it enables a detailed description of atomic processes in the plasma, which are especially relevant for the SOL plasma power balance in the presence of an LMD. An alternative, which has been considered in the early stages of the present work, consists in adopting the faster, but less accurate, *bundled charge state model* [35], as it was done in [192].

Simulation domain

The simulation domain was shown in Figure 5.1, together with the quadrilateral grid on which the multi-fluid equations are solved. The domain extends inside the separatrix (in the core plasma region) for $\sim$ 10 cm to approximately include the

pedestal region, and in the SOL for ~ 6 cm to include several power decay lengths (both distances are measured from the OMP).

Species considered

The plasma species included in the simulations are:

- D^0 (fuel neutrals), D^+(main plasma ions);
- Li^0 (Li vapor), Li^+, Li^{2+}, Li^{3+} (Li ionized species), in case of an LMD using Li;
- Sn^0 (Sn vapor), Sn^+, Sn^{2+}, ... Sn^{50+} (Sn ionized species), in case of an LMD using Sn;
- Ar^0 (Ar neutrals), Ar^+, Ar^{2+}, ... Ar^{18+} (Ar ionized species), in case Ar seeding is considered.

Each species is treated as a fluid, relying on Braginskii-like equations.

Fluid equations, flux limiters and diffusion coefficients

Classical parallel transport is considered, with coefficients according to [219]. Flux-limiters for electron and ion heat conductivities, and ion viscosity, are included. Friction and thermal forces are treated according to [194]. Anomalous perpendicular transport is instead considered by providing radially variable diffusivities ($D_\perp$, χ_e, χ_i) to the code. Specifically, uniform values are used in the SOL ($D_\perp = 0.42$ m^2/s and $\chi_e = \chi_i = 0.18$ m^2/s), to reproduce a power decay length $\lambda_q \sim 3$ mm. This value has been selected in view of the uncertainties regarding the actual extent of the SOL power width for the EU DEMO. Indeed, while the application of experimental scalings (e.g. the Eich scaling [48]) or heuristic models (e.g. the Goldston model [64]) validated in present-ray devices would predict $\lambda_q \sim 1$ mm, recent gyrokinetic calculations by Chang et al. suggest larger values [29]. It should be noticed that it would be interesting to have a sense of how much difference it would make to adopt the basic Eich scaling, and alternatively a much greater width as estimated by Chang for ITER. Although there was no time to perform this study, it is foreseen to repeat the same set of simulations varying λ_q to assess the effect of this choice on the simulation results. Inside the separatrix, transport coefficients are increased to simulate the presence of an Edge Transport Barrier (ETB), as expected in H-mode operation, see figure 5.4. However, it should be noticed that the treatment of the pedestal physics provided in this work is far from being comprehensive, and a self-consistent modelling including the core plasma would be necessary, as it will be explained in a later section.

Drifts and self-consistent electric currents are not included in the simulations, again for the sake of simplicity. Based on recent SOLPS-ITER simulations considering the ITER SOL plasma with Ne seeding and a full treatment of drifts and currents [99], it is expected that including these effects would lead to an increased

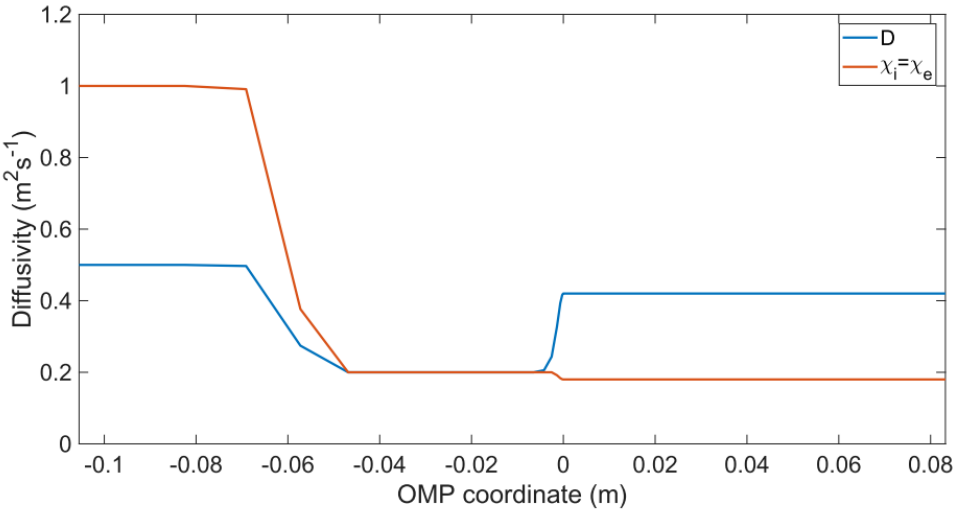

Figure 5.4: Radial distribution of anomalous perpendicular diffusivities provided to the code [191]

inboard/outboard asymmetry, due to the transport of impurities from the outboard to the inboard divertor region [107].

Boundary conditions

As far as the power balance is concerned:

- Core boundary: according to the H-mode scaling for the EU DEMO, the power crossing the separatrix P_{SOL} must be at least 150 MW to guarantee H-mode operation [120]. In the simulations here presented, the separatrix is an internal surface, therefore the power crossing it is not strictly speaking a boundary condition. However, by fixing P_{SOL} among the various simulations, it is possible to provide a fair comparison between the cases analysed (for instance, core radiation is expected to be more significant for Sn than for Li). For this reason, an amount of power $P_{pedestal} > P_{SOL}$ is introduced in the domain from the innermost flux surface (the difference being associated with radiation in the pedestal), manually checking a posteriori that $P_{SOL} \sim 150$ MW. Errors up to ~ 1 MW in the power actually crossing the separatrix are tolerated when manually calibrating $P_{pedestal}$. By resorting to this tactic, the presence of additional seeded impurities used as core radiators, such as Xe, is neglected, leaving the problem of performing integrated simulations including the core to future studies.
- Targets: the heat deposited on the targets is evaluated assuming a sheath heat transfer coefficient of 2.5 for ions and of 0.90 for electrons, which is the default choice for SOLPS-ITER.

- Walls: a radial decay length is imposed, since the grid does not extend up to the wall. Preparatory studies have shown that the simulation results are weakly dependent on the actual strength of this boundary conditions, which confirmed that the radial extent of the grid in the SOL was sufficient.

As far as the particle balance is concerned:

- Core boundary: a D^+ flux of $5 \cdot 10^{20}$ s^{-1} is imposed, consistently with previous EU DEMO scenario modelling studies [192].
- Targets: 100% fuel recycling, 100% deposition of other species.
- Walls: a leakage B.C. is imposed both at the wall boundary and at the private plasma boundary. This implies that the outgoing flux is proportional to the local particle density. This condition is selected to simulate the redeposition on the FW.

5.3.2 Neutral species

A fluid model is also employed for vapor and fuel neutrals. It is recognized that a more accurate solution would be obtained by relying on a kinetic model, such as the one provided by EIRENE, the Monte Carlo neutral transport code included in SOLPS-ITER [162]. This choice allowed for relatively inexpensive parametric scans to be performed, at the cost of some approximations:

- Neutrals in regions of low collisionality are not correctly represented by a fluid model.
- Molecular effects are neglected.
- The simulation domain for the neutral species does not extend up to the physical wall, except for the divertor targets - the neutral domain actually coincides with the plasma domain, see again figure 5.1. This implies that condensation on the FW and neutral pumping from the sub-divertor region cannot be accounted for in detail. For this reason, to mimic pumping and condensation, suitable boundary conditions were imposed on the outermost surfaces included in the computational domain. It should be noticed that the EIRENE domain would instead extend up to the wall [17], allowing to model e.g. condensation, provided that suitable condensation/reflection kinetic models are adopted.

These shortcomings do not prevent a detailed account of vapor shielding, which occurs in the proximity of the strike point - where the vapor source is located, which is also far from pumping ducts - and involves a non-negligible vapor collisionality. A fluid modelling approach is therefore regarded as acceptable for the scope of the present study.

5.3.3 Target erosion model

Erosion processes

The erosion rate for Li is computed as:

$$\begin{aligned}\Gamma_{Li,gross} = &\Gamma_{D^+} f(\beta)\left[\frac{Y_{phys,D^+\rightarrow Li}(E_{D^+})}{3} + \frac{Y_{ad}}{1+A\exp\left(\frac{E_{eff}}{kT}\right)}\right] \\ &+ \Gamma_{Li^+} f(\beta)\left[\frac{Y_{phys,Li^+\rightarrow Li}(E_{Li^+})}{3} + \frac{Y_{ad}}{1+A\exp\left(\frac{E_{eff}}{kT}\right)}\right] + \dots \\ &+ \Gamma_{Ar^+} f(\beta)\left[\frac{Y_{phys,Ar^+\rightarrow Li}(E_{Ar^+})}{3} + \frac{Y_{ad}}{1+A\exp\left(\frac{E_{eff}}{kT}\right)}\right] + \dots \\ &+ \eta \cdot \frac{p_v(T,\beta) - p_a}{\sqrt{2\pi m_{Li} kT}}\end{aligned} \tag{5.1}$$

where:

- Γ_{D^+}, Γ_{Li^+},... are particle fluxes of impinging ions, and E_{D^+}, E_{Li^+}, ... are the energies of the impinging ions. The dots "..." at the end of each line stand for the ionized species not explicitly reported in the formula above (Li^{2+}, Li^{3+}, Ar^{2+}, ...).
- β is the D concentration at the surface, which is neglected in the present study based on the assumption of negligible D retention in Li, which is in turn motivated by the large surface temperature (therefore the formula above is employed with $f(\beta) = 1$).
- Y_{phys} is the physical sputtering yield evaluated according to the empirical formula reported in appendix 1 of [205]. Input data for the empirical formula are as follows: surface binding energy $Es = 1.63$ eV, surface density $\rho = 530$ kg/m^3. The factor 1/3 accounts for the fact that 2/3 of sputtered Li consists of ions [7].
- Thermal sputtering (second term in square parentheses) is evaluated according to the adatom model, as proposed in [2]. Fitting parameters are $Y_{ad} = 2.9$, $A = 9.6 \cdot 10^{-6}$ and $E_{eff} = 0.7$ eV [1]. It should be noticed that these fitting parameters have been obtained for D^+ impinging on Li, and have been adopted also for Li self-sputtering and sputtering associated to Ar due to lack of data.
- Evaporation is calculated according to the Hertz-Knudsen equation, as indicated in the formula above. The vapor pressure is calculated according to the formulations reported in Appendix A. A sticking coefficient of $\eta = 0.75$ is used, which is the default in SOLPS-ITER.

The erosion rate for Sn is computed as:

$$\begin{aligned}\Gamma_{Sn,gross} = &\Gamma_{D^+} f(\beta) \left[Y_{phys,D^+\rightarrow Sn}(E_{D^+})\right] \\ &+ \Gamma_{Sn^+} f(\beta) \left[Y_{phys,Sn^+\rightarrow Sn}(E_{Sn^+})\right] + \dots \\ &+ \Gamma_{Ar^+} f(\beta) \left[Y_{phys,Ar^+\rightarrow Sn}(E_{Ar^+})\right] + \dots \\ &+ \eta \cdot \frac{p_v(T,\beta) - p_a}{\sqrt{2\pi m_{Sn} kT}}\end{aligned} \tag{5.2}$$

where:

- Γ_{D^+}, Γ_{Sn^+},... are particle fluxes of impinging ions and E_{D^+}, E_{Sn^+} ,... are the energies of the impinging ions. The dots "..." at the end of each line stand for the ionized species not explicitly reported in the formula above (Sn^{2+}, Sn^{3+},..., Ar^{2+},...).
- β is the D concentration at the surface, which is neglected in this work based on the assumption of negligible D retention in Sn (therefore the formula above is employed with $f(\beta) = 1$).
- Y_{phys} is the physical sputtering yield evaluated according to the empirical formula reported in appendix 1 of [205]. Input data for the empirical formula area as follows: surface binding energy $Es = 3.14$ eV, surface density $\rho = 7300$ kg/m^3.
- Evaporation is calculated according to the Hertz-Knudsen equation, as indicated in the formula above. The vapor pressure is calculated according to the formulations reported in Appendix A. A sticking coefficient $\eta = 0.75$ is employed, corresponding to the default in SOLPS-ITER.

For both Li and Sn, when calculating the evaporated flux, $p_a \sim 0$ is assumed, consistently with [154]. Other authors suggested to assume $p_a \sim p_{plasma}$ in vapor shielding regime, see [86, 201]. This aspect should be subject to further studies. The proposed formulation allows to compute the poloidal profile of $\Gamma_{Li/Sn,gross}$ along the target (one value for each grid cell boundary at the target, then multiplied times the area of each grid cell).

Prompt redeposition

Prompt redeposition is taken into account for both Li and Sn as:

$$\Gamma_{Li/Sn,\ net} = \Gamma_{Li/Sn,\ gross} \cdot (1 - f_{redep}) \tag{5.3}$$

This means that promptly redeposited particles are not emitted in these simulations (i.e. they are not emitted-then-redeposited). To calculate f_{redep}, the following formulation based on [30] is adopted:

$$f_{redep} = 1 - \frac{p^2}{1 + p^2} \tag{5.4}$$

with $p = \tau_{ion} \cdot \omega_{gyro} = \lambda_{ion}/\rho_{Li^+/Sn^+,max}$, where:

- τ_{ion} is the ionization time of Li^0/Sn^0
- ω_{gyro} is the angular gyro-frequency of the Li^+/Sn^+ ion
- $\lambda_{ion} = \frac{v_\perp}{\langle \sigma v \rangle_{iz} n_e}$ is the ionization length of Li^0
- $\rho_{Li^+/Sn^+,max} = \frac{m_{Li/Sn} v_\perp}{qB}$ is the Li^+/Sn^+ Larmor radius calculated for the case when ion velocity is perpendicular to the magnetic field

This formulation is included in the routines of the SOLPS-ITER code dedicated to plasma-wall interactions, although it was not applied to particles eroded via processes other than sputtering. In this work, it was therefore ensured that the same prompt redeposition fraction is applied also to evaporated particles. Since the formulation depends on plasma parameters in the proximity of the target, a poloidal profile of the prompt redeposition fraction is calculated and applied, self-consistently with the plasma state. This formula neglects the possibility of multiple ionizations in the sheath edge, as well as the effects of different ion and electron temperature, which are included e.g. in the formulation proposed by Tskhakaya [197].

Non-prompt redeposition

Particles emitted ($\Gamma_{Li/Sn,net}$) represent a source term for the model employed to follow the neutral atoms in the SOL. Due to ionization, and according to the local force balance, particles are allowed to return to the target plate, thus yielding an additional redeposition contribution.

Calculation of the target surface temperature distribution

The Li gross erosion rate, computed according to the formulation (5.1), depends on the surface temperature through the adatom sputtering term and the vapor pressure appearing in the evaporation rate. The same thing applies to Sn, albeit in this case the adatom contribution has been neglected, see equation (5.2). To self-consistently evaluate the surface temperature, two different models were adopted for the two designs here considered, in view of their different geometries.

The Li target, shown in Figure 5.2, has a flat geometry which can be conveniently simulated by decomposing it into a number of simple 1D finite difference thermal models (each representing a poloidal location along the target length). The W substrate and the LM-filled CPS were considered as two adjacent layers, neglecting any possible thermal resistance between them, as shown in Figure 5.5. Due to the slow motion of the LM in the CPS and based on the assumption that no droplet ejection nor splashing phenomena occur, the CPS+LM system was treated as a stationary medium having an equivalent thermal conductivity [133], i.e. a solid layer with averaged thermal properties evaluated by law of mixtures. Moreover, the Li is assumed to be pure, thereby neglecting any property variation associated to the presence of impurities on the surface or in the bulk of the LM. Evaporation cooling,

temperature-dependent properties, enthalpy of refilling metal were included. The active cooling provided by atomized water was taken into account by imposing a Robin-type boundary condition on the cooled surface, setting a heat transfer coefficient of $8 \cdot 10^4$ W/m^2/K and a water temperature of 20°C, common to all the radial location - having assumed a uniform cooling of the back of the plate.

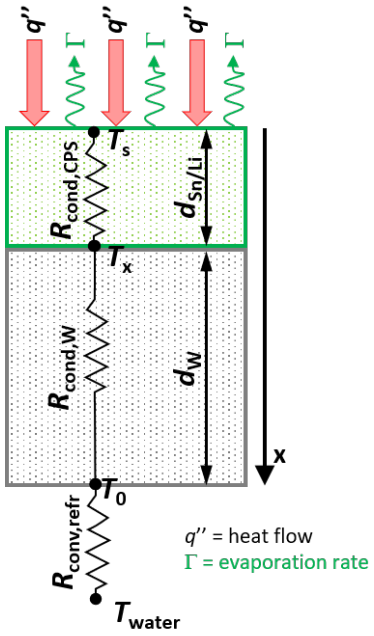

Figure 5.5: Schematic of the 1D model adopted for determining the surface temperature of the Li divertor.

The Sn target geometry is more complex, see Figure 3.11. For this reason, for each poloidal location along the target, a 2D model based on the Finite Element Modelling (FEM) method was adopted to describe the temperature behavior of the single module unit and then coupled to SOLPS-ITER. This was achieved by modifying the target heat transfer model developed by Carli [23], originally intended for computing the temperature in an ITER W divertor based on heat fluxes from SOLPS-ITER, see Figure 5.6 (left). In the present thesis work, the coupling between the two codes was made self-consistent, and the necessary modifications were carried out to take into account evaporation cooling, the specific geometry and materials of the ENEA design, see Figure 5.6 (right). It must be acknowledged that the application to the latest ENEA design was performed by G. Fiorita in his BSc thesis [61]. The assumptions for the CPS (treated as a stationary medium) were consistent with those for Li. As a final remark, due to the very limited coolant temperature increase along the target (a few K) the thermal coupling via coolant advection was neglected, thus leading to each "slice" being considered individually.

This assumption allowed to simplify the model, while representing a conservative choice (the resulting peak surface temperature will be larger neglecting the heat transfer along the poloidal direction). The heat transfer coefficient is computed according to the formulations suggested in [167], and the coolant temperature was set to 120°C.

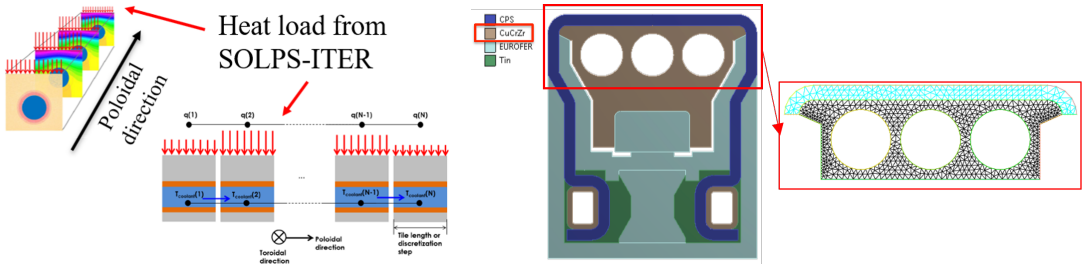

Figure 5.6: Schematic of the FEM model adopted in [23] to simulate the thermal behavior of the ITER W divertor (left) and CAD of a single Sn divertor module unit [167] with the computational mesh adopted to model each radial slice of the Sn divertor in the present thesis [61] (right).

For convenience, the poloidal sections were chosen so to correspond to the baricenters of the SOLPS-ITER grid cell. Thus, an array of 36 temperatures is passed at each time step to SOLPS-ITER, which in turn employs this temperature distribution to evaluate thermal sputtering and evaporation. At the end of the time step, a corresponging array of 36 plasma heat fluxes is passed back to the thermal model.

As a conclusive remark, it should be noticed that the SOLPS-ITER heat fluxes also include the power associated with surface recombination, whereas they do not include radiation power load. Although the latter cannot be accounted for self-consistently during the simulation, it is possible to verify *a posteriori* that its contribution is negligible by post-processing the SOLPS-ITER results using e.g. ray-tracing codes such as CHERAB [27, 26, 134], taking as input the computed radiation power source distribution and providing the heat flux over the PFSs.

5.3.4 Coupling implementation

Calculations are initialized by running SOLPS-ITER up to steady state using the built-in material erosion routines, which have been modified to include the formulation reported in section 5.3.3. As it is well known, this requires long computer times, even with a fluid neutral model: several days for D+Li, a couple of weeks for D+Sn. Once a steady state SOLPS-ITER solution is found, the heat flux distribution along the target is passed to the target model, so that an initial temperature distribution is found. At this point, both simulations (SOLPS-ITER and target) are converged to a steady-state which is however not yet self-consistent. Therefore,

time evolution for both simulations is started, and data are exchanged at each time step. Specifically, the heat flux profile is passed from SOLPS-ITER to the target model, while the latter provides the temperature profile, which is then used by the material erosion routines embedded in SOLPS-ITER, which have been purposely modified. The data exchange at each time step is performed via file exchange - although more elaborate options based on e.g. the OpenPALM coupling framework [44] have also been implemented, but disregarded for the moment due to the lack of time to perform thorough testing.

5.4 Results and discussion

To assess the effect of the presence of an LMD in different reactor operating conditions, it is convenient to perform parametric studies varying the upstream electron density at the OMP separatrix, $n_{e,sep}$. The range $3.5 \cdot 10^{19}$ m^{-3} $< n_{e,sep} <$ $4.5 \cdot 10^{19}$ m^{-3}, corresponding to $\sim$ 40% - 52% of the Greenwald density [207], was selected. After performing D+Li and D+Sn simulations, the effect of seeding Ar in terms of reduced target erosion rate and heat flux was assessed.

5.4.1 Results without Ar seeding

The particle balance shall first be discussed, starting from the vapor source term, i.e. the target erosion rate. Figure 5.7 shows that, as expected, the total (net) erosion rate for Li (Γ_{Li}) is $\sim$ 2 orders of magnitude larger than the total (net) erosion rate for Sn (Γ_{Sn}). For Li, evaporation represents the dominant erosion mechanism, and the relative contributions of the three erosion mechanisms considered is weakly dependent on $n_{e,sep}$. For Sn, consistently with the results presented in [153], evaporation is again found to be the dominant erosion mechanism, especially at large values of $n_{e,sep}$.

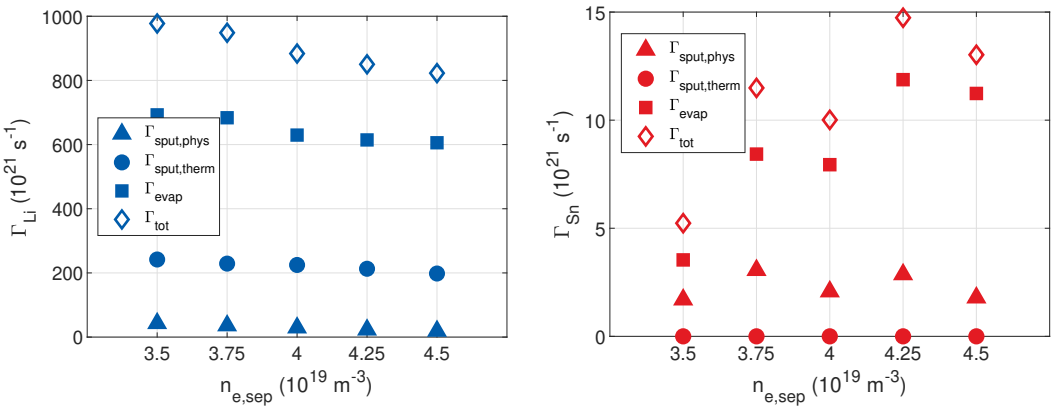

Figure 5.7: Total target emission rate as a function of $n_{e,sep}$ for Li (left) and Sn (right). The different contributions to the target erosion are also indicated. Note the different y scale.

For Li, the three contributions to the target erosion (evaporation, thermal sputtering and physical sputtering) all show an inverse dependence on $n_{e,sep}$. As for the sputtering rate, this behavior is consistent with simple two-point model considerations [190], since increasing $n_{e,sep}$ leads to a reduced target electron temperature, and therefore lower erosion. Moreover, as shown in Figure 5.8 (left), the radiation rate in front of the OT associated to Li vapor shielding, $q^{Li}_{rad,OT}$, increases with $n_{e,sep}$, thus further decreasing the target electron temperature. This can be explained in

terms of the radiated power density $L_Z^{Li}(T_e,n_e)n_{Li}n_e$, where the increase in n_e more than compensates for the lower n_{Li} associated to the weaker erosion. The same trend is observed in the power radiated via interactions with fuel neutrals $q^D_{rad,OT}$. The stronger radiation in front of the OT also leads to a mitigation of the heat flux to the target and, consequently, to a lower target surface temperature, which explains the trend in thermal sputtering and evaporation. It should be noticed that another effect that contributes to reduce the erosion rate is the increase of the prompt redeposition rate with $n_{e,sep}$ (not reported here). For the IT the same trend is observed, but it is not reported here for the sake of clarity, since IT erosion only accounts for a small percentage of the total.

For Sn, having neglected thermal sputtering, only physical sputtering and evaporation contribute to the erosion rate. Figure 5.8 (right) shows that the physical sputtering rate remains almost constant with $n_{e,sep}$, while the evaporation rate globally increases, although both quantities show a non-monotonic behavior. This can be explained in terms of two competing effects: the radiation in the OT region due to Sn vapor shielding $q^{Sn}_{rad,OT}$ decreases as $n_{e,sep}$ increases, dominating over the increase in $q^D_{rad,OT}$, as shown in Figure 5.8 (right). This tends to determine a larger target electron temperature and heat flux. Conversely, as for Sn, the prompt redeposition rate increases as $n_{e,sep}$ increases.

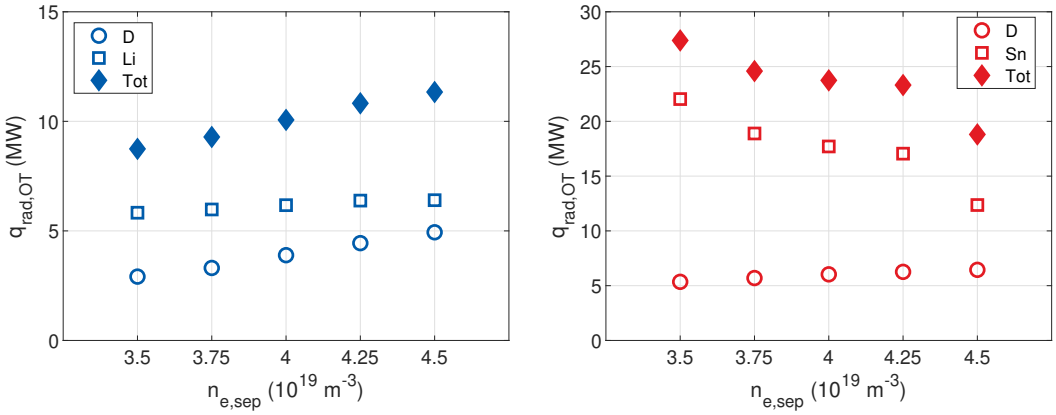

Figure 5.8: Radiated power density for to D and Li/Sn, integrated over the OT region, as a function of $n_{e,sep}$: Li (left) and Sn (right). Note the different y scale.

Figure 5.9 shows the resulting distribution of impurity concentration ($\frac{n_{Li/Sn}}{n_e}$) in the simulated domain, for the cases corresponding to $n_{e,sep} = 4.5 \cdot 10^{19}$ m^{-3}. For both Li and Sn, the largest concentration is found close to the OT strike point (where the strongest Li/Sn particle source is located) and in the far SOL, where n_e is low. As anticipated above, the strong asymmetry between conditions at IT and at OT is associated to the inboard/outboard heat load asymmetry. Indeed, due to the lower heat flux on the IT, the surface temperature is lower, and so the evaporation rate. The low ion temperature at the IT also implies a small contribution from

sputtering. As already mentioned, this asymmetry is probably underestimated, having neglected drifts.

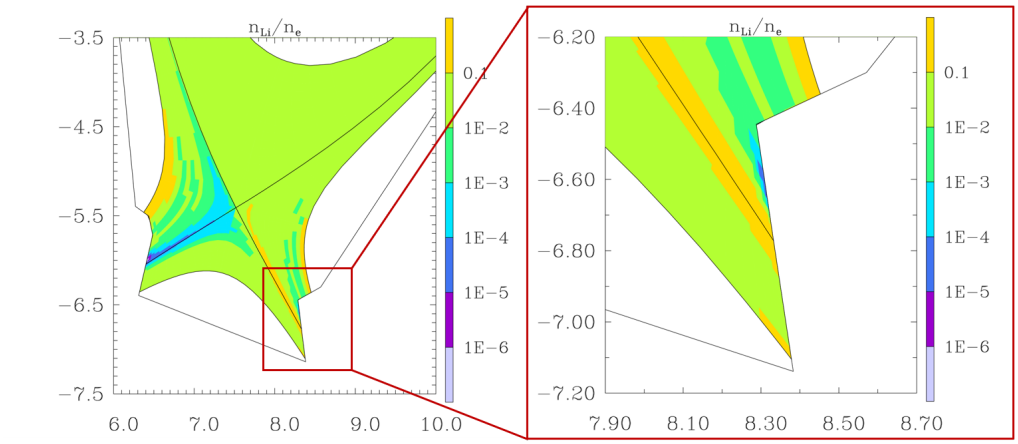

(a)

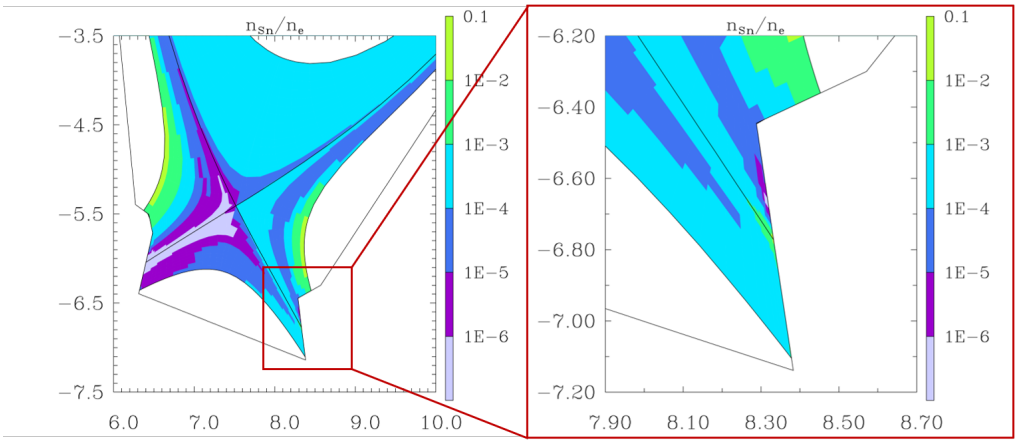

(b)

Figure 5.9: Computed 2D distributions of the Li concentration, n_{Li}/n_e (a), and of the Sn concentration, n_{Sn}/n_e (b), for the case $n_{e,sep} = 4.5 \cdot 10^{19}$ m^{-3}. The enlargements show conditions in front of the OT.

Figure 5.10 (left) compares Li and Sn in terms of average impurity concentration in the pedestal, $\left\langle n_{Li/Sn}/n_e \right\rangle_{pedestal}$. Also indicated in the plot are "plasma cleanness limits" which have been calculated in [153] based on the results of integrated target-SOL-core simulations performed with the COREDIV code: $\left\langle \frac{n_{Li}}{n_e} \right\rangle_{pedestal} < 3\%$ for Li (corresponding to a 20% reduction of the fusion power with respect to the case of pure D-T plasma) and $\left\langle \frac{n_{Sn}}{n_e} \right\rangle_{pedestal} < 0.05\%$ for Sn (corresponding to a back-transition from H to L mode due to the reduction of P_{sep} following from excessive core radiation). The results here reported indicate that, for Li, plasma dilution

is an issue, for the entire range of $n_{e,sep}$ considered in the present study. For Sn, instead, the concentration is ~ 2 orders of magnitude lower with respect to the case of Li, and at sufficiently large values of $n_{e,sep}$ it is lower than the above-mentioned "plasma cleanness limit", thus suggesting the existence of an operational window for which an Sn divertor is compatible with the EU DEMO core plasma performance requirements. The corresponding value of the effective charge Z_{eff} averaged over the pedestal region included in the simulation domain, $\langle Z_{eff} \rangle_{pedestal}$, is reported in Figure 5.10 (right). Again, it should be noticed that a more careful assessment of the core plasma conditions, achieved by e.g. coupling SOLPS-ITER to a core transport code, should be performed to allow for a fully self-consistent calculation of the SOL and core conditions in the presence of an LMD, thus enabling more quantitative conclusions on the core plasma compatibility of this concept to be drawn.

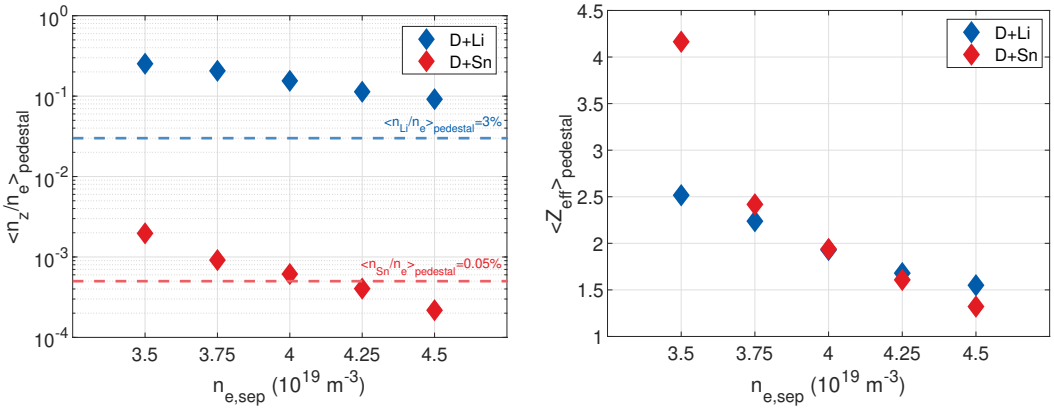

Figure 5.10: Impurity concentration (left) and Z_{eff} (right) averaged over the pedestal region: comparison Li vs. Sn.

The power balance can now be discussed. Figure 5.8, which was shown before to support the discussion concerning the trends in erosion rate for Li and Sn, already indicated a stronger OT radiation for Sn with respect to Li. In Figure 5.11, the distributions of the radiated power density for Li and Sn are compared, for the case corresponding to $n_{e,sep} = 4.5 \cdot 10^{19}$ m^{-3}. In this respect, Li performs better than Sn. Indeed, while both LMs cause beneficial plasma cooling in front of the target, Li only negligibly radiates in the core plasma, where it exists almost only in the fully stripped charge state. However, it was shown above that this plasma cooling is not sufficient to prevent an excessive core plasma dilution associated to the presence of Li. For Sn, a non-negligible pedestal radiation is found, which however was shown above to be marginally compatible with core plasma performance. The other main qualitative difference with respect to Li is the significant radiation along the SOL (not just in front of the OT). This implies a mitigation of the plasma power entering the vapor shielding region in front of the target, thus reducing the evaporation rate

necessary to sustain the vapor shielding regime.

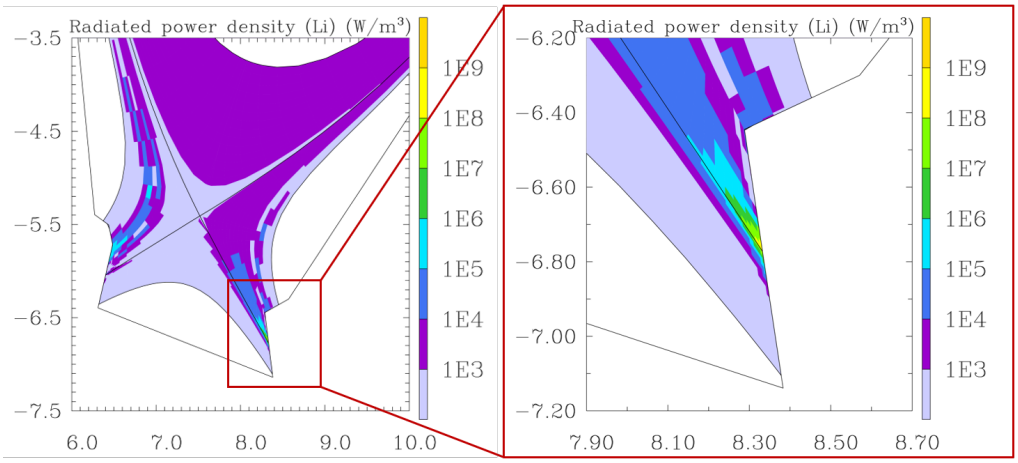

(a)

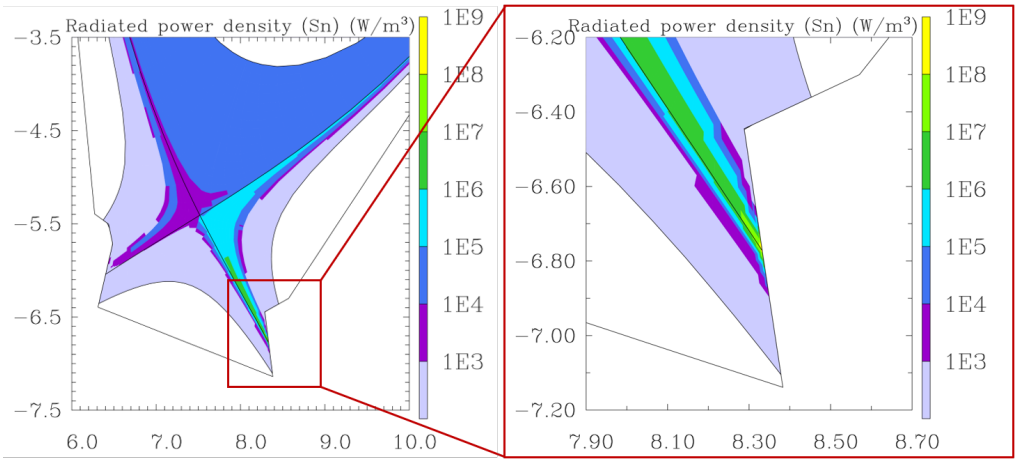

(b)

Figure 5.11: Computed 2D distributions of the radiated power density for the case $n_{e,sep} = 4.5 \cdot 10^{19}$ m^{-3}, for Li (a) and Sn (b). The enlargements show conditions in front of the OT.

Figure 5.12 summarizes the total radiated power density (due to the metal vapor, ions, fuel neutrals and main plasma ions) integrated over different regions of the computational domain, for the case $n_{e,sep} = 4.5 \cdot 10^{19}$ m^{-3}. As it was already evident from the 2D plots of Figure 5.11, radiation in the pedestal and along the SOL is significant for Sn, whereas it is negligible for Li. It should be noticed that, due to this fact, for the case with Sn at $n_{e,sep} = 4.5 \cdot 10^{19}$ m^{-3} it was necessary to increase P_{in} up to ~ 170 MW, to keep $P_{SOL} \sim 150$ MW. The value of the required P_{in} was found to be inversely proportional to $n_{e,sep}$, due to the decreasing trend of the pedestal radiation with increasing $n_{e,sep}$. The situation is more balanced in the

OT region, where still Sn radiates more. Finally, for Li a weaker inboard-outboard asymmetry in plasma cooling is computed, since the inboard target erosion is not completely negligible.

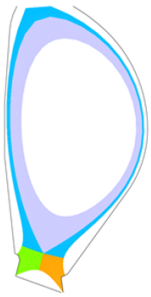

Total radiated power (MW)		OT	IT	SOL	Pedestal	TOT
	D+Li	11	8	3	3	25
	D+Sn	19	1	11	19	50

Figure 5.12: Schematic of the simulation domain with the regions highlighted and summary table of the total radiated power density integrated over different regions of the simulation domain for the cases D+Li and D+Sn, $n_{e,sep} = 4.5 \cdot 10^{19}$ m^{-3}.

To conclude this section, the effect of plasma-vapor interactions on the target heat flux are discussed. Figure 5.13 shows the computed heat flux profiles on the OT for the case $n_{e,sep} = 4.5 \cdot 10^{19}$ m^{-3}, for both Li and Sn. On the same plot, a reference heat flux profile for a pure D plasma, again computed using SOLPS-ITER and a consistent simulation setup, is reported. The beneficial reduction of the target heat flux (∼50% for Li and ∼30% for Sn) associated to the vapor shielding effect, for the cases where an LM target is adopted, is evident. Nevertheless, the peak heat load for Li (∼ 31 MW/m^2) is larger than the power handling limit of the specific target design here considered, i.e. ∼ 20MW/m^2. Similarly, the peak heat load for Sn (∼ 44MW/m^2) is slightly larger than the power handling limit of the ENEA target design, i.e. ∼ 40MW/m^2. The corresponding peak temperatures are ∼ 900°C for Li and ∼ 1700°C for Sn. These temperatures are responsible for the significant target evaporation, which represents the dominant contribution to the erosion rate, as discussed above.

For both Li and Sn, the heat flux computed by SOLPS-ITER far from the strike point appears to be negligible. However, this calculation does not take into account the possibly relevant radiative heat flux. For this reason, separate calculations, not shown here, were performed with the aim of evaluating the radiative contribution $q''_{rad,OT}$ to the heat load on the OT. This could be of interest e.g. to determine whether the temperature far from the strike point is lower than the Li retention limit, or to estimate whether radiation can be sufficient to keep the LM molten along the entire target. The radiation load was estimated with the Monte Carlo ray-tracing code CHERAB for the case $n_{e,sep} = 4.5 \cdot 10^{19}$ m^{-3}. The estimated peak value of $q''_{rad,tar}$ is 1.33 MW/m^2 in the case of Li and 1.97 MW/m^2 with Sn, i.e. ∼ 4% and ∼ 6% of the advection/conduction peak heat flux. Away from the strike

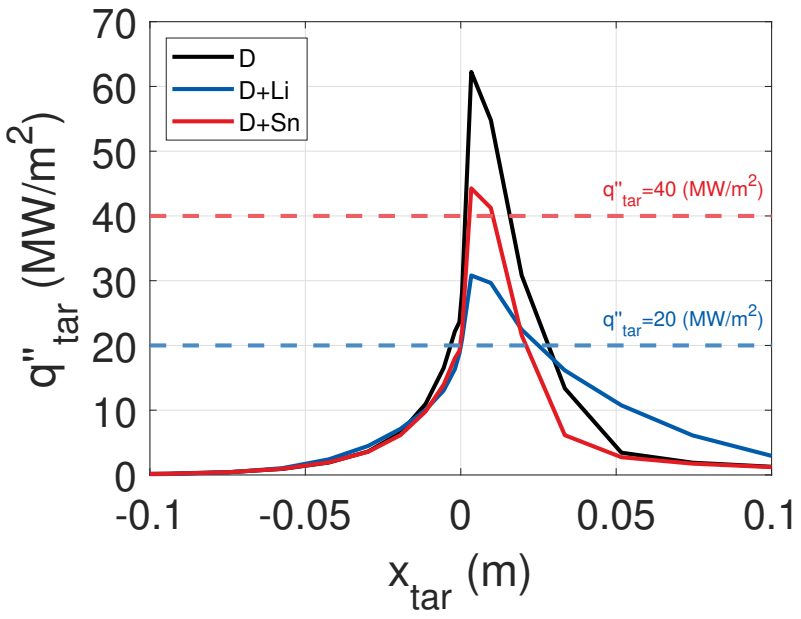

Figure 5.13: Target profiles of plasma advection/conduction heat flux for the cases D+Li and D+Sn compared with a reference case with D, for $n_{e,sep} = 4.5 \cdot 10^{19}$ m^{-3}.

point, moving upwards along the OT, the relative contribution of the radiative heat load increases to $\sim$ 30% for Li and $\sim$ 80% for Sn (at $x_{tar} = 0.2$ m). This indicates that, notwithstanding the additional heat load contribution associated to radiation, the LM will freeze far from the strike points (at least with the target cooling schemes here considered).

To summarize the outcomes of calculations without Ar seeding:

- For Li, an excessive plasma dilution is computed, for the entire range of $n_{e,sep}$ considered in this study. Moreover, notwithstanding the self-regulation of the target heat flux, the power handling limit of the LMD target design here considered is overcome.
- For Sn, the calculations suggest that plasma contamination could be tolerable, at sufficiently large values of $n_{e,sep}$. Nevertheless, the peak target heat flux is found to be slightly larger than the heat handling limit of the ENEA design here considered, notwithstanding the self-protection provided by vapor shielding.

These results suggest that the operational window for liquid Li or Sn divertor targets employed for the EU DEMO without any additional impurity seeding might be too narrow, if it exists. In addition, at least for the ITER-like target configuration considered in this chapter, Sn appears more promising than Li. This motivates further calculations to assess the effect of purposely seeding an additional impurity (e.g. Ar) to serve as a SOL radiator. Thanks to the additional plasma cooling provided by Ar, which is known to radiate mostly along the SOL, the target heat

flux is expected to be reduced, so lowering the metal erosion rate, eventually also limiting the core contamination.

5.4.2 Results with Ar seeding

For this second set of simulations, Ar was injected from the wall boundary of the calculation domain with a uniform distribution, to obtain a total seeding rate $\Gamma_{Ar} = 5 \cdot 10^{20} - 1 \cdot 10^{21}$ s^{-1}. This is consistent with [192], while a detailed study on the optimization of the injection location is outside the scope of the present work. Specifically, three Ar seeding rates, $\Gamma_{Ar} = 5 \cdot 10^{20}$ s^{-1}, $\Gamma_{Ar} = 7 \cdot 10^{20}$ s^{-1} and $\Gamma_{Ar} = 1 \cdot 10^{21}$ s^{-1}, were considered. Again, to provide a fair comparison between the cases here considered, it was ensured that the power crossing the separatrix was always kept equal to $P_{SOL} = 150$ MW. Figure 5.14 confirms that Ar injection effectively reduces the target erosion. In particular, at large $n_{e,sep}$, even the lowest Ar seeding rate here considered, $\Gamma_{Ar} = 5 \cdot 10^{20}$ s^{-1}, is capable of reducing the erosion rate by approximately one order of magnitude, for both Li and Sn. As expected, for a given value of $n_{e,sep}$, increasing the Ar seeding rate leads to a monotonic reduction of the erosion rate. To analyze the causes of this behavior, Figure 5.14 shows the various contributions to the erosion rate of Li (left) and Sn (right), for all the cases considered in this second part of the chapter (i.e. $n_{e,sep}$ from $3.5 \cdot 10^{19}$ m^{-3} to $4.5 \cdot 10^{19}$ m^{-3} and $\Gamma_{Ar,SOL}$ from 0 to $1 \cdot 10^{21}$ s^{-1}). The observed reduction in both evaporation and sputtering can be correlated to the power radiated in the SOL due to interactions with the seeded Ar, shown in Figure 5.16. Indeed, as the power radiated along the SOL increases:

- the target electron temperature is reduced, which implies a lower sputtering rate;
- the power entering the "vapor shielding region" in front of the OT is reduced, thus leading to a lower evaporation rate.

For Li, which does not significantly radiate far from the target – due to the fact that it is soon fully stripped of its electrons - the presence of Ar determines a significant increase in the SOL radiation rate with respect to the D+Li case. For Sn, instead, Ar radiation in the SOL has to compensate for the previously significant Sn radiation in the same region. This compensation is always effective, except for the case with $n_{e,sep} = 3.5 \cdot 10^{19}$ m^{-3} and $\Gamma_{Ar} = 5 \cdot 10^{20}$ s^{-1}, where the reduction in Sn radiation is larger than the Ar radiation in the SOL. This explains the otherwise surprising non-monotonic trend in Γ_{Sn} with increasing Γ_{Ar} for $n_{e,sep} = 3.5 \cdot 10^{19}$ m^{-3}. For a given Ar seeding rate, increasing $n_{e,sep}$ is found to always lead to a reduction in the erosion rate. This is due to the fact that the Ar radiation $P_{rad} = L_Z^{Ar}(T_e, n_e) n_{Ar} n_e$, which dominates the SOL power balance for both Li and Sn (as shown in Figure 5.14), increases with increasing $n_{e,sep}$ due to the global increase of n_e.

Figure 5.17 shows the resulting distribution of impurity concentration ($\frac{n_{Li/Sn}}{n_e}$)

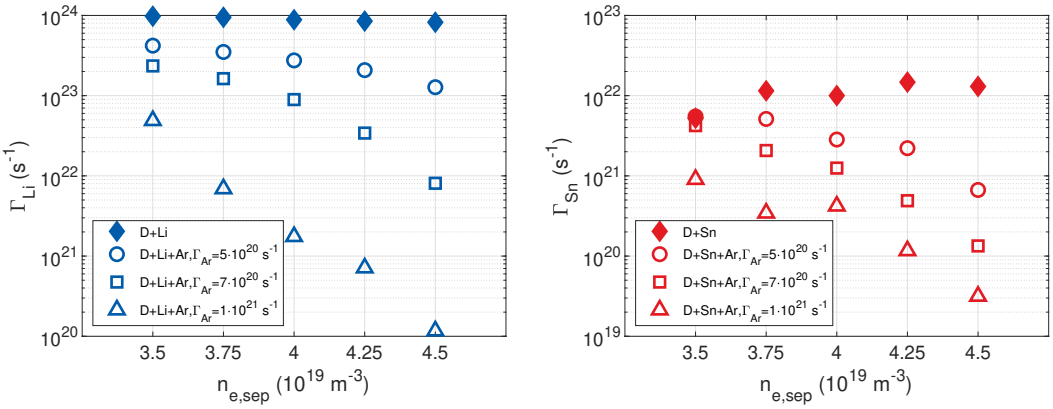

Figure 5.14: Total target erosion rate as a function of $n_{e,sep}$ for the different Ar seeding rates considered, for Li (left) and Sn (right). Note the different y scale.

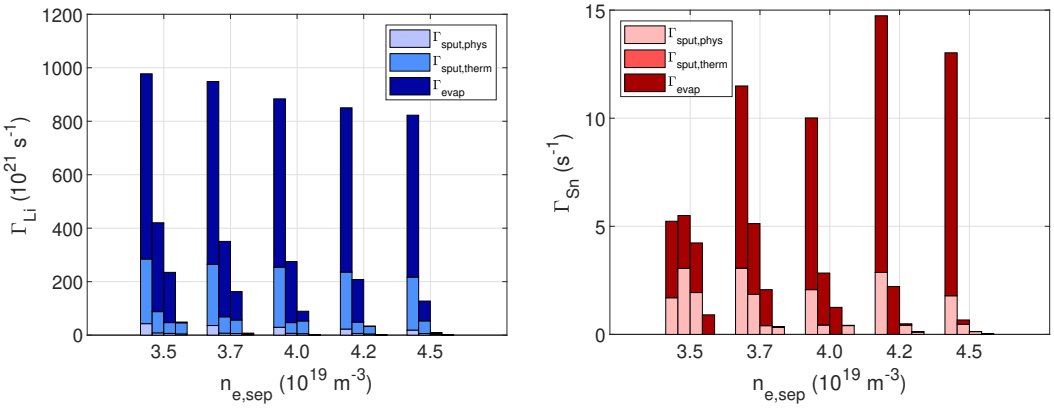

Figure 5.15: Contributions to the target erosion rate for Li (left) and Sn (right). For each value of $n_{e,sep}$ the four bars correspond to increasing Ar seeding levels, from $\Gamma_{Ar} = 0$ to $\Gamma_{Ar} = 1 \cdot 10^{21}$ s^{-1}. Note the different y scale.

in the simulated domain, for the cases corresponding to $n_{e,sep} = 4.5 \cdot 10^{19}$ m^{-3}, for the various Ar seeding rates considered in this work. The reduced target erosion rate determined by Ar seeding clearly results in a lower Li/Sn concentration over all the computational domain. The concentration remains relatively large in the far SOL and in the private flux region, where the electron density is low.

To support a more quantitative discussion, Figure 5.18 shows the Li/Sn concentration averaged over the pedestal region, for the entire set of $n_{e,sep}$ and Γ_{Ar} considered in this chapter, compared to the above-mentioned "plasma cleanness limits". Consistently with the results shown in Figures 5.14, 5.15 and 5.17, for a given $n_{e,sep}$, a larger Γ_{Ar} determines a lower concentration in the pedestal. As a consequence, the allowed operational window - in terms of core plasma performance - for the two LMD concepts considered in this paper, is significantly widened. For

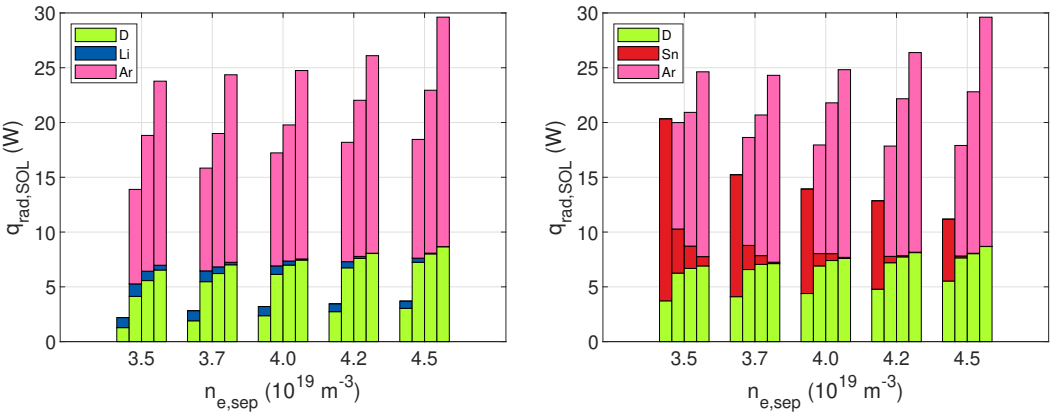

Figure 5.16: Contributions to the radiated power density, integrated over the SOL region, for Li (left) and Sn (right). For each value of $n_{e,sep}$ the four bars correspond to increasing Ar seeding levels, from $\Gamma_{Ar} = 0$ to $\Gamma_{Ar} = 1 \cdot 10^{21}$ s^{-1}.

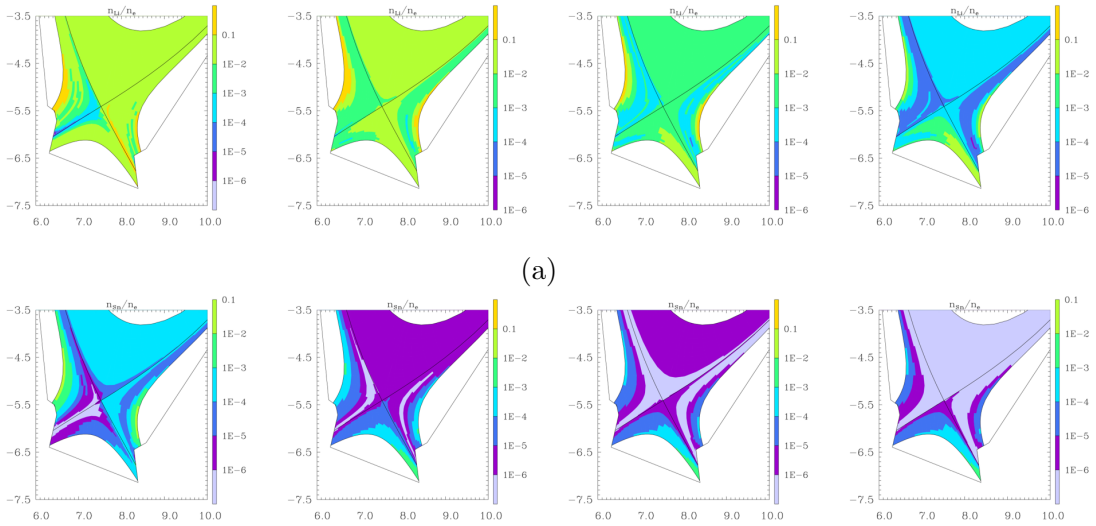

(a)

(b)

Figure 5.17: Computed 2D distributions of the relative concentrations for the case $n_{e,sep} = 4.5 \cdot 10^{19}$ m^{-3}, for Li (a) and Sn (b). Increasing Ar seeding rates are considered (from $\Gamma_{Ar} = 0$ to $\Gamma_{Ar} = 1 \cdot 10^{21}$ s^{-1}, moving from left to right).

the sake of completeness, Figure 5.19 shows the computed Ar concentration, averaged over the pedestal region, for the entire set of calculations performed. This density is well below ~ 0.5, which is the tolerability limit suggested in [161], thus confirming that Ar does not represent a threat for plasma purity.

The beneficial effect of Ar seeding in terms of the improvement of the core plasma compatibility of an LMD is reflected by the significant reduction of the

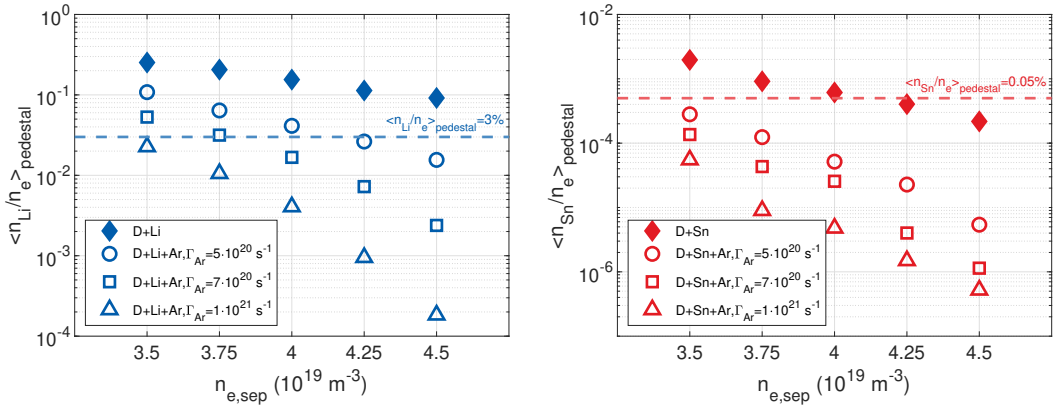

Figure 5.18: Impurity concentration (Li or Sn) averaged over the pedestal region, for various Ar seeding intensities: Li (left) and Sn (right). Note the different y scale.

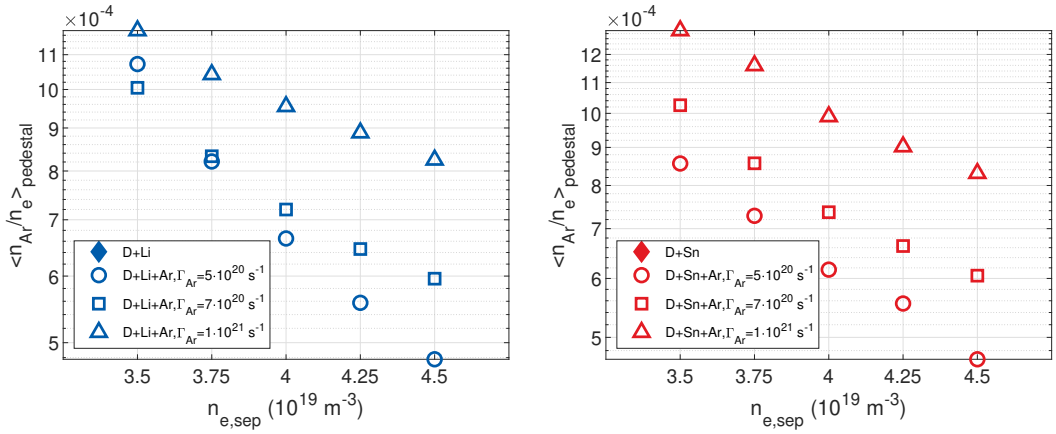

Figure 5.19: Ar concentration averaged over the pedestal region, for various Ar seeding intensities, for the cases D+Li+Ar (left) and D+Sn+Ar (right). Note the different y scale. The Ar tolerability limit suggested in [161], ~ 0.5, is not shown for the sake of clarity.

effective charge Z_{eff} averaged over the pedestal, $\langle Z_{eff,pedestal} \rangle$, shown in Figure 5.20 (left) for the cases $\Gamma_{Ar} = 0$ and $\Gamma_{Ar} = 1 \cdot 10^{21}$ s^{-1}. This result indicates that, while Ar seeding is effective in mitigating the plasma power load to the divertor targets (mostly thanks to SOL radiation, as discussed above), it does not represent a threat for the core plasma purity, at least for the values of Γ_{Ar} considered in this work, as it was discussed before based on the Ar tolerability limits computed in [161], see again Figure 5.19. Another interesting feature of the result shown in Figure 5.20 is that, for $\Gamma_{Ar} = 1 \cdot 10^{21}$ s^{-1}, the difference between the cases D+Li+Ar and D+Sn+Ar in terms of $\langle Z_{eff,pedestal} \rangle$ becomes negligible. This is a consequence of the fact that Ar has become the dominant plasma impurity for these cases, whereas

the density of Li/Sn is negligible. To complete the discussion, Figure 5.20 (right) shows the radiated power density, integrated over the pedestal region, for the cases $\Gamma_{Ar} = 0$ and $\Gamma_{Ar} = 1 \cdot 10^{21}$ s^{-1}. For Li, the reduction of the core plasma dilution associated to Ar occurs at the expense of a slight increase of core radiation due to the presence of Ar (whereas core radiation due to Li was negligible). For Sn, instead, the reduction of the core plasma radiation associated to Sn more than compensates for the moderate increase in radiation associated to Ar. Again, for the case $\Gamma_{Ar} = 1 \cdot 10^{21}$ s^{-1} a very similar behavior is observed for the cases D+Li+Ar and D+Sn+Ar.

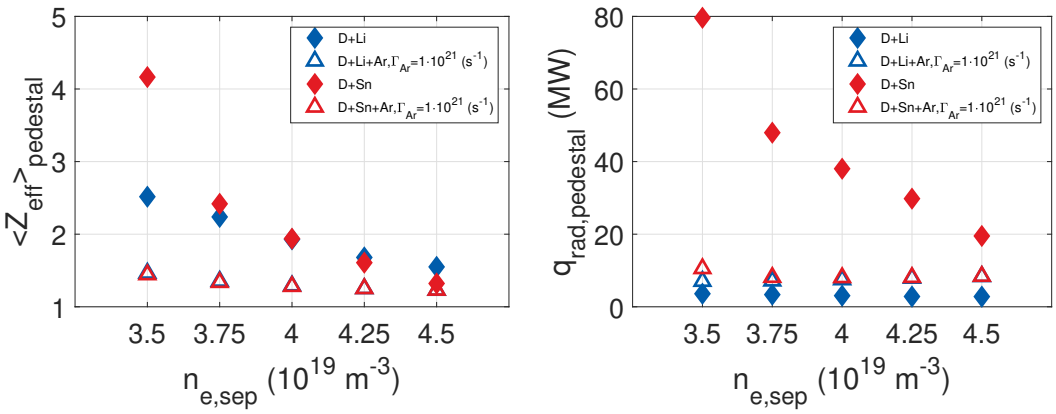

Figure 5.20: Average Z_{eff} in the pedestal region for different Ar seeding rates: comparison Li vs. Sn (left), and radiated power density integrated over the pedestal region for various Ar seeding rates: comparison Li vs. Sn (right). Only the cases with $\Gamma_{Ar} = 0$ and $\Gamma_{Ar} = 1 \cdot 10^{21}$ s^{-1} are shown, for clarity.

To summarize the discussion on the particle balance for the cases with Ar seeding, it can be stated that the operational window for an LMD in terms of core plasma compatibility appears significantly widened, for both Li and Sn. Moreover, even though a detailed discussion on the LM recollection from the FW is beyond the scope of the present work, the reduction of the net erosion rate (by more than 2 orders of magnitude, for the largest $n_{e,sep}$ considered) might significantly affect the design of the recollection system, or even make it unnecessary.

The power balance for the cases with Ar seeding can now be discussed. The results reported in Figure 5.16, which was already commented during the discussion concerning the mitigation of the target erosion rate associated with Ar seeding, indicate that Ar represents the dominant contribution to SOL radiation, for all the values of $n_{e,sep}$ and Γ_{Ar} considered in this study. Moreover, Figure 5.20 showed how the radiation in the core is reduced for the case D+Sn+Ar with respect to the case D+Sn thanks to the lower Sn erosion rate. To better visualize these effects, Figure 5.21 shows the distribution of the radiated power density due to Li/Sn *and* Ar for the cases D+Li and D+Li+Ar (a), and D+Sn and D+Sn+Ar (b)

corresponding to $n_{e,sep} = 4.5 \cdot 10^{19}$ m^{-3}, for all the Ar seeding rates considered. The similarity between the cases D+Li+Ar and D+Sn+Ar is apparent, and is associated to Ar radiation becoming the dominant contribution to the power balance in both the SOL and the pedestal. The enlargements shown in Figure 5.22, reporting only the Li/Sn contribution, show that in the OT region, for the lowest values of Γ_{Ar} considered, the vapor shielding (i.e. radiation associated to the interactions with the eroded Li or Sn) still plays a non-negligible role. However, as Γ_{Ar} is further increased, this effect is reduced, as the function of mitigating the heat load is performed by Ar. An interesting conclusion can therefore be drawn: purposely seeding Ar allows to move from a vapor shielding regime - where the heat load mitigation is performed by the eroded metal close to the OT - to a regime in which the mitigation of the plasma power leaving the separatrix occurs in the SOL due to Ar radiation. It should however be remarked that, even though vapor shielding is not exploited as a heat load mitigation mechanism during normal operation, it could still provide target self-protection in the case of off-normal events such as disruptions or unmitigated ELMs, as suggested in [165].

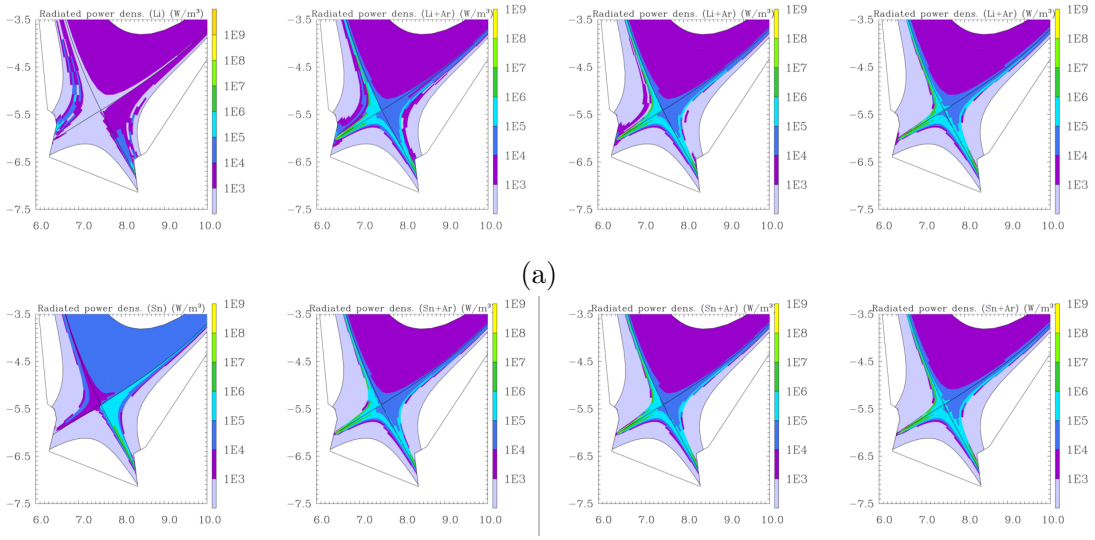

Figure 5.21: Computed 2D distributions of the radiated power density due to Li + Ar (a) and Sn + Ar (b), for the case $n_{e,sep} = 4.5 \cdot 10^{19}$ m^{-3}. Increasing Ar seeding rates are considered (from $\Gamma_{Ar} = 0$ to $\Gamma_{Ar} = 1 \cdot 10^{21}$ s^{-1}, moving from left to right).

To provide an insight into the parametric dependencies of the effects just described, the power radiated in the various regions of the calculation domain is now discussed in more detail, distinguishing among the contributions of the various species. Figure 5.23 (left) shows that, for the case D+Li+Ar, Ar determines the

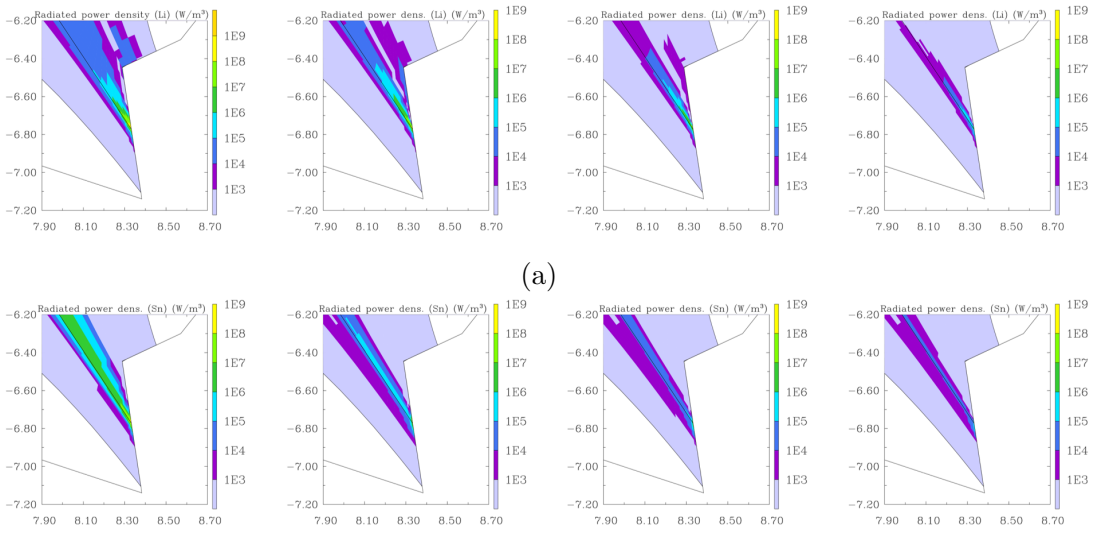

Figure 5.22: Computed 2D distributions of the radiated power density due to Li (a) and Sn (b), for the case $n_{e,sep} = 4.5 \cdot 10^{19}$ m^{-3}, in front of the OT. Increasing Ar seeding rates are considered (from $\Gamma_{Ar} = 0$ to $\Gamma_{Ar} = 1 \cdot 10^{21}$ s^{-1}, moving from left to right).

anticipated increase of the power radiated in the pedestal. This increase is significant in relative terms, but it is not believed to represent a threat for core plasma performance. Indeed, the Ar concentration is based on the tolerability limit for the density of Ar in the pedestal . Figure 5.23 (right) instead shows that, for the case D+Sn+Ar, the dominant effect in the pedestal is the reduction of Sn radiation due to the lower Sn density. Figure 5.24 (left) indicates that, for Li, Ar radiation in the OT more or less compensates for the reduced vapor shielding effect, especially at large densities. Figure 5.24 (right), instead, indicates that for Sn the dominant effect in front of the OT is the reduction in Sn radiation. This is made possible by Ar radiation in the SOL, as already pointed out by results in Figure 5.16).

In the foregoing discussion, the effectiveness of Ar seeding in terms of mitigated erosion rate and plasma contamination was shown. To conclude this section, it is necessary to assess whether Ar seeding is also effective in reducing the target heat flux on the OT – the most loaded between the two targets. To this aim, Figure 5.25 shows the target heat flux profiles for the case $n_{e,sep} = 4.5 \cdot 10^{19}$ m^{-3}, for the various Ar seeding rates considered. For both Li and Sn, the peak heat flux is reduced by a factor up to ~ 2, which is sufficient to ensure compliance with the power handling limit of the two LMD target designs considered in this work. These results suggest that LMDs based on the CPS concept using either Li or Sn, used in combination with Ar seeding, could be compliant with the EU DEMO plasma scenario in terms

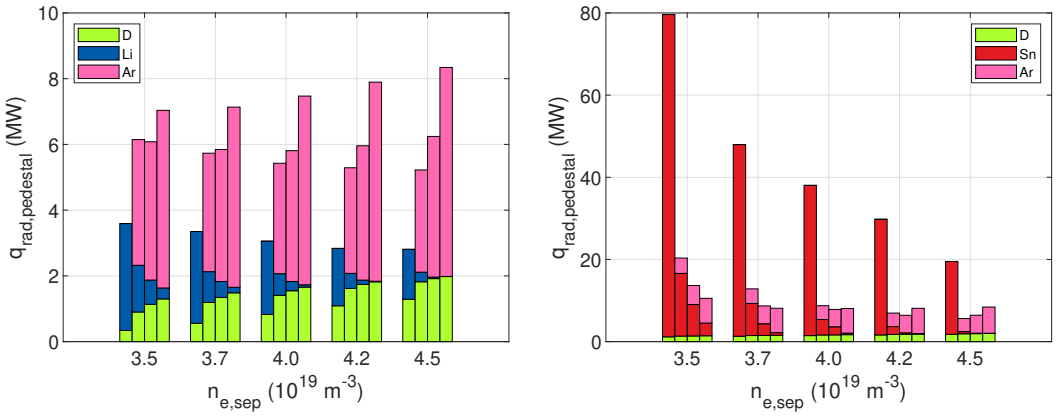

Figure 5.23: Contributions to the radiated power density, integrated over the pedestal region, for Li (left) and Sn (right). For each value of $n_{e,sep}$, the four bars correspond to increasing Ar seeding levels, from $\Gamma_{Ar} = 0$ to $\Gamma_{Ar} = 1 \cdot 10^{21}$ s^{-1}. Note the different y scales.

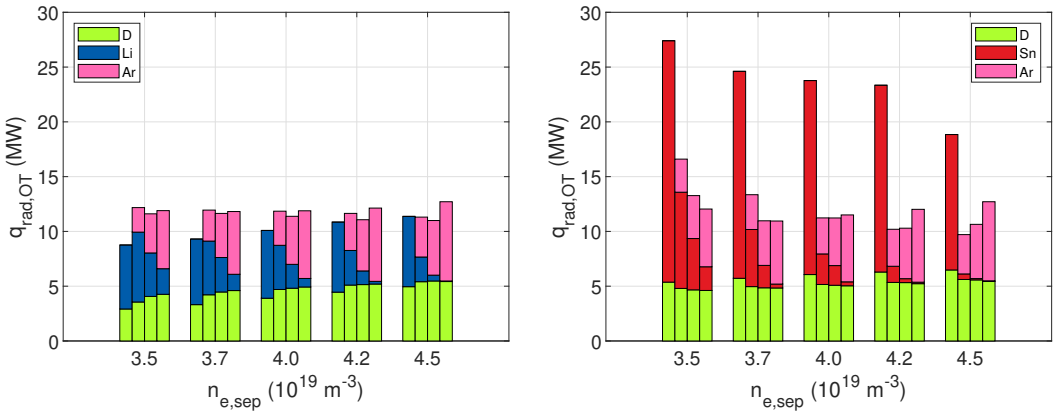

Figure 5.24: Contributions to the radiated power density, integrated over the OT region, for Li (left) and Sn (right). For each value of $n_{e,sep}$, the four bars correspond to increasing Ar seeding levels, from $\Gamma_{Ar} = 0$ to $\Gamma_{Ar} = 1 \cdot 10^{21}$ s^{-1}. Note the different y scales.

of both plasma dilution/contamination and target heat handling limit. Again, it should be noticed that Sn appears to have a wider operational window with respect to Li, in terms of minimum $n_{e,sep}$ and Γ_{Ar} required to satisfy the above-mentioned constraints.

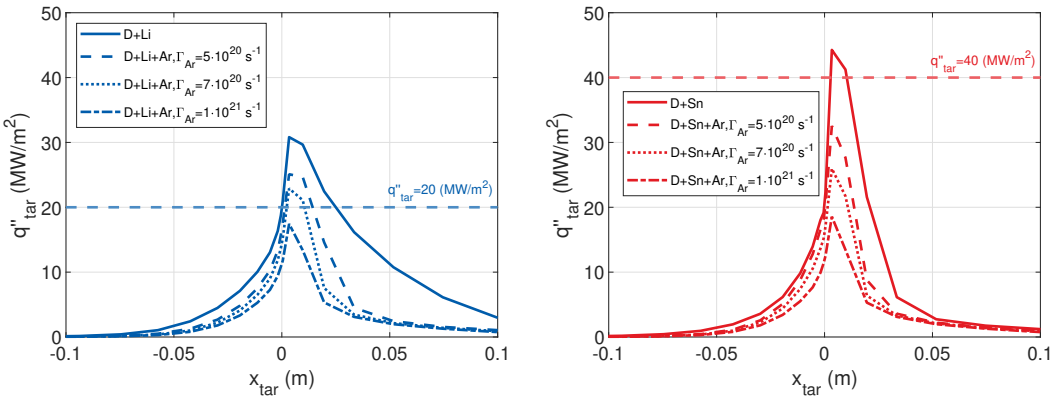

Figure 5.25: Outboard target profile of plasma advection/conduction heat flux for D+Li+Ar (left) and D+Sn+Ar (right), for the various Ar seeding rates considered, for $n_{e,sep} = 4.5 \cdot 10^{19}$ m^{-3}

5.5 Conclusions and perspective

In this chapter, a methodology for simulating the EU DEMO plasma in the presence of an ITER-like LMD based on the CPS concept was presented. The SOLPS-ITER code has been used, accounting for the plasma-vapor interactions self-consistently thanks to the coupling to a purposely developed target model including the relevant erosion phenomena (evaporation, thermal sputtering, physical sputtering) and accounting for prompt redeposition. The proposed strategy allowed to fairly compare the performance of selected LMD designs using Li and Sn, performing a parametric scan over a range of outboard midplane electron densities at the separatrix, $n_{e,sep}$. In this first study, for the sake of simplicity, a fluid model was adopted for the neutral species.

For both Li and Sn, simulation results indicate that the targets operate in a *vapor shielding* regime, characterized by relatively strong evaporation inducing significant radiation in the proximity of the OT, in turn determining a self-mitigation of the target heat load. For Li, the resulting core plasma dilution was found to be excessive, and the peak target heat load was larger than the power handling limit of the LMD design considered in this work. For Sn, the core plasma contamination was computed to be tolerable only at sufficiently large values of $n_{e,sep}$, and the computed peak heat flux was again close to the power handling limit of the design considered. Based on these results, it was concluded that the operational window for the EU DEMO equipped with an ITER-like LMD is narrow, if it exists, in the absence of any additional impurity seeding.

These results motivated a further study considering the effects of seeding Ar. It was found that the increased SOL radiation due to the presence of Ar can effectively replace the self-mitigation of the target heat load which was associated to vapor shielding in the cases without Ar. This led to a significant reduction of the erosion

rate for both Li and Sn, thus noticeably widening the operational window from the point of view of core plasma compatibility. Moreover, the reduction in peak target heat flux allows to comply with the heat handling limits of the LMD designs here considered. A significant outcome of the present study is that, based on the above-described results, an LMD could be operated in a plasma scenario similar to the one of a solid divertor (high recycling, very low evaporation/vapor shielding, power exhaust via impurity seeding), thus avoiding the need to re-design the machine operation and minimizing the required modifications to other reactor components. At the same time, an LMD would still be more resilient to off-normal events with respect to a solid divertor, thanks to the target self-protection (via vapor shielding) and self-replenishment (via capillary forces).

These encouraging results should of course be supported by more refined modelling and experiments. Three possible lines of activitiy in this respect are the following:

- A **kinetic model for the neutral species** (both fuel neutrals and metal vapor) should be included. Using SOLPS-ITER, the natural choice is to switch from the fluid neutral model used in this work to the kinetic model provided by the EIRENE code, which is included in the SOLPS-ITER code package. This would allow to describe more accurately the vapor dynamics and removal via e.g. condensation on the FW, as well as to account for the pumping of fuel neutrals and He ash from the sub-divertor region. In this way, the shortcomings of the modelling approach here presented, which are associated with both the fluid nature of the model employed and to the limited extension of the grid, could be removed, thus obtaining a more realistic description of the neutral behavior. This activity is ongoing, at the time of writing the present thesis. It should be mentioned that SOLPS-ITER simulations for a Li divertor with kinetic neutrals and a fixed evaporation source have recently been published by Emdee et al. [51].
- To systematically assess the plasma compatibility of the impurity flux entering the separatrix, **integrated simulations** which self-consistently include not only erosion from the target, transport in the SOL and interactions with the plasma, but also transport in the core, are required. This could be obtained e.g. by coupling SOLPS-ITER to ASTRA, see [178, 179].
- To give confidence in the application of these models to predict the behavior of an LMD for the EU DEMO, **validation** is essential. A first validation of the erosion model could be performed relying on data from LM target exposures in linear plasma devices [132]. Moving to tokamaks, recent experiments on the COMPASS tokamak with a small LMD module inserted, which were briefly mentioned in section 3.1.4, could represent a first source of data [38]. Furthermore, the test of a small, actively cooled LM sample using Sn on the ASDEX-Upgrade tokamak is foreseen in the next few years within the framework of EUROfusion WPPRD work package. This would provide an

excellent test bench for the modelling strategy here proposed.
The resulting improved, validated and integrated modelling strategy, which would allow to confirm, from the modelling point of view, the compatibility of an LMD with an EU DEMO scenario, is summarized in Figure 5.26.

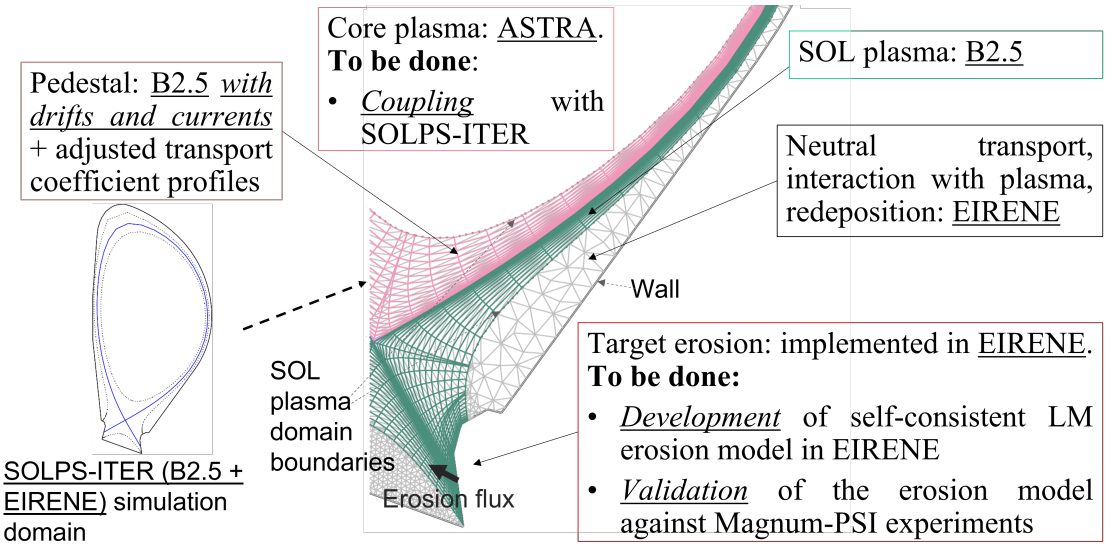

Figure 5.26: Schematic of the proposed integrated modelling strategy, with highlighted the needed future developments.

The author wishes to point out a number of aspects concerning both the modelling choices and the analysis of results which are worth further investigations in the future:

- It could be interesting to assess the effect of the sweeping foreseen for some period of time after loss of detachment in the case of an LMD.
- The present study did not target detached plasma operation (which would require larger $n_{e,sep}$ and/or Γ_{Ar}), which is left for future studies.
- An increase of the "puff and pump" effect could reduce upstream impurities, helping to keep the impurities in the divertor region.
- Some strategies to address the recollection of material from the main chamber walls should be devised, also based on the amounts estimated in this work.
- The vapor model could be extended to evaluate the deposition of Li/Sn onto the target based on Langmuir flux, with a sticking coefficient.
- It is expected, based on the results here obtained, that the Sn concentration and radiation will rise dramatically if the Ar puffing fails or the separatrix density falls. It has been mentioned in the conclusions that this should be a positive aspect, because it makes the system more stable, preserving the divertor from failing in such cases. However, this sudden increase in radiation might drive disruptions, similarly to what happens for W injections.

5.6 Data availability

To promote reproducibility of the results here presented, simulations have been uploaded to the MDSplus database, maintained at IPP Garching. The identification numbers (MDSplus IDs) of the simulations are reported in Table 5.1.

		$n_{e,sep} = 3.5 \cdot 10^{19}$ m^{-3}	$n_{e,sep} = 3.75 \cdot 10^{19}$ m^{-3}	$n_{e,sep} = 4.0 \cdot 10^{19}$ m^{-3}	$n_{e,sep} = 4.25 \cdot 10^{19}$ m^{-3}	$n_{e,sep} = 4.5 \cdot 10^{19}$ m^{-3}
D+Li		182286	182287	182288	182289	182290
D+Sn		182222	182223	182398	182399	182226
D+Li+Ar	$\Gamma_{Ar} = 5 \cdot 10^{20}$ s^{-1}	182275	182276	182277	182278	182279
	$\Gamma_{Ar} = 7 \cdot 10^{20}$ s^{-1}	182280	182281	182282	182283	182284
	$\Gamma_{Ar} = 1 \cdot 10^{21}$ s^{-1}	182270	182271	182272	182273	182274
D+Sn+Ar	$\Gamma_{Ar} = 5 \cdot 10^{20}$ s^{-1}	182233	182234	182235	182330	182237
	$\Gamma_{Ar} = 7 \cdot 10^{20}$ s^{-1}	182238	182239	182246	182241	182242
	$\Gamma_{Ar} = 1 \cdot 10^{21}$ s^{-1}	182444	182445	182229	182230	182231

Table 5.1: MDSplus IDs of the simulations performed during the presented work.

Chapter 6

Numerical modelling of an LM vapor box divertor for the DTT

In this chapter, a self-consistent model for an LM box-type divertor is presented. The model is applied to a possible box-tipe divertor for the DTT. A comparison between Li and Sn (used as LMs) is performed in terms of the operating temperatures and of the flux of vapor which exits the divertor system towards the Main plasma Chamber (MC). For Li, as expected, results indicate that a relatively large density of vapor can be confined within the divertor chambers, a condition that is not reached with Sn due to the weaker evaporation. For both Li and Sn, the flux of vapor lost towards the MC was computed to be ~ 2 orders of magnitude lower than the evaporated flux.

This chapter is organized as follows: in section 6.1, some background on the vapor box divertor is provided, to complement the brief introduction provided in section 3.3. The DTT divertor here considered is described in section 6.2. The specific aspects of the phenomenology of a vapor box divertor are discussed in section 6.3. The three coupled modules of the code implementing the self-consistent model (LM, SOL and walls, respectively) are then described in section 6.4. The simulation setup for the calculation is described in section 6.5, and finally the results are presented in section 6.6. Section 6.7 indicates conclusions and perspective of this work.

The content of this chapter represents a rearrangement of the preparatory material for the article [138].

6.1 Background and motivation

In 2009 Nagayama [136] proposed four different LM divertor concepts, the simplest of which consisted in an LM pool contained in the so-called Evaporation Chamber (EC). In order to reduce the flux of Li atoms towards the MC, the author proposed to add a Differential Chamber (DC), where the Li vapor could condense and the necessary pumping of hydrogenic species could also take place. The concept was based on evaporation cooling, i.e. in the usage of the LM latent heat of evaporation to exhaust the heat coming from the plasma. In parallel, Ono et al. proposed an *active radiative liquid Li* divertor concept which relied on non-coronal Li radiation to exhaust the plasma heat, whereas evaporation of a liquid substrate was considered only as the last layer of defense [147].

Those two ideas were then put together and further developed by Goldston et al., who proposed an innovative concept, called *Lithium vapor box divertor*, where both effects were exploited [65, 67]. To this aim, they proposed a box structure intended to confine a large density of Li in the divertor region, while allowing for a modest flux towards the Main plasma Chamber (MC). In this work, a concept halfway between the Nagayama proposal and the Goldston's vapor box divertor is considered: a system with two boxes where the evaporation is determined by the plasma impinging on the LM target (a pool or a CPS) rather than imposed by fixing the temperature of the EC walls as in [67].

For this system, a simplified but self-consistent 0D model for the vapor in the chambers, the temperature of the walls and the energy lost by the plasma via interactions with the vapor was proposed in [140]. According to that extremely simplified model, the Li vapor seemed to be effective in redistributing the plasma heat load over the chamber walls. Moreover, passive pumping due to LM vapor re-condensation in the EC and DC allowed for a reduction of main plasma chamber contamination. The power balance within the vapor box was found to be dominated by Li vapor radiation, thereby motivating a more thorough treatment of the underlying physics. Although the vapor box divertor was originally proposed using Li as an LM, in view of the increasing attention received by Sn, it is of interest to assess the performance of this system also for this LM.

The aim of the work here presented is therefore to develop a self-consistent model of a box-type LM divertor which is able to catch the most relevant physical phenomena occurring in such a system while maintaining the computational time reasonably low, so that it can be applied for preliminary studies. The DTT facility was chosen as a test bench for the resulting code and for drawing preliminary conclusions concerning the comparison between Li and Sn. The comparison between Li and Sn should point out the differences in terms of operating temperatures of both the LM and of the box structures, of impurity flow towards the main plasma chamber and of recirculating LM flow rate.

6.2 System description

Starting from the latest available CAD of the tokamak chamber [40], a tentative layout of a box-type LM divertor which is compatible with the available space has been suggested for the DTT, see Figures 6.1 and 6.2.

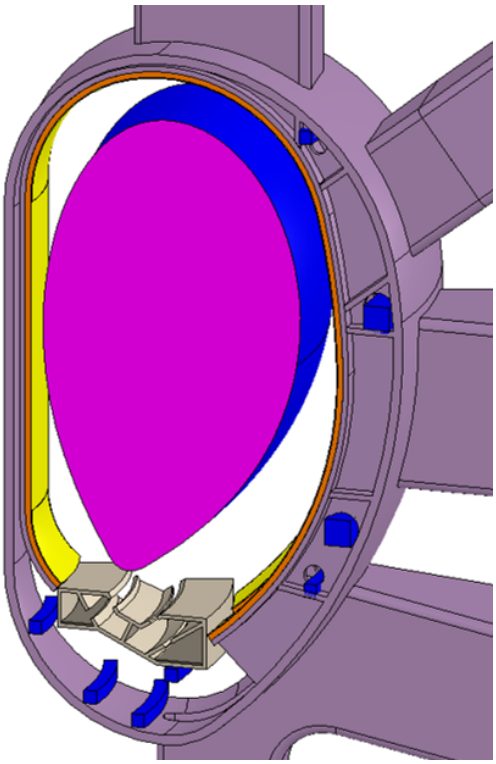

Figure 6.1: CAD of a DTT sector [40] with the proposed vapor box divertor inserted.

The proposed CAD accounts for geometrical constraints such as the dimension of the tokamak chamber and the presence of two in-vessel copper coils (C1 and C4 in Figure 6.3) which are thought for plasma control or local field modification in the divertor region. Figure 6.3 also shows the most relevant dimensions of the system at hand and introduces the nomenclature which shall be used throughout this chapter concerning the various chambers: Inboard Evaporation Chamber (IEC), Inboard Differential Chamber (IDC), Outboard Evaporation Chamber (OEC), Outboard Differential Chamber (ODC).

As very schematically shown in the picture, the position of the apertures has been chosen according to the latest available reference SN equilibrium for the DTT machine [216]. The choice of the apertures width follows instead from a trade-off. Indeed, one should keep them as small as possible to avoid excessive vapor flux from the IDC and ODC to the main plasma, but should also be concerned about the

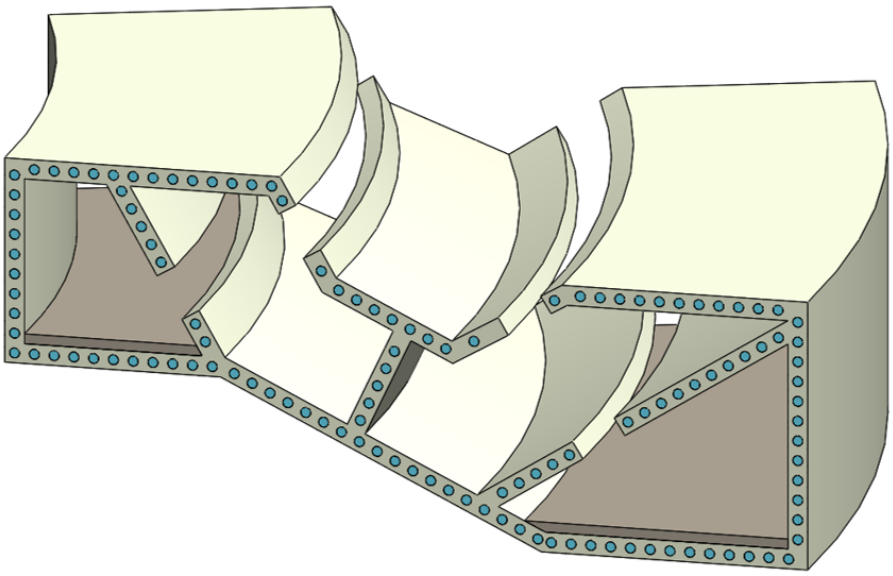

Figure 6.2: CAD of the possible LM box divertor sector for the DTT.

sputtering production which would occur, should the relatively high temperature SOL plasma touch the aperture borders. Consequent impurities would frustrate the improvement of the plasma purity which should be one of the main motivations for employing a LM divertor. Of course, a more severe misalignment would cause the melting of the box structure. Based on these considerations, a conservative value of 5 cm has been selected for the four apertures of the system. This value is based on an expected particle scrape-off width of $\sim$ 1 cm close to the entrance of the plasma in the DCs, according to the model proposed by Goldston [64] and assuming an expansion factor $f_{exp} \sim 3$ [52]. It is however recognized that this narrow aperture width represents a potential downside of a box structure, since it greatly limits flexibility of plasma operation. Moreover, thinking in EU DEMO perspective, it should be noticed that the allowance for a large ($\sim$ 70 cm in that case) strike point sweeping is among the EU DEMO divertor design requirements, which requires significantly larger apertures. These aspects will not be discussed further in the present thesis, but it should be pointed out that recently a simplified version of the vapor box divertor has been proposed [50] with reduced or removed baffles, which could be easier to integrate in a fusion reactor.

The fact that the chosen number of chambers is 2, as in the original Nagayama proposal [136], rather than a larger number (as proposed in [65]) deserves a separate comment. Two is the minimum number of chambers which is needed to realize the proposed concept of evaporation-radiation-condensation within a "closed" system with only a limited flux of metal atoms towards the MC. A larger number of chambers might be needed in case the vapor flux towards the main plasma was calculated to be excessively large, but this will possibly be the subject of further

studies, should this concept be considered for reactor implementation. In conclusion, there is no principle limit to the number of chambers that can be foreseen in the system except for space constraints - nor, as it will be clarified later, to the number of chambers that the proposed model can take into account. What is instead limited is the maximum extension of the "interaction region" between the SOL plasma and the metal vapor. Indeed, that extension is constrained by the shape of the plasma chamber and by the location of the X-point. This is relevant for the performance of the system, since a larger interaction length would allow for a larger amount of the plasma power to be radiated.

Figure 6.3 shows IEC and OEC connected to separate differential chambers. The two systems are only communicating via the common wall between IDC and ODC, but this coupling is expected to be modest due to the presence of the embedded cooling channels.

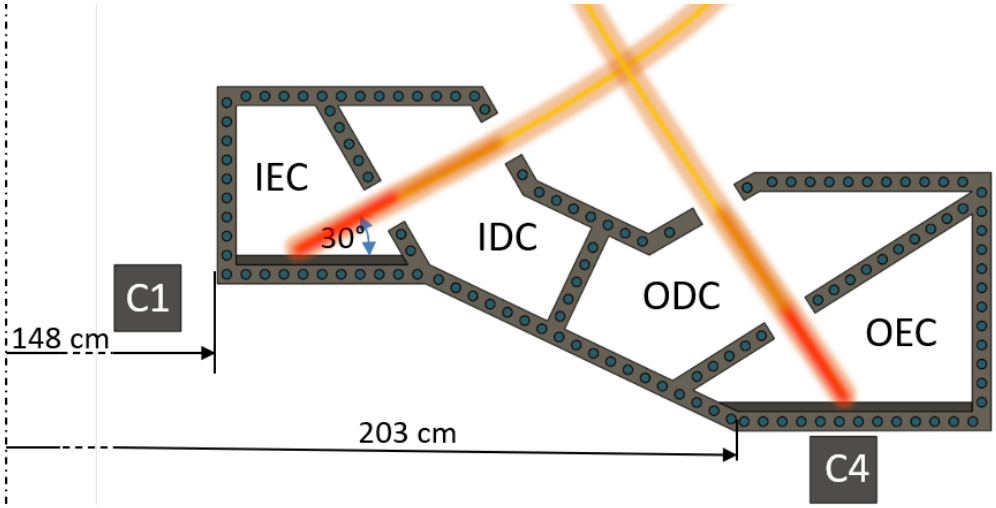

Figure 6.3: Cross section of the DTT closed vapor box divertor geometry. Radial coordinates start from the symmetry axis of the torus. The interaction region between SOL plasma and metal vapor is schematically indicated.

6.3 Phenomenology of a vapor-box divertor

6.3.1 Overview

With respect to an ITER-like LMD, the vapor box design involves additional physics aspects that should be discussed. The above-mentioned evaporation, sputtering, D retention and fuel recycling still occur. A short review of the phenomena to be taken into account in order to correctly describe the behavior of a "closed" LMD as the one presented in the foregoing section follows:

- Evaporation/condensation: one important feature of the vapor box divertor is that recondensation of the vapor mostly occurs on the EC and DC walls, rather than on the FW. The condensed metal is then recirculated to the target - e.g. via capillary forces, if the walls are coated with a CPS. In this respect, a vapor box divertor is similar to a heat pipe, where the heat is deposited inside the system rather than outside. One consequence of this behavior is that the latent heat of evaporation is spread over the chamber walls, where condensation occurs.
- Vapor expansion: between the EC and the DC, vapor flow occurs. If the pressure difference is sufficiently large, as it is expected for the envisaged operating conditions of this system, *choked flow* conditions occur.
- Since the pressure of Li/Sn in the EC is expected to be between 1 and 1000 Pa (this estimate is based on the saturation pressure at the operating temperature), the DC will effectively serve as a chamber for providing *differential pumping*, in order to "isolate" the EC from the MC. Indeed, the pressure difference between the EC and the MC is significant, as the latter is of the order of $\sim 10^{-3}$ Pa during tokamak operation. As a side remark, these figures suggest that the validity of the ideal gas assumption and the applicability of continuum models should be assessed. This topic will be addressed in some detail in the following sections.
- The presence of electric current loops in the LM pool/film represents a concern, and for this reason the actual implementation of this divertor concept should also involve the use of a CPS.

Next sections contain a more detailed consideration of the above-mentioned phenomena, as well as a review of the available correlations and formulations in order to take them into account.

6.3.2 Erosion processes

Evaporation

The net evaporation rate from the i-th surface (i.e., the pool surface or the walls in contact with the Li/Sn vapor) has been evaluated by means of the Hertz-Knudsen equation [174]:

$$\dot{N}_{ev,net,i} = \dot{N}_{ev,i} - \dot{N}_{condens,i} = \eta \cdot A_i \cdot 10^3 \cdot \left(\frac{p_{sat}(T_i) \cdot N_{Av}}{\sqrt{2\pi m_{Li/Sn} R_0 T_i}} - \frac{p_v \cdot N_{Av}}{\sqrt{2\pi m_{Li/Sn} R_0 T_v}} \right) \tag{6.1}$$

where

- $\dot{N}_{ev,net,i}$ is the net evaporation rate from the i-th surface in atoms/s
- $\dot{N}_{ev,i}$ is the evaporation rate from the i-th surface in atoms/s
- $\dot{N}_{condens,i}$ is the condensation rate to the i-th surface in atoms/s
- T_i is the temperature of the i-th surface in K
- T_v is the temperature of the Li/Sn vapor in K
- $p_{sat}(T_i)$ is the saturation pressure evaluated at T_i in Pa
- p_v is the pressure of Li/Sn vapor in Pa
- η is an empirical coefficient estimated in [174] to be equal to 1.66
- A_i is the surface area of the i-th surface in m^2
- $m_{Li/Sn}$ is the molar mass of Li/Sn in g/mol
- N_{Av} is the Avogadro number
- R_0 is the universal gas constant in J/(kmol K)

This formulation for the evaporation source term allows to distinguish among the different surfaces facing the Li/Sn vapor which, in general, will have different temperatures. Note that the formulation remains unchanged if each wall is further discretized, e.g. if a 2D model for the thermal behavior of the walls is employed. In that case, the *local* values of temperature and pressure can be employed in the same formulation.

While this expression is likely to be appropriate for describing the LM evaporation/condensation fluxes from/to the pool, it has to be considered only as a very first approximation for the Li/Sn evaporation/condensation fluxes from/to the walls, due to the strong effect of the wall temperature on the interface. It should be remarked that the walls of the EC are assumed to be coated by Li/Sn (either a liquid film - as in the Nagayama proposal - or an LM-filled wick - in case a CPS is employed).

Sputtering

The adopted formulation for the sputtering part of the erosion flux of Li/Sn from the pool under D plasma bombardment is consistent with the one described in section 5.3.3.

6.3.3 Vapor transport

The first quantity to be determined is the pressure characterizing the evaporation chamber. Indeed, thanks to the nature of the vapor box concept, a larger pressure

will exist in the EC with respect to the DC. The simplest possible assumption is to consider the pressure in the EC equal to the saturation pressure of Li/Sn at its temperature. This clearly represents an overestimation of the actual pressure, in view of e.g. the effect of cold walls, which would locally lead to a reduction of the pressure due to the associated particle sink. This point will be addressed in some detail later.

Differential pumping

As mentioned above, the motivation for the presence of a DC in the original Nagayama proposal stems from the necessity to reduce the core plasma contamination associated to the evaporated/sputtered Li/Sn flowing out of the EC. The physical principle is *differential pumping*, i.e. the connection of two chambers having different pressures by means of one or more intermediate chambers, actively and/or passively pumped (see Figure 6.4). In the system here considered, the high and low pressure chambers are the EC and MC, respectively.

The intermediate chamber(s) induce a progressive reduction in mass flow rate from the high pressure box to the low pressure box, and therefore a gradual passage between the two extreme pressures of the system. In the system here considered, this differential pumping is achieved by means of net condensation of Li/Sn vapor on the walls of the DC, i.e. by a passive pumping mechanism. In such a system, when a large pressure difference is involved, choked flow is likely to occur between successive chambers [200]. It should be noticed that, as it willbe discussed later, Figure 6.4 implicitly assumes equilibration of the flowing vapor within each box, which is questionable.

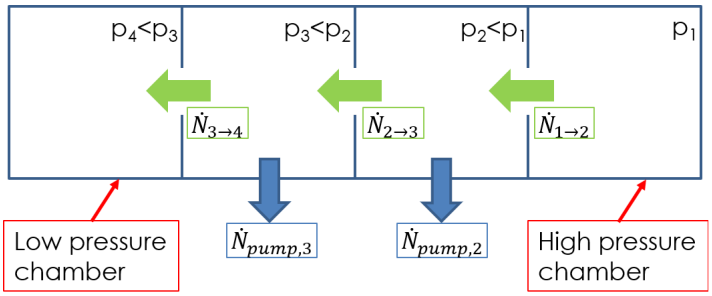

Figure 6.4: Schematic of a differentially pumped system.

As it will be pointed out later, the presence of the SOL plasma further reduces the Li/Sn efflux between successive chambers (and, eventually, towards the main plasma chamber), thanks to ionization of Li/Sn vapor.

Vapor flow between successive chambers

If an open EC is considered, then it is necessary to properly evaluate the Li/Sn vapor mass flow rate towards the DC, as well as the outflow of Li/Sn from the DC to the main plasma chamber.

If the effect of the SOL plasma as an ionizing medium is neglected, i.e. if the Li/Sn vapor efflux is treated as in simple continuum gas dynamics, the aperture between two successive chambers can be treated as a nozzle. From a basic application of the First Law of Thermodynamics between a point upstream the aperture and a point within the aperture itself, assuming adiabatic flow, the following well known result is found:

$$\dot{N}_{noz,1\to2} = \left[\rho_{aperture} \cdot A_{aperture} \cdot \sqrt{2 \cdot \frac{\gamma}{\gamma-1} \cdot \left(\frac{p_1}{\rho_1} - \frac{p_{aperture}}{\rho_{aperture}}\right)}\right] \cdot \frac{N_{Av}}{m_{Li/Sn}} \cdot 10^3 \quad (6.2)$$

where:

- $\dot{N}_{noz,1\to2}$ is the particle flow rate from box 1 (i.e. the EC) and box 2 (i.e. the DC), in s^{-1}
- ρ is a density in kg/m^3
- A is the passage area between boxes in m^2
- γ is the isentropic exponent, evaluated for an ideal gas as $\gamma = \frac{c_p}{c_v}$
- The values of the specific heats c_p and c_v, both in J/kg/K, are:
  - $c_p = \frac{5}{2} \cdot R^*$
  - $c_v = \frac{3}{2} \cdot R^*$
  - $R^* = R_0/PM_{Li/Sn}$ being the specific gas constant of Li/Sn in J K/kg

The subscript *aperture* refers to gas conditions at the passage between two successive chambers. In particular:

- if $\frac{p_2}{p_1} \leq \left(\frac{2}{\gamma+1}\right)^{\frac{\gamma}{\gamma-1}}$, then $p_{aperture} = p_1 \cdot \left(\frac{2}{\gamma+1}\right)^{\frac{\gamma}{\gamma-1}}$: this is the so called choked flow condition
- if $\frac{p_2}{p_1} > \left(\frac{2}{\gamma+1}\right)^{\frac{\gamma}{\gamma-1}}$, then $p_{aperture} = p_2$: this condition is also known as subcritical flow

In both cases, $\rho_{aperture} = \rho_1 \cdot \left(\frac{p_{aperture}}{p_1}\right)^{\frac{1}{\gamma}}$ (adiabatic expansion).

The optimization of the shape and relative location of successive nozzles is beyond the scope of this document, but useful results for future developments of the present concept are presented in [200] and could be used for an optimized design of the nozzle chain.

6.3.4 Flow of re-condensed Li/Sn back to the pool

In this study the condensed Li/Sn is assumed to flow back to the Li/Sn pool both from the EC (by gravity) and from the DC (by means of an external circuit, not

modeled). The most promising option in terms of stability of the liquid metal and robustness appears to be the application of a CPS, thus achieving a configuration similar to the ones currently employed in heat pipes.

6.3.5 Plasma entrainment

The foregoing discussion concerning the Li/Sn "vapor shield" effect is relevant for the plasma energy balance. However, the effect of ionization on the vapor itself should also be considered, since it affects both the mass and the energy balance of the Li/Sn vapor system. From the point of view of the vapor mass balance, indeed, the fact that Li/Sn atoms get entrained by the SOL plasma implies a reduction of the flux from the EC and consequently from the DC to the main plasma chamber.

One possible strategy to account for plasma entrainment while adopting a 0D treatment for the vapor is to rely on the statistical mechanics formulation of the particle flux striking on a surface (Langmuir flux), which assumes a Maxwellian distribution of the atoms. The nature of this expression is exactly the same as the Hertz-Knudsen one adopted at evaporating/condensing surfaces, but for a "purely condensing wall" [65], since plasma cannot release entrained atoms until recombination has occurred: *locally*, it acts as a perfect particle sink. Therefore, the following additional sink is added to the particle balance within each box :

$$\dot{N}_{entrainment,k} = \frac{p_{v,k} \cdot N_{Av}}{\sqrt{2\pi m_{Li/Sn} R_0 T_{v,k}}} \cdot 10^3 \cdot A_{w,k} \tag{6.3}$$

where k is the number identifying the box.

Recombination is assumed to occur within the lowest box and not on the pool based on preliminary estimations of plasma parameters. This estimates suggested that a sufficiently low temperature for recombination of Li/Sn atoms to occur should be reached before the SOL plasma reaches the target, i.e. somewhere upstream with respect to the target itself, but downstream with respect to the low LM vapor density differential chamber. As it will be explained shortly, this assumption depends on the SOL plasma behavior, for which the modelling approach will be outlined in the following section.

It is also important to recognize that even if all of the lithium vapor is contained in the boxes, some lithium will flow as charged particles upstream along the magnetic field lines - also suggesting that at some point there will be diminishing returns from using more boxes.

6.4 Model description

6.4.1 Introduction

An engineering model of the system should contain the essential aspects of its rich physics. The most relevant phenomena are the following:

- Vapor condensation on the chamber walls, which requires knowledge of vapor pressure and temperature within the chambers as well as of wall temperature.
- LM evaporation from the target, which can be estimated from a power balance on the liquid-vapor system.
- Vapor flow between the chambers.
- Plasma-vapor interactions, estimated starting from the plasma temperature and density profiles - which determine the cooling rate - and the vapor density.
- Active cooling of divertor structures.

The actual thermodynamic state of the system is determined by the interactions among the above-mentioned phenomena, which should therefore be taken into account self-consistently, as explained in the introduction. For example, the plasma cooling effect due to interactions of the SOL plasma with the intrinsic impurities affects the heat flux reaching the target, since part of the upstream power has been radiated and therefore will not reach the pool. The resulting heat flux to the pool determines the LM evaporation, which is the source term for the vapor mass balance in the boxes and therefore influences the vapor density, which in turn affects the extent of plasma cooling. Moreover, the role of the cold chamber walls cannot be determined a priori, since their low temperature should allow for vapor condensation, but they are also subject to a non-negligible radiation heat load, which could in principle raise the temperature up to the point where the vapor cannot condense anymore (reflecting surfaces).

In order to obtain the desired self-consistency, the following three models have been developed, implemented and finally coupled together:

1. A 0D Li/Sn thermodynamic model, which requires as an input the power from the SOL plasma - split among the advective/conductive and radiative channels - and the temperatures of the box walls. This module determines the thermodynamic state of the Li/Sn vapor in both chambers according to the formulations presented in section 6.3, as well as the evaporation/condensation rates and the consequent power deposition on the walls. This model is essentially unchanged with respect to [139], and therefore only essential aspects will be reported here.
2. A 2D FEM thermal model for the divertor walls, which takes into account the condensation and radiation load on the walls and the heat sink associated to active cooling of the walls, as well as the heat transfer with the LM pool. The output is the temperature distribution over the divertor structure. This distribution can outline potential concerns associated to excessive temperatures

or temperature gradients, and it is used again in the calculations to evaluate the condensation rates.

3. A 1D SOL plasma model, which takes as an input upstream plasma conditions ($q_{//,omp}$ and $n_{e,OMP}$) and returns the 1D SOL temperature, density, velocity and parallel heat flux profiles by taking into account plasma cooling self-consistently. At this level, self-consistency means that the plasma temperature distribution is determined by the amount of plasma cooling, which in turn depends on the plasma temperature distribution). The outcome of this module which is directly used by other modules is the power re-partition among the two channels, conductive/convective and radiative.

While developing this model, attention has been payed to keeping the computational cost reasonably low, in order to make the model suitable for comparative studies.

The coupling strategy between the various models is schematically represented in Figure 6.5, where the meaning of the symbols is the following:

- q''_{rad} ($\frac{\mathrm{W}}{\mathrm{m}^2}$) is the radiative heat flux distribution on the divertor chamber walls, which follows from plasma-vapor interactions
- T_{walls} (K) is the temperature distribution over the chamber walls
- $\dot{N}_{evap}$ (s^{-1}) is the evaporation particle flow rate from the pool
- n_z (m^{-3}) is the vapor particle density within the various chambers
- n_e (m^{-3}) is the plasma density along the SOL
- T_e (eV) is the plasma temperature along the SOL
- $\dot{q}_{rad}$ ($\frac{\mathrm{W}}{\mathrm{m}^3}$) is the radiated energy distribution along the SOL
- $q_{rad,EC}$ (W) is the integral of that radiated energy over the flux tube corresponding to the EC
- $q_{rad,DC}$ (W) is the integral of that radiated energy over the flux tube corresponding to the DC

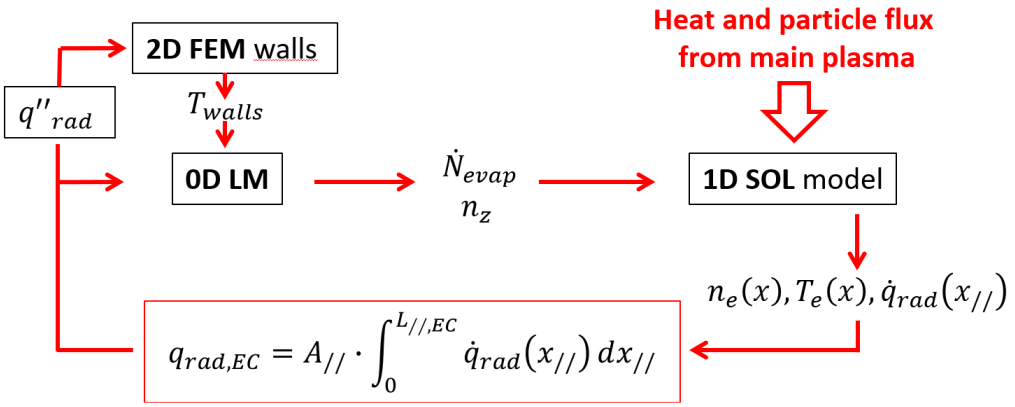

Figure 6.5: Schematic of the coupling strategy between the modules of the code.

In brief, the calculation is started by feeding upstream plasma conditions in

terms of parallel heat flux along the field lines and plasma density to the 1D SOL model. Once the inner iterations of this module have reached convergence, the total radiated power within each box as well as the power reaching the target are passed to the other modules. The power reaching the target along the advection/-conduction channel, together with the fraction of radiated power reaching the pool, is fed to the LM thermodynamic model. The radiated power on the walls is instead passed to the 2D FEM model of the walls, together with the latest available estimate of the load associated to condensation. The modules are run iteratively up to convergence. The coupling between the various models has been implemented according to an explicit scheme.

6.4.2 Thermodynamic model for the LM and vapor

As mentioned above, the aim of the simplified 0D model is to compute the thermodynamic state of the Li/Sn liquid-vapor system within the various chambers. The equations are essentially unchanged with respect to the ones presented in [140], but they are now only solved to find the steady state solution, since the other two modules are steady state and therefore no detail concerning the transient behavior is needed - consistently with the requirement of minimizing the computer time needed for a simulation. The assumptions and the model equations shall be briefly recalled in the following for the sake of completeness, but the reader is redirected to [140] for further details and for a thorough justification of the assumptions.

The main assumptions of the model are the following:

- The Li/Sn vapor is approximated as an ideal, monoatomic gas which is optically thin with respect to radiation - i.e. radiation generated due to plasma-vapor interaction does not interact with the vapor itself, but is deposited on the surface. The vapor is partly lost as a neutral gas towards the main plasma chamber, and the amount which is lost is replaced by a replenishing flux of liquid Li/Sn to the pool to ensure mass conservation within the system. Vapor in the EC is assumed to be in thermodynamic equilibrium with the pool. Finally, isenthalpic vapor flow between chambers is taken into account, as well as the *plasma entrainment* effect, i.e. the fact that, due to the low ionization potential of Li/Sn, vapor can be ionized and brought back to the lower chambers.
- The Li/Sn pool receives a fraction of the total radiated load in the EC which is approximated as $f_{rad,pool} \sim \frac{A_{pool}}{\left(A_{w,EC}+A_{pool}\right)}$. All radiation received is assumed to be absorbed, whereas thermal radiation exchange between the pool and the walls is neglected. Moreover, all the Li/Sn which is condensed on both the EC and the DC walls, together with an amount of replenishing LM corresponding to the vapor flux towards the MC, is returned to the pool.
- The effects of plasma particle influx on the LM surface are neglected, i.e. no

account is given here about retention, sputtering and non-condensable gases. Only evaporation is considered as a source of metal vapor for the system.

It is worth remarking that this model only provides the pool temperature and a single value of vapor temperature and density for a given box, thus smearing any variation of the vapor density across the field lines and across the field lines within each box. Given the low ionization potential of Li vapor, this can represent a strong assumption.

As already mentioned, neglecting the H retention for Li/Sn is reasonable due to the operating temperatures of the system, while for Sn no H retention is expected. Sputtering should also be much less important than evaporation for both LMs due to the expected high target temperature and low plasma temperature at the target. The selected configuration is the simplest pool option. While for an open divertor configuration this would not be feasible due to instabilities associated to $\vec{j} \times \vec{B}$ forces, for a closed-box this might be applicable. However, it should be recognized that the CPS solution should not only ensure the absence of droplet emission, but also guarantee a more uniform wetting of the PFS and a larger flexibility in terms of surface orientation. This shall not be discussed further in the present thesis, but it is worth mentioning that the model here proposed would also be applicable to the case of an LM-filled CPS used as PFS.

For the EC, the mass source coming from evaporation is considered as an internal transfer term, since vapor and liquid are assumed to be in equilibrium. The actual mass sources are instead the replenishment mass flow rate and the entrained Li/Sn mass flow rate (see explanation below), whereas the sink is represented by the outflow through the aperture between EC and DC. For the DC, the EC→DC mass flow rate represents a mass source, whereas the sink is provided by DC→MC mass flow rate, the condensation on the DC walls and the entrained Li/Sn mass flow rate. The energy balance for the EC is determined by the plasma heat load reaching the LM surface, whereas the energy sinks are provided by condensation and EC→DC mass flow rate - i.e. the Li/Sn carries its enthalpy when it leaves the system.

Figure 6.6 schematically shows the energy balance for the EC. The nomenclature employed is the following:

- $q_{condens}$ (W) is the heat load associated to condensation, evaluated as the product of the condensation mass flow rate and the enthalpy associated to phase change. This quantity is a sink for the energy balance of LM in the EC and a source term for the 2D thermal model of the walls.
- q_{noz} (W) is the heat load associated to the vapor flux from EC to DC, evaluated as the product of the EC→DC mass flow rate and the corresponding enthalpy. This quantity represents a sink for the energy balance of LM in the EC but becomes a source for the energy balance of vapor in the DC.
- q_{entr} (W) is the heat load associated to the entrained vapor flux returning to the EC together with the plasma flow, evaluated as the product of the entrained mass flow rate of vapor in the EC and the corresponding enthalpy.

This quantity represents a source for the energy balance of the LM in the EC.

- q_{SOL} (W) is the amount of power carried by the SOL plasma within the EC. Of this power, an amount q_{rad} will be radiated due to plasma-vapor interactions. A fraction $(1-f_{rad,pool})$ of the latter, which in the schematic is called $q_{rad,walls}$, will represent a source term for the energy balance of the walls, whereas the remaining fraction $f_{rad,pool}$ will contribute to the energy balance of the EC as a source term.
- $q_{pool\to wall}$ (W) is the amount of heat lost from the LM pool to the cold walls. It is evaluated by assuming only heat conduction to be relevant in the pool, see eq. (6.4):

$$q_{pool\to wall} = 2\pi \int_{A_{pool\to wall}} x h_{pool} \left(T_{pool} - T_{wall}\right) dA \tag{6.4}$$

  Where:
  - $A_{pool\to wall}$ is the contact area between pool and wall
  - x is the radial coordinate, which has been included in the integral to take into account axisymmetry (together with the 2π factor)
  - h_{pool} $\left(\frac{\mathrm{W}}{\mathrm{m^2K}}\right) \sim \frac{k_{pool}}{s_{pool}}$ is the equivalent heat transfer coefficient due to thermal conduction
  - T_{pool} is the pool (and vapor) temperature in the EC
  - T_{wall} is the temperature distribution over the surfaces of the box structures which are in contact with the LM pool.

The coupling of this module with the other two has already been discussed. The relevant engineering outcomes of this module are actually:

- The LM pool temperature
- The vapor outflow towards the main plasma chamber
- The amount of recirculating mass flow rate

6.4.3 FEM model for the walls

Preliminary calculations showed that the parameters chosen for active cooling can strongly affect the thermodynamic state of the system. Indeed, the temperature of the box walls facing the Li or Sn vapor and the pool affects q_{cond} and $q_{pool\to wall}$. This has motivated a more accurate description of the wall temperature field with respect to the simple 0D balance proposed in [140], which was unable to take into account the actual proposed cooling strategy nor the temperature gradients in the walls. A 2D model treated by means of Finite Element Modelling (FEM) appeared feasible in terms of required computational effort, and was therefore selected.

The main assumptions for the model and for the boundary conditions are here reported. As for the model:

- All the cooling channels share the same value of coolant temperature and heat transfer coefficient. A detailed analysis of the cooling strategy itself is

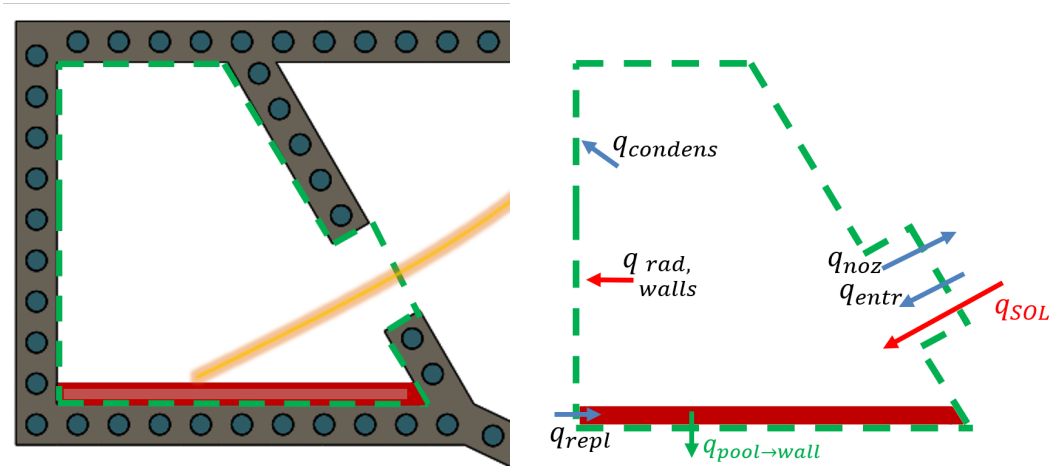

Figure 6.6: 0D model domain for the IEC (left) and schematic of the 0D LM energy balance in the same chamber.

indeed beyond the scope of the present work. The code, however, may take into account different values of both surface temperature and heat transfer coefficient, should different cooling strategies be motivated in the future (e.g. by heating/cooling different walls in different ways to promote/hinder evaporation/condensation as needed).

- All the internal surfaces of a given chamber share the same radiation and condensation heat flux, due to the 0D nature of the thermodynamic model.

As for the boundary conditions:

- Outer walls are adiabatic (heat exhaust is only allowed via the cooling channels).
- The heat transfer between pool and wall is modeled with an equivalent heat transfer coefficient h_{pool}, as already described in section 6.4.2 .
- The heat load on the walls which are not in contact with the LM pool is evaluated as the sum of $q_{condens}$ and $q_{rad,walls}$. In the DC, $q_{rad,walls}$ is equivalent to q_{rad} since no pool is present. The corresponding heat flux to be provided to the 2D model of the walls is evaluated by dividing $q_{condens}$ and $q_{rad,walls}$ by the surface area available for condensation and radiation, respectively. This means that no details are given concerning the actual distribution of the load on the chamber walls. In order to obtain such distribution, it would be necessary to implement a 2D description of the vapor within the chambers - in order to evaluate $q''_{condens}$ - and to determine how the energy radiated in the SOL distributes over the walls. Those two points are left for future work.
- The active cooling is characterized by a coolant temperature $T_{coolant}$ and a heat transfer coefficient h.

A schematic of the boundary conditions is provided in Figure 6.7. The IEC is considered as an example, but a corresponding strategy is employed for the other

chambers. In the schematic $q'' = q''_{rad} + q''_{cond}$.

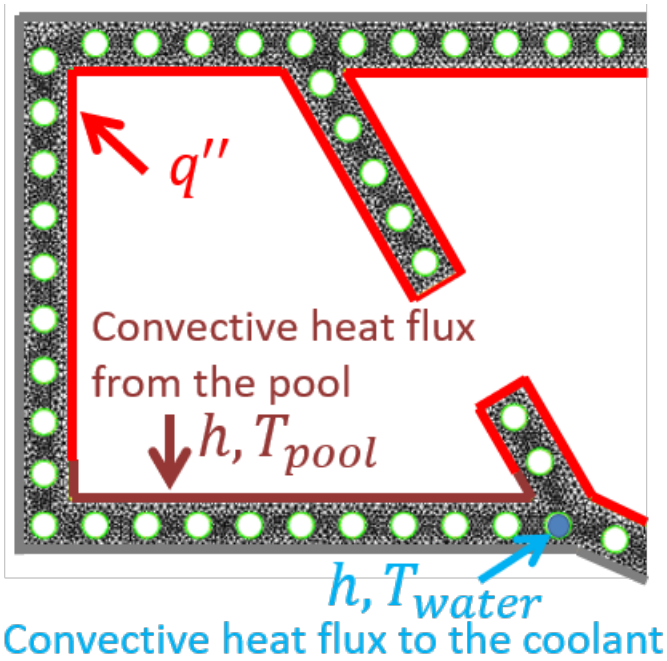

Figure 6.7: 2D FEM mesh of the IEC walls, with the quantities exchanged with the 0D model schematically indicated.

The problem has been solved via a code written in the open-source object-oriented language FreeFem++ [82], which has been coupled to the other two modules, written instead in Fortran 90.

6.4.4 SOL model

In order to provide a description of the variation of SOL plasma parameters along the field lines while keeping the computational time reasonably low, 1D modeling was regarded as the best compromise. The adopted model derives from a modification of the 1D SOL plasma model proposed in [97]. The latter was intended to model partially detached operation obtained via purposely seeded impurities. It has been modified in order to take into account the boundary conditions available in the present case as well as the presence of intrinsic impurities such as the LM vapor, which are the only non-plasma species included in this modelling.

Figure 6.8 represents a schematic of the domain considered. The model approximates the SOL plasma by means of a 1D model representing a flux tube of width λ_q. Both inboard and outboard flux tubes are assumed to start at OMP. This flux bundle extends for a length L from the outboard midplane to both targets. The width of the flux bundle is increased of a factor f_{exp} at the divertor entrance (i.e.

the location where the SOL plasma flowing towards the target along the field lines enters in the IDC/ODC) in order to roughly take into account flux expansion. The assumed location for this sudden flux expansion which is chosen in the model has been shown in [97] to have a negligible impact in terms of the calculation results. A fixed non-coronal parameter τ along the SOL plasma is assumed, which is parametrically varied in order to assess the possible effects of the non-coronal enhancement of the impurity radiation due to Li/Sn, which [65, 129] and other authors suggested to be relevant. Further assumptions are a single plasma temperature for electrons and ions ($T_e = T_i = T$) as well as a single plasma density ($n_e = n_i = n$). As suggested in [97], however, when writing the equations, the subscripts are sometimes retained to remark which species is involved in each physical process. The plasma cooling associated to the presence of the intrinsic impurities is directly proportional to the density of the impurity itself, which is a result of the 0D thermodynamic model and therefore uniform within each chamber.

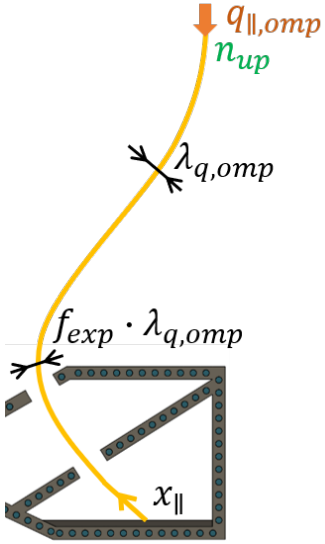

Figure 6.8: Schematic of the 1D SOL plasma model.

A description of the model equations follows. Equations are solved for both divertor legs.

Continuity for neutrals

Two groups (or "families") of fuel neutrals are considered: a slow one, and a fast one. The corresponding continuity equation is stated as follows:

$$\begin{cases} \frac{d(n_{0,i}v_{0,i})}{dx_{//}} = -R_{iz}n_e n_{0,i} + R_{rec}n_e n_i \delta_{i1} \\ \sum_{i=1}^{2} \Gamma_{0,i,tar} = \Gamma_{se} \cdot RC \\ \Gamma_{0,1,tar} = \Gamma_{0,2,tar} \end{cases} \tag{6.5}$$

The first equation of (6.5) states the conservation of the i-th family of neutrals. Neutrals are lost due to ionization, while slow neutrals arise from plasma recombination. The fact that neutrals from recombination are accounted for only in the slow group is formally expressed by the Kronecker symbol δ_{i1}. The recycling neutral flux at the target is artificially split in two velocity groups in order to take into account the (relatively cold) neutrals coming from Franck-Condon interactions and reflection and the relatively fast neutrals coming from charge-exchange. The assumed fraction of neutrals in the two groups has been shown in [97] not to significantly affect the result of the calculation. The first, "slow" group has a velocity corresponding to a neutral temperature $T_0 = 5$ eV, and the velocity along the flux bundle is assumed to be 1/4 of the mean thermal speed, as supposed by [97]:

$$v_0 = \frac{1}{4}\sqrt{\frac{8eT_0}{\pi m_0}} \tag{6.6}$$

The second group is started at the target with a velocity which is larger by a factor 10. The boundary condition represents the usual recycling relation, where Γ_{se} is the plasma particle flux at the sheath edge and RC is the recycling coefficient, which is assumed to be equal to 1, as discussed in section 3.5. The total amount of recycling neutrals is equally split among the two groups. The subscript *tar* indicates quantities at $x_{//} = 0$, whereas in the following the subscript *omp* will indicate quantities at $x_{//} = L$.

Continuity for plasma

The continuity equation for the D plasma is stated as follows:

$$\begin{cases} \frac{d(nv)}{dx_{//}} = R_{iz}n_e n_0 - R_{rec}n_e n_i \\ v_{tar} = -c_s\left(T_{tar}\right) \end{cases} \tag{6.7}$$

This equation is employed to evaluate the plasma flow velocity, which is negative since integration is performed from the target to the OMP. c_s is the sound speed, meaning that the typical Bohm condition at the sheath edge is employed to provide a boundary condition for this equation.

Energy equation for plasma

The energy conservation equation for the D plasma is stated as follows:

$$\begin{cases} \frac{dq_{//}}{dx_{//}} = -L_z\left(T_e, n_e\tau\right) n_e n_z - eT_i R_{CX}\left(T_i, n_e\right) n_i n_0 - eE_{iz} R_{iz}\left(T_e, n_e\right) n_e n_0 \\ q_{//}\left(x_{//} = L\right) = q_{//,omp} \end{cases} \tag{6.8}$$

Where:

- $q_{//} = q_{//,cond} + q_{//,conv}$ is the total parallel heat flux
- L_z is the cooling rate associated to plasma-vapor interactions, as introduced in section 3.5.4 and reported in Figure 3.7
- R_{CX} is the charge-exchange rate coefficient
- R_{iz} is the ionization rate coefficient
- E_{iz} is the ionization potential of H

This equation is integrated from midplane - where an upstream parallel heat flux corresponding to the upstream power which is directed towards each of the two divertor targets - to target. Evaluating $q_{//,omp}$ requires the knowledge of the power scrape-off width, which has been evaluated according to [64]:

$$\lambda_{q,omp} = \frac{5671 P_{SOL}^{1.8}\left(1+k^2\right)^{5/8} a^{17/8} B^{1/4}}{I_P^{9/8} R}\left(\frac{2\overline{A}}{1+\overline{Z}}\right)^{7/16}\left(\frac{Z_{eff}+4}{5}\right)^{1/8} 1.6 \tag{6.9}$$

Where:

- P_{SOL} is the total power leaving the separatrix in W
- k is the plasma elongation
- a is the plasma minor radius in m
- $B$is the total magnetic field in T
- $I_P$is the plasma current in A
- R is the major radius of the machine in m
- $\overline{A}$ and $\overline{Z}$ are assumed to be equal to 2 and 1, respectively
- Z_{eff} is the effective charge of all ions in the plasma

The parallel heat flux at midplane can now be evaluated by dividing the upstream power by the cross-sectional area of the plasma flux bundle.

$$q_{//,omp} = \frac{P_{up}}{2\pi R_{omp}} \lambda_{q,omp} \sin\left(\tan^{-1}\left(\frac{B_\theta}{B_\phi}\right)\right) \tag{6.10}$$

Where B_θ and B_ϕ are the poloidal and toroidal component of the magnetic field, respectively.

The three terms on the right hand side of equation 6.8 are associated to power loss mechanisms which decrease the total parallel heat flux, and specifically plasma cooling due to plasma-vapor interactions, charge-exchange and ionization of neutrals, respectively. It is expected that the last two terms will only be relevant very close to the target, where the neutral density is high.

As mentioned above, to take into account flux expansion, at a distance from the target $x_{//} = L_{EC} + L_{DC} = L_{DIV}$ the heat flux is reduced by a factor $f_{\exp}$.

Hydrogen radiation has been neglected, since it is expected to be several orders of magnitude weaker than the other contributions to the plasma energy balance.

Fourier equation

Contrarily to what is typically encountered in the literature, [97] proposes to obtain the temperature distribution by means of the typical plasma conduction equation:

$$\begin{cases} q_{//,cond} = -k_0 T_e^{5/2} \frac{dT}{dx_{//}} \\ T\left(x_{//} = 0\right) = \frac{q_{//,tar}}{\gamma \cdot e \cdot \Gamma_{se}} \end{cases} \tag{6.11}$$

Where $k_0 \sim 2390 \ \frac{\mathrm{W}}{\mathrm{m \cdot eV^{7/2}}}$ and the boundary condition is given by the usual sheath heat transfer relation, where γ is the sheath heat transfer coefficient. To obtain $q_{//,cond}$ from $q_{//}$ it is necessary to subtract the convective contribution,

$$q_{//,conv} = \left(5eTn + \frac{1}{2} m_i n v^2\right) v \tag{6.12}$$

which is obviously more relevant close to the target due to the increase of the plasma flow speed and contributes to flattening the temperature profile (since, for a given $q_{//}$, a larger $q_{//,conv}$ implies a smaller $q_{//,cond}$ and therefore a less significant temperature decrease.

Momentum conservation for plasma

Momentum is lost due to CX and recombination. As suggested in [97], a positive contribution associated to ionization is neglected.

$$\begin{cases} \frac{d\left[n\left(m_i v^2 + 2eT\right)\right]}{dx_{//}} = -m_i v R_{CX} n_i n_0 - m_i v R_{rec} n_e n_i \\ n_{omp} = n_{up} \end{cases} \tag{6.13}$$

Where n_{up} has been related to the average core plasma density by means of a relation proposed by [190]:

$$n_{up} = 0.00236 \overline{n}_e k^{1.11} B_\phi^{0.78} \tag{6.14}$$

Where k is the plasma elongation. However, the resulting upstream density is only to be intended as a reference value to start parametric scans.

Summary

It is convenient to summarize the most relevant modifications with respect to the model proposed in [97]:

- The original model imposes the plasma temperature at the target (i.e. at the sheath edge), whereas in this work that temperature is evaluated by means of the sheath heat transfer coefficient relation (see discussion later). Conversely, the equation for plasma density is now solved from OMP to target, taking as a boundary condition the upstream temperature.
- The original model proposes to fix $q_{//,tar}$ - the parallel heat flux at target - which was compatible to the $q_{//,omp}$ - the parallel heat flux at outboard midplane - corresponding to the prescribed P_{sol} - the power reaching the separatrix. The matching of the two values was then obtained via an iterative procedure. In this work, instead, integration of the energy conservation equation has been reversed, so that the $q_{//,omp}$ corresponding to P_{sol} can be directly imposed as a boundary condition for the equation.

As already mentioned, the original model was developed with the aim of investigating partially detached conditions, and the electron temperature at the target was fixed to a value consistent with that condition. Conversely, the present 1D SOL model does not fix the plasma temperature at the target, which could therefore decrease up to the point where plasma completely recombines and does not touch the target anymore (*detachment*, see e.g. [159]). However, the model is not able to handle fully detached cases, since it heavily relies on the sheath heat transfer coefficient relation which would not be applicable anymore. Therefore, if in a simulation one (or both) divertor legs are found to be in such a "fully detached" condition, the entire parallel heat flux for that leg is assumed to be radiated in the corresponding EC. Regarding this assumption, it should be noticed that it is unlikely that the load will actually be uniformly spread on the chamber walls. Further studies would be necessary to determine a more realistic distribution of the radiation profile over the walls.

6.5 Simulation setup

6.5.1 Machine parameters

Table 6.1 summarizes the input data assumed for the calculation. The model is applied to a proposed LM divertor for DTT, but it must be stressed that it would be readily applicable to an analogous design for the EU DEMO.

As already mentioned, the value of the recycling coefficient in equation (6.5) is taken equal to 1. As already discussed, this is reasonable for both Li and Sn.

As a final remark, data for reaction coefficients of H come from Atomic Data and Analysis Structure (ADAS). The values corresponding to the local value of plasma density and temperature and to the selected particle dwell time are obtained via bivariate linear interpolation of the tables contained in those databases.

Quantity	Unit	Value	Meaning
$P_{SOL,inboard}$	MW	10.6	Power leaving the separatrix along the inboard divertor leg
$P_{SOL,outoard}$	MW	21.3	Power leaving the separatrix along the outboard divertor leg
$A_{//,omp}$	m^2	$6.14 \cdot 10^{-3}$	Cross sectional area of flux bundle
$q_{//,omp,out}$	GW/m^2	2.2	Upstream parallel heat flux, outboard divertor leg
$q_{//,omp,inb}$	GW/m^2	1.1	Upstream parallel heat flux, inboard divertor leg
$n_{0,omp}$	m^{-3}	$1.23 \cdot 10^{20}$	Upstream plasma density
$T_{0,1}$	eV	5	Electron temperature of the slow group of neutrals
$T_{0,2}$	eV	50	Electron temperature of the fast group of neutrals
$f_{0,1}$		0.5	Flux fraction of neutrals in the slow group
M_{tar}		1	Mach number at targets
γ_{se}		7	Sheath heat transmission coefficient
Z_{eff}		1.2	Effective plasma charge
f_{exp}		3	Flux expansion factor
R		1	Recycling coefficient at targets
$f_{rad,pool}$		0.169	Fraction of radiated power towards LM pool
τ	ms	$0.1 - 10$	Impurity particle dwell time in the SOL
$\lambda_{SOL,OMP}$	mm	2.1	Scrape-off layer width at outboard midplane
$L_{connection}$	m	18.9	Connection length
$L_{//,IEC}$	m	0.52	Parallel-to-B distance within the various chambers
$L_{//,OEC}$	m	0.58	
$L_{//,IDC}$	m	1.25	
$L_{//,ODC}$	m	1.31	

Table 6.1: Machine parameters and geometry inputs for the application of the self-consistent model for the vapor-box divertor to the DTT.

6.5.2 Divertor cooling strategy

Following current DTT specifications [52], the divertor is assumed to be divided into 18 sectors, each one independently cooled by means of pressurized water. Even though it is mentioned in [3] that each sector is made up of 5 different subsectors, we assume here that they are cooled in series. Following a simple energy balance between the entrance and the exit of the cooling tubes for each sector, the heat transfer coefficient is preliminarily evaluated, at least as an order of magnitude. We assume the temperature increase along a single sector to be $\Delta T_{sector} = 80$ °C, and consider the inlet coolant temperature to be $T_{in,sector} = 50$ °C. The power load to each sector is:

$$q_{sector} = \frac{P_{SOL,inboard+outboard}}{N_{sectors}} = \frac{32}{18} = 1.78MW = \dot{m}_{sector} c_p \Delta T_{sector} \tag{6.15}$$

A water mass flow rate of $\dot{m}_{sector} \sim 3.5$ kg/s is then necessary to remove the deposited power. The corresponding flow velocity is evaluated by splitting the flowrate equally among the 125 cooling channels, and the Reynolds number is evaluated accordingly. Finally, the heat transfer coefficient is estimated according to the Dittus-Boelter correlation [88]:

$$Nu_D = 0.023 Re_D^{4/5} Pr^n \tag{6.16}$$

Where $n = 0.4$ when the fluid is heated, as it will be the case here. The parameters for active cooling are summarized in Table 6.2. Obviously, the cooling configuration is subject to improvements which are, however, beyond the scope of the present work. The only objective of this very preliminary evaluation was to obtain a reasonable value for the heat transfer coefficient in order to carry out the calculations.

Quantity	Unit	Value	Meaning
$T_{coolant}$	°C	80	Coolant temperature
h_{IEC}, h_{OEC}, h_{IDC}, h_{ODC} assumed equal for all chambers	W/(m^2 K)	5000	Heat transfer coefficient for cooling channels

Table 6.2: Parameters for active cooling.

6.6 Results and discussion

In the following section the results of the calculations are shown for the two LMs selected for this study (Li and Sn). For Li, two different values of the particle dwell time τ are considered, namely $\tau = 1$ ms and $\tau = 10$ ms. This is motivated by the fact that the radiative loss function for Li is strongly dependent on this quantity (non-coronal enhancement of radiation), as reported in Figure 3.7. For Sn, instead, the results are nearly independent on τ due to the weak dependence of the radiative loss function on this quantity, see again Figure 3.7. Therefore, for Sn, only results for $\tau = \infty$ (corresponding to the *coronal equilibrium* condition) will be presented.

6.6.1 SOL plasma profiles

In this section, a comparison between Li and Sn in terms of SOL plasma profiles. Only results for the outboard divertor leg shall be presented. Indeed, the upstream

parallel heat flux is much larger and the connection length shorter for the outboard side than for the inboard side, therefore it is expected that load conditions - in terms of heat flux reaching the target and electron temperature - will be more severe.

Figure 6.9 (left) shows the calculated temperature profiles. The discontinuous first derivatives of the temperature profiles around $x_{//} = L_{DIV} \sim 1.8$ m are due to the assumed localized flux expansion at the divertor entrance (the parallel heat flux suddenly decreases by a factor equal to f_{exp}, and therefore the temperature profile flattens). After this point, the flux bundle has entered the divertor region where the energy loss term associated to plasma-vapor interactions becomes important. Therefore, for a given $x_{//} < L_{DIV}$, the plasma temperature will be lower with respect to the corresponding one in the case of absence of impurities (not shown). The extent to which the temperature will be lower depends on the plasma cooling function, which in turn depends on the value of τ. From Figure 6.10 it is evident that, for Li, the assumption of a larger value of τ implies a weaker plasma cooling effect and therefore a larger T_{tar}, and globally a larger T within the divertor region. The final strong temperature drop close to $x_{//} = 0$ is associated to the plasma energy losses due to ionization of the neutrals, which locally overwhelms all the other terms. The behavior for the case of Sn is only slightly different with respect to the Li, $\tau = 10$ ms case. This somewhat surprising similar shall be explained in the following.

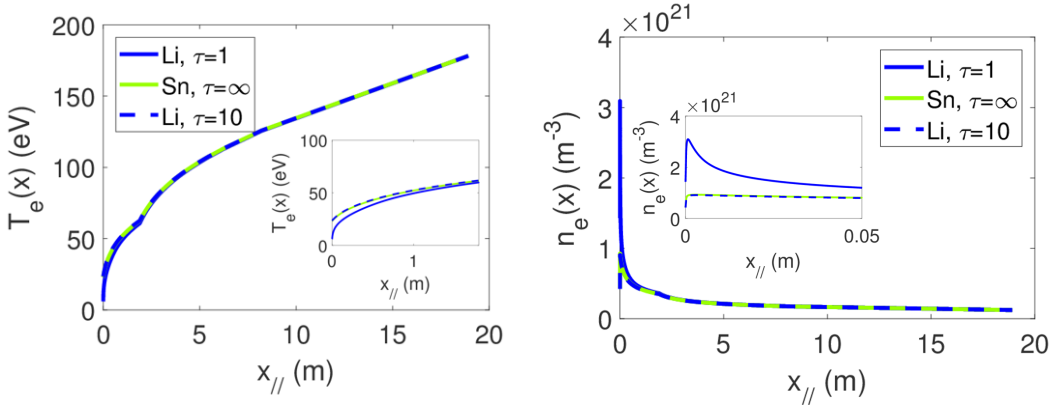

Figure 6.9: Computed plasma temperature (left) and density (right) spatial profiles along the outboard divertor leg field lines for Li ($\tau = 1$ ms and $\tau = 10$ ms) and Sn.

Density profiles corresponding to these temperature profiles are shown in Figure 6.9 (right). As expected, the profiles for the three cases considered are comparable up to the entrance in the divertor region, where the different amount of plasma cooling causes differences in the profiles. The high radiation scenario corresponds to the lowest temperature, and therefore to the highest density (due to total pressure conservation). Pressure conservation holds up to the point where plasma-neutral interactions become important. At this point, close to the target,

the expected density peak associated to ionization of recycling neutrals is retrieved. This peak is much more significant for the high radiation case - i.e. low temperature, high density - than for the low radiation case - i.e. high temperature, low density. This fact is not straightforward to explain, since both temperature and density positively affect the ionization rate. The latter is indeed stronger at higher temperature (due to the temperature dependence of the ionization rate coefficient) and at higher densities (there is a relatively weak density dependence for the ionization rate coefficient, but the ionization rate is evaluated as $R_{iz}\left(T_e, n_e\right) n_e n_0$, therefore the density dependence is slightly more than linear). For both cases at hand, however, the temperature several ionization mean free paths far from the target is larger than 10 eV, a condition where the density effect dominates over the temperature effect. Finally, the observed density drop close to the target is associated both to the presence of the aforementioned ionization source and to the flow acceleration up to $Ma = 1$ at the sheath edge.

The electron temperature and the particle dwell time determine the actual local value of the cooling rates. The resulting spatial distribution along the flux bundle is shown in Figure 6.11 (left) for the three cases considered. The values shown there result from the self-consistent evaluation of the plasma state and of the plasma cooling. The value of this function is reported only in the divertor region, since Li/Sn vapor is assumed to be only present there. As expected, values for Sn are always several orders of magnitude larger than the ones for Li (for both values of τ considered). The most interesting feature outlined by this plot is perhaps the following: the strong non-linearity of the cooling rate implies that a larger τ is not necessarily associated - locally - to a lower cooling rate, since the latter is strongly dependent also on the plasma temperature, see also Figure 3.7.

The combination of L_z, vapor density and plasma density results in the density of power which is lost by the plasma due to interactions with the vapor. This quantity is shown in Figure 6.10. The discontinuity at $x_{//} = L_{//,OEC} \sim 0.6$ m is due to the corresponding discontinuity in $n_z(x_{//})$ (see Figure 6.11 (right)) which is associated to the 0D nature of the model employed for describing the Li vapor. Indeed, a single density for each chamber is computed by the 0D model.

The combination of the information coming from Figure 6.9, Figure 6.11 (left) and Figure 6.11 (right) therefore explain the result in Figure 6.10, and in particular the somewhat surprising similarity between the case Sn, $\tau = 1$ ms and the case Li, $\tau = 10$ ms. For the OEC, for example, the electron density is similar, and the three orders of magnitude difference between the loss functions are approximately compensated by a three orders of magnitude difference between the vapor densities.

It is important to recall here that the plasma cooling effect is due to both radiation and ionization of Li atoms. Therefore, the curves shown in Figure 6.10 do not correspond to power radiated. An assumption concerning the location where the power committed to ionization is released, i.e. to the location where recombination of the Li plasma occurs, is necessary. This result is not provided by the present

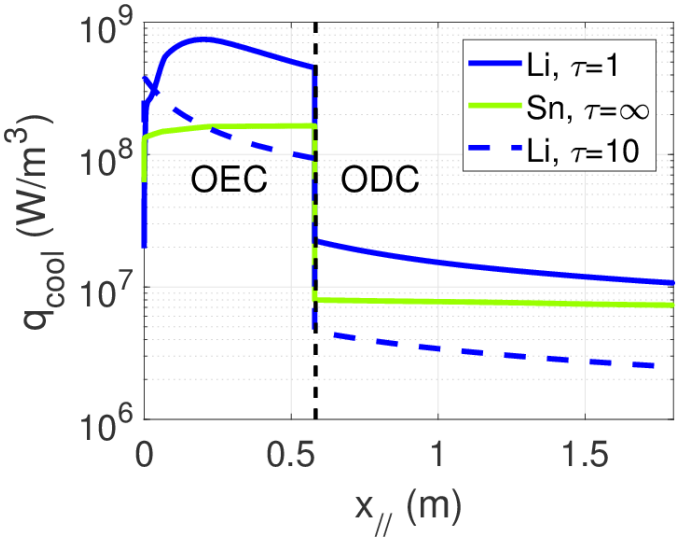

Figure 6.10: Power lost by the plasma per unit volume due to interactions with metal vapor within the outboard divertor region for Li ($\tau = 1$ ms and $\tau = 10$ ms) and Sn.

model, which only includes a simplified treatment of Li (or Sn) neutrals. For simplicity, recombination of Li plasma is assumed to occur before the target is reached. This assumption is subject to further improvements in the future.

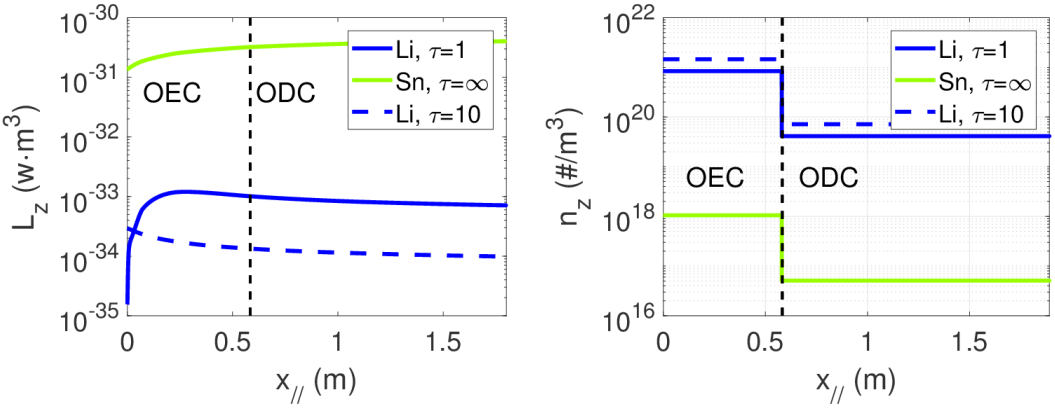

Figure 6.11: Spatial profiles of the cooling function (left) and vapor concentration (right) within the outboard divertor region for Li ($\tau = 1$ ms and $\tau = 10$ ms)and Sn

The results of this section show that the value of τ, which is one of the physical unknowns of the problem, indeed affects the result in the case of Li. However, it is anticipated from Figure 6.11 (left) that the thermodynamic state of the LM-vapor system is not much sensitive to this assumption (density of Li vapor n_z is similar for the cases $\tau = 1$ ms and $\tau = 10$ ms). The following section shall further analyze

this point, which is one of the most significant outcomes of the present work.

6.6.2 Temperatures of the system

As already stated, both inner and outer divertor targets have been included in the study. While, for convenience, results for the inner target have not been shown in the previous section, in the following the behavior of the entire divertor system is discussed.

Figure 6.12 shows the temperatures evaluated in the outboard divertor chambers for Li, $\tau = 1$ ms (top) and Sn (bottom). The temperature distribution in the structures is evaluated by means of the 2D finite element model, whereas the (uniform) temperature of the vapor is evaluated by the thermodynamic 0D model. For Li, results for $\tau = 1$ ms are shown.

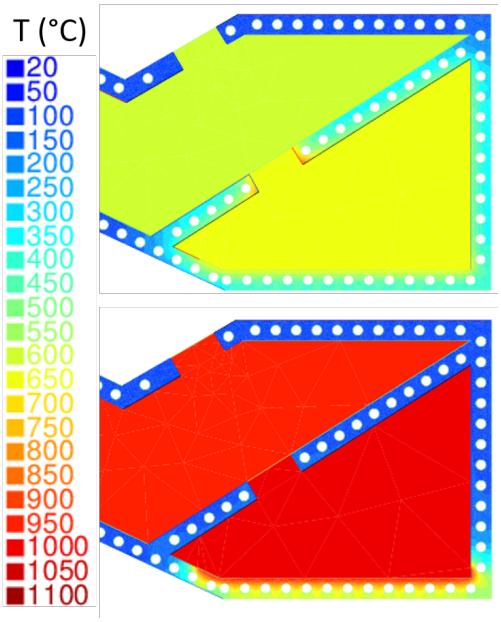

Figure 6.12: Temperature field of the structures and 0D temperature of the LM-vapor system in the ECs and of the vapor in the DCs for Li, $\tau = 1$ ms (top) and Sn (bottom).

For the sake of completeness, the operating temperatures of the LM and vapor in both divertor chambers are shown in Figure 6.13. The significant difference between the two LMs is a consequence of the interplay between the many phenomena occurring and can be explained by looking at the power balance, which is detailed in Figure 6.14. For the case of Sn, a larger amount of power is allowed to reach the pool without being mitigated by radiation nor by evaporation/condensation cooling and therefore a larger temperature is reached - given a similar global heat

transfer coefficient between the power deposition zone and the cooling channels for the two cases.

A simple explanation for this different split of the power entering the system shall now be proposed. If neither radiation nor evaporation were present, i.e. if the pool behaved like a solid, the only difference between the two LMs would be represented by their thermal conductivity, and therefore the different resistance offered by the pool to the flow of heat - this is strictly correct if sputtering is neglected. Since this difference is relatively small, it does not significantly influence the global heat transfer coefficient between the top of the pool and the cooling water. Therefore, the system would reach a similar steady state temperature in the two cases, which is much larger than the temperatures actually computed the code. In the steady state analyzed by the code, the power which is not radiated heats the target, but evaporation partly accommodates for it, exhausting part of this power on the walls thanks to condensation. Indeed, above a certain temperature, evaporation becomes significant, and consequently effects associated to the presence of vapor start to be relevant. As already mentioned, the other relevant contribution to the heat load mitigation, occurring on top of the cooling provided by evaporation/condensation, is represented the cooling of the plasma induced by the presence of a non-negligible amount of vapor in the chambers. The temperature at which evaporation starts to become significant is much lower for Li than for Sn (see again Figure 3.6), i.e. Sn is much more difficult to evaporate, and this explains why $q^{Sn}_{pool \to wall} > q^{Li}_{pool \to wall}$ in Figure 6.14. Therefore, the overall result is that a larger amount of heat will reach the pool unmitigated in the case of Sn. In all cases, q_{noz}, i.e. the power loss associated to the flow of vapor out of the DC, is computed to be negligible.

Moreover, the difference between the distribution of the "mitigated" power between evaporation/condensation and radiation is due to the much larger values of the cooling function for Sn, Figure 3.7, even with respect to Li far from coronal equilibrium-. The amount of evaporated Sn is lower with respect to the amount of evaporated Li, and this explains the much lower condensation contribution. Conversely, the small amount of Sn present in the chambers is sufficient to radiate a not negligible amount of power due to the much larger value of the cooling function.

Similar arguments can be employed to explain the interesting result shown in Figure 6.15, where the parametric scan on the τ parameter is presented for Li. This bar plot explains why, according to the present calculations, this parameter does not significantly affect the operating temperature of the system (see error bars in Figure 6.13) notwithstanding the large difference in radiated power (see again Figure 6.14). Indeed, the lower amount of power radiated in the case $\tau = 10$ ms implies a larger heat flux to the pool, which is accommodated by a more significant evaporation without a large temperature increase (from Figure 3.6 it is clear that for Li at the temperatures considered here, a small temperature variation is sufficient to increase the evaporation rate by an order of magnitude).

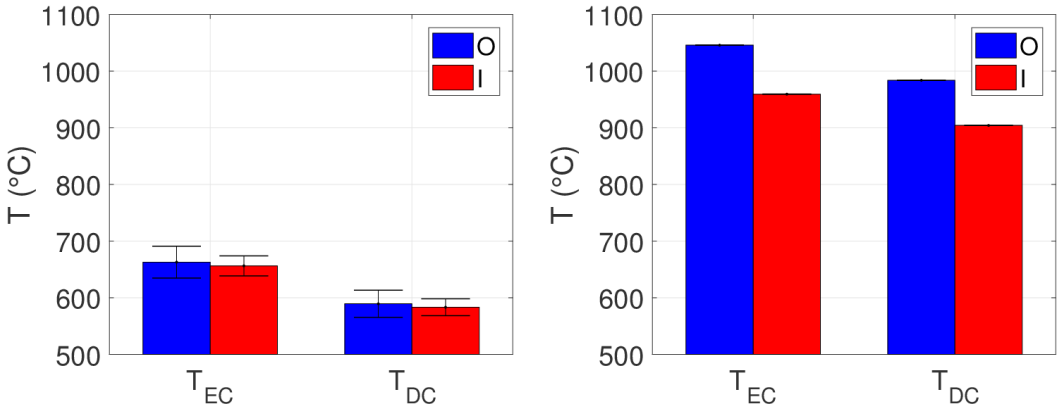

Figure 6.13: Temperatures of the LM-vapor system within the various chambers for Li (left) and Sn (right). Error bars account for uncertainty on τ (very small effect for Sn).

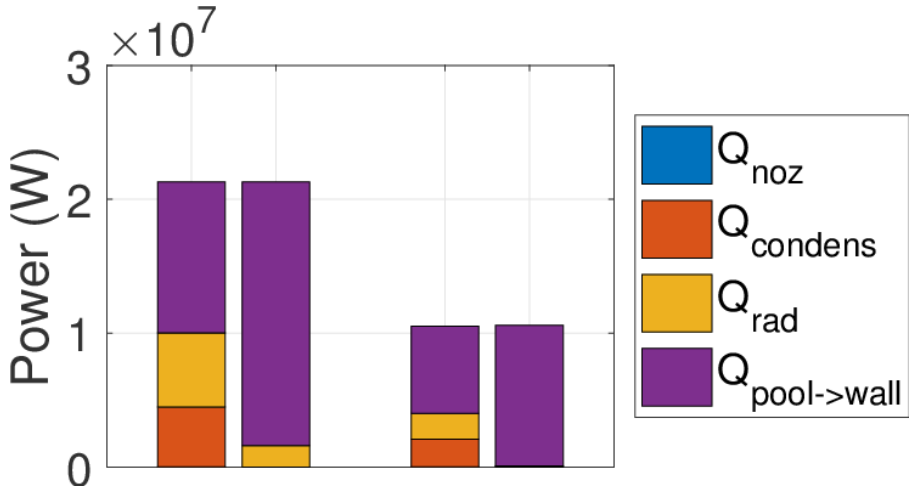

Figure 6.14: Power balance for Li, $\tau = 1$ ms and Sn. The two bars on the left refer to the OEC, those on the right to the IEC.

A final comment shall now be made concerning the power distribution, and specifically the - relatively low - mitigation of the incoming power. It should be stressed that the configuration hereby analyzed is characterized by a small L_{DIV}, which determines the interaction length between the SOL plasma and the metal vapor confined in the box structure. If the divertor boxes were designed in such a way as to increase this quantity, the radiated power fraction would also increase. Moreover - somewhat paradoxically - a worst cooling of the structure could be partially mitigated by a larger amount of radiated power due to the larger temperature and consequent larger vapor density. However, this would also cause a larger amount

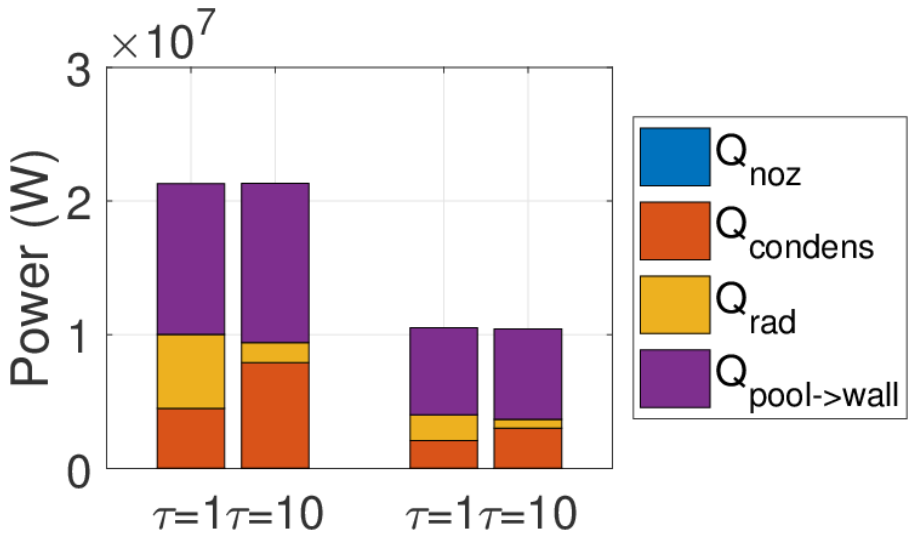

Figure 6.15: Power balance for Li, $\tau = 1$ ms and Li, $\tau = 10$ ms. The two bars on the left refer to the OEC, those on the right to the IEC.

of vapor flowing out of the DCs, and the consequences on the plasma should be assessed. For Sn, the operating temperature is more dependent on the target cooling strategy since the heat flux actually reaching the pool is larger.

A very final comment concerns the similar thermodynamic state of the LM - vapor system in inboard and outboard target. This is mainly due to the different areas available for condensation on the walls. Indeed, the two chambers appear to be less unbalanced for Li, where condensation has been shown to play a significant role.

6.6.3 Mass flow rates

The calculation of the mass flow rates circulating in the system or leaving it through the apertures is among the most significant outcomes of hte code. The most relevant ones are:

- The condensation mass flow rate within the EC, $G_{condens,EC}$, i.e. the amount of LM "recirculating" within this chamber.
- The condensation mass flow rate within the DC, $G_{condens,DC}$. As already discussed, since a strategy for collecting this amount of condensed metal should be devised, this mass flow rate is to be considered as an input for the design of e.g. the external LM purification loop.
- The amount of vapor escaping through the aperture of the DC towards the main plasma chamber $G_{DC \rightarrow MC}$. In the case of Li, this amount of LM might provide the beneficial effects already discussed on the plasma discharge. However, plasma dilution should also be avoided, therefore this quantity should

not be too large. Moreover, it should be kept in mind that a mechanism for collecting and finally recirculating also this LM which condensed within the MC should be devised. For Sn, this amount of vapor might be harmful for the plasma purity and should therefore be kept low.

The computed $G_{condens,EC}$, $G_{condens,DC}$, $G_{DC\rightarrow MC}$ are reported in Figure 6.16 (left) for Li and Figure 6.16 (right) for Sn. The results should become an input for the design of the external LM recirculation/purification system and for an assessment of the acceptability of the flux of vapor to the MC. A feedback from these assessments could be employed for modifying the target cooling strategy ($T_{in,sector}$, heat transfer coefficient, pool thickness.

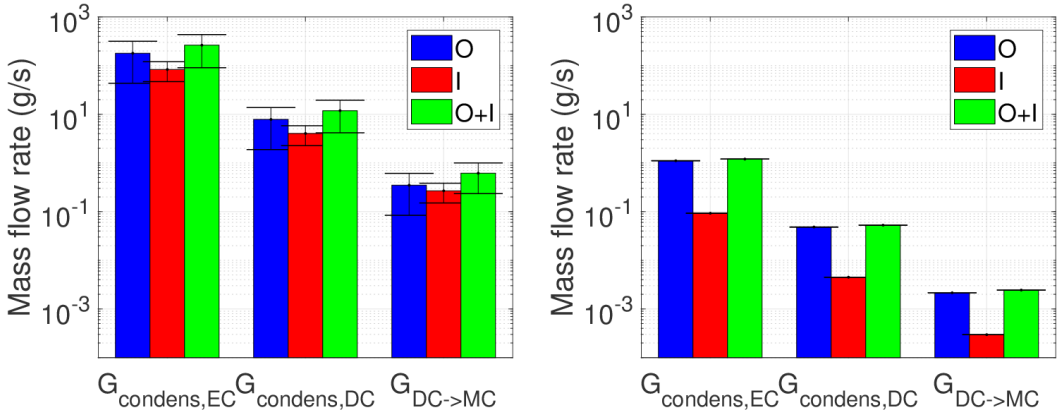

Figure 6.16: Mass flow rates of LM condensed in the divertor chambers and of vapor entering the MC as evaluated by the code for Li (left) and Sn (right). Error bars account for uncertainties on the parameter τ.

6.7 Conclusions and perspective

A self-consistent model for an LM divertor of box-type has been developed and preliminary results have been obtained for the test case of the DTT.

For Li, the calculations here performed confirm the anticipated effectiveness of this LM for use in a system, since both evaporation and radiation cooling significantly contribute to a reduction of the target heat load. However, more detailed investigations are required in order to determine whether the amount of Li vapor flowing out of the DCs is sufficiently low to avoid plasma dilution. The present calculations suggest that an operating condition characterized by a significant amount of power exhausted via the "alternative" channels, namely radiation and evaporation/condensation - the availability of which represents one of the the main advantages of this type of divertor - can be already obtained with just two chambers.

However, should the vapor flux towards the MC be too large, the number of chambers can be increased to provide a more effective differential pumping and hence further reduce this flux, compatibly with the available space.

For Sn, a much less significant importance of evaporation/condensation cooling has been computed. Indeed, a very small density of Sn vapor is foreseen to be present in the system. This result indicates that the additional complexity associated to this divertor structure would not be justified by an enhancement of the plasma cooling. However, also for Sn the reduction in vapor flux towards the main plasma chamber was found to be significant, which could represent an important feature since it could allow the *local* recollection of Sn.

The present study did not only provide a tool for comparing the behaviour of Li and Sn in a box-type closed divertor of this kind. Indeed, a deeper understanding of the interplay within the different physics mechanisms involved has been obtained. In particular, several design parameters have been pointed out that, according to this model, could provide a more efficient operation of this system in terms of heat load spreading on the chamber wall surfaces. Those parameters are:

- The heat transfer coefficient, or equivalently the temperature of the coolant flowing within the cooling channels below the pool. Compatibly with other constraints, this could allow for a larger density of vapor to be confined in the EC, and thus to a more effective load spreading.
- The interaction length between the plasma and the Li vapor, which should be increased - compatibly with the chamber geometry and coil system, which will be considered fixed when designing this system- in order to obtain a stronger cooling of the plasma.
- As for conventional divertors, a larger upstream plasma density would imply a lower electron temperature at the target.

These parameters can be varied separately or together. An extrapolation of the results presented in this chapter which accounts for an optimized configuration suggests that a large density of Li can be confined within the system. This density could be sufficient to induce plasma detachment - promoted by the vapor itself, rather than by seeded impurities, as already suggested in [67]. Even though further studies would be needed concerning this point, it is clear that this perspective is particularly attractive.

Even though this model accounts for much of the physics underlying the system at hand, some important features are missing. In particular, no account has been given to the pressure buildup of neutral H in the system, which may affect the condensation rates, and no detail concerning the possible strategy for actively (or passively) pump those neutrals has been proposed. Moreover, the model is steady state, hence it does not follow the initial evolution of the system (which is, in principle, interesting) nor potential ELM-driven transients. The greatest limitation is perhaps represented by the impossibility to determine the target hotspot temperature due to the 0D approach employed to model the LM pool and the vapor,

which only allows to compute average surface temperatures. This means that only semi-quantitative conclusions can be drawn from the model application.

Some envisaged future improvements of the model are the following:

- Remove assumption of uniform wall and pool loading (in order to fully exploit the 2D wall model and evaluate hotspot temperatures).
- Include a more detailed analysis of Li vapor dynamics[1].

As a final remark, it is recognized that it seems natural to ask how well the model of the present chapter matches the results of chapter 5. Such a benchmark would provide a more quantitative assessment of the capability of the simplified model here presented to simulate the plasma and vapor behavior in the vapor shielding region. This activity is therefore envisaged for the near future.

[1]A dedicated study using the Direct Simulation Monte Carlo (DSMC) method was performed to assess the validity of the 0D approximation for the vapor, which is reported in the appendix of [138]. A very brief summary of the obtained results is reported in Appendix B.

Chapter 7

Conclusions and perspective for Part I

To conclude Part I of the present thesis, it is convenient to summarize here its content, including the introduction to the topic, the original methodologies and results obtained, the relations among them and their relevance for the field, together with future perspective.

The topic of the power exhaust in tokamaks, together with the associated concerns for a fusion reactor, was first introduced. Liquid metal divertors were then presented as one among the possible alternatives to the baseline strategy currently adopted to address the PEX problem. To conclude the introductory part, an overview of the state-of-the-art methods and tools for SOL plasma modelling was provided.

A survey of the state of the art of SOL plasma modelling in the presence of an LMD pointed out the need for developing self-consistent models, so to take into account the mutual interactions between the evaporating divertor target surface and the SOL plasma. In the present thesis, two approaches have been presented: the first relies on the 2D multi-fluid plasma code B2.5, which was coupled to a model for the target to self-consistently determine evaporation and sputtering; the second, which is less detailed and requires a significantly shorter computer time, is based on a 1D SOL plasma model for the D^+ ions and for electrons, coupled to a 0D model for the metal vapor and an analytical model for the fuel neutrals, where the effect of impurities on the plasma is taken into account in a simplified way. The first approach was applied to the simulation of an ITER-like LMD for the EU-DEMO, whereas the second one was adopted to qualitatively estimate the operating conditions of a vapor-box LMD for the DTT tokamak. It can be stated that the present thesis work has successfully accomplished the task of developing and applying self-consistent models for modelling the SOL plasma including its interactions with the metal arising from an LMD. The 1D model is implemented in a fast-running code, which is therefore suitable for scoping studies such as the

one here presented. The 2D model is indeed more suitable for supporting more advanced phases of the divertor design.

The application of these two models to the comparison of Li vs. Sn not only did represent an ideal test bench, but also provided outcomes which are relevant for the divertor design. For the ITER-like design, the 2D calculations confirmed that Sn behaves better than Li, although it appears that only a very narrow operational window exists if no seeded impurities are adopted. If Ar seeding is adopted, the results suggest the existence of a a promising operational scenario with a liquid Sn divertor and a relatively low amount of seeded Ar, working in high-recycling regime. This scenario is similar to the baseline one, but has the advantage of being more forgiving in case of off-normal events or ELMs. For the vapor-box divertor, instead, Li was confirmed to represent an optimal candidate to exploit the specific features of this design. Moreover, the results were presented so to identify the different power exhaust mechanisms and possible strategy to enhance them, thus providing useful guidelines for the design phase.

The perspective applications and improvements of the two individual models were already described in the respective chapters. It shall here be sufficient to point out the perspective application of the combination of the two models/approaches. Provided that a thorough benchmark between the two approaches is realized[1], they could be used in synergy: the simplest one for scoping studies, and the detailed one to provide inputs (especially heat and particle load profiles) to the divertor design, while ensuring that the impact on the core plasma performance is not excessive.

[1] This requires to implement a simplified model for the metal vapor, thus allowing the simulation of e.g. an ITER-like divertor, since the currently implemented model is indeed limited to a vapor-box divertor geometry.

Part II

Liquid metal-cooled nuclear fission reactors

Chapter 8

Generation IV fission reactors and the lead-cooled fast reactor

The design of Generation IV fission reactors is currently ongoing within the Generation IV International Forum (GIF), with the objective to improve sustainability, economically competitiveness, safety, security, reliability and proliferation resistance with respect to the current nuclear fission reactor fleet.

This chapter aims at providing an overview of the international framework for the efforts oriented towards the development of the next-step nuclear fission reactors, as well as the specific features of the lead-cooled fast reactor concept, to which this second part of the present thesis is devoted. Section 8.1 describes the objectives of the Generation IV of nuclear fission reactors. Section 8.2 describes the potential advantages of fast neutron spectrum reactors, among which the ones representing the specific interest of the second part of this thesis are those cooled with liquid metals, and particularly by heavy liquid metals. Section 8.3 introduces the ALFRED project as a demonstrator for the lead-cooled fast reactor design. Finally, section 8.4 describes the need for the development of numerical tools oriented at informing the core design phase of an LM-cooled fission reactor. Addressing this need represents the main focus of the present work.

8.1 Generation IV fission reactors

Nuclear fission is currently the first low-carbon electricity source in OECD countries, where it provides 18% of the electricity supply. Notwithstanding this significant contribution to meet the sustainable development goal of clean energy, the public acceptance and efficiency of current generation power plants are affected by several known open issues:

1. production of long-lived radioactive waste;
2. low efficiency in fuel utilization;
3. risk of proliferation;
4. reliability of active safety systems.

In view of the shortcomings indicated above, the GIF initiative was started in 2001 as an international cooperation to research and develop the next generation (the so-called *fourth generation*) of nuclear energy systems by assessing their feasibility and capabilities, see Figure 8.1.

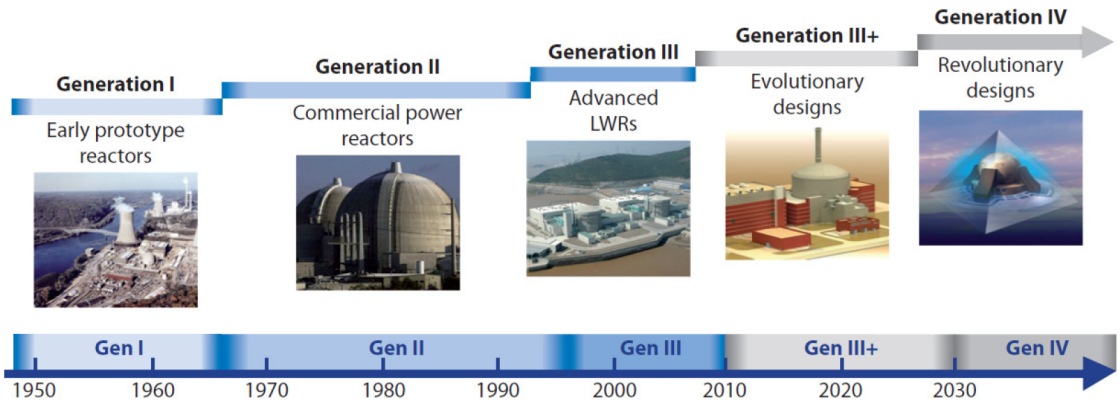

Figure 8.1: Sketch of the successive generations of nuclear reactors with approximate time spans for deployment [145].

.

The objectives of GIF can be summarized as follows [144, 145]:

- **Sustainability-1**: improved fuel utilization;
- **Sustainability-2**: minimization of long-term waste;
- **Economics-1**: reduction of life cycle costs to improve competitiveness with other sources;
- **Economics-2**: minimization of financial risk;
- **Safety & Reliability-1**: operational safety and reliability;
- **Safety & Reliability-2**: reduced core damage probability;
- **Safety & Reliability-3**: eliminate the need for off-site emergency response;
- **Proliferation resistance and physical protection**: minimize susceptibility to diversion of undeclared production and vulnerability of installations.

Based on the objectives listed above, GIF selected six reactor technologies among ~ 130 proposed concepts:

- Very-High-Temperature Reactor (VHTR);
- Molten Salt Reactor (MSR);
- SuperCritical-Water-cooled Reactor (SCWR);
- Sodium-cooled Fast Reactor (SFR);
- Gas-Cooled Reactor (GCR);
- Lead-cooled Fast Reactor (LFR).

The GIF identified three phases for the delopyment of each of the above-listed systems:

1. **Viability**: test basic concepts under relevant conditions, identify and solve all potential technical issues;
2. **Performance**: operate prototypes to verify and optimize processes on an engineering scale;
3. **Demonstration**: detailed design of the *demonstrator* for the concept, followed by *licensing*, construction and operation.

8.2 Fast reactors

Three out of the six concepts selected by GIF are Fast Reactors (FRs), i.e. reactors characterized by a fast neutron spectrum. This feature brings desirable advantages in terms of sustainability (the first two among the GIF objectives):

1. The long-term radiotoxicity of spent nuclear fuel is mostly associated to actinides (Pu, Minor Actinides (MAs)). While Light Water Reactors (LWRs) only allow for Pu recycling, FRs can also effectively burn MAs.
2. The capability to breed fuel leads to an increased fuel utilization efficiency.

On the other hand, the higher burnup and increased damage levels in the core lead to increased thermo-mechanical requirements for fuel and structures. Moreover, if the coolant is an LM, *corrosion* can represent a significant issue. Additionally, the relevant presence of Pu causes a worsening of kinetic paramters. Moreover, since the reactor is not in the most reactive configuration, events such as core cmpaction, fuel melting or coolant losses can increase the reactivity.

The focus of the present thesis is on Liquid Metal Cooled Reactors (LMCRs), characterized by a fast neutron spectrum due to the low moderation provided by the coolant. More specifically, the focus is on Heavy Liquid Metal Cooled Reactors (HLMCRs), and in particular on the Lead-cooled Fast Reactor (LFR) concept. In the following section, the main advantages and drawbacks of HLMCRs are presented.

8.2.1 Potential advantages

The main advantages of HLMCRs are:

- high core outlet temperature, which increase the thermal efficiency of the reactor;
- no need for coolant pressurization to prevent boiling, thereby allowing to operate at ~ 1 atm core outlet pressure, with a consequently reduced required vessel thickness;
- good coolant heat transfer properties;
- no core voiding, thanks to the high boiling point;
- low reactivity with air and water (as opposed to the SFR);
- high coolant density, providing enhanced natural circulation capabilities;
- good retention properties of volatile fission products;
- good shielding of gamma rays.

8.2.2 Main disadvantages

The main disadvantages of HLMCRs are:

- large fissile inventory required due to the low moderation;
- harsh neutron damage due to the fast neutron spectrum;
- corrosion of structures;
- potential formation of Polonium (Po), which is particularly relevant if Lead-Bismuth Eutectic (LBE) is used as a coolant;
- strong coolant-structure interactions and buoyancy of components, implied by the high coolant density;
- erosion of structural materials;
- risk of coolant freezing due to the high melting point (327 °C);
- difficult inspection due to the coolant opacity.

8.3 ALFRED: an LFR demonstrator

In view of the above-mentioned challenges associated to the LFRs, R&D is clearly needed in terms of reactor components, thermal-hydraulics, neutronics, structural materials, instrumentation, coolant and cover gas chemistry, in order to increase the level of technological readiness of this concept. To this aim, a full-scale demonstration plant, Advanced Lead-cooled Fast Reactor European Demonstrator (ALFRED), is planned, for which the schematic layout is shown in Figure 8.2. The Fostering ALfred CONsortium (FALCON) agreement, signed in 2013, has the objective of bringing LFR technology to industrial maturity through the design, construction and operation of ALFRED.

The strength of the ALFRED reactor is represented by its noticeable safety features:

- "safe by design" approach;
- prompt detection of any deviation from expected behavior;
- adoption of proper margin from the early design stage;
- implementation of several lines of defense.

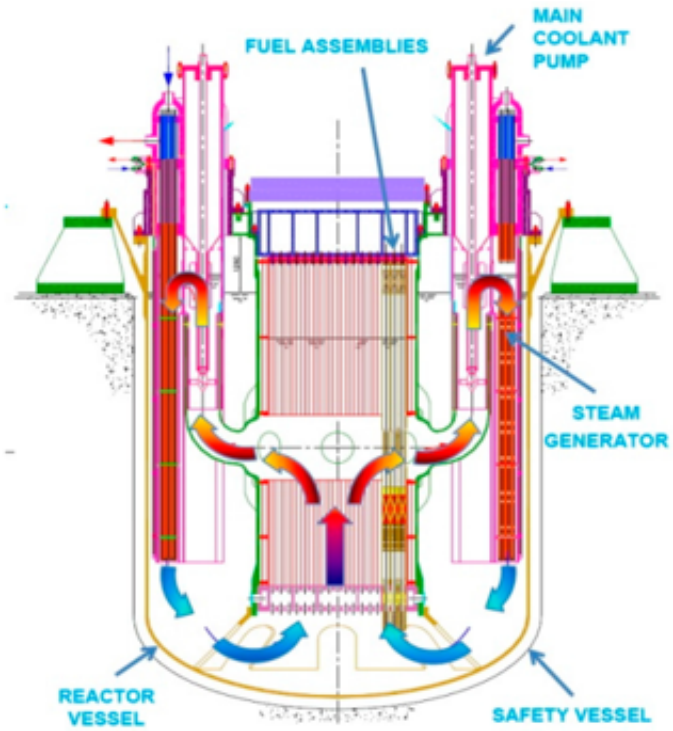

Figure 8.2: Conceptual configuration of ALFRED, reproduced from [19].

.

8.4 The role of numerical tools in LFR core design

8.4.1 A comprehensive approach to core design

The design of an LFR core is a multi-disciplinary task which deals with a large number of tightly interconnected physical/engineering parameters associated to the three "pillars" of core design: neutronics, thermal-hydraulics and thermo-mechanics.

A comprehensive approach to core design involves:

- identification of technological constraints, from which design guidelines are derived;
- inclusion of safety principles and criteria early in the design;

- management of interfaces between the core and other reactor systems;
- design of individual components;
- optimization of performances by working on available margins.

The reactor design then undergoes a *verification* phase, where the actual behavior of the system is assessed both in nominal and in accidental conditions. The design and verification phase occur iteratively and have different needs which call for different tools.

8.4.2 Design-oriented codes

Design-Oriented Codes (DOCs) are intended to support the design process by clearly characterizing a particular core configuration in terms of its effectiveness in meeting design targets and constraints. A DOC achieves this objective while requiring only a short computational time thanks to a well defined application domain. Within this domain, the code results are comparable to the ones calculated by benchmark codes. The models to be implemented are selected according to a trade-off between complexity and accuracy [113]. One of the specific features of a DOC is the attempt to attain balanced contributions from the various error sources. Summarizing, the key feaures of a DOC are:

- equilibrium;
- low computational time;
- a clear application domain.

8.4.3 Verification-oriented codes

Verification-Oriented Codes (VOCs) feature a comprehensive treatment of one or more of the NE, TH and TM problems, relying on sophisticated models and numerical methods. The required input for VOCs is usually detailed, including the specific geometry and material composition, making these codes suitable for the verification phase. The required accuracy for a VOC is reached at the expense of longer simulation times and less clear relations between inputs and outputs.

Chapter 9

Design, development and preliminary validation of the TIFONE code

In this chapter, the development, verification and validation of TIFONE, a DOC for the TH modelling of the inter-SA coolant in the full core of HLMCRs, is presented. Specific care is devoted to describe the development rationale and procedures, performed in compliance with ENEA software quality standards.

First, an introduction regarding the motivations for developing TIFONE and the quality assurance framework is provided in sections 9.1 and 9.2.

Then, from section 9.3 to section 9.9, the code structure and the selected approach to solve the problem are described. Specifically, the general guidelines for the code design and the global features of the code are summarized in section 9.3. The calculation domain and its spatial discretization are discussed in section 9.4. Section 9.5 describes the set of subchannel (SC) equations adopted in TIFONE. The solution strategy is reported in sections 9.6 and 9.7. The closure relations for the empirical parameters appearing in the equations are reported in section 9.8. The connection logic implemented in the code is described in section 9.9.

Sections 9.10 to 9.16 are intended to give a glance of the software development procedures. Specifically, sections 9.11 and 9.12 provide technical details concerning the input and output structures. In section 9.13, the data structures employed by the code are described in detail. The code functional modeling is described in section 9.14. Programming guidelines followed during the code implementation phase are described in section 9.15. The detailed code design in the form of a pseudocode for selected code components is presented in section 9.16.

Finally, section 9.18 reports the verification and validation of the code. Specifically, the guidelines followed during the verification phase of the code are reported in section 9.17. Finally, the preliminary validation against experimental data from the KALLA facility is presented in section 9.18.

9.1 Introduction and motivation

The presence of the Inter-Wrapper (IW) region is inherent in core designs characterized by closed SA. Among the goals of the core TH design of LFRs exploiting the closed sub-assembly (SA) option, cold by-passes must be avoided and excessive thermal gradients among opposite faces of the assembly ducts prevented. To achieve these goals, a suitable coolant flow outside the assemblies themselves must be guaranteed, compatibly with the IW gap, the latter being established by the core thermo-mechanical design. Moreover, for wrapped assemblies, the possibility of gagging arises, giving an extra degree of freedom to the designer for leveling thermal gradients at the assemblies' outlet. Therefore, the design process requires knowledge of the axial and radial coolant temperature profiles in the IW gaps throughout the whole core (i.e., including all core SAs), as well as the axial and perimetrical wrapper temperature profiles, and notably the (possibly) different values of each side of the wrapper itself which could induce SA bowing. The above-mentioned requirements point out the necessity of a DOC for solving the IW flow and heat transfer problem.

To address this need, a DOC, Termo-Idraulica delle Fughe che Occorrono nel Nocciolo fra gli Elementi (TIFONE), was developed and verified according to the Software Quality Management System in place within ENEA's SICNUC division [75]. The SC approach was chosen, since it allows to achieve a sufficient level of spatial resolution while retaining the key features of a DOC, namely equilibrium, a low computational time and a clear application domain. The current version of TIFONE solves, for an HLMCR exploiting the closed SA option in hexagonal geometry, the inter-assembly coolant mass, energy and momentum equations, as well as the convection equations between the coolant and the wrapper. The calculation domain extends radially over the IW region of the entire core, and axially between the dividing and the merging points of the inter- and intra-SA coolant flows. The required inputs are the core geometry, as established by the core TM design, the axial and perimetrical distribution of the heat flux flowing out of all the SAs in the core, and the coolant inlet temperature and flow rate, and the fraction of the core inlet mass flow rate flowing along the IW region. Among the perspective applications of TIFONE is the coupling with codes for the thermal-hydraulic analysis of the single SA, so to allow for a full-core simulation. The code has been preliminarily validated against experimental data from the Karlsruhe Liquid metal LAboratory (KALLA) IW flow and heat transfer experiment, showing satisfactory agreement. This first application of TIFONE confirmed its ability in reproducing the measured data in its anticipated validity domain.

9.2 Quality assurance framework

According to ENEA Quality Assurance procedures for nuclear software development, the initial phases of the development of a new computational tool are as follows:

- Initial planning: definition of the general plan for the project and of the specific plan for the quality assurance, reported in a Software Quality Assurance Plan (SQAP) document [78].
- Requirements definition: identification of measurable requirements of the code to be developed, in order to satisfy the general requirements specified in the first phase. Requirements are organized in a Software Requirements Specification (SRS) document [76].
- Software design: development of a conceptual design of the code, where models, methods and algorithms are discussed which satisfy the requirements specified in the foregoing phase. The software design is reported in the Software Design and Implementation Document (SDID) document, where the design choices, along with their rationales, and the resulting code structure to be implemented, are described. The *design elements* (software structure, components, interfaces and data which are necessary for the implementation phase) are presented. For each design element, compliance with the requirements defined in the SRS document [76] is explicitly demonstrated.
- Code development: coding and production of code documentation which is compliant with the requirements specified above.
- Code validation: while verification procedures are carried out and documented during the code development phase to qualify compliance with the design indicated in the SDID, the code validation phase involves comparing the code with experimental data and/or results of more accurate codes to assess the capability of the product to meet the specified requirements within its anticipated validity domain.

Reporting all the steps above would be out of the scope of a PhD thesis. It was therefore necessary to operate a selection. In particular, the initial stages of the software development process (up to the requirements definition phase) will not be described in detail - the introduction to this chapter already described the motivations for the development of TIFONE and the key associated requirements. Therefore, in the following, the material corresponding to the scope of an SDID, together with the code validation phase, are presented. Therefore, the remainder of this chapter will include the the physico-mathematical model selected to address the IW flow and heat transfer problem, solution algorithms and validation results. Additionally, it was also chosen to report the key elements of the software design phase, with the aim of providing future software developers of DOCs for nuclear applications with a robust code design strategy.

9.3 Code design overview

9.3.1 Problem description

In compliance with the software requirements specified in the SRS document, TIFONE solves, for an LFR exploiting the closed sub-assembly (SA) option in hexagonal geometry, the inter-assembly coolant mass, energy and momentum conservation equations, as well as the convection equations between the coolant and the wrapper.

9.3.2 Calculation domain

The calculation domain extends radially over the Inter-Wrapper (IW) region of the entire core, and axially between the dividing and the merging points of the inter- and intra-SA coolant flows. Figure 9.1 provides a convenient visualization of the axial extension and composition of the calculation domain, while figure 9.2 shows the calculation domain corresponding to the inter-wrapper gap between several SAs. This drawing conveys the peculiar shape of the domain, which consists in a thin region (a few mm) extending axially and radially over the whole core.

9.3.3 Required spatial resolution and selected modelling approach

The required spatial resolution of the calculation is such to discriminate at least each gap between adjacent SAs and to distinguish among different axial elevations. In compliance with these requirements, TIFONE discretizes the IW region over the entire core both axially and radially. Radially, the coarsest admissible discretization is one featuring a single control volume for each gap between adjacent SAs. This represents a lower bound for the domain discretization refinement. Conversely, the code is required to run in at most several minutes on an average single-core computer to reflect the characteristics of a DOC. This renders a detailed approach (e.g. RANS-based CFD) unattainable. Based on these considerations, the subchannel (SC) method is believed to represent an ideal trade-off between computational speed and spatial resolution, as schematically indicated in Figure 9.3. This method has been widely used in nuclear reactor design and analysis in the past, and still represents an important tool, see for example [125].

9.3.4 Literature review

A number of codes evaluating the Thermal-Hydraulic (TH) behavior of closed SAs for Liquid Metal Cooled Reactors (LMCRs), aimed at both design and safety studies, has been developed in the past. Before starting the TIFONE code design, a

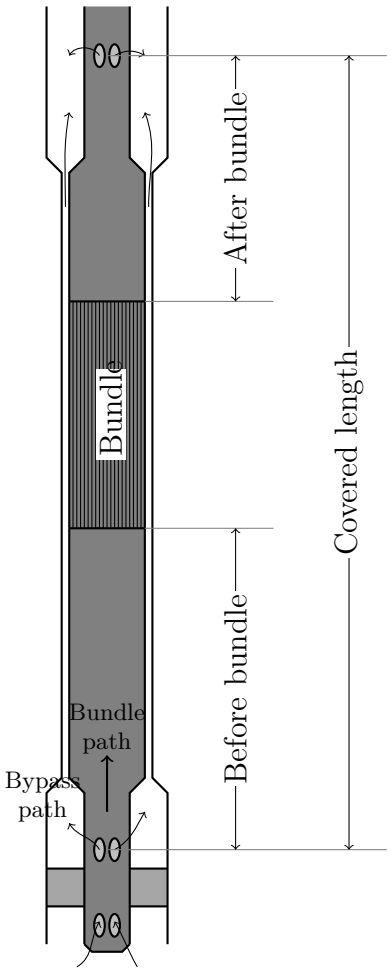

Figure 9.1: Schematic of the bypass flow domain, adapted from [113].

survey of existing LMCR thermal-hydraulic codes has been carried out, with particular attention to the ones featuring a module for the inter-SA heat transfer. The survey focused on codes based on the SC method. Indeed, as discussed in section 9.3.3, this method is considered to provide a suitable compromise between accuracy of the result and complexity of the calculation.

1. COBRA-WC [63] is a transient reactor safety analysis tool based on the SC method. This code solves the thermal-hydraulics of each SA, and takes into account the inter-SA heat transfer by assuming pure conduction across a stagnant coolant in the IW region. The IW coolant is therefore not consistently modeled with an ad-hoc set of conservation equations.
2. NETFLOW [131] is another transient reactor safety analysis tool. The approach for inter-SA heat transfer is analogous to the one used by COBRA.
3. SUPERENERGY-II [12] is a multi-SA, steady state computer code for LMCR

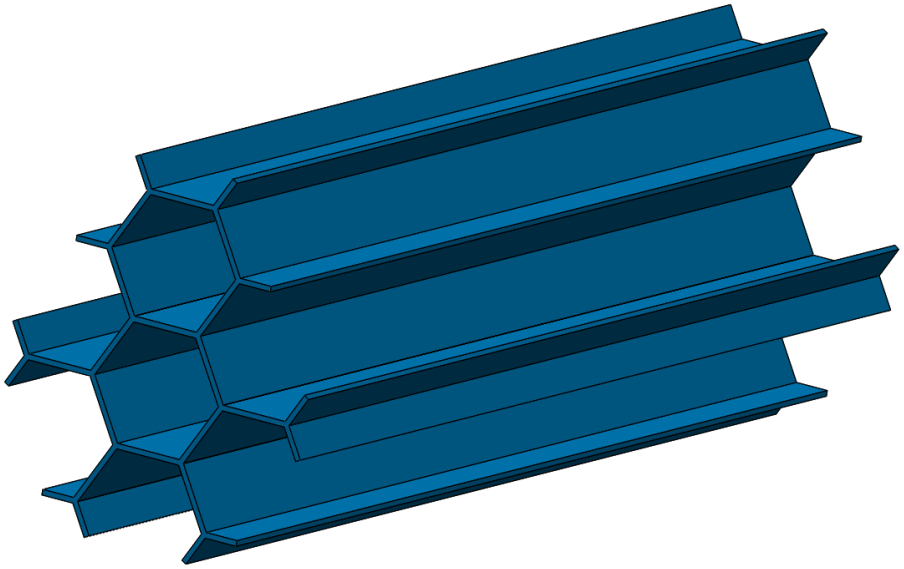

Figure 9.2: Representation of the inter-wrapper flow domain.

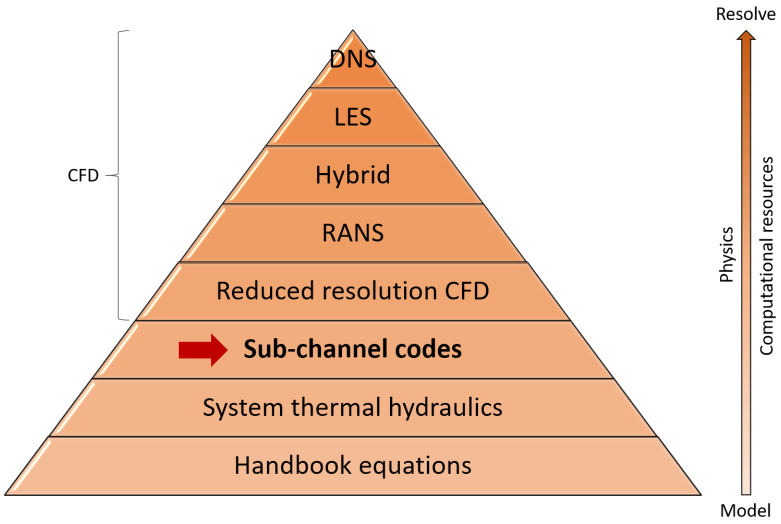

Figure 9.3: Complexity scale of thermal-hydraulic calculation approaches, inspired by [168].

core thermal-hydraulic analysis based on the SC method. SUPERENERGY-II is part of the ENERGY code series, developed at MIT in the late 70s-early 80s. This code was specifically aimed at providing a fast, full-core solution in steady state to support the design of LMCRs. As far as the IW heat transfer is concerned, SUPERENERGY-II offers the possibility to choose between two different approaches. The first approach is based on the simplifying assumption of stagnant liquid metal in the gap, whereas the second includes

the effect of convective heat transfer and the energy exchange between SCs in the IW region. SUPERENERGY-II can therefore be regarded as a Design-Oriented Code (DOC) featuring an IW heat transfer calculation capability. These features make the SUPERENERGY-II code a sound reference for the design of TIFONE.

4. ANTEO+ [114] is a design-oriented, SC code for single-SA thermal-hydraulics which has been developed and validated at ENEA. To provide consistent, non adiabatic conditions to the SA, a simplified model for the IW flow region surrounding the SA can be adopted for the calculation. This approach cannot however fully take into account the inter-SA heat transfer. The code has recently been extended to mixed convection regime inside the bundle [112].

Moreover, a technical document concerning a possible approach to the TH analysis of the IW coolant in fast reactors has been retrieved at ENEA [189]. This document provides a thorough description of the problem and proposes an approach based on the SC method, similar to [12] and [31] but featuring a more detailed treatment of the transverse momentum equation (see section 9.5).

The literature review has pointed out that at present no DOC is capable of solving the IW flow problem with the level of detail required by the SRS. However, in the past considerable effort has been devoted to this subject, thus representing a sound basis for this work. While, of course, learning from the problem formulation adopted in the above-mentioned codes, TIFONE adapts it to the specific needs indicated in the SRS while taking advantage of modern scientific software development techniques.

9.3.5 Coupling with SA thermal-hydraulic codes

According to the SRS, TIFONE must be able to accept as input the core-wide distribution of the power discharged in the inter-assembly coolant by the SAs. The self-consistent coupling of TIFONE to an SA TH code such as ANTEO+ to perform full-core TH calculations is therefore beyond the scope of the first version of TIFONE, whose design is presented in this thesis.

Nevertheless, it is recognized that the possibility to extend the code so that the power crossing the wrapper is computed self consistently based on the knowledge of the coolant temperature and velocity fields both inside and outside SA would be a desirable feature for future code versions. This vision has driven some of the design choices.

9.3.6 Code high-level architecture

The high-level architecture for TIFONE is schematically shown in Figure 9.4. This flow-chart contains the essential elements required for an SC code to solve the IW flow problem, namely:

- Read input: read user-defined information characterizing the problem.
- Generate connection logic: the domain is discretized and the connections among control volumes are computed and stored to be used in the solution phase.
- Compute flow split: the subdivision of the mass flow rate entering the IW region among the SCs is determined.
- Solve forced convection problem: determine the TH solution by assuming no net radial mass exchange between adjacent SCs.
- Assess forced convection assumption: once the forced convection solution is available, apply a criterion for determining whether a mixed convection solution is required. In case the criterion is not met, the forced convection solution is the solution of the problem. Otherwise, the mixed convection problem is solved.
- Output: relevant design-oriented outputs of the calculation, as well as the full problem solution, are printed.

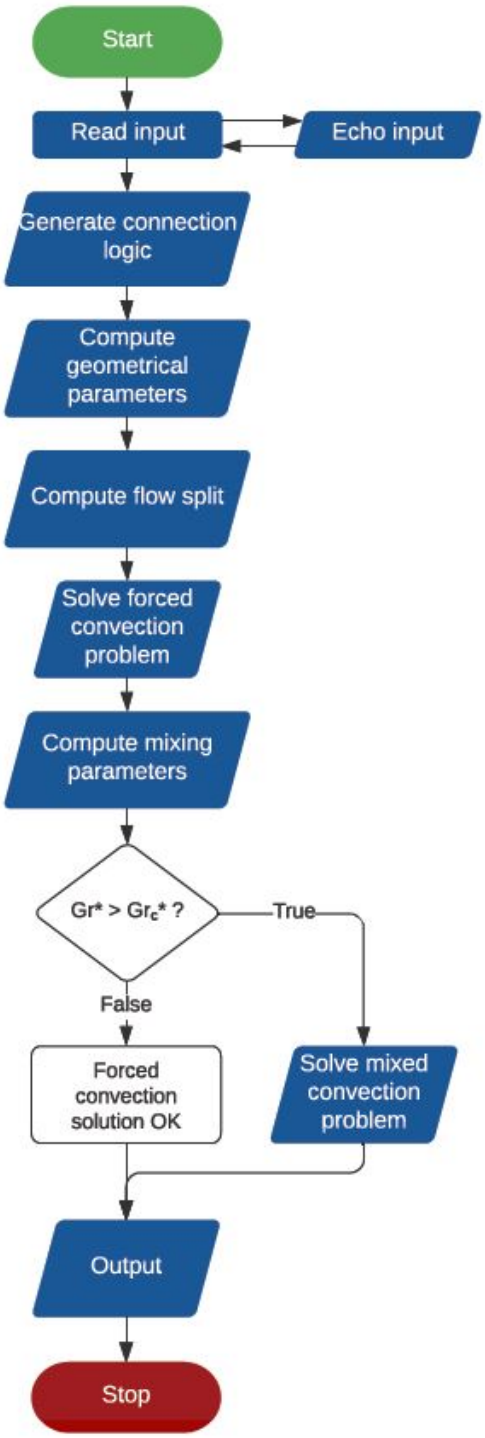

Figure 9.4: Flowchart representing the logical sequence of operations to be executed by the code.

9.4 Spatial discretization

9.4.1 Inter-assembly gap

Radial discretization

As stated in section 9.3.3, the radial resolution of the calculation must be at least capable of distinguishing each gap between adjacent SAs.

While designing TIFONE, three possible alternatives have been considered to radially subdivide each IW gap (the space between the sides of two neighboring SAs):

(a) One possibility is to subdivide the gap between adjacent SAs into a number of SCs (called *edge SCs*). These *edge SCs* are indicated in red in Figure 9.5 (a). The region between three hydraulically connected gaps is associated to a single SCs (called *corner SC*), indicated in green in Figure 9.5 (a). A 3D sketch of a *corner SC* is provided in Figure 9.6.
This choice allows to take into account the thermal-hydraulic connection between adjacent gaps, as well as to take advantage of the most detailed information available for the heat crossing the wrapper. This discretization has been adopted in [12], as well as in the simplified treatment of the IW thermal-hydraulics in the ANTEO+ code.

(b) Another possibility is to employ a "corner-based" subdivision that can be obtained from a simplification of option (a) - corresponding to a number of *edge SCs* equal to zero. The *corner SCs* are thus extended up to the center of the gap. This option reduces the overall number of SCs while retaining the connection between different gaps.

(c) Finally, a "side-based" option has been considered. This option consists in adopting a single SC for each gap between adjacent SAs. The difficulties associated to that choice are mostly due to the connection between adjacent SCs. Indeed, it is difficult to identify acceptable inter-SC mixing correlations in this particular geometry.

TIFONE adopts subdivision (a), as it allows for the greatest user flexibility - for instance, it can be coarsened up to the limiting case of option (b) if needed. Indeed, depending on the particular application and on the spatial resolution of the input data (heat flux flowing out of the SA and heat deposited inside the IW gap), the user is able to choose between two possibile approaches for the radial discretization of the domain:

1. "Default" approach: the user indicates the number of *edge SCs* for each gap. This number is used to evenly subdivide the side of each SA into a corresponding number of nodes, in such a way that the side length of each node (including the *corner* nodes) is equal. This choice is the simplest and allows the automatic generation of the nodalization for the entire core starting from a single number specified in input.

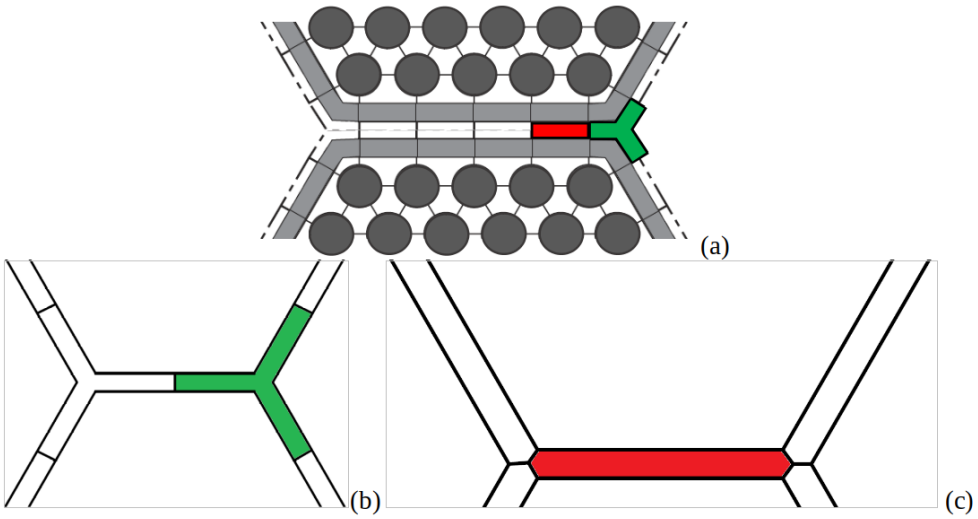

Figure 9.5: Inter-assembly gap SC subdivision options.

2. "Manual" approach: the user manually indicates the number and location of the radial node boundaries for each SA (assumed equal for all sides of a given SA). In this case, each SAs is allowed to have an independent radial nodalization. This second approach is useful to retrieve the discretization shown in Figure 9.5 (a), with the inter-SC boundaries distributed according to the location of the boundaries between the edge SCs of the neighboring SAs. In the event that the two neighboring SAs have a different number of *edge SCs*, the finest discretization is employed.

Guidelines for quantifying the effect of the selected nodalization on the code accuracy will be provided based on the outcomes of the code verification phase.

The possibility to further split the IW gap between the neighboring assemblies (with boundaries at the gap centerline) has also been considered. However, this would provide an unnecessary level of detail, while potentially hindering code stability. This option is therefore disregarded.

Axial discretization

Each SC is axially subdivided in a number of control volumes which are by default of equal length. The user is free to choose arbitrarily the actual distribution of axial nodes (see section 9.11). The code is therefore capable of determining the axial variation of the quantities of interests. Recommendations concerning the choice of the axial discretization step, according to both stability and convergence requirements, stem from from the numerical tests performed during the verification phase of the code.

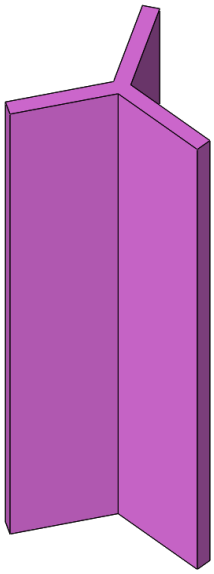

Figure 9.6: 3D drawing of a corner SC.

9.4.2 SA wrapper

The wrapper is discretized as well. For the sake of simplicity, the wrapper axial and radial discretization is consistent with the nodalization adopted for the IW region, see Figure 9.5(a). Each wrapper control volume can exchange heat with the adjoining coolant inside and outside the SA, as well as with neighboring wrapper nodes located at the same axial position.

9.5 Governing equations

9.5.1 Assumptions

As already indicated in section 9.3, TIFONE aims at determining the TH behavior of inter-assembly coolant over the entire core of an LFR, as well as the wrapper outer temperature for each SA. This is done adopting the SC method, using the discretization identified in section 9.4. The underlying assumptions of the SC method, as indicated in [196], are:

1. The control volume is fixed and common to all the conservation equations, except the transverse momentum equation;
2. The transverse flow (i.e. the flow between neighboring SCs) "loses memory of" his original direction when passing from an SC to the neighboring one.

Additional simplifying assumptions have been adopted in the present work, with the aim of achieving a balance between code complexity and accuracy of the results, which is an essential feature of a DOC:

1. The problem is solved in steady state;
2. The IW channel cross section is axially constant;[1]
3. Energy deposition by viscous dissipation in the coolant is neglected;
4. Axial heat and momentum transfer via conduction and turbulent momentum flux, respectively, are neglected;
5. The channel is assumed to be vertical, therefore gravity only contributes as a body force to the axial momentum balance;
6. Molecular and turbulent momentum transfer in transverse direction between adjoining SCs are neglected, i.e. friction between neighboring SCs is not taken into account.

In the following, the governing equations for the SC method are presented and simplified according to the above-mentioned assumptions for the problem at hand. Boundary conditions are also indicated. The formulation is consistent with [31].

[1] The entrance and exit regions located at the bottom and top of the core, respectively, are actually characterized by an axially variable cross section, see Figure 9.1. However, these regions - which are part of the computational domain - are not directly modeled. Their presence is instead accounted for simply by means of localized pressure loss coefficients.

It is noticed that, in the future, the code could be extended to simulate the situation where the hexagonal assemblies are deformed, thus yielding a variable flow cross section. However, this feature is beyond the scope of the first version of the code. Nevertheless, it is to be noticed that consistent programming practices have been adopted during the code development phase, to simplify potential future extensions.

9.5.2 Conservation of mass

Conservation of mass describes the axial evolution of the mass flow rate in each SC. The mass flow rate for a given SC can indeed change due to net mass exchange with the neighboring ones. This transfer can be caused by either pressure differences or density differences (buoyancy effects). In the following, the formulation, simplifications and boundary conditions adopted for TIFONE will be described.

Formulation

The complete form of the mass conservation equation for the i-th SC reads:

$$A_i \Delta z \frac{\partial}{\partial t} \langle \rho_i \rangle + \Delta \dot{m}_i = -\Delta z \sum_{j=1}^{N_{nei,i}} W_{ij} \tag{9.1}$$

where Δz is the axial length of the SC - which will also be called *control volume* in the following. Here and thereafter, the axial variation of a quantity ψ between z (i.e. the axial coordinate of the inlet of the control volume) and $z + \Delta z$ (i.e. the axial coordinate of the outlet of the control volume) is expressed as $\Delta\psi = \psi_{z+\Delta z} - \psi_z$. The operator $\langle\ \rangle$ indicates volume averaged quantities over the control volume. The subscript j denotes quantities related to one of the $N_{nei,i}$ neighbors of SC i. N_{nei} is equal to 2 for *edge SCs* and to 3 for *corner SCs*. The subscript ij indicates exchange quantities between SC i and SC j. A is the cross-sectional SC flow area, ρ is the fluid density, v is the fluid velocity, $\dot{m} = \{\rho v A\}$ is the axial mass flow rate (where the $\{\ \}$ operator represents a surface average over the flow area) and W is a mass flow rate per unit length in kg/(m s). In steady state, the equation becomes:

$$\frac{\Delta \dot{m}_i}{\Delta z} = -\sum_{j=1}^{N_{nei,i}} W_{ij} \tag{9.2}$$

Boundary conditions

The code takes in input both the total core mass flow rate and its repartition between the SAs and the IW region (the latter representing the calculation domain for TIFONE). Once the mass flow rate entering the IW calculation domain is known, TIFONE further subdivides it radially among the SCs. The approach for doing so depends on the choice concerning the treatment of the transverse momentum conservation equation, as described in section 9.5.4. The user is nevertheless left with the possibility to independently choose the flow repartition among SCs in the IW region. This capability will, for example, allow the designer to test the effectiveness of an ad-hoc, local variation of the by-pass flow gagging scheme to tune the mass flow rate in a subset of the IW SCs.

9.5.3 Conservation of energy

Conservation of energy describes the axial evolution of the coolant enthalpy in each SC. The enthalpy variation along a given SC is due to energy deposition in the SC, heat transfer with the portion of the wrapper wetted by the SC and net energy exchange with neighboring SCs. The latter can be caused by either net mass exchange (with the consequent energy transport) or by mixing effects which do not imply a net mass exchange (conduction and turbulent mixing, see section 9.5.3). In the following, the formulation, simplifications and boundary conditions adopted for TIFONE will be described.

Formulation

The energy conservation equation can be stated as follows:

$$A_i \Delta z \frac{\partial}{\partial t} \left[\langle \rho h \rangle_i \right] + \Delta \left[\dot{m}_i \left\{ h_i \right\} \right] = A_i \Delta z \dot{q}_{eq,i} - \Delta z \sum_{j=1}^{N_{nei,i}} \left[\left\{ W_{ij}^{*D} h_i \right\} - \left\{ W_{ji}^{*D} h_j \right\} \right] - \Delta z \sum_{j=1}^{N_{nei,i}} W_{ij} \left\{ h^{\star} \right\} + A_i \Delta z \left\langle \frac{dP_i}{dt} \right\rangle \tag{9.3}$$

where h is the fluid enthalpy, $\dot{q}_{eq,i}$ is the equivalent power per unit volume deposited in the SC due to either heat transfer with the adjacent SAs or the volumetric heat generation, W_{ij}^{*D} and W_{ji}^{*D} are turbulent interchange flow rates per unit length between SCs, $\{h^*\}$ is an effective enthalpy transported by the cross flow (averaged over the contact area between SCs i and j) and P is the static pressure.

For the sake of simplicity, it can be assumed that $\{\rho h_i v\} \sim h_i \{\rho v\}$, where v is the flow axial velocity. Based on the axially-averaged nature of the equation, this is tantamount to assuming that h_i is representative of both the area-averaged enthalpy $\{h_i\}$ and of the volume-averaged enthalpy $\langle h_i \rangle$ for SC i. Consistently, $\left\{W_{ij}^{*D} h_i\right\} - \left\{W_{ji}^{*D} h_j\right\} \sim W_{ij}^{*D} h_i - W_{ji}^{*D} h_j$. Moreover, for single phase flow, $W_{ij}^{*D} h_i - W_{ji}^{*D} h_j = W_{ij}^{*H} (h_j - h_i)$, where W_{ij}^{*H} is the effective mass flow rate per unit length for energy exchange between SCs i and j. By applying these simplifications, the steady state energy conservation equation becomes:

$$\frac{\Delta}{\Delta z} (\dot{m} h_i) = A_i \dot{q}_{eq,i} - \sum_{j=1}^{N_{nei,i}} W_{ij}^{*H} (h_j - h_i) - \sum_{j=1}^{N_{nei,i}} W_{ij} \left\{ h^* \right\} \tag{9.4}$$

In the IW region, the effective energy exchange between SCs i and j, $W_{ij}^{*H} (h_i - h_j)$, is in general associated to two contributions:

$$W_{ij}^{*H} (h_i - h_j) = q''_{ij} s_{ij} \Big|_{conduction} + q''_{ij} s_{ij} \Big|_{turbulence} \tag{9.5}$$

where q'' is a heat flux and s is the width of the gap between adjacent SCs. The *conduction* contribution can be expressed as follows:

$$q''_{ij}s_{ij}\Big|_{conduction} = \bar{\rho}_{ij}s_{ij}\kappa_{ij}\left(\frac{\bar{\alpha}_{ij}}{\eta_{ij}}\right)(h_i - h_j) \tag{9.6}$$

where α is the fluid thermal diffusivity, η is the centroid-to-centroid distance between the SCs, $\kappa = \frac{\eta}{l}$ is the *conduction shape factor*, i.e. the ratio between the centroid-to-centroid distance and the *effective mixing length* l. Quantities characterized by a bar ($\bar{}$) are averaged between SCs i and j. Note that, to simplify notation, here and thereafter the volume average nature of the physical quantities appearing in the equations is not explicitly stated (e.g. $\bar{\rho}_{ij} = (\langle\rho_i\rangle + \langle\rho_j\rangle)/2$ would simply be written as $(\rho_i + \rho_j)/2$). Details concerning the specific approximation adopted to evaluate the averaged quantities are provided in sections 9.6 and 9.7. The *turbulence* contribution can be characterized as follows:

$$q''_{ij}s_{ij}\Big|_{turbulence} = W^{T,H}_{ij}(h_i - h_j) \tag{9.7}$$

where $W^{T,H}$ is the effective mass exchange rate between adjacent SCs due to turbulent interchange. Cheng ([31]) proposed to correlate $W^{T,H}$ to the eddy diffusivity (ε) concept, thus writing:

$$W^{T,H}_{ij} = \bar{\rho}_{ij}s_{ij}\left(\frac{\varepsilon_{ij}}{\eta_{ij}}\right) \tag{9.8}$$

Correlations for κ_{ij} and ε_{ij} - or, alternatively, $W^{T,H}_{ij}$ - are presented in section 9.8.4.

The energy source term $\dot{q}_{eq,i}$ can be characterized as follows:

$$\dot{q}_{eq,i} = \dot{q}_i + \sum_{m=1}^{N_{w,i}} \frac{q''_{w,o,m}p_{h,m}}{A_i} \tag{9.9}$$

where the first term on the right-hand side, $\dot{q}_i$, is the heat deposited in the coolant per unit volume (e.g. due to gamma rays) and the second one represents the contribution of heat transfer with the wrapper. The summation runs over the number of wrapper walls in contact with the SC (N_w=2 for *edge SCs* and N_w=3 for *corner SCs*). $q''_{w,o,m}$ is the heat flux crossing the m-th wrapper outer surface (hence the subscript o) in contact with SC i. $p_{h,m}$ is the heated perimeter associated to the m-th wall in contact with SC i. Details concerning the calculation of $q''_{w,o,m}$ are provided in section 9.5.5.

Boundary conditions

The inlet temperature distribution is specified by the user. Care has been devoted to ensure that it is straightforward for the user to set a uniform inlet temperature

(see section 9.11), as this situation frequently occurs.

9.5.4 Conservation of momentum

Conservation of momentum describes the axial and radial evolution of the coolant momentum in each SC. The momentum variation for a given SC is due to gravity, friction with the portion of the wrapper wetted by the SC, localized pressure losses and net momentum exchange with neighboring SCs. The latter can be caused by either net mass exchange (with the consequent momentum transport) or by mixing effects (which do not imply a net mass exchange, see section 9.5.4). In the following, the formulation, simplifications and boundary conditions adopted for TIFONE will be described.

Formulation

Axial The axial momentum conservation can be stated as follows:

$$\begin{aligned}\Delta z \frac{\partial}{\partial t}\left\langle \dot{m}_i \right\rangle + \Delta\left[\dot{m}_i\left\{v_i\right\}\right] = & -A_i \Delta z \left\langle \rho_i \right\rangle g - A_i \Delta\{P\} \\ & - \Delta z \sum_{j=1}^{N_{nei}} \left[\left\{W_{ij}^{*D} v_i\right\} - \left\{W_{ji}^{*D} v_j\right\}\right] - \Delta z \sum_{j=1}^{N_{nei}} W_{ij}\left\{v^{\star}\right\} \\ & - \Delta z \frac{1}{2}\left\langle \rho_i \right\rangle v_i^2 A_i \frac{f_i}{D_{H,i}} - A_i \Delta P_{form,i}\end{aligned} \tag{9.10}$$

where W_{ij}^{*D} and W_{ji}^{*D} are turbulent interchange flow rates per unit length between SCs, v^* is an effective velocity transported by the cross flow (averaged over the contact area between SCs i and j), g is the gravitational acceleration, f is the friction factor with the walls, $D_H = 4A/p_w$ is the hydraulic diameter (where p_w is the wetted perimeter), ΔP_{form} is the form (localized) pressure loss per unit length.

Consistently with the assumptions adopted in section 9.5.3 for the energy conservation equation, for the sake of simplicity, it can be assumed that $\{\rho v v\} \sim v\{\rho v\}$, which, based on the the axially-averaged nature of equation (9.10), corresponds to assuming that v_i is representative of both the area-averaged axial velocity $\{v_i\}$ and of the volume-averaged axial velocity $\langle v_i \rangle$ for SC i. Consistently, $\left\{W_{ij}^{*D} v_i\right\} - \left\{W_{ji}^{*D} v_j\right\} \sim W_{ij}^{*D} v_i - W_{ji}^{*D} v_j$. Moreover, for single phase flow, $W_{ij}^{*D} v_i - W_{ji}^{*D} v_j = W_{ij}^{*M}\left(v_j - v_i\right)$, where W_{ij}^{*M} is the effective mass flow rate per unit length for momentum exchange between SCs i and j. By applying these simplifications, the steady state axial momentum conservation equation becomes:

$$\begin{aligned}\frac{\Delta\left(\dot{m}_i v_i\right)}{\Delta z} &= -A_i \left\langle \rho_i \right\rangle g - A_i \frac{\Delta\left\{P\right\}}{\Delta z} \\ &- \sum_{j=1}^{N_{nei}} W_{ij}^{*M}\left(v_i - v_j\right) - \sum_{j=1}^{N_{nei}} W_{ij}\left\{v^*\right\} \\ &- \frac{1}{2}\left\langle \rho_i \right\rangle v_i^2 A_i \frac{f_i}{D_{H,i}} - A_i \frac{\Delta P_{form,i}}{\Delta z}\end{aligned} \tag{9.11}$$

The effective momentum exchange term W_{ij}^{*M}, similarly to the W_{ij}^{*H} term encountered in equation (9.4), is composed by a molecular (diffusive) contribution and a turbulent contribution which is proportional to an equivalent mass flow rate for unit length. The molecular contribution to the axial momentum exchange between SCs is usually neglected [31]. The equivalent mass flow rate per unit length for turbulent contribution $W_{ij}^{T,M}$ is instead considered equal to its energy counterpart $W_{ij}^{T,H}$ and related to the eddy diffusivity concept. For simplicity, in the following it will be referred to simply as W_{ij}^{T}. Empirical correlations for this quantity will be discussed in section 9.8.4.

Radial The radial momentum conservation can be generally stated as follows:

$$\frac{\partial}{\partial t}\left\langle W_{ij} \right\rangle + \frac{\Delta}{\Delta x'}\left[W_{ij}\left\{u\right\}\right] + \frac{\Delta}{\Delta z}\left[W_{ij}\left\{v\right\}\right] = -\left[s_{ij}\frac{\Delta}{\Delta x}\left\{P_j\right\}\right] - \left\{\frac{F_{ix}}{\Delta x' \Delta z}\right\} \tag{9.12}$$

where u is the local transverse velocity, $\Delta x'$ indicates the transverse characteristic length and F_{ix} is a force acting on the fluid along the transverse direction due to interactions with the solid. This equation is typically treated by considering a different control volume with respect to the one adopted for the foregoing equations. The control volume boundaries for the radial momentum balance can e.g. coincide with the barycenters of the two neighboring SCs [196]. Solving this equation introduces significant complexity in the code structure. Moreover, the phenomena it describes - namely, cross flow driven by pressure differences between neighboring SCs - are only important in the case of flow area variations and/or flow obstructions, otherwise they can be regarded as second-order effects. For the problem at hand, and in compliance with the required simplicity of a DOC, these effects can be neglected. Therefore, this equation reduces to imposing an equal pressure drop among all the SCs for each axial step:

$$P_i = P_j \quad \forall i, j \tag{9.13}$$

Boundary conditions

As the radial momentum equation has been reduced to the equality of the pressures among SCs for each axial level, boundary conditions have to be imposed for the axial momentum balance equation only.

Axial The inlet pressure is assumed to be equal among all the SCs. The absolute value of the pressure is irrelevant - for incompressible flow, only the pressure differences are important - and therefore the inlet pressure can be arbitrarily specified by the user for all the SCs.

9.5.5 Heat transfer in the wrapper

Imposed heat flux at the wrapper outer surface

TIFONE evaluates the axial distribution of the outer wrapper temperature, with a required radial resolution at least sufficient to distinguish each of the six sides of the wrapper. Compliance with this requirement is ensured by the wrapper discretization approach described in section 9.4.2.

In section 9.3.5 it has been mentioned that the code must be able to receive as input the distribution of the heat flux flowing out (or in) the wrapper outer surface, $q''_{w,o}$. To ensure a suitable flexibility of the user input, the user is allowed to specify an arbitrary axial and radial resolution of $q''_{w,o}$, which is then interpolated to compute the heat source $q''_{w,o,m}$ appearing in equation (9.9). Once $q''_{w,o,m}$ is known, the outer wrapper temperature can be computed as:

$$T_{w,o,m} = T_{sc} + q''_{w,o,m}/\alpha_o \tag{9.14}$$

where T_{sc} is the mass flow averaged temperature of the IW coolant wetting wrapper surface m and α_o is the corresponding heat transfer coefficient. Correlations for the Nusselt number, allowing the evaluation of the heat transfer coefficient, are presented in section 9.8.3.

In view of the potential interest of the designer for knowledge of the wrapper *inner* temperature distribution, the following estimate is proposed:

$$T_{w,i,m} = T_{w,o,m} + \frac{q''_{w,o,m} k_w}{s_w} \tag{9.15}$$

where k_w is the wrapper thermal conductivity and s_w is the wrapper thickness. This formulation neglects heat deposition in the wrapper, and is therefore to be regarded as a first approximation.

Imposed heat flux at the wrapper inner surface

In case the distribution of the heat flux crossing the wrapper inner surface, $q''_{w,i,k}$ is known, then $q''_{w,o,k}$ is calculated as follows:

$$q''_{w,o,k} = q''_{w,i,k} + \dot{q}_{w,eq,k}\delta_w \tag{9.16}$$

where $\dot{q}_{w,eq,k}$ is the equivalent power deposited in the wrapper per unit volume in the k-th wrapper node and δ_w is the wrapper thickness. $\dot{q}_{w,eq,k}$ is composed by two contributions:

$$\dot{q}_{w,eq,k} = \dot{q}_{w,k} + \sum_{j=1}^{N_{nei,k}} \left(\bar{T}_{w,j} - \bar{T}_{w,k}\right) \frac{k_{w,k}}{\eta_{kj} l_k} \tag{9.17}$$

where $\dot{q}_{w,k}$ is the actual power per unit volume deposited in the wrapper by gamma rays and the summation, running over the $N_{nei,k}$ neighboring wrapper nodes to k, represents the contribution of heat conduction in the wrapper. $\bar{T}$ is the temperature of a wrapper node, averaged over the wrapper thickness. $k_{w,k}$ is the thermal conductivity of the wrapper node k, η_{kj} is the inter-nodal distance between k and j and l_k is the radial extension of node k. To avoid introducing unnecessary complexity, the following approximation is introduced for the average temperatures:

$$\bar{T}_{w,j} - \bar{T}_{w,k} \sim T_{w,o,j} - T_{w,o,k} \tag{9.18}$$

where $T_{w,o}$ is the wrapper temperatures at the outer face.

Coupling with codes computing the SA thermal-hydraulics

Although not relevant for the first version of TIFONE, in view of the future perspective of coupling it with an SA TH code (e.g. ANTEO+) to obtain a full-core thermal-hydraulic solution, two other possible inputs in terms of heat flux are here mentioned: In case TIFONE should be coupled with a code providing the coolant temperature (e.g. ANTEO+), two additional equations must be added to the system [88]:

$$\alpha_i \left(T_{sc} - T_{w,i}\right) = -\dot{q}_{w,eq,k}\frac{\delta_w}{2} - \frac{k_w}{\delta_w}\left(T_{w,o} - T_{w,i}\right) \tag{9.19}$$

$$\alpha_o \left(T_{w,o} - T_{bp}\right) = \dot{q}_{w,eq,k}\frac{\delta_w}{2} - \frac{k_w}{\delta_w}\left(T_{w,o} - T_{w,i}\right) \tag{9.20}$$

where T_{sc} is the temperature of the neighboring SC to the wrapper inside the SA, $T_{w,i}$ and $T_{w,o}$ are the wrapper temperatures at the inner and outer face, respectively. α_i and α_o are the corresponding heat transfer coefficients. In this case, the wrapper and coolant temperatures must be determined self-consistently, knowing the coolant temperature and heat transfer coefficient at the inner side of the wrapper and the

heat deposition in the wrapper itself. Equations (9.19) and (9.20) need therefore to be included in the linear system.

9.6 Forced Convection Solution

The forced convection approximation consists in neglecting not only the pressure-driven cross-flow (as already indicated in section 9.5.4) but also the buoyancy-driven cross-flow. In this section, the simplifications of the governing equations and the solution strategy are described.

9.6.1 Treatment of the governing equations

According to the forced convection assumption, the radial velocity distribution is considered constant along the axial coordinate. For this reason, energy and momentum equations are decoupled - apart from the temperature dependence of the coolant thermophysical properties.

Conservation of mass

The mass conservation equation for SC i reduces in this case to:

$$\dot{m}_i = const \tag{9.21}$$

The actual value of $\dot{m}_i$ for each SC, i.e. the radial subdivision of the inlet mass flow rate among the SCs, is determined by means of a flow split model (see section 9.6.1).

Conservation of energy

The term $\sum_{j=1}^{N_{nei}} W_{ij} \{h^*\}$ in equation (9.4) is neglected according to the forced convection assumption. The resulting equation to be solved is:

$$\dot{m}_i \frac{\Delta h_i}{\Delta z} = A_i \dot{q}_{eq,i} - \sum_{j=1}^{N_{nei}} \bar{\rho}_{ij} s_{ij} \left[\kappa_{ij} \left(\frac{\bar{\alpha}_{ij}}{\eta_{ij}} \right) + \left(\frac{\varepsilon_{ij}}{\eta_{ij}} \right) \right] (h_j - h_i) \tag{9.22}$$

Conservation of momentum

Axial The term $\sum_{j=1}^{N_{nei}} W_{ij} \{v^*\}$ in equation (9.11) is neglected according to the forced convection assumption. The resulting equation to be solved is:

$$\begin{aligned} A_i \frac{\Delta P_i}{\Delta z} = & -A_i \rho_i g - \dot{m}^2 \frac{\Delta}{\Delta z} \left(\frac{1}{\rho_i A_i} \right) - A_i \frac{f_i}{D_{e,i}} \frac{\rho_i v_i^2}{2} \\ & - \sum_{j=1}^{N_{nei}} s_{ij} \left[\left(\frac{\varepsilon_{ij}}{\eta_{ij}} \right) \right] (v_j - v_i) - A_i \frac{\Delta P_{form,i}}{\Delta z} \end{aligned} \tag{9.23}$$

Radial - flow split model Due to the simplified treatment of the radial momentum conservation equation adopted for TIFONE, a way of specifying how the inlet flow rate in the IW region distributes among the SCs is required. To this purpose, a flow split model is employed.

According to equation (9.13), the pressure drop among all the SCs is assumed to be equal. By equating the expressions for the pressure drop associated to each SC, a set of nonlinear equations is obtained having as unknowns the flow fractions for each SC i, X_i [113]. Starting from the difference form of equation (9.13):

$$\Delta P_i = \Delta P_j \quad \forall i, j \tag{9.24}$$

For incompressible flow in parallel hydraulic channels of constant cross sections, ΔP is due to head losses (both localized and distributed) and to the hydro-static pressure. The latter being equal for all SCs, the equation can be written as:

$$v_i^2 \frac{f_i}{D_{H,i}} L + \xi_i v_i^2 = v_j^2 \frac{f_j}{D_{H,j}} L + \xi_j v_j^2 \tag{9.25}$$

where L is the total axial length of the domain and the form pressure loss term has been expressed as $\Delta P_{form} = \frac{1}{2}\rho \xi_i v_i^2$, where ξ is the sum of the localized pressure loss coefficients for SC i. The term $\frac{1}{2}\rho$ has been simplified in equation (9.25).

f, D_H and ξ are shared by SCs of the same type (i.e. having the same shape - *corner* or *side* - and the same cross section). It is therefore convenient to classify SCs among N_{cat} categories before proceeding to the solution of the flow split system, thus eliminating redundant equations. In the following, i and j will therefore indicate different SC categories.

It is customary to introduce a flow split parameter $X = \frac{v}{v_{ave}}$ where v_{ave} is the velocity averaged over all the SCs in the domain. Equation (9.25) can thus be written as:

$$\frac{X_i}{X_j} = \sqrt{\frac{f_j \frac{L}{D_{H,j}} + \xi_j}{f_i \frac{L}{D_{H,i}} + \xi_i}} \quad \forall i, j \tag{9.26}$$

These $N_{cat} - 1$ equations must be closed by relying on the continuity equation:

$$\sum_{i=1}^{N_{cat}} \frac{N_i A_i}{A_{tot}} X_i = 1 \tag{9.27}$$

The resulting nonlinear system of equations has the following form:

$$\begin{bmatrix} 1 & -K_{21} & 0 & \dots & 0 & 0 \\ 0 & 1 & -K_{32} & & 0 & 0 \\ \vdots & & & \ddots & & \vdots \\ 0 & 0 & 0 & & 1 & -K_{N_{cat}\,N_{cat}-1} \\ \frac{N_1 A_1}{A_{tot}} & \frac{N_2 A_2}{A_{tot}} & \frac{N_3 A_3}{A_{tot}} & \dots & \frac{N_{N_{cat}-1} A_{N_{cat}-1}}{A_{tot}} & \frac{N_{N_{cat}} A_{N_{cat}}}{A_{tot}} \end{bmatrix} \begin{bmatrix} X_1 \\ X_2 \\ \vdots \\ X_{N_{cat}-1} \\ X_{N_{cat}} \end{bmatrix} = \begin{bmatrix} 0 \\ 0 \\ \vdots \\ 0 \\ 1 \end{bmatrix} \tag{9.28}$$

where $K_{ji} = \sqrt{\frac{f_j \frac{L}{D_{H,j}} + \xi_j}{f_i \frac{L}{D_{H,i}} + \xi_i}}$. The solution of the linear system at each iteration is achieved via the traditional Gauss Elimination Method (e.g. via the implementation provided in the DGETRF and DGETRS routines included in the BLAS/LAPACK libraries [15]).

Heat transfer in the wrapper

The wrapper temperature calculation is in this case straightforward (i.e. it can be computed after having solved the problem for the coolant) and can be performed by simply evaluating equation (9.14) for each wrapper node m.

9.6.2 Solution strategy

Conservation of energy

Equation (9.22) can be solved by means of a forward approximation, processing subsequent axial levels k. In the following, equations are written for SC i at a given axial level k. Subscripts z and $z + \Delta z$ indicate quantities evaluated at the inlet and at the outlet of axial node k. By approximating SC-averaged enthalpies as $h_i \sim h_{i,z+\Delta z/2} \sim h_{i,z} + \frac{\Delta h_i}{2}$, equation (9.22) can be written having as unknowns the enthalpy increments Δh:

$$\Delta h_i = \frac{\Delta z}{\dot{m}_i} \cdot \left\{ A_i \dot{q}_{eq,i} - \sum_{j=1}^{N_{nei}} \bar{\rho}_{ij} s_{ij} \left[\kappa_{ij} \left(\frac{\bar{\alpha}_{ij}}{\eta_{ij}} \right) + \left(\frac{\varepsilon_{ij}}{\eta_{ij}} \right) \right] \cdot \left(h_{j,z} + \frac{\Delta h_j}{2} - h_{i,z} - \frac{\Delta h_i}{2} \right) \right\} \tag{9.29}$$

This equation can be easily cast in matrix form, where each row corresponds to the energy conservation equation written for a SC:

$$\begin{aligned}\boldsymbol{\Delta h_i}\left[1-\frac{\Delta z}{2\dot{m}_i}\sum_{j=1}^{N_{nei}}M_{ij}\right]+\frac{\Delta z}{2\dot{m}_i}\sum_{j=1}^{N_{nei}}\left(M_{ij}\boldsymbol{\Delta h_j}\right)\\ =\frac{\Delta z}{\dot{m}_i}A_i\dot{q}_{eq,i}-\frac{\Delta z}{\dot{m}_i}\sum_{j=1}^{N_{nei}}M_{ij}\left(h_{j,z}-h_{i,z}\right)\end{aligned} \tag{9.30}$$

where

$$M_{ij}=\bar{\rho}_{ij}s_{ij}\left[\kappa_{ij}\left(\frac{\bar{\alpha}_{ij}}{\eta_{ij}}\right)+\left(\frac{\varepsilon_{ij}}{\eta_{ij}}\right)\right] \tag{9.31}$$

In equation (9.30), the unknowns are indicated in bold. Each row of the solution matrix can have up to three nonzero off-diagonal terms (in case of *corner SCs*, which have three neighbors). The thermophysical properties required to evaluate the term M_{ij} are evaluated at node $k-1$.

The solution of the linear system is achieved via the traditional Gauss Elimination Method (e.g. via the implementation provided in the `DGETRF` and `DGETRS` routines included in the BLAS/LAPACK libraries). It should be noticed that exploiting already existing numerical libraries reduces the time for code development, maintenance and V&V, in that it allows to focus on the high-level code development, to access optimized solutions. Also, this improves code portability.

Conservation of momentum

Consistently with the assumptions adopted in the derivation of the flow split model, the acceleration pressure drop and the inter-SC friction terms are neglected in forced convection conditions. The resulting axial momentum conservation equation to be solved to obtain the axial pressure drop for SC i corresponding to axial level k can then be written as:

$$\Delta P_{i,k}=-\Delta z\rho_i g-\Delta z\frac{f_i}{D_{e,i}}\frac{\rho_i v_i^2}{2}-\Delta P_{form,i} \tag{9.32}$$

Thanks to the approximations introduced for the transverse momentum equation, it is sufficient to evaluate the pressure drop for a single SC ($\Delta P_k \sim \Delta P_{i,k}$). Thermophysical properties appearing in this expression are evaluated at the radially averaged temperature for axial level k.

9.7 Mixed convection solution

9.7.1 Treatment of governing equations

A convenient solution method for SC equations in mixed convection regime has been proposed by Chen [31]. The equations are first re-written so that the unknowns are the density and velocity variations for each SC, as well as the axial pressure drop (which is the same among each SC, due to the simplification of the transverse momentum equation). To achieve this result, the increments of the quantities appearing in the equations of a generic control volume i located between the axial locations z and $z + \Delta z$ are expressed as follows:

$$\begin{aligned}
&\Delta \dot{m}_i = (\rho_i v_i A_i)_{z+\Delta z} - (\rho_i v_i A_i)_z \\
&\Delta \left(\dot{m}_i h_i\right) = (\rho_i v_i A_i h_i)_{z+\Delta z} - (\rho_i v_i A_i h_i)_z \\
&\Delta \left(\dot{m}_i v_i\right) = \left(\rho_i v_i^2 A_i\right)_{z+\Delta z} - \left(\rho_i v_i^2 A_i\right)_z \\
&A_i \Delta \left\{P_i\right\} = A_i \Delta P \\
&\rho_{z+\Delta z} = \rho_z + \Delta\rho \\
&h_{z+\Delta z} = h_z + \Delta h \\
&v_{z+\Delta z} = v_z + \Delta v
\end{aligned} \tag{9.33}$$

Moreover, the enthalpy is eliminated in favor of the density, taking advantage of the relation $\Delta h \sim R\Delta\rho$ where $R = \left(\frac{\partial h}{\partial \rho}\right)$.

The form of the equations obtained by adopting these approximations and re-arranging terms is discussed in the following sections.

Conservation of mass

The mass conservation equation is not solved directly for each SC. The total mass balance is instead enforced at each axial level to close the system of equations:

$$\sum_{i=1}^{N_{subc}} \Delta \dot{m}_i = 0 \tag{9.34}$$

which can be conveniently written as [31]:

$$\sum_{i=1}^{N_{subc}} A_i \left(v_{i,z} + \Delta v_i\right) \Delta\rho_i + \sum_{i=1}^{N_{subc}} A_i \rho_{i,z} \Delta v_i = 0 \tag{9.35}$$

A more compact notation is the following:

$$\sum_{j=1}^{N_{subc}} \left(C_{\rho i} \Delta\rho_i + C_{vi} \Delta v_i\right) = 0 \tag{9.36}$$

where:

$$C_{\rho i} = A_i(v_{i,z} + \Delta v_i) \tag{9.37}$$

$$C_{vi} = A_i \rho_{i,z} \tag{9.38}$$

Conservation of energy

First, the term $\sum_{j=1}^{N_{nei}} W_{ij} \{h^*\}$ is approximated as $H_i^* \sum_{j=1}^{N_{nei}} W_{ij}$, where the auxiliary quantity H_i^* is formally defined as:

$$H_i^* = \frac{\sum_{j=1}^{N_{nei}} \left[|x_{ij}| \left(h_i + h_j\right) - x_{ij} \left(h_i - h_j\right)\right]}{2 \sum_{j=1}^{N_{nei}} |x_{ij}|} \tag{9.39}$$

where $x_{ij} = \Delta \dot{m}_i - \Delta \dot{m}_j$, thus representing an indicator of the net mass exchange between SCs i and j occurring in the axial interval Δz. However, it has been observed that using this expression for H_i^* could hinder the code convergence [113]. For this reason, the user is allowed to select via the input file whether to use the simpler approximation $H_i^* \sim h_i$. Guidelines for the selection of the approximation are determined during the code verification phase and eventually included in the user manual.

The resulting equation to be solved for each SC i is:

$$\frac{\Delta}{\Delta z} \left(\dot{m} h_i\right) = A_i \dot{q}_{eq,i} - \sum_{j=1}^{N_{nei}} \bar{\rho}_{ij} s_{ij} \left[\kappa_{ij} \left(\frac{\bar{\alpha}_{ij}}{\eta_{ij}}\right) + \left(\frac{\varepsilon_{ij}}{\eta_{ij}}\right)\right] \left(h_i - h_j\right) - H_i^* \sum_{j=1}^{N_{nei}} W_{ij} \tag{9.40}$$

By enforcing the continuity equation to be satisfied, $\frac{\Delta \dot{m}_i}{\Delta z} = -\sum_{j=1}^{N_{nei}} W_{ij}$, and by recalling the definition of the mass flow rate axial variation along an interval Δz provided in equation (9.33), the energy equation can be re-written as:

$$\begin{aligned} \left(\rho_i v_i A_i h_i\right)_{z+\Delta z} - \left(\rho_i v_i A_i h_i\right)_z = {} & A_i \Delta z \dot{q}_{eq,i} \\ & - \Delta z \sum_{j=1}^{N_{nei}} \bar{\rho}_{ij} s_{ij} \left[\kappa_{ij} \left(\frac{\bar{\alpha}_{ij}}{\eta_{ij}}\right) + \left(\frac{\varepsilon_{ij}}{\eta_{ij}}\right)\right] \left(h_i - h_j\right) \\ & + H_i^* \left[\left(\rho_i v_i A_i\right)_{z+\Delta z} - \left(\rho_i v_i A_i\right)_z\right] \end{aligned} \tag{9.41}$$

Rearranging again the terms, and denoting as above the axial variation of a quantity ψ between z and $z + \Delta z$ as $\Delta \psi = \psi_{z+\Delta z} - \psi_z$, the energy equation for subchannel i can be written as:

$$S_i \Delta \rho_i + B_i \Delta v_i = Q_i \Delta z + EEX_i \tag{9.42}$$

where:

$$S_i = (v_{i,z} + \Delta v_i)\left[-H_i^* + h_{i,z} + R\left(\rho_{i,z} + \Delta\rho_i\right)\right] \tag{9.43}$$

$$B_i = \rho_{i,z}\left(h_{i,z} - H_i^*\right) \tag{9.44}$$

$$EEX_i = -\frac{\Delta z}{A_i}\sum_{j=1}^{N_{nei}} \bar{\rho}_{ij} s_{ij}\left[\kappa_{ij}\left(\frac{\bar{\alpha}_{ij}}{\eta_{ij}}\right) + \left(\frac{\varepsilon_{ij}}{\eta_{ij}}\right)\right](h_i - h_j) \tag{9.45}$$

Conservation of momentum

Axial The first step towards the solution is again represented by a rearrangement of the terms. First, the term $\sum_{j=1}^{N_{nei}} W_{ij}\{v^*\}$ is approximated as $V_i^* \sum_{j=1}^{N_{nei}} W_{ij}$, where the auxiliary quantity V_i^* is defined by an expression analogous to equation (9.39):

$$V_i^* = \frac{\sum_{j=1}^{N_{nei}}\left[|x_{ij}|\left(v_i + v_j\right) - x_{ij}\left(v_i + v_j\right)\right]}{2\sum_{j=1}^{N_{nei}}|x_{ij}|} \tag{9.46}$$

This expression for V_i^* could determine convergence issues which are similar in nature to those already pointed out for H_i^*. For this reason, the user is allowed to select via the input file whether to use the simpler approximation $V_i^* \sim v_i$. Guidelines for the selection of the approximation are determined during the code verification phase and eventually included in the user manual. The resulting equation to be solved is:

$$\begin{aligned}\frac{\Delta}{\Delta z}\left[\dot{m}\{v_i\}\right] = &-A_i\rho_i g - A_i\frac{\Delta P}{\Delta z} - A_i\frac{f_i}{D_{e,i}}\frac{\rho_i v_i^2}{2} \\ &- \sum_{j=1}^{N_{nei}} s_{ij}\left[\left(\frac{\varepsilon_{ij}}{\eta_{ij}}\right)\right](v_i - v_j) - V_i^*\sum_{j=1}^{N_{nei}} W_{ij}\end{aligned} \tag{9.47}$$

As it has been done in section 9.7.1, by enforcing the continuity equation to be satisfied and by explicitly writing the term $\Delta\dot{m}_i$, the equation can be written as:

$$\begin{aligned}\left(\rho_i A_i v_i^2\right)_{z+\Delta z} - \left(\rho_i A_i v_i^2\right)_z = &-A_i\Delta z\rho_i g - A_i\Delta P - A_i\Delta z\frac{f_i}{D_{e,i}}\frac{\rho_i v_i^2}{2} \\ &- \Delta z\sum_{j=1}^{N_{nei}} \bar{\rho}_{ij} s_{ij}\left[\left(\frac{\varepsilon_{ij}}{\eta_{ij}}\right)\right](v_i - v_j) \\ &+ V_i^*\left[\left(\rho_i v_i A_i\right)_{z+\Delta z} - \left(\rho_i v_i A_i\right)_z\right]\end{aligned} \tag{9.48}$$

Rearranging the terms, the momentum equation for SC i can be written as:

$$E_i \Delta\rho_i + F_i \Delta v_i + \Delta P = G_i + MEX_i \tag{9.49}$$

where:

$$E_i = (v_{i,z} + \Delta v_i)\,(v_{i,z} + \Delta v_i - V_i^*) + \frac{f_i \Delta z}{16 D_{e,i}}\,(2v_{i,z} + \Delta v_i)^2 + \frac{g \Delta z}{2} \tag{9.50}$$

$$F_i = \rho_{i,z} \left[\left(2 + \frac{f_i \Delta z}{2 D_{e,i}} \right) v_{i,z} + \left(1 + \frac{f_i \Delta z}{8 D_{e,i}} \right) \Delta v_i - V_i^* \right] \tag{9.51}$$

$$G_i = -\rho_{i,z} \left(g \Delta z + \frac{f_i \Delta z}{2 D_{e,i}} v_{i,z}^2 \right) \tag{9.52}$$

$$MEX_i = -\frac{\Delta z}{A_i} \sum_{j=1}^{N_{nei}} \bar{\rho}_{ij} s_{ij} \left(\frac{\varepsilon_{ij}}{\eta_{ij}} \right) (v_i - v_j) \tag{9.53}$$

Radial - flow split model The flow split model to be used for the mixed convection solution is identical to the one adopted for the forced convection solution, described in section 9.6.1.

Heat transfer in the wrapper

The wrapper temperature calculation for the mixed convection solution is identical to the one adopted for the forced convection solution. It can be performed after having solved the problem for the coolant by simply evaluating equation (9.14) for each wrapper node m.

9.7.2 Solution strategy

Forced convection initialization

As mentioned in section 9.3.6, TIFONE first solves the forced convection problem. This allows to verify whether the criterion for forced convection (reported in section 9.8.5) is met. In case a mixed convection solution is required, the previously computed forced convection solution is employed to initialize the calculation.

Matrix form of the system

The solution process involves treating one "slice", i.e. one axial level, at a time. For each axial level k, the system of equations (9.36), (9.42) and (9.49) is solved to find the increment $\Delta\rho_i$ and Δv_i for each SC, as well as the pressure drop ΔP,

which has been assumed to be equal for all the SCs. The matrix form of the system of equations is the following:

$$\begin{bmatrix} S_1 & B_1 & 0 & 0 & \dots & 0 & 0 & 0 \\ E_1 & F_1 & 0 & 0 & & 0 & 0 & 1 \\ 0 & 0 & S_2 & B_2 & & 0 & 0 & 0 \\ 0 & 0 & E_2 & F_2 & & 0 & 0 & 1 \\ \vdots & & & & \ddots & & & \vdots \\ 0 & 0 & 0 & 0 & & S_{N_{subc}} & B_{N_{subc}} & 0 \\ 0 & 0 & 0 & 0 & & E_{N_{subc}} & F_{N_{subc}} & 1 \\ C_{\rho 1} & C_{v1} & C_{\rho 2} & C_{v2} & \dots & C_{\rho N_{subc}} & C_{vN_{subc}} & 0 \end{bmatrix} \begin{bmatrix} \Delta\rho_1 \\ \Delta v_1 \\ \Delta\rho_2 \\ \Delta v_2 \\ \vdots \\ \Delta\rho_{N_{subc}} \\ \Delta v_{N_{subc}} \\ \Delta P \end{bmatrix} = \begin{bmatrix} Q_1\Delta z + EEX_1 \\ G_1 + MEX_1 \\ Q_2\Delta z + EEX_2 \\ G_2 + MEX_2 \\ \vdots \\ Q_{N_{subc}}\Delta z + EEX_{N_{subc}} \\ G_{N_{subc}} + MEX_{N_{subc}} \\ 0 \end{bmatrix} \tag{9.54}$$

The solution of system (9.54) is necessarily iterative due to its nonlinear nature. For each axial node k, the forced convection solution for $\Delta\rho_i$, Δv_i and ΔP is used as a starting guess for the iterative process, thus allowing to estimate ρ and v at the end of the node, thereby allowing to compute the matrix coefficients. The linear system is then solved to update the guess for $\Delta\rho_i$, Δv_i and ΔP. The solution is achieved via either the Gauss Elimination Method (as for the forced convection system, see section 9.6.2) or the Greene method suggested in [31]. The procedure is repeated up to convergence. The convergence check is posed on $\Delta\rho_i$, Δv_i and ΔP, as well as on the total mass conservation.

Once the solution for node k is available, the values of the unknowns at the beginning of node $k+1$ are computed and the procedure is repeated until all the axial nodes have been processed.

Coolant and wrapper temperature calculation

As already mentioned, a consequence of the solution method adopted is the fact that the enthalpy increase Δh does not appear explicitly among the unknowns of the system of equations. Therefore, after having solved the system, Δh is determined from the density variation according to the relation $\Delta h \sim R\Delta\rho$, where $R = \left(\frac{\partial h}{\partial \rho}\right)$.

This eventually allows to determine the temperature T_{sc} for each SC at the axial node between z and $z + \Delta z$ as $T_{sc} = T_{sc,z} + \frac{\Delta h}{2c_p}$.

Once the coolant temperature is known, as already mentioned, the wrapper temperature is simply computed according to equation (9.14) for each wrapper node.

9.8 Constitutive relations

Constitutive equations required by TIFONE include:

- localized pressure loss coefficients;
- correlations for the friction factor;
- correlations for the Nusselt number;
- correlations to characterize the internodal mixing;
- empirical criterion to determine whether a mixed convection solution is required.

9.8.1 Localized pressure loss coefficient

Due to the assumption concerning the geometry of the channel, the only localized pressure losses are associated to the inlet and outlet sections (see Figure 9.1). The associated pressure loss coefficients - falling outside the scope of TIFONE - are therefore specified by the user, so that the input file and associated reader can include means to provide such information.

9.8.2 Friction factor

As far as pressure losses are concerned, the behavior of liquid metals is similar to that of more common fluids (such as, e.g., water) [141]. Correlations for circular ducts are adapted to the duct geometry relevant for the present work by means of the hydraulic diameter concept: $D_h = 4A_c/p_w$, where p_w is the wetted perimeter of the SC, and by a corrective factor which accounts for the different shape of the SC.

Blasius

Blasius [16] has proposed a simple correlation for the friction factor in a smooth circular tube:

$$f = \frac{0.316}{Re_{D_h}^{0.25}} \tag{9.55}$$

where $Re_{D_h} = (\rho v D_h)/\mu$ is the Reynolds number computed using the hydraulic diameter as the characteristic length. This correlation is applicable in turbulent regime up to $Re < 10^5$. No general accuracy is specified inside the validity range.

Since this correlation has been derived for a circular tube, the correction factor $k_{\mathrm{non-c}}$ discussed in section 9.8.2 is applied to finally obtain the distributed pressure drops.

Colebrook

Colebrook [33] has proposed an empirical fit of the pipe flow pressure drop data which is valid for turbulent flow, $Re < 10^8$:

$$\frac{1}{\sqrt{f}} = -2.0 \log \left(\frac{\varepsilon / D_h}{3.7} + \frac{2.51}{Re_{D_h} \sqrt{f}} \right) \tag{9.56}$$

An accuracy of $\sim 15\%$ can be expected from using this formula for a noncircular duct applying the hydraulic diameter concept.

Again, since this correlation has been derived for a circular tube, the correction factor $k_{\mathrm{non-c}}$ discussed in section 9.8.2 is applied to finally obtain the distributed pressure drops.

Haaland

Haaland [81] has proposed a formula approximating the Colebrook/Moody chart which explicitly correlates f to Re, D_h and ε, the latter representing the surface roughness:

$$\frac{1}{\sqrt{f}} = -1.8 \log \left(\left(\frac{\varepsilon / D_h}{3.7} \right)^{1.11} + \frac{6.9}{Re} \right) \tag{9.57}$$

Again, since this correlation has been derived for a circular tube, the correction factor $k_{\mathrm{non-c}}$ discussed in section 9.8.2 is applied to finally obtain the distributed pressure drops.

Corrective factor for non-circular geometries

To any of the above correlations that is selected to represent a reference circular duct, a corrective factor is to be introduced to account for the actual, non-circular shape of the considered SCs. For this, according to the Idelchik handbook [87], depending on the case-specific dimensions, a corrective factor $k_{\mathrm{non-c}}$ can be introduced to finally obtain the distributed pressure drops.

For laminar flow ($Re < 2000$) in rectangular channels the correction factor lies in the range $0.89 < k_{\mathrm{non-c,lam}} < 1.5$, with the specific value depending on the aspect ratio of the channel. The limit for a plane slot ($a/b \to 0$), which is the relevant geometry for *edge SCs*, is $k_{\mathrm{non-c,lam,edge}} = 1.5$.

For turbulent flow ($Re > 2000$) in rectangular channels the correction factor lies in the range $1.0 < k_{\mathrm{non-c,turb}} < 1.1$, with the specific value depending again on the aspect ratio of the channel. The limit for a plane slot ($a/b \to 0$), is $k_{\mathrm{non-c,turb,edge}} = 1.1$.

Liang

A numerical and experimental study has recently been performed by Liang et al. [110]. An experimental setup consisting of three converging gaps and using deionized water as a working fluid has been employed to validate a numerical model both in laminar and in turbulent conditions. The validated numerical model has then been adopted to extrapolate the friction factor correlations to other values of the channel aspect ratio β.

The recommended correlation for the friction factor in the IW region in laminar flow regime ($Re < 2500$) is the following:

$$f \cdot Re = C_l \tag{9.58}$$

where:

$$C_l = 96\left(1 + 0.2149\beta + 0.01572\beta^2 - 0.0256\beta^3 + 0.02413\beta^4 - 0.008649\beta^5\right) \tag{9.59}$$

The authors of this study recommended that the correlation proposed by Sadatomi is used for the turbulent flow regime ($Re > 3200$) [173] :

$$f = \frac{C_t}{Re^{0.25}} \tag{9.60}$$

where C_t is a geometry factor for turbulent flow, which is computed as:

$$\frac{C_t}{C_{t,0}} = \sqrt[3]{0.0154\frac{C_l}{C_{l,0}} - 0.012} + 0.85 \tag{9.61}$$

where C_t,$0 = 0.3164$ and $C_{l,0} = 64$ are the constants for circular pipe in laminar and turbulent regime, respectively, and C_l can be computed by means of equations (9.58) and (9.59).

9.8.3 Nusselt number

To what concerns correlations for the Nusselt number, the literature review performed in the latest edition of the NEA liquid metal handbook ([141]) is here followed.

Kays

The correlation by Kays [101] is the only one available for nonuniform heating at the two sides of a rectangular channel:

$$Nu\Big|_{q_w=constant} = \frac{Nu_0}{1 - \gamma\varphi} \tag{9.62}$$

where γ is a tabulated correction factor and φ is the heat flux ratio between the two sides of the duct. Values for Nu_0, γ and φ as a function of Re and Pr are provided in Table 1 of [101]. No information is provided concerning the expected accuracy within its validity range, $10^4 < Re < 10^6$ and $0 < Pr < 1000$.

Duchatelle

The correlation provided by Duchatelle [45] has been developed for the specific case of a duct with one heated side and one adiabatic side. This physical situation is anticipated to occur only for peripheral SCs.

$$Nu = 5.85 + 0.00341 Pe^{1.29} \tag{9.63}$$

The correlation is claimed to be valid for $0 \leq Pr \leq 0.04$ and $10^4 \leq Re \leq 10^5$. No information is provided concerning the expected accuracy within its validity range.

Dwyer

The correlation proposed by Dwyer [47], similarly to the one proposed by Duchatelle, has been developed for the specific case of a duct with one heated side and one adiabatic side.

$$Nu = 5.60 + 0.01905 Pe^{0.775} \tag{9.64}$$

The correlation is claimed to be valid for $0 \leq Pr \leq 0.04$ and $10^4 \leq Re \leq 10^5$. No information is provided concerning the expected accuracy within its validity range.

Sleicher/Rouse

In [100], it has been shown that the correlation proposed by Sleicher and Rouse ([186]) agrees well with Direct Numerical Simulation (DNS) results for the case of uniform heating. The proposed correlation is the following:

$$Nu = 6.3 + 0.0167 Re^{0.85} Pr^{0.93} \tag{9.65}$$

which is claimed to be valid for $0.004 < Pr < 0.1$ and $10^4 < Re < 10^6$. No information is provided concerning the expected accuracy within its validity range.

9.8.4 Internodal mixing

No correlations for the empirical parameters describing the inter-SC mixing have been found in the literature for the specific geometry here considered. However, in view of the possibility that correlations might become available (thanks to e.g.

reduction of new experimental data or Direct Numerical Simulations), the code foresees the possibility to implement them in a straightforward way. Due to this limitation, simplifying assumptions are proposed to be adopted in the first version of TIFONE, which are now discussed.

Conduction shape factor

The conduction shape factor κ appearing in the term EEX (equation (9.45)) is taken equal to 1 for each couple of SCs, due to the lack of better information. Due to the simple geometry, this is believed to represent a reasonable approximation for the energy exchange between *edge SCs*. This assumption might instead be questionable for the energy exchange between *edge SCs* and *corner SCs*. The effect of this assumption will be investigated during the validation phase.

Eddy diffusivity

No correlation for the eddy diffusivity ε_{ij} has been found for in the literature for the particular SC geometry relevant for TIFONE. Therefore, the eddy diffusivity is put to zero (0) (i.e. the internodal energy exchange is assumed to be purely conductive). This approach was adopted also in [12] for the IW region.

9.8.5 Criterion for mixed convection

After the first forced convection solution is available, TIFONE decides whether a mixed convection solution is required. This is done according to available empirical models.

Jackson

Jackson [90] proposed a criterion for the onset of buoyancy effects for the case of sodium flowing inside a vertical pipe:

$$\frac{Gr}{Re^2} > 0.002 \tag{9.66}$$

9.9 Generation of connection logic

The connection logic is generated at the beginning of the code execution. Connection logic involves SCs numbering, identification of neighboring SCs and wrapper nodes and generation of connectivity matrices. The latter are then employed to compute the exchange terms between neighboring SCs and to collocate them in the matrix formulation of the problem, equation (9.54).

The connectivity matrices can be logically subdivided into three categories:

- SA-based maps, containing the connections between SAs, between SAs and gaps, between SAs and corners and between SAs and SCs.
- gap-based maps, containing the connections of each gap to the neighboring SAs and to the neighboring corners, as well as to the *edge SCs* located along the gap.
- corner-based maps, containing the connections of each corner to the neighboring SAs and to the neighboring gaps, as well as to the corresponding *corner SCs*.
- SC-based maps, containing the connection of each SC which the gap or corner where it is located, as well as with the number and indexes of the neighboring SCs and wrapper nodes.

9.9.1 SA numbering

The criterion adopted for the enumeration of the SAs in the xy plane is shown in figure 9.7. The origin is placed at the central SA, which is associated to the 0 index. The numbering proceeds by sextant, each time continuing from the final number of the previous sextant. Within the sextant, each SA row is filled from the center of the lattice to the boundary. Once the boundary is reached, the numbering continues on the next row, parallel to the one that has just been completely filled and neighboring counter-clockwise. At the end of each sextant, the next one (moving counter-clockwise) is addressed.

The adopted numbering criterion is based on sextants and is suitable for an LFR core - which represents the application domain for TIFONE. However, recent experimental studies carried out at the KALLA facility [199], which yielded invaluable data for the code validation phase, have been carried out using only three SAs, see Figure 9.8 (left). TIFONE must therefore be sufficiently flexible to simulate also this configuration. To this aim, the user is allowed to specify the missing sextants, which in the case of the KALLA experiment are {3,4,5,6}.

For each SA, the sides and corners are numbered as indicated in figure 9.9.

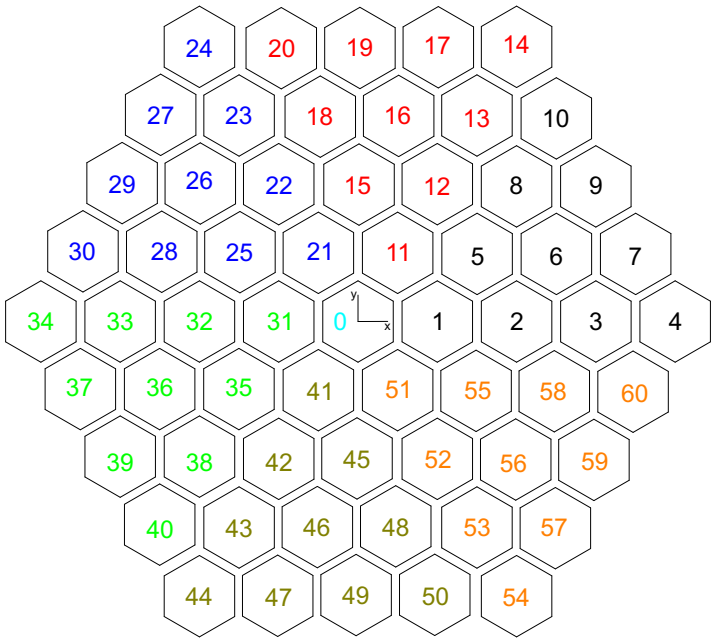

Figure 9.7: Numbering convention for a sample hexagonal lattice.

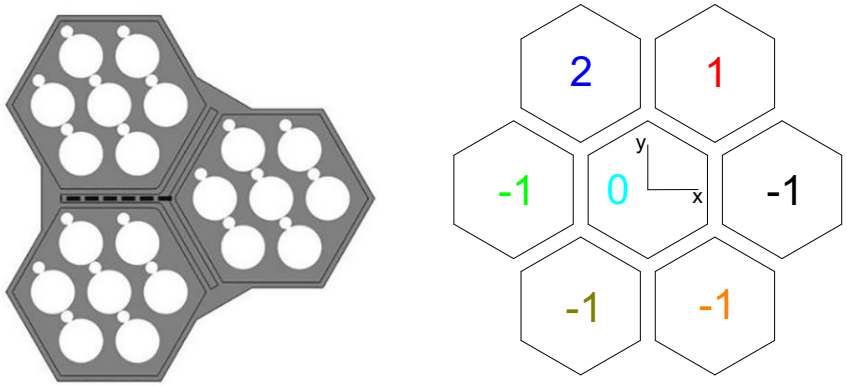

(a) KALLA experiment layout.

(b) SA numbering for KALLA.

Figure 9.8: Configuration of the KALLA experiment and numbering convention for this case.

9.9.2 SA-based maps

It is of interest to determine which are the neighboring SAs to a given SA. It is also helpful to know which sides of the neighboring SAs are facing each other. To this aim, the regularity of the lattice is exploited. Each sextant is mapped to a table, as

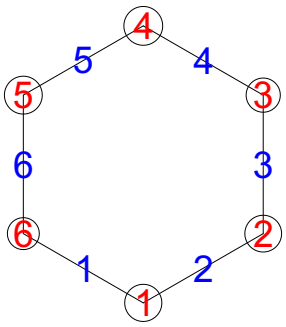

Figure 9.9: Numbering convention for sides (blue) and corners (red, circled) for a given SA.

shown in Figure 9.10. The 0 SA is placed at the left of the first SA of the sextant. The rows of the sextant are then listed. On the left side of the table, below the 0 element, the SAs of the first row of the following sextant are listed. At the center of the top row, the remaining neighboring SAs to the current sextant (belonging to the previous sextant, or, in the case of the first sextant, to sextant 6) are listed. The remaining cells of the table are filled with -1, indicating regions outside the core.

Each SA of the current sextant is then connected to 6 of the 9 neighbors in the table, as shown in Figure 9.10. The connection starts from the neighbor on the top and proceeds clockwise. The number indicated on the connection line indicates the side of the current SA which confines with the neighboring SA. This procedure is repeated for sextant 2, with the only modification of a circular shift of the sides associated to each connection (notice the difference between SA #1 and SA #11 in the left and right frames of Figure 9.10, respectively.

-1	51	55	58	60	-1
0	1	2	3	4	-1
11	5	6	7	-1	-1
12	8	9	-1	-1	-1
13	10	-1	-1	-1	-1
14	-1	-1	-1	-1	-1

-1	1	5	8	10	-1
0	11	12	13	15	-1
21	15	16	17	-1	-1
22	18	19	-1	-1	-1
23	20	-1	-1	-1	-1
24	-1	-1	-1	-1	-1

Figure 9.10: Strategy to determine connectivity between SAs. Example for sextants 1 (left) and 2 (right).

The result of this procedure is a map connecting each side of a given SA to the corresponding neighboring SAs. In case the SA confines with the core boundary for a given side, the map contains -1, which can be easily interpreted by the code.

9.9.3 Gap-based maps

As already mentioned in section 9.4, the IW region is made of *gaps* (i.e. the regions between two neighboring SAs) and *corners* (i.e. the regions where three SAs confine). To promote a structured generation of the SCs numbering and connectivity, it is necessary to define a global numbering of gaps and corners. This is simply achieved by cycling over the sides of each SA, starting from number 1, incrementing a counter and ensuring that a gap is not counted more than once. During this processing it is straightforward to produce the maps associating each gap to the two neighboring assemblies, taking also note of the side indexes. For the sake of clarity, the resulting gap numbering for the sample lattice shown in Figure 9.7 is reported - only for the first sextant - in Figure 9.11, where the core boundary is also schematically reported.

For specific cases, the gaps along the core boundary may not be present (this is the case for KALLA, see again Figure 9.8). Therefore, the user is allowed to select whether or not to include the gaps along the core boundary in the calculation domain.

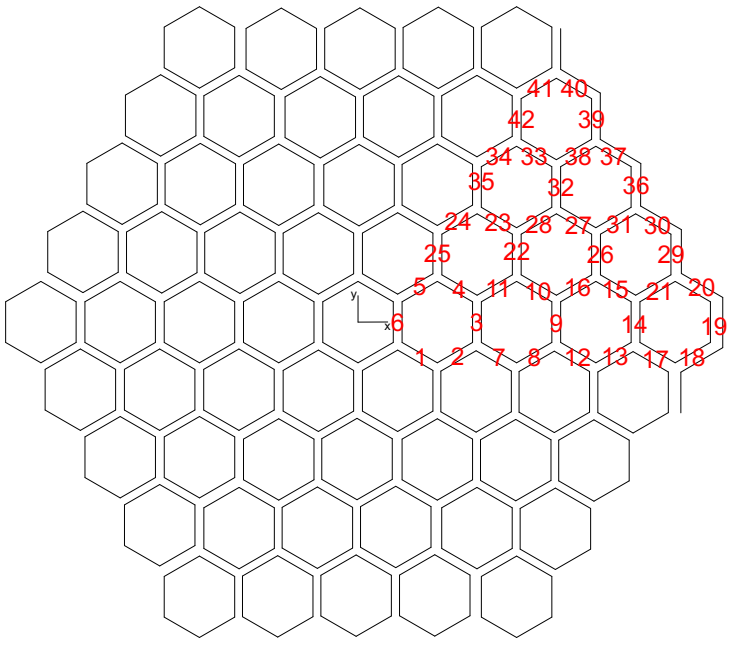

Figure 9.11: (Partial) gap numbering for the sample geometry.

9.9.4 Corner-based maps

The numbering of the corners inside the domain, as well as the connections between corners and SAs and between corners and gaps, is generated adopting the same approach as the one employed for gap-based maps. For the sake of clarity, the resulting corner numbering for the sample lattice shown in Figure 9.7 is reported - only for the first sextant - in Figure 9.12.

Moreover, once the numbering of the corners is determined, it is straightforward to generate a map connecting each gap to the two neighboring corners, taking into account the possibility that one of the two neighbors may be non-existent (in cases where SCs on the core boundary are not included in the simulation domain, see 9.9.3).

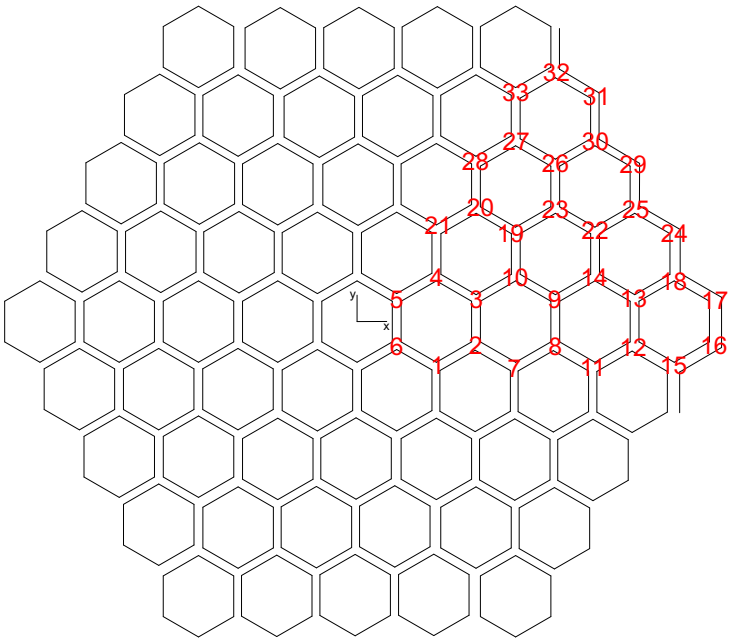

Figure 9.12: (Partial) corner numbering for the sample geometry.

9.9.5 SC-based maps

The ultimate goal of this section is to describe how the numbering and the connections between SCs are generated in TIFONE. The selected solution takes advantage of the availability of a numbering of the gaps, as described in section 9.9.3, and of the map describing the connection between gap and corners discussed in section 9.9.3.

The procedure starts by initializing the SC index to 1. Gap #1 is then selected, and the current SC index is assigned to the first of the two neighboring corners to gap #1, according to the map describing the connections between gap and corners[2]. The SC index is then incremented and the corresponding SC assigned to the *edge SC* adjacent to the first corner. The procedure is repeated until the user-specified number of *edge SCs* is reached. At this point, the subsequent SC index is assigned to the second neighboring corner to the current gap.

During this procedure, each time the SC index is incremented - thus defining a new SC - the inter-SC neighboring map is updated. In this way, after a gap has been processed, the corresponding SCs numbering and connections have been computed, and the next gap can be processed.

There are a few exceptions to be handled by the code:

- The first (or second) neighboring corner to a gap may be non-existent if it is located on the core boundary, in the case where SCs on the core boundary are not included in the simulation domain. In this case, the first (or last) of the *edge* SCs for that gap is assigned as first (or second) neighbor -1. This allows to easily keep track of the SCs during the problem solution.
- In case the first (or second) neighboring corner to a gap has already been assigned a SC number, that number is retrieved so to correctly build the connection matrices for the *edge SCs* of the given gap. Moreover, the number of times a corner has been encountered is exploited to determine the index of neighbor map to which the neighboring SC along the current gap is to be assigned.

At the end of this procedure, the connections between SCs, between SCs and gaps and between SCs and corners are available for the code calculation phase.

[2]The notion of "first" and "second" neighboring corner to a given gap derives from the following convention: the SA which was first associated to the gap during the gap numbering phase is considered as a reference to assign the gap orientation, and therefore the "first" neighboring corner to a given gap is the one that is encountered first by moving counter-clockwise along the reference SA.

9.10 Overview of the code design procedure

In the foregoing sections, the problem to be solved by the TIFONE code has been described, and the selected methodologies to address this problem while complying with the requirements of a DOC have been presented in detail. The next phase of the code development procedure is the *code design*, which is typically documented in the SDID document. The steps involved in the code design shall be presented in the next sections. For the sake of clarity, the present section contains an overview of the procedure.

9.10.1 Definition of the code inputs and outputs

The first step involves the identification of the required inputs and outputs to the codes. The level of detail of input and output quantities is typically specified in the SRS document. Inputs and outputs are then subdivided into categories, in order to identify an exhaustive set of interfaces between the code and the user.

9.10.2 Data modelling

At this point, based on the selected problem solving procedure, the data to be treated by the code can be thoroughly described and organized into *datasets*. The output of this *data modeling* procedure is organized in tables, where the proposed variable names, their foreseeable dimension and a brief description of their meaning is included. In this phase, it is convenient to adopt variable names which are consistent with the chosen naming convention for the code.

It should be noticed that the *datasets* are only intended to organize the data treated by the code into logical categories and to identify the data dimensions. *Datasets* do not prescribe a specific data organization in the source code (e.g. into derived data types). This choice is left to the code developers.

9.10.3 Code functional modelling

To support a structured code design, a code *functional model* can then be produced. The functional model translates the physico-mathematical approach proposed for the solution of the problem into the series of transformations undergone by the data contained in the *data dictionary*. Each transformation corresponds to a code function.

The code functional modelling procedure involves the description of the code functions (i.e. the transformations undergone by the data) with an increasing level of detail, until the single functions are highly *consistent* (i.e. the scope of the data treated in each function is sufficiently limited). At the end of this *functional*

modelling phase, the individual functions to be performed by the code, as well as the input and output data for each function, are systematically identified.

The outcomes of the code functional modelling phase are graphically represented by means of Data Flow Diagrams (DFDs).

9.10.4 Detailed code design

Once the individual functions to be performed by the code, as well as the interfaces of each function to the rest of the code, have been identified, the last step to be performed is the *detailed code design*. This task is performed top-down: at the higher levels, the detailed code design simply translates the information flow described in the DFDs into the *sequence* of macro-functions to be performed by the code. Each macro-function is then detailed, going deeper in each functional unit. The result, which can be presented by means of Program Design Language (PDL) or via flowcharts, is intended to provide the required input for the actual code implementation. At the end of the detailed code design, for each functional unit, both the interfaces and the detailed processing algorithm are specified. The procedure calls are now indicated, thus clarifying the logical connection between each functional unit (whereas the functional modelling phase was only concerned with the flow of data).

9.11 Input description and formatting

9.11.1 Input description

The code reads input data from formatted input files. Required input for the code can be subdivided among different categories, which are hereafter described.

Case description

The user specifies information that can be useful to identify the run, namely the name of the user, the name of the project and the specific reactor core simulated. Two user-specified labels (a short one and a long one) are also made available, so that the user can describe the simulated problem with an arbitrary level of detail. The two labels are then be echoed to the output files (see section 9.12).

The above mentioned information is contained in a Fortran namelist, `/caseDescription/`. Details concerning the contents of the two entries in this namelist are provided in section 9.16.2.

Geometry

The user specifies the geometrical characteristics of the SAs and of the IW gaps, namely the wrapper axial length and thickness, the IW gap thickness and the wrapper outer flat-to-flat distance. These quantities are assumed to be equal among all the SAs.

The core arrangement is defined by specifying, for each sextant, the number of SA rows and the number of SAs per row, as mentioned in section 9.9.2. This information is used by the code to generate the connection logic, as well as to determine the coordinates of the baricenter of each SA.

The above mentioned data is contained in two Fortran namelists, `/geometry1/` and `/geometry2/`.

Boundary conditions

The total coolant mass flow rate in the core and the fraction of that flowrate flowing in the IW region are specified in input. The core inlet temperature and pressure are provided as well.

The above mentioned data is contained in the Fortran namelist `/bc/`.

Source terms

The axial and radial distribution of the heat flux flowing in/out the outer side of the wrapper for each SA, as well as the axial and radial distribution of the heat deposited in the IW coolant, are specified in input. This means that the source terms are specified "SA-based", as opposed to, e.g., "gap-based".

The user is allowed to specify a different heat flux grid for each SA. It is instead assumed that the grid is the same among the sides of a given SA. The user is also allowed to specify a different heat deposition grid - not necessarily coinciding with the heat flux grid - for each SA. It is instead assumed that the grid is the same among the sides of a given SA.

The above mentioned data is contained in two separate input files, one for the heat flux and one for the heat deposition.

Materials

The input allows the user to choose the coolant and wrapper materials. Indeed, even though the code is specifically intended to support the design of LFRs, it is possible that experimental measurements to be used in validating the code are only available with other LMs, e.g. LBE or sodium.

The user can also select one among the available correlations for the LM density, viscosity, specific heat and thermal conductivity, as well as for the wrapper thermal conductivity.

The materials and correlations chosen by the user are contained in the Fortran namelist `/materials/`.

Models

Constitutive relations of empirical nature are employed by TIFONE, as indicated in section 9.8. In particular, the user is allowed to choose among the available correlations for: localized pressure loss coefficient; friction factor; Nusselt number; conduction shape factor; eddy diffusivity; onset of buoyancy (mixed convection) effects.

The user choice for each correlation is specified in the Fortran namelist `/models/`.

Numerics

The user-specified quantities affecting the numerical behavior of TIFONE are associated to both the spatial discretization and the requested tolerances for the problem solution.

The spatial discretization approach has been discussed in section 9.4. The user can specify the radial discretization approach selected (uniform or manual). In case a uniform radial subdivision is required, TIFONE only requires the specification of the number of SCs for each gap. In case a manual subdivision is required, instead, TIFONE reads a separate file containing the radial discretization detail (for each SA, the number and location of the radial nodes. The axial discretization is provided by the user by specifying the number and location of the axial nodes.

As discussed in section 9.7.2, the mixed convection solution can be considered to be converged when the errors on the global mass balance, core IW coolant pressure

drop, enthalpy increase and velocity increase are below their respective, user-defined tolerances.

The specifications concerning the radial and axial discretization, as well as the tolerances, are contained in the Fortran namelist `/numerics/`. If needed (i.e. if the "manual" radial discretization has been selected), the radial discretization detail is contained in a separate input file.

9.11.2 Input formatting

The input categories listed above point out the necessity of the following input files:

1. `input.inp`: contains the namelists `/caseDescription/`, `/geometry1/`, `/geometry2/`, `/bc/`, `/materials/`, `/models/` and `/numerics/`;
2. `heatFlux.inp`: contains the heat flux crossing the outer side of the wrapper for each SA;
3. `heatDeposition.inp`: contains the heat deposited in the coolant for each SA;
4. `radialDiscr.inp`: contains the heat deposited in the coolant for each SA.

The `input.inp` file is formatted according to the above-mentioned design choices, using Fortran namelists. While recognizing that more structured and readable input formats are available, the Fortran namelist has been selected as a trade-off between complexity and effectiveness. Moreover, files containing Fortran namelists allow for an arbitrary number of comments throughout their length. The presence of comments and the usage of self-explanatory variable names will ensure an acceptable level of readability for the input file.

The `heatFlux.inp` and `heatDeposition.inp` files are both formatted according to the structure indicated in listing 9.1. The same structure is repeated for each SA. `nAxQo` and `nRadQo` are the number of points for which the heat flux is specified in the axial and radial direction, respectively. The corresponding coordinates are contained in the vectors `zAxQo` and `xRadQo`. `qOut` contains the heat flux values.

```
!*******************************************************
! Input file heatFlux.inp for TIFONE
!*******************************************************
  !Heat flux input for SA #0
  nAxQo nRadQo

  zAxQo(1) zAxQo(2) ... zAxQo(nAxQo)

  xRadQo(1) xRadQo(2) ... xRadQo(nRadQo)

  qOut(1,1) qOut(2,1) ... qOut(nRadQo(0),1)
  qOut(1,2) qOut(2,2) ... qOut(nRadQo(0),2)
  ...
  qOut(1,nAxQo) qOut(2,nAxQo) ... qOut(nRadQo,nAxQo)

```

```
16   !Heat flux input for SA #1
17
18   ...
```

Listing 9.1: Structure of the heatFlux.inp file.

The `radialDiscr.inp` file is formatted according to the convention indicated in listing 9.2.

```
1  !*******************************************************
2  ! Input file radialDiscr.inp for TIFONE
3  !*******************************************************
4    !Radial discretization for SA #0
5    nRadNod
6
7    xRadNod(1) xRadNod(2) ... xRadNod(nRadNod)
8
9    !Radial discretization for SA #1
10
11   ...
```

Listing 9.2: Structure of the radialDiscr.inp file.

9.11.3 Input error handling and default behavior

The code detects inconsistencies in the provided input, and stops the execution with suitable error messages. The error messages points to:

1. The line (or block) of the file where the inconsistency has been found;
2. The line (or block) in the code where the error occurred/was caught;
3. The keyword, if available, in which the error occurred;
4. A description of the detected error and a hint on corrective actions to be taken to correct it.

The user is allowed to omit the input parameters which can be safely assigned a default value. In sections 9.13.1 to 9.13.4, the default settings for selected variables will be indicated. For all the other variables, omitting the input triggers an error message.

9.12 Output description and formatting

The code output consists of two parts: a short *summary report* and a comprehensive *detailed output*. The first is human readable, while the second is straightforward to post-process. In the following, the structure of both output files is described.

9.12.1 Summary report

The *summary report* is designed so that it can be attached as-is to a technical report. It therefore contains all the necessary information to reproduce the specific simulation at hand, as well as the most relevant engineering parameters.

The *summary report* starts with a header summarizing the code version, date and time of the simulation, the name of the user, the name of the project, the specific reactor core simulated and two user-specified labels (a short one and a long one) as indicated in section 9.11. With the exception of the date and time, which are retrieved at runtime from the PC where the simulation is performed, and of the code version, which is retrieved from the git repository, this information is found in the *caseDescription* dataset.

Subsequently, it contains a human-readable outline of the code inputs, i.e. it prints the content of datasets *Core geometry*, *Boundary conditions*, *Materials*, *Numerics*, *Models* (see section 9.13).

The *Source terms* dataset is too large to be conveniently reported as-is in the *summary report*. Nevertheless, summarized information about the source terms are desirable. To this aim, the *summary report* also includes the following:

- Total heat to IW coolant from the wrapper;
- Total heat deposited in the IW coolant;
- Maximum heat flux to the IW coolant from the wrapper;
- Maximum volumetric heat deposition inside the IW coolant.

Information on the SC categories (defined in section 9.6.1 during the discussion regarding the flow split model) are also provided. Specifically, for each category, the geometrical data adopted to perform the flow split calculation (namely, D_h, f and A), as well as the output of that calculation (in terms of X_i,X_2, ..., $X_{N_{cat}}$) are included in the *summary report*.

The *summary report* then indicates whether the mixed convection solution has been computed or not, specifying the numerical values of Re and Gr used in the mixed convection criterion and comparing explicitly the ratio Re/Gr with the assumed threshold value.

The subsequent section of the *summary report* contains key simulation results, namely:

- Value and location of maximum wrapper temperature, and complete temperature distributions (in coolant and wrapper) for such SA;

- Value and location of maximum temperature difference between wrapper sides, and complete temperature distributions (in coolant and wrapper) for such SA;
- Value and location of maximum coolant temperature, and complete temperature distributions (in coolant and wrapper) for such SA;
- Average coolant temperature at core inlet;
- Average coolant temperature at core outlet;
- IW coolant pressure drop.

Finally, the *summary report* includes the convergence history for the flow split calculation. In case the mixed convection solution is computed, the *summary report* also indicates the maximum number of iterations which were needed to reach convergence with respect to $\Delta\rho_i$, Δv_i, ΔP and the total mass conservation, respectively.

9.12.2 Detailed output

The detailed output is aimed at providing complete information concerning the simulation, in a format that allows to conveniently post-process and visualize the results via suitable post-processing scripts. For this purpose, the user is able to choose a finite set of axial locations for which the following quantities are printed in the detailed output:

- radial distribution of the coolant mass flow rate;
- radial distribution of the coolant temperature;
- radial distribution of the coolant velocity;
- coolant pressure;
- outer wrapper temperature.

For the sake of completeness, the detailed output also contains the following:

- cross sectional area for each SC;
- coordinates of the baricenter of each SC;
- heat flux flowing in/out of each wrapper node;
- heat deposited inside each SC;
- axial and radial distribution of the Nusselt number;
- axial and radial distribution of the friction factor;
- inner wrapper temperature.

The user will probably benefit from the availability of the connection logic internally used by TIFONE, e.g. to produce plots and/or to perform detailed post-processing. For this reason, the content of the Connectivity dataset is also present in the detailed output.

Due to the relatively large number of output quantities to be written, a number of plain text files is needed for the *detailed output*. To reduce the disk usage and the total number of files produced, as well as to simplify the inclusion of metadata, the code could take advantage of the HDF5 fortran library [195] in the future, to

promote easy storage of the output files and enhance case reproducibility. In this case, the single `.h5` file containing the detailed output will contain an attribute (i.e. a metadata of type string) describing the problem at hand. The attribute will be the same as the one adopted for the *summary report*.

9.13 Data modeling

In the foregoing sections, the problem solving approach and the corresponding mathematical formulation have been described. The required input and output quantities for the code have been identified in compliance with the requirements specification contained in the SRS document. At this point, the data to be treated by the code can be thoroughly described and organized into *datasets*. The result of this *data modeling* procedure represents the first step of the code design procedure, and is organized in tables. The proposed variable names have been chosen consistently with the naming conventions specified in section 9.15.2.

It should be noticed that the *datasets* are only intended to group the data treated by the code into logical categories and to identify the data dimensions. *Datasets* do not prescribe a specific data organization in the source code (e.g. into derived data types). This choice is left to the code developers.

In the following, only a few representative datasets, among those employed in TIFONE, are reported, for the sake of simplicity.

9.13.1 Core geometry

Core geometry			
Column	**Data type**	**Description**	**Notes**
`lAx`	float	Axial length of the domain	
`thickWrap`	float	Wrapper thickness	Assumed equal for each SA
`thickGap`	float	Inter-assembly gap thickness	Assumed equal for the gap between each couple of SAs
`flatToFlat`	float	Outer size of each SA	
`nSide`	int	Number of sides for each SA	`nSide`=6 is defined inside the code
`nRowSext`	int	Number of SAs rows for each sextant	Assumes that the geometry can be decomposed in 6 geometrically identical sextants
`nSaRow`	int(`nRowSext`)	Number of SAs for each row	Not including the central SA
`saBaric`	float (`nSa`,2)	(x,y) coordinates of the baricenter of each SA, reference frame placed at the center of the central SA	This array is internally computed by the code (not a user input)

Table 9.1: Core geometry dataset.

9.13.2 Boundary conditions

Boundary conditions			
Column	**Data type**	**Description**	**Notes**
`tempInlet`	float	Core inlet temperature	
`mdotIn`	float	Total core mass flow rate	
`iwFrac`	float	Fraction of the core mass flow rate flowing in the IW region	The IW flow rate is then distributed among the SCs based on the flow split calculation
`presInlet`	float	Core inlet pressure	Defaults to 0.0 Pa

Table 9.2: Boundary conditions dataset.

9.13.3 Materials

Materials			
Column	**Data type**	**Description**	**Notes**
`cLm`	string	Label identifying the coolant type	
`cWrap`	string	Label identifying the wrapper material	
`cLmDens`	string	Label identifying the selected correlation for coolant density	
`cLmVisc`	string	Label identifying the selected correlation for coolant viscosity	
`cLmCp`	string	Label identifying the selected correlation for coolant specific heat capacity	
`cLmCondTh`	string	Label identifying the selected correlation for coolant thermal conductivity	
`cWrapCondTh`	string	Label identifying the selected correlation for wrapper thermal conductivity	

Table 9.3: Materials dataset.

9.13.4 Numerics

Numerics			
Column	**Data type**	**Description**	**Notes**
`nAxNod`	int	Number of axial nodes	
`zAxNod`	float (`nAxNod`+1)	Axial coordinates of node boundaries	
`cRadDiscr`	string	Label identifying the selected approach for the radial discretization	
`nScSide`	int	Number of nodes for each side of the wrapper	Used in case `cRadDiscr`="default". Same for each SA
`nRadNod`	int(`nSa`)	Number of nodes for each side of the wrapper	Used in case `cRadDiscr`="manual", i.e., user-defined radial discretization
`xRadNod`	for each SA, float (`nRadNod`(iSa)+1)	Location of the radial node boundaries for each side	Used in case `cRadDiscr`="manual"
`cSolMethod`	string	Label identifying the selected method for matrix system solution	
`maxItSplit`	int	Maximum number of iterations for the solution of the flow split problem	
`maxItMixed`	int	Maximum number of iterations for the solution of the mixed convection system for each axial level	
`tolFlowSplit`	float	Tolerance for flow split calculation	
`tolMassBal`	float	Tolerance for total mass balance	
`tolPres`	float	Tolerance for pressure	
`tolVelc`	float	Tolerance for velocity	
`tolTemp`	float	Tolerance for temperature	

Table 9.4: Numerics dataset.

9.13.5 Models

Models			
Column	**Data type**	**Description**	**Notes**
`cLoc`	string	Label identifying the selected correlation for localized inlet and outlet pressure losses	
`cFrc`	string	Label identifying the selected correlation for friction factor	
`cNus`	string	Label identifying the selected correlation for Nusselt number	
`cKappa`	string	Label identifying the selected correlation for conduction shape factor	
`cEps`	string	Label identifying the selected correlation for eddy diffusivity	
`cVelcStar`	string	Label identifying the selected approach for evaluating exchange term $V*$	
`cEnthStar`	string	Label identifying the selected approach for evaluating exchange term $H*$	
`cMixedConv`	string	Label identifying the selected criterion to assess whether the flow regime is forced or mixed	

Table 9.5: Models dataset.

9.13.6 Problem dimensions.

Problem dimensions			
Column	**Data type**	**Description**	**Notes**
`nSc`	int	Total number of SCs in the IW region	
`nWr`	int	Total number of wrapper nodes	
`nGaps`	int	Number of IW gaps in the calculation domain	
`nCor`	int	Number of corners in the IW region	

Table 9.6: Problem dimensions dataset

9.13.7 SC TH data

SC TH data			
Column	**Data type**	**Description**	**Notes**
`temp`	float(`nSc`, `nAxNod`)	Temperature	
`velc`	float(`nSc`, `nAxNod`)	Flow velocity	
`dens`	float(`nSc`, `nAxNod`)	Coolant density	
`enth`	float(`nSc`, `nAxNod`)	Enthalpy	
`pres`	float(`nSc`, `nAxNod`)	Pressure	
`qHeat`	float(`nSc`, `nAxNod`)	Total external heat source to SC iSc at axial node iAxNod	

Table 9.7: SC TH dataset.

9.14 Code functional modeling

To support a structured code design, a code *functional model* has been produced. This model translates the approach proposed for the solution of the problem at hand (described in sections 9.3-9.12) into the series of transformations undergone by the data contained in the *data dictionary* (reported in section 9.13). Each transformation corresponds to a code function.

The transformations are outlined with an increasing level of detail, until the single functions are highly *consistent* (i.e. the scope of the data treated in each function is sufficiently limited). At the end of this *functional modelling* phase, the functions to be performed by the code, as well as the input and output data for each function, are identified. The detail design of the single code units will be described in section 9.16.

The graphical representation for requirements modeling selected for TIFONE is the Data Flow Diagram (DFD)[3] [158]. The legend to interpret the DFDs is provided in Figure 9.13. The top-level representation of the information flow and transformations is contained in level 0 DFD. Level 1 DFD contains the high-level representation of TIFONE, where the main code functions are indicated and connected to the relevant data structures. Each of the main code functions is then detailed in level 2 DFDs. The input and output variables to each functions are indicated. For the two most complex functions (*Generate internals* and *Solve*) a level 3 DFD has also been produced, together with a detailed functional model, obtained from the level 3 DFD itself according to the guidelines contained in [158]. In the present thesis, DFDs associated to the *Read Input*, *Solve* and *Write Output* functions are shown. The level 2 and 3 DFDs associated to *Generate Internals* are instead not reported for the sake of simplicity.

Figure 9.13: Legend for the TIFONE DFDs.

[3]The DFD is a relatively simple and structured representation for the *functional model* of a code. DFDs are particularly suited for procedural ("call-and-return") architectures - such as the one selected by TIFONE. For *object-oriented* architectures, alternatives such as Unified Modeling Language (UML) diagrams would instead be more suitable.

9.14.1 Level 0 and level 1 DFDs

The level 0 DFD is a top-level representation of the code, identifying its connections with the "environment". In the present case, the code reads input files and writes output files, while potentially informing the user about the progress of the calculation and/or about errors and inconsistencies via messages on the screen and in the summary report (see section 9.11).

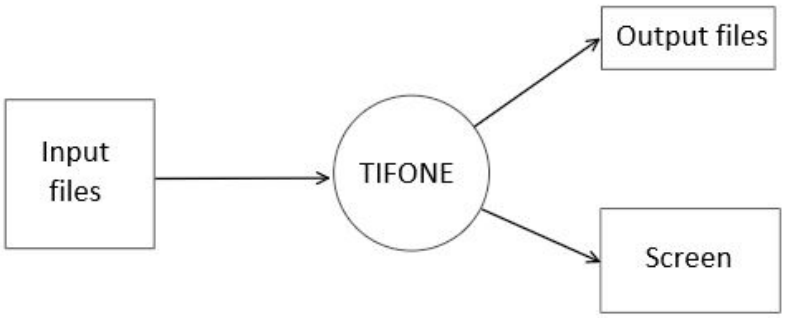

Figure 9.14: Level 0 (context-level) DFD for TIFONE.

The level 1 DFD represents a first step towards the identification of the code functional units. The main functions to be performed by the code (*Read input*, *Generate internals*, *Solve* and *Write output*) are indicated, together with their interactions with the data structures already defined in the *data dictionary*. In the following, level 2 (and possibly level 3) DFDs for the main code functions are presented and discussed.

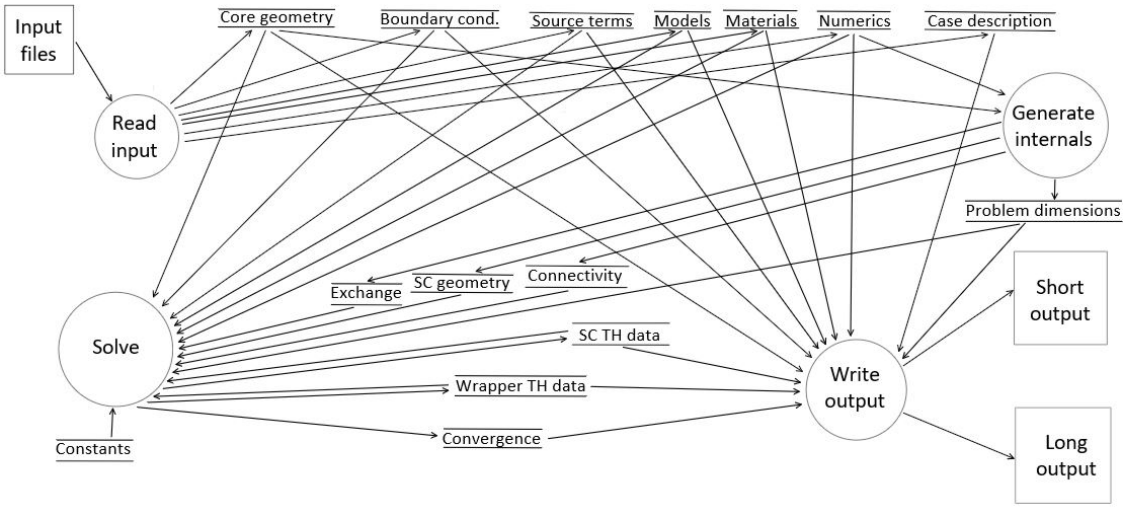

Figure 9.15: Level 1 DFD for TIFONE.

9.14.2 Level 2 DFD for *Read Input*

Figure 9.16 shows the level 2 DFD for *Read Input*. The user input is contained in input files. These external entities are read and stored into data structures that are accessible to the "working" sections of the code.

Two types of input files (containing Fortran namelists and distributions, respectively) are foreseen, according to the specifications of section 9.11. Each of the input data categories indicated in section 9.11 is read by a separate function.

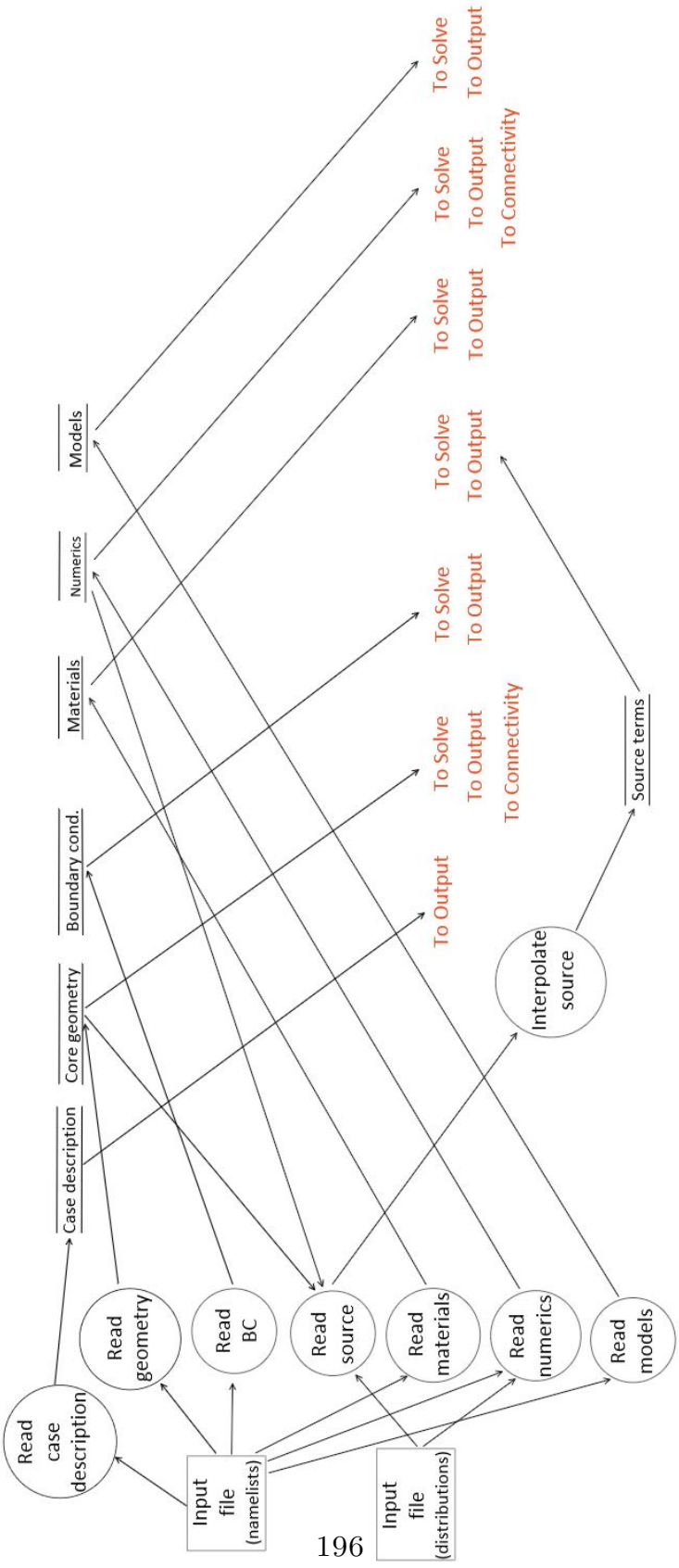

Figure 9.16: Level 2 DFD for *Read Input*.

9.14.3 Level 2 and level 3 DFDs for *Solve*

Figure 9.17 shows the level 2 DFD for *Solve*. This graph outlines the links between functional units and data structures related to the solution of the IW flow and heat transfer problem.

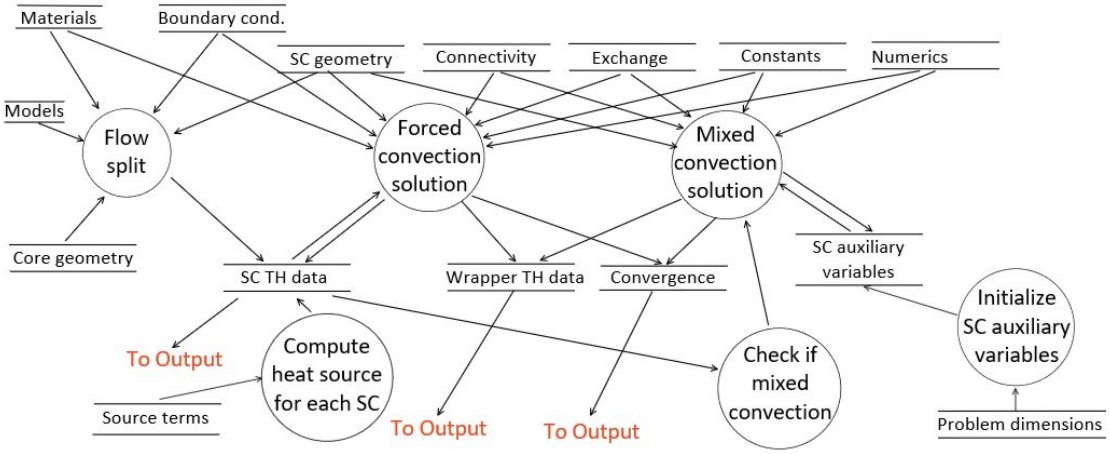

Figure 9.17: Level 2 DFD for *Solve*.

Due to the complexity of this function, a level 3 DFD is required to ensure that each functional unit is sufficiently coherent. This is shown in Figure 9.18. The same approach was adopted for *Generate Internals* (not shown here),

The user inputs (materials, boundary conditions, source terms and models) as well as the SC geometry previously computed within *Generate Internals*, are used to solve the flow split problem (see section 9.7.1). This allows to determine the inlet velocity for each SC. At this point, the solution matrix is built for each axial level, relying on the connection maps computed in *Generate Internals* and the problem is solved. To this aim, the auxiliary quantities contained in the matrix coefficients, as well as the heat flux discharged by the wrapper to each distinct SC, are first allocated, initialized and calculated.

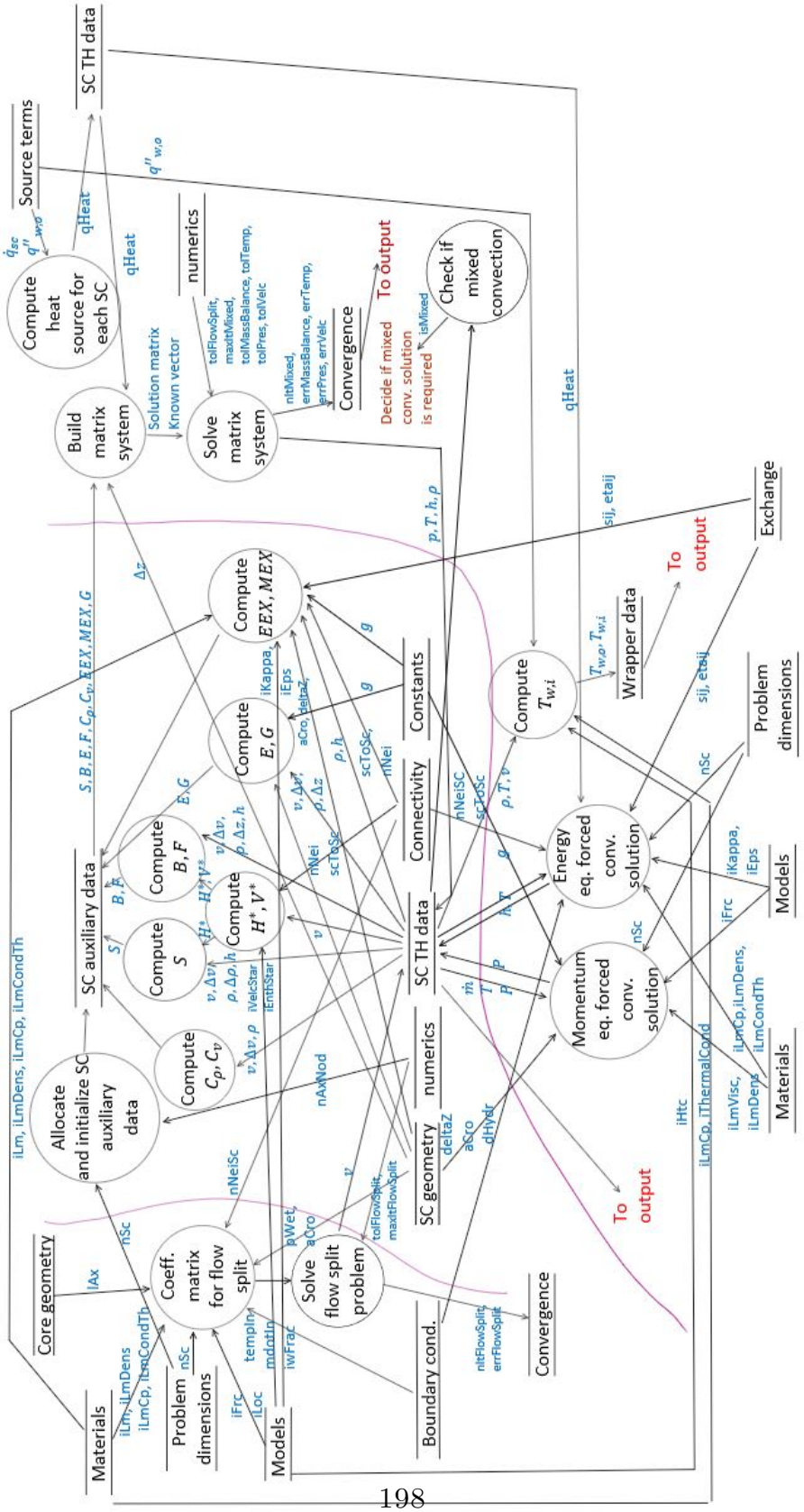

Figure 9.18: Level 3 DFD for *Solve*.

Figure 9.19 shows the functional model for *Solve*, obtained from the corresponding level 3 DFD by means of the *transform mapping* technique. The four main tasks performed by *Solve* (namely, *Flow split*, *Forced convection initialization*, *Prepare variables* and *System assembly and solution*) are clearly identified as independent lines of action, thus simplifying the detailed design of each individual routine. The latter will be described in detail in section 9.16.

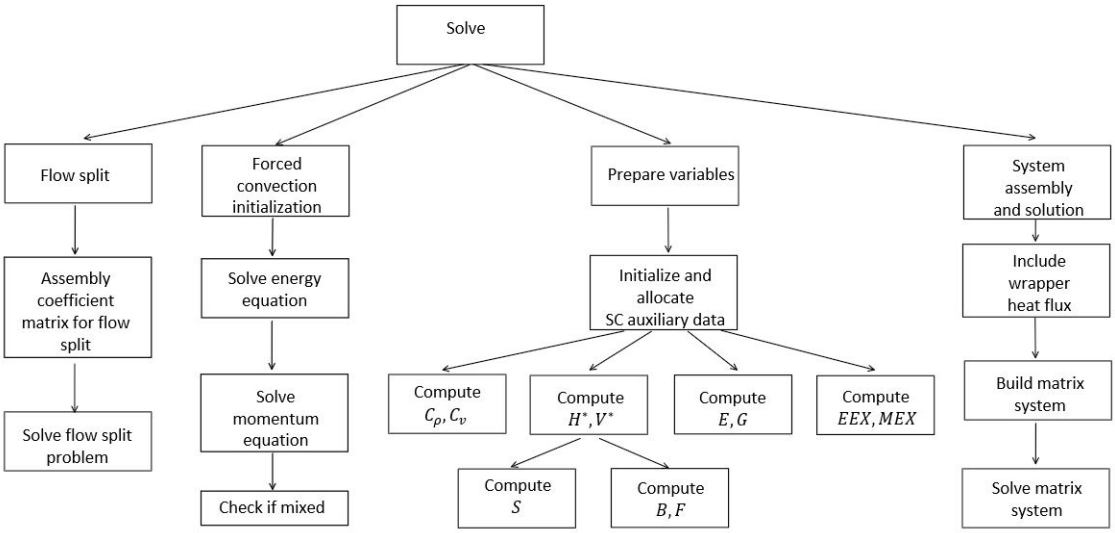

Figure 9.19: Functional model for *Solve*.

It should be stressed, once again, that the representation provided by DFDs and functional models is of *functional* nature, as opposed to the *procedural* nature of the information specified during the detailed code design phase (see section 9.16. During the code functional modelling phase, the flow of the data previously identified during the *data modelling* phase is designed and associated to the required input/outputs of code functional units. At this level, information related to *causality* and *consequentiality* are not yet specified. For example, in Figure 9.19, the flow split, forced and mixed convection solution are put at the same level, whereas they will obviously be processed sequentially by the code.

9.14.4 Level 2 DFD for *Write Output*

The information processed by the code is written to two output files ("short" and "long" output) according to the specifications provided in section 9.12. The functions writing each of the two files, as well as the information retrieved from data structures after the code processing phase, are reported in the level 2 DFD shown in Figure 9.20.

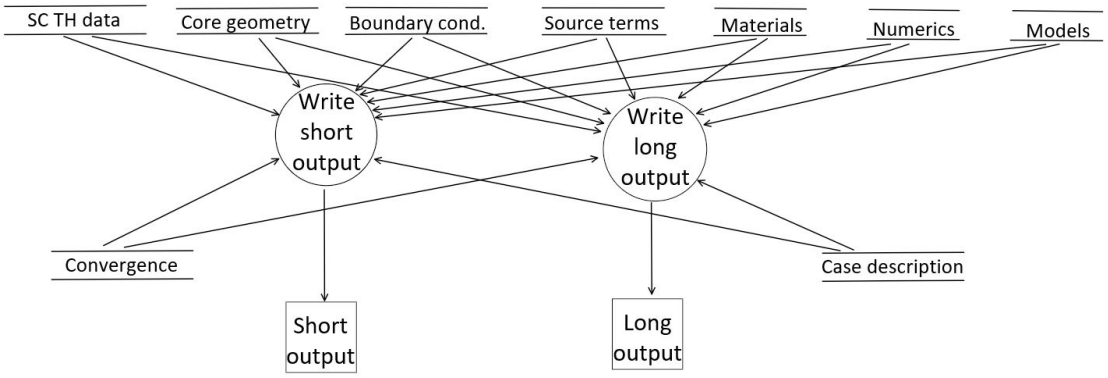

Figure 9.20: Level 2 DFD for WriteOutput.

9.15 Programming guidelines

In this section, the guidelines to be followed while implementing TIFONE to meet the requirements related to code compilation and readability are listed.

Adherence to a programming standard is necessary to reliably compile the code. The usage of consistent practices for variable names, line indentation, comments, error handling and data management throughout the entire code promotes instead its readability. These aspects are described in the following.

9.15.1 Language and hardware

The code is written in strict adherence to the latest Fortran programming language standard [89]. This guarantees consistent behavior of the code in case different compilers and/or operating systems are used. In particular, this ensures that any Unix-based system featuring the open source `gfortran` compiler will be able to compile and run the code. The code compilation options are specified in a Makefile produced by means of the open source CMake utility [32]. This allows to robustly link the code with the external libraries which are required, for instance, for the solution of the system of equations (see section 9.6.2), thereby increasing the code portability.

9.15.2 Code formatting and variable naming conventions

The code is written in free-form Fortran90, and composed of files with the .f90 extension. Standard indentation rules are adopted for readability, using blanks (i.e., no tabs), with an indentation depth per level of two spaces. The `implicit none` statement is used throughout the code so that all variables have to be explicitly defined. Intrinsic keywords are lowercase (e.g. `module`), as most text editors foresee syntax highlighting for Fortran and therefore no further specification for these variables is needed. Subroutine and function names have their first character capitalized, and dummy arguments have spaces around (e.g. `subroutine LocScTh( nSc, nAxNod )`). Spaces are also employed around `if` statement parentheses (e.g. `if ( iAxNod .le. nAxNodes )`). Array names are instead lowercase, and there are no spaces between the arguments and the round brackets (e.g. `a = matrix(i, j)`). Variables with the `parameter` attribute have uppercase names (e.g. `MAX_NODES`). Functions from third-party libraries are also uppercase (e.g. `call DGETRF( n, n, mat, n, ipiv, info )`). Variable definitions are always preceded by double colon:

```
1 double precision, dimension(1:nAxNods, 1:nRadNodes), intent(in) ::
2   alpha, epsilon
```

As shown in the previous example, the `intent()` attribute is the last of the list. Although .f90 files allow for longer lines, conventionally no more than 80 characters per row are employed, to promote code readability. At the beginning

of a subroutine, all dummy arguments are listed first, followed by local variables. The latter are recognizable by the absence of the intent attribute. Names for user-defined types are followed by `_t` (e.g. `type_t`), and names for modules are followed by `_mod` (e.g. `module_mod`).

9.15.3 Comments

As far as comments are concerned, particular attention has been devoted to properly clarify:

- the function of each routine or class;
- the meaning and role of exchanged and local variables in each routine;
- the meaning and role of all the global variables and data structures (consistently with the description provided in section 9.13).

In particular, the comments are written so as to allow the `Doxygen` software ([43]) to automatically generate an exhaustive developer manual for the TIFONE code. The developer (or programmer's) manual is part of the software documentation, according to [74], and using `Doxygen` will help during this later phase of the activity.

9.15.4 Data management

Subroutines implementing controller-level functions, such as *Flow Split* (see Figure 9.19), are in charge of calling worker-level subroutines to execute the low-level functions. This code structure allows to limit the module visibility to the controller level, thus promoting code modularity.

According to this strategy, modules (where global variables are stored and organized) are only visible at the component level, where they are invoked. The content of the modules is then passed by reference to worker-level subroutines, to ensure that the scope of the latter remains limited. This will prevent modules to be called at low level, thus promoting code modularity.

An exception in this respect is represented by the allocation routines, which are logically located at the worker level but need to invoke modules in order to allocate variables within them.

9.15.5 Error handling

All expected error situations, and the corresponding error messages, have been defined in advance at the time of detailed code design (section 9.16) to allow for a critical design review also in this respect. Checks for all such errors have been integrated in the appropriate positions of the code, so that, if not passed, an error message could be issued and the execution stopped.

The specific nature of the error messages is such that the location of the error in the input files and the nature of the error are indicated, as well as suggestion of corrective actions, where applicable.

Input errors

Code listing 9.3 indicates the structure of a typical error message corresponding to a detected inconsistency in the input files.

```
'ERROR. <geometry feature name> must be [in] <range>.'
'       Please check value of <associated variable> in:'
'       FILE=<input file> :: NML=<associated namelist>.'
```

Listing 9.3: Sample error message on input variables.

Allocation errors

Code listing 9.4 indicates the structure of a typical error message corresponding to a failure during the allocation of a variable.

```
'ERROR: failed to allocate memory for <type of variable> <variable
   name> in function <name of function>.'
```

Listing 9.4: Sample error message on variable allocation.

Processing errors

Code listing 9.5 reports an example of a generic error message issued by subroutine `FunctionName`, associated to an inconsistency detected during the code processing phase.

```
'ERROR. Unacceptable value for variable <variable name>:'
'       in function <function name>,'
'       <actual value> was found, while expecting [in <range>] [
   type]'
'       Please check input value in:'
'       FILE='//trim(infile)//'' :: NML=NUMERICS.'
```

Listing 9.5: Sample error message on processing.

Floating point exceptions

Floating point exceptions (division by zero, overflow, and invalid operation) are trapped at code execution. This is the default behavior in Fortran and therefore no specific compiler option is required.

9.16 Detailed code design

The detailed code design has been performed by relying on Program Design Language (PDL). This approach has been selected instead of the more common *flowchart* because it is faster to write and review.

The detailed code design was performed top-down. At the higher levels, the detailed code design simply translating the information flow described in the DFDs (or, for the most complex functions, in the functional model) into the *sequence* of macro-functions to be performed by the code. Each macro-function is then detailed, going deeper in each functional unit.

The code design is such that:

- all interfaces are defined;
- procedure calls are specified;
- the detailed processing algorithm is specified.

In the DFDs, code components were presented by short sentences indicating their functions (e.g. *Allocate and initialize SC TH data*). In the PDL, instead, the proposed names for the code components (subroutines) to be eventually adopted in the source code are used. This simplifies the source code writing phase. To compensate for this choice in terms of readability, the PDL is commented so that each Fortran subroutine name can be easily traced back to the corresponding function. The same strategy is adopted for data structures, which are mapped to the corresponding Fortran modules. The names employed in the PDL are consistent with the programming guidelines indicated in section 9.15.

The conventions adopted to describe the interfaces between subroutines are indicated in the following.

Inside the calling routine, after the name of the function to be called, the list of variables to be exchanged with the called subroutines is included in round brackets. If the variables belong to modules - which contain the data structures defined in section 9.13 - the nomenclature `modulename_mod%[varname1,varname2]` is employed, see Listing 9.6 as an example.

```
1 ...
2  ReadGeomCore(geomCore_mod%[lAx,thickWrap,thickGap,nSa,nRowSext,
     nSaRow,nPinSa]) !Read Geometry
3 ...
```

Listing 9.6: Example of function call in PDLs.

Inside the called routine, the same interface is explicitly stated at the beginning of the subroutine. Exchanged variables are labeled by means of an attribute (`in` for inputs, `out` for outputs, `inout` for input/output varables), see Listing 9.7 as an example.

```
1 subroutine ReadGeomCore
2
3 !Interface
```

```
4
5 out :: lAx,thickWrap,thickGap,nSa,nRowSext,nSaRow,nPinSa
6
7 ...
```

Listing 9.7: Example of interface definition within a called function in PDLs.

In the following, a selection of PDLs is shown, to convey the approach used during the detailed code design while conveniently avoiding to report here the full pseudocode. To provide a representative overview, after the main program is presented, the PDLs for the subroutines `ReadInput` and `Solve` are reported. Consistently with the DFD for the *Read Input* function shown in Figure 9.16, the `ReadInput` subroutine has many first-level sub-functions, of which only the first one is here reported. The structure of `Solve`, implementing the *Solve* function, is more complex (see Figure 9.19), and therefore only `Mixed` is here reported as an example, with a limited number of the sub-level functions.

9.16.1 Main program

Listing 9.8 contains the top-level PDL for TIFONE. At this level, the main functions to be performed are called. Each of these functions is then described in the respective subsection.

```
1 program TIFONE
2
3  ReadInput !Read Input
4
5  GenerateInternals !Generate internals
6
7  Solve !Solve
8
9  WriteOutput !Output
10
11 end program TIFONE
```

Listing 9.8: PDL for TIFONE main program.

9.16.2 Read Input

The *Read Input* function, implemented in the subroutine `ReadInput`, is the first among the main code functions indicated in the level 1 DFD (Figure 9.15) for which the detailed design is presented. The *Read Input* function is logically located at the controller level, i.e. it is in charge of calling worker-level subroutines to execute the low-level functions. Consistently with the data management strategy proposed for TIFONE (see section 9.15.4) modules are invoked in `ReadInput` and the content of the modules is then passed by reference to worker-level functions.

```
subroutine ReadInput

 use module caseDescr_mod     !Case description
 use module geomCore_mod      !Core geometry
 use module boundaryCond_mod  !Boundary conditions
 use module heatSrc_mod       !Source terms
 use module matOpts_mod       !Materials
 use module numOpts_mod       !Numerics
 use module modelOpts_mod     !Models

 !Read case description
 ReadCaseDescription(caseDescr_mod%[codeVersion,userName,
   projectName,coreName,labelShort,descriptionLong])

 !Read Geometry
 ReadGeomCore(geomCore_mod%[nSa,nRowSext,nSaRow,lAx,thickWrap,
   thickGap,flatToFlat,nSa])

 !Read BC
 ReadBoundaryCond(boundaryCond_mod%[tempInlet,mdotIn,iwFrac,
   presInlet])

 !Read numerics
 ReadNumerics(numerics_mod%[nAxNod,zAxNod,iRadDiscr,nScSide,
   iSolMethod,tolMassBal,tolPres,tolVelc,tolTemp,tolFlowSplit])

 !Read materials
 ReadMaterials(materials_mod%[iLm,iWrap,iLMDens,iLmVisc,iLMCp,
   iLMCondTh,iWrapCondTh])

 !Read models
 ReadModels(models_mod%[iLoc,iFrc,iNus,iKappa,iEps,iVelcStar,
   iEnthStar,iMixedConv])

end subroutine ReadInput
```

Listing 9.9: PDL for *Read Input*.

Read case description

The function *ReadCaseDescription* is performed by the subroutine `ReadCaseDescription`. The PDLs for this subroutine (listing 9.10) represents the first example in this document of a worker-level subroutine for which a detailed design is presented. Consistently with the data management strategy described in 9.15.4, no module is called at this level, since variables are passed by reference to the caller subroutine, which is responsible for storing the data in the modules.

```
subroutine ReadCaseDescription

```

```
!Interface
out :: codeVersion,userName,projectName,coreName
out :: labelShort,labelLong

namelist /caseDescription/ codeVersion,userName,projectName,
  coreName, labelShort,labelLong

open input_file
read namelist /caseDescription/
close input_file

!---------------------------------------------------------------------
! echo
!---------------------------------------------------------------------

open echo_file for /caseDescription/ namelist
write /caseDescription/ namelist
close echo_file

end subroutine ReadCaseDescription
```

Listing 9.10: PDL for *Read case description*.

9.16.3 Solve

The function *Solve* is performed by the subroutine `Solve`. The corresponding PDL is presented in listing 9.11. With respect to the functional model of Figure 9.19, the function *Read source* has been moved inside `Solve` rather than included in the `ReadInput` subroutine. This choice allows to avoid the necessity to store the input distributions of the heat flux (exchanged between the wrapper and the IW coolant) and of the volumetric heat generation (deposited in the IW coolant), since the source terms are immediately included at an SC level. This would not have been possible before the generation of the SCs and of the connectivity matrices.

```
subroutine Solve

use module materials_mod
use module problemDims_mod
use module models_mod
use module numerics_mod
use module geomSc_mod
use module conn_mod
use module scTh_mod
use module heatSrc_mod
use module conv_mod

!Read boundary conditions
temp(1,1:nSc) = boundaryCond_mod%[tempInlet]
pres(1) = boundaryCond_mod%[presInlet]
```

```
16
17  !Flow split
18  FlowSplit(geomCore_mod%[lAx],
19            problemDims_mod%[nSc],
20            materials_mod%[iLm,iLmDens,iLmVisc,iLmCp,iLmCondTh],
21            modelOpts_mod%[iFrc,iLoc],
22            conn_mod%[nNeiSc],
23            geomSc_mod%[pWet,aCro],
24            boundaryCond_mod%[tempInlet,mDotInlet,iwFrac],
25            scTh_mod%[velc],
26            numerics_mod%[tolFlowSplit,maxItFlowSplit],
27            conv_mod%[errFlowSplit,nItFlowSplit])
28
29  !Allocate and initialize SC TH data
30
31  LocScTh(nSc,nAx)
32
33  !Read input heat flux and source
34
35  ReadHeatSrc(coreGeom_mod%[nSa,nSide],
36              numerics_mod%[nAxNod,iRadDiscr,nScSide,nRadNod],
37              heatSrc_mod%[qOut,qSrc])
38
39  !Initialize via forced convection calculation
40
41  do for each axial level iAx up to problemDims_mod%nAxNod
42
43   Forced(problemDims_mod%[nSc],
44          geomSc_mod%[deltaZ,aCro,dHyd],
45          materials_mod%[iLm,iLmDens,iLmVisc,iLmCp,iLmCondTh],
46          models_mod%[iFrc,iKappa,iEps],
47          src_mod%[qSrc,qOut],
48          scTh_mod%[mDot,temp(1:nSc,iAx),pres(1:nSc,iAx),
49                    enth(1:nSc,iAx),temp(1:nSc,iAx+1),
50                    pres(1:nSc,iAx+1),enth(1:nSc,iAx+1)
51                   ],
52          conn_mod%[nNeiSc,scToSc],
53          exchange_mod%[sij,etaij],
54          constants_mod%[grav]
55         )
56
57  end do
58
59  CheckMixed(dHydr,temp,beta,isMixed)
60
61  if isMixed then
62
63    do for each axial level iAx up to problemDims_mod%nAxNod
64
65     Initialize errMassBal, errPres, errVelc, errTemp to 1.0
```

```
66
67      !Mixed Convection solution
68
69      iItMixed = 1
70
71      do while any of (errMassBal,errPres,errVelc,errTemp)
72                   is above its tolerance
73               and iItMixed < maxItMixed
74
75        Mixed(iAx,problemDims%[nSc,nAx],
76              materials_mod%[iLm,iLmDens,iLmVisc,iLmCp,iLmCondTh],
77              scTh_mod%[temp(1:nSc,iAx),velc(1:nSc,iAx),
78                        dens(1:nSc,iAx),enth(1:nSc,iAx),
79                        pres(1:nSc,iAx),temp(1:nSc,iAx+1),
80                        velc(1:nSc,iAx+1),dens(1:nSc,iAx+1),
81                        enth(1:nSc,iAx+1),pres(1:nSc,iAx+1),
82                        qHeat,cVelc,cDens,enthStar,velcStar,
83                        bEne,sEne,eMom,gMom,fMom,eex,mex
84                       ],
85              const_mod%[grav],
86              conv_mod%[errMassBal,errPres,errVelc,errTemp],
87              iItMixed
88             )
89
90        Convergence check
91
92        iItMixed = iItMixed + 1
93
94      end do
95
96      conv_mod%nItMixed = iItMixed
97
98      if conv_mod%nItMixed = maxItMixed,
99         inform the user that maximum number of mixed convergence
100        iterations for axial node iAx has been reached without
101        convergence and specify which variables have not converged.
102
103    end do
104  else
105    Inform the user that the forced convection solution has been
     used
106
107 end subroutine Solve
```

Listing 9.11: PDL for *Solve*.

Allocate and initialize SC TH data

```
1 subroutine LocScTh
2
```

```
 !Interface

 in :: nSc, nAxNod

 allocate variables from scTh_mod:
  temp,velc,dens,enth,pres,deltaEnth,deltaVelc,deltaDens,deltaPres,
    cDens,cVelc,enthStar,velcStar,bEne,sEne,eMom,gMom,eex,mex

 if any allocation fails then
  error message
  stop execution

 Initialize temp, velc, dens, enth, pres, deltaEnth, deltaVelc,
    deltaDens, deltaPres, cDens, cVelc, enthStar, velcStar, bEne,
    sEne, eMom, gMom, eex, mex to -1.0

end subroutine LocScTh
```

Listing 9.12: PDL for *Allocate and initialize SC TH data.*

Mixed convection solution

```
subroutine Mixed

 !Interface
 in :: nSc,nAx
 in :: iLm,iLmDens,iLmVisc,iLmCp,iLmCondTh
 in :: tempIn,velcIn,densIn,enthIn,presIn
 inout :: tempOut,velcOut,densOut,enthOut,presOut
 in :: qHeat
 out :: cVelc,cDens,enthStar,velcStar
 out :: bEne,sEne,eMom,gMom,fMom
 out :: eex,mex
 in :: grav
 out :: errMassBal,errPres,errVelc,errTemp
 in :: iItMixed

 temp(1:nSc) = (tempIn(1:nSc)+tempOut(1:nSc))/2.0
 velc(1:nSc) = (velcIn(1:nSc)+velcOut(1:nSc))/2.0
 dens(1:nSc) = (densIn(1:nSc)+densOut(1:nSc))/2.0
 enth(1:nSc) = (enthIn(1:nSc)+enthOut(1:nSc))/2.0
 pres = (presIn+presOut)/2.0

 deltaVelc(1:nSc) = velcOut(1:nSc) - velcIn(1:nSc)
 deltaDens(1:nSc) = densOut(1:nSc) - densIn(1:nSc)
 deltaEnth(1:nSc) = enthOut(1:nSc) - enthIn(1:nSc)
 deltaPres = presOut - presIn

 !Variables for convergence check
 tempOld(1:nSc) = temp(1:nSc)
```

```
velcOld(1:nSc) = velc(1:nSc)
deltaPresOld = deltaPres

ComputeCoeffMixed(nSc,nNeiSc,scToSc,
                  deltaZ,dHyd,aCro,
                  iLm,iLmDens,iLmVisc,iLmCp,iLmCondTh
                  iKappa,iEps,
                  sij,etaij,epsij,
                  qOut,qSrc,
                  mDot,
                  velcIn,densIn,enthIn,presIn,
                  deltaVelc,deltaDens,deltaEnth,deltaPres,
                  temp,velc,dens,enth,pres,
                  iVelcStar,iEnthStar,
                  grav,
                  cDens,cVelc,enthStar,velcStar,
                  bEne,sEne,eMom,gMom,eex,mex,qHeat)

SolveSysMixed(mat,knownVec,iSolMethod,deltaVelc,deltaDens,
  deltaPres)

!Update variables at the end of the axial node

velcOut(1:nSc) = velcIn(1:nSc) + deltaVelc(1:nSc)
densOut(1:nSc) = densIn(1:nSc) + deltaDens(1:nSc)
enthOut(1:nSc) = enthIn(1:nSc) + deltaEnth(1:nSc)
cp(1:nSc) = SpecificHeat(iLm, iLmCp, temp(1:nSc))
tempOut(1:nSc) = tempIn(1:nSc) + deltaEnth(1:nSc)/cp(1:nSc)
presOut = presIn + deltaPres

!Update errors
errMassBal = 0.0
do for each SC iSc
  deltaMassBal = deltaMassBal +
                 aCro(iSc)*(
                           (velcIn(iSc)+deltaVelc(iSc))*
                           deltaDens(iSc) +
                           densIn(iSc)*deltaVelc(iSc)
                          )
end do
errMassBal = deltaMassBal
errPres = abs(presOut - presOutOld)/presOutOld
errVelc = max(abs(velc(1:nSc) - velcOld(1:nSc))/velcOld(1:nSc))
errTemp = max(abs(temp(1:nSc) - tempOld(1:nSc))/tempOld(1:nSc))

end subroutine Mixed
```

Listing 9.13: PDL for *Mixed convection solution.*

```
subroutine ComputeCoeffMixed

```

```
!Interface

in :: nSc
in :: nNeiSc,scToSc
in :: deltaZ, dHyd, aCro
in :: iLm,iLmDens,iLmVisc,iLmCp,iLmCondTh
in :: iKappa,iEps
in :: sij,etaij,epsij
in :: qOut, qSrc
in :: mDot
in :: velcIn,densIn,enthIn,presIn
in :: deltaVelc,deltaDens,deltaEnth,deltaPres
in :: temp,velc,dens,enth,pres
in :: iVelcStar,iEnthStar
in :: grav
out :: cDens,cVelc,enthStar,velcStar,bEne,sEne,eMom,fMom,gMom,eex,
  mex,qHeat

!Compute thermophysical variables
do for each SC iSc
 cp(iSc) = SpecificHeat(iLm, iLmCp, temp(iSc))
 dens(iSc) = Density(iLm, iLmDens, temp(iSc))
 condTh(iSc) = ThermalConductivity(iLm, iLmCondTh, temp(iSc))
 alpha(iSc) = condTh(iSc) / dens(iSc) / cp(iSc)
 pWet(iSc)=4.0*aCro/dHydr
 sumqOut = 0.0
 do for each neighboring wrapper node iNeiWr to SC iSc
  sumqOut = sumqOut + qOut(iSc)*pWet(iSc)/aCro(iSc)
 end do
 qHeat(iSc) = qSrc(iSc) + sumqOut
 visc(iSc) = (iLm, iLmVisc, temp(iSc))
 reyn(iSc) = Reynolds (dens(iSc),visc(iSc),dHydr(iSc),velc(iSc))
 fric(iSc) = FrictionFactor (reyn(iSc), dHyd(iSc), rough(iSc))
end do !iSc

do for each SC iSc
 do for each neighbor iNei to SC iSc
  kappaij(iSc,iNei) = ConductionShapeFactor(iKappa)
  epsij(iSc,iNei) = EddyDiffusivity(iEps)
  densAveij(iSc,iNei) = (dens(iSc)+dens(scToSc(iSc,iNei)))/2.0
  alphaAveij(iSc,iNei) = (alpha(iSc)+alpha(scToSc(iSc,iNei))/2.0
 end do !iNei
end do !iSc

computeVelcStar(nSc,iVelcStar,nNeiSc,scToSc,mDot,velc,velcStar)

computeEnthStar(nSc,iEnthStar,nNeiSc,scToSc,mDot,velc,enthStar)

computeSene(nSc,velcIn,deltaVelc,enthStar,enthIn,densIn,deltaDens,
  sEne)
```

```
51
52  computeBene(nSc,densIn,enthIn,enthStar,bEne)
53
54  computeEmom(nSc,deltaZ,dHyd,fric,velcIn,deltaVelc,velcStar,grav,
      eMom)
55
56  computeFmom(nSc,deltaZ,dHyd,fric,densIn,velcIn,deltaVelc,velcStar,
      fMom)
57
58  computeCdens(nSc,velcIn,deltaVelc,aCro,cDens)
59
60  computeCvelc(nSc,densIn,cVelc)
61
62  computeEex(nSc,deltaZ,aCro,nNeiSc,scToSc,sij,etaij,kappaij,epsij,
      densAveij,alphaAveij,dens,alpha,enth,eex)
63
64  computeMex(nSc,deltaZ,aCro,scToSc,sij,etaij,epsij,dens,densAveij,
      mex)
65
66  computeGMom(nSc,deltaZ,dHyd,fric,densIn,velcIn,grav,gMom)
67
68 end subroutine ComputeCoeffMixed
```

Listing 9.14: PDL for Compute matrix coefficients for mixed convection solution.

```
1  subroutine computeVelcStar
2
3   !Interface
4   in :: nSc
5   in :: iVelcStar
6   in :: nNeiSc,scToSc
7   in :: mDot,velc
8   out: velcStar
9
10  if iVelcStar = 1 then
11   !Complete formulation
12   do for each SC iSC
13     sumNum = 0.0
14     sumDen = 0.0
15     do for each neighbor iNei to SC iSc
16       xij = mDot(iSc) - mDot(scToSc(iSc,iNei))
17       sumNum = sumNum + abs(xij)*(velc(iSc)+velc(scToSc(iSc,iNei)))
18                       - xij*(velc(iSc)-velc(scToSc(iSc,iNei)))
19       sumDen = sumDen + abs(xij)
20     end do !iNei
21
22     velcStar(iSc) = sumNum/2.0/sumDen
23
24   end do !iSc
25
26  else if iVelcStar = 2 then
```

```
27    !Simplified formulation
28    velcStar(1:nSc) = velc(1:nSc)
29   else
30    error 'Error in scToSc or nNei maps'
31    stop execution
32
33 end subroutine computeVelcStar
```

Listing 9.15: PDL for *Compute* V^*.

```
1  subroutine computeSene
2
3    !Interface
4    in :: nSc
5    in :: velcIn,deltaVelc,enthStar,enthIn,densIn,deltaDens
6    out :: sEne
7
8    r(1:nSc)=der(enth,rho)
9
10   sEne(1:nSc)=(velcIn(1:nSc)+deltaVelc(1:nSc))*(-enthStar(1:nSc)+
      enthIn(1:nSc)+r(1:nSc)*(densIn(1:nSc)+deltaDens(1:nSc)))
11
12 end subroutine computeSene
```

Listing 9.16: PDL for *Compute* S.

```
1  subroutine computeEex
2
3   !Interface
4   in :: nSc
5   in :: deltaZ,aCro
6   in :: nNeiSc, scToSc
7   in :: sij, etaij, kappaij, epsij
8   in :: densAveij, alphaAveij
9   in :: dens, alpha, enth
10  out :: eex
11
12  do for each SC iSc
13   sum = 0.0
14   do for each neighbor iNei to SC iSc
15    densAveij=(dens(iSc)+dens(scToSc(iSc,iNei)))/2.0
16    alphaAveij=(alpha(iSc)+alpha(scToSc(iSc,iNei)))/2.0
17    sum = sum +
18          densAveij*sij(iSc,iNei)*
19          (
20           kappaij(iSc,iNei)*alphaAveij/etaij(iSc,iNei) +
21           epsij(iSc,iNei)/etaij(iSc,iNei)
22          )
23          *(enth(iSc)-enth(scToSc(iSc,iNei))
24   enddo
25   eex(iSc)=-deltaZ/aCro(iSc)*sum
```

```
 enddo

end subroutine computeEex
```

Listing 9.17: PDL for *Compute EEX*.

```
subroutine SolveSysMixed

 !Interface
 in :: bEne,sEne,eMom,gMom,eex,mex
 in :: tolMassBal,tolPres,tolVelc,tolTemp
 out :: deltaVelc, deltaDens, deltaPres

 !Build matrix system
 BuildMat(nSc,bEne,sEne,eMom,fMom,cDens,cVelc,gMom,eex,mex,mat,
   knownVec)

 !Solve matrix system
 SolveMat(mat,knownVec,iSolMethod,deltaVelc,deltaDens,deltaPres)

end subroutine SolveSysMixed
```

Listing 9.18: PDL for System assembly and solution.

```
subroutine BuildMat

 !Interface
 in :: nSc
 in :: sEne, bEne, eMom, fMom, cDens, cVelc, gMom, eex, mex, qHeat
 out :: mat,knownVec

 Initialize matrix elements to 0.0

 Current matrix row iRow = 1

 do for each SC iSc
  mat(iRow,iRow) = sEne(iSc)
  mat(iRow,iRow+1) = bEne(iSc)
  mat(iRow+1,iRow) = eMom(iSc)
  mat(iRow+1,iRow+1) = fMom(iSc)
  mat(iRow+1,2*nSc+1) = 1.0

  mat(2*nSc+1,iRow) = cDens(iSc)
  mat(2*nSc+1,iRow+1) = cVelc(iSc)

  knownVec(iRow) = (qHeat(iSc)*deltaZ + eex(iSc))
  knownVec(iRow) = (gMom(iSc)+mex(iSc))
  iRow=iRow+2
 enddo

```

```
27 end subroutine BuildMat
```

Listing 9.19: PDL for Build matrix system.

```
1  subroutine SolveSys
2
3   !Interface
4   in :: mat, knownVec
5   in :: iSolMethod
6   out :: deltaVelc, deltaDens, deltaPres
7
8   if iSolMethod = 1 then
9     call  DGESV
10  else if iSolMethod = 2 then
11    greeneMethod(mat,knownVec,deltaVelc,deltaDens,deltaPres)
12
13 end subroutine SolveSys
```

Listing 9.20: PDL for Solve matrix system.

9.17 Guidelines for code verification

A key point of the ENEA SQAP related to the development of a new computational tool is the clear definition of a test (verification) program, and a corresponding validation program. In the present thesis, only validation results are shown, for the sake of simplicity. Nevertheless, guidelines that were followed during the verification phase are reported here for the sake of completeness.

Verification is aimed at ensuring that the software correctly implements the desired functions. Contrary to design, which is conceptualized and presented top down, the code is implemented and tested bottom up.

More specifically, four types of tests have been implemented sequentially as the code was built: *Unit tests*, *Integration tests*, *Validation tests* and *System tests*.

Unit tests

Unit tests concentrate on each software component as implemented in the source code. *Unit tests* mostly rely on *white-box* testing, i.e. the testing strategy is derived from the procedural design of the single code units, as described in the PDL of section 9.16. *White-box* tests aim at detecting errors in the coverage of independent control paths, logical decisions, loop boundaries.

Unit testing is performed as coding is being carried out. Each code component is developed, reviewed and verified for correspondence to component-level design, before starting with the unit tests. Each test case requires a set of expected results to be manufactured. Driver routines are developed ad-hoc to perform unit tests, as each program component is not a standalone program. Stub routines replace components that are called by the one that is being tested.

Integration tests

Integration tests focus on the design and construction of the architecture. During this *integration test* phase, tests are mostly of the *black-box* type. Nevertheless, a limited number of *white-box* tests can be still performed to ensure full coverage of control paths.

Functional tests

Functional tests aim at validating requirements established as a part of software requirements analysis and explicitly stated in the SRS document. Validation criteria are indicated in the SRS itself. The successful verification of these criteria confirms that the software meets all functional, behavioural and performance requirements. At this stage, only *black-box* tests are executed (as the code was already *integrated*, i.e. built). At the same time, the source code was inspected for completeness and coherence with the formal requirements;

System tests

System tests aim at testing the software as a whole, in a given environment and with typical users.

For TIFONE, *physical* and *logical* tests were devised. From the *physical* point of view:

1. The behavior of a single sub-channel is tested against analytical models, first using constant thermophysical properties and then taking into account their variation;
2. The behavior for a small set of sub-channels is tested against an analytical model employing the computed mass transfer rates.
3. The convergence and stability requirements for the axial discretization step is assessed by a posteriori testing.

From the *logical* point of view:

1. The numbering and the assignment of geometrical and thermophysical properties to the various subchannels is carefully tested;
2. The correctness of the connectivity matrix is tested;
3. A full-core printout allows to assess the correct behavior of the `BuildGeom` routine.

Test plan

A test plan aims at promoting the orderly construction of the software and at identifying errors *during* the construction process, rather than afterwards. Testing activities are organized according to clear milestones. Indeed, as they are conducted *during* the code development phase, which is close to stringent deadlines, the progress of the activity must be measurable.

9.18 Preliminary validation

Validating the code against experimental data is of paramount importance to quantify the confidence in the code predictions within the aticipated validity domain. In this section, the very first comparison of TIFONE results with experimental data is presented, followed by guidelines for future work in this respect.

9.18.1 KALLA facility

Within the framework of the SESAME project, an experimental campaign aimed at investigating the IW flow and heat transfer was recently carried out at KALLA facility [199]. Specifically, the experiments provide detailed thermal measurements for the inter-wrapper flow and heat transfer in the gap between three SAs cooled by LBE. The experiments record is reported in a SESAME deliverable [151] and selected results are contained in a related paper [150].

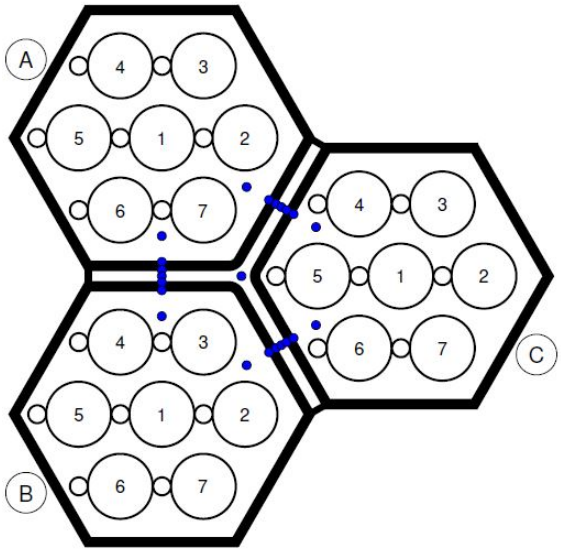

Figure 9.21: Thermo-couple location for each measurement level in KALLA facility, reproduced from [151].

Test section geometry

The main geometrical parameters of the KALLA inter-wrapper flow test section are reported in Table 9.8. These parameters have been specifically chosen according to a scaling of the MYRRHA-7 design.

Quantity	Unit	Value	Meaning
Outer dimensions			
FF	mm	65.00	Outer flat-to-flat distance
w	mm	2.0	Wall thickness
δ	mm	3.0	Gap width
Bundle dimensions			
D	mm	16.0	Rod diameter
L_{heat}	mm	600.0	Rod heated length
L_{tot}	mm	1400.0	Rod total length
P	mm	20.50	Rod pitch
d	mm	4.40	Wire diameter
H	mm	262.0	Wire pitch
W	mm	20.75	Wall distance
Ratios			
P/D	-	1.281	Pitch-to-diameter
H/D	-	16.375	Wire pitch-to-diameter
W/D	-	1.297	Wall-distance-to-diameter
Flow areas			
A_{bdl}	mm^2	1704.2	Bundle cnannels (A-C)
A_{int}	mm^2	73.6	Bundle internal sub-channels
A_{edge}	mm^2	152.9	Bundle edge sub-channels
A_{corner}	mm^2	57.5	Bundle internal sub-channels
A_{gap}	mm^2	331.9	Gap channel (D)
Hydraulic diameters			
$d_{h,bdl}$	mm	10.31	Bundle channels (A-C)
$d_{h,int}$	mm	9.1	Bundle internal sub-channels
$d_{h,edge}$	mm	11.6	Bundle edge sub-channels
$d_{h,corner}$	mm	9.1	Bundle internal sub-channels
$d_{h,gap}$	mm	5.85	Gap channel (D)

Table 9.8: Main geometrical parameters of the KALLA inter-wrapper flow test section. Values from [151].

Available measurements

The following measurements are available:

- The radial temperature distribution is measured at two selected axial locations with the sensor layout indicated in Figure 9.21.
- The axial temperature distribution is measured by six thermocouples placed along the only *corner* present in the setup.
- A movable Pitot tube is used to measure the local velocity profile at the outlet section of gap AB.

- The radial temperature distribution at the outlet of the test section is measured by six sensors placed along the gaps AC and BC, as well as by a movable probe attached to the above-mentioned Pitot tube. This information, combined with the outlet velocity profile, is employed to evaluate the mean outlet temperature.

9.18.2 Description of symmetric case 1

Cases 1 is *symmetric*, i.e. the three SAs are heated (and cooled) in the same way. The IW mass flow rate is equal to 0.686 kg/s, which is the largest among those considered and leads to turbulent flow conditions. For this case, measurement of the temperature and velocity profiles along the wing AB at the test section outlet are available. Wall temperature measurements are also available at two axial locations.

The boundary conditions adopted for TIFONE to reproduce the experimental setup are reported in Table 9.9. As a first approximation, the axial distribution of the heat flux was computed via a standalone ANTEO+ simulation, courtesy of Dr. Francesco Lodi (ENEA Bologna). It was verified that the total power discharged to the IW coolant was consistent with the available calorimetric measurement. Resorting to an external tool was necessary due to the unavailability of the actual heat flux distribution over the surfaces facing the IW gap. Indeed, for each surface, the inner and outer wall temperatures are only available at two axial locations, the measuring points being placed radially at half the length of the corresponding wing. These measurements therefore only allow to determine the heat flux at two points for each wall, which is not sufficient to identify the correct heat flux shape to be input in TIFONE[4]. Another possibility would have been represented by providing to TIFONE a heat flux distribution computed via CFD calculations performed on the KALLA setup [199]. However, it was preferred to use ANTEO+ due to the following reasons:

- ANTEO+ calculations can be prepared and performed in a shorter time;
- the final goal of the TIFONE code will be to run in synergy with multiple instances of a SA TH code such as ANTEO+, in order to simulate the thermal-hydraulics of the whole core of an LFR. The proposed application in the framework of the validation of TIFONE against data from the KALLA experiment would represent a scaled test case for the future application of TIFONE.

The discussion of the TIFONE results for case 1 offers an opportunity to describe the code behavior. First, the convergence of the flow split calculation is reported in Figure 9.22. It can be seen that an oscillatory solution was found for the first 20

[4]This is also due to the presence of wire spacers inside the SAs. The resulting heat flux distribution is non uniform, and the temperature measurement might be influenced by local effects, albeit of second order.

Quantity	Unit	Value	Meaning	Notes
$\dot{m}$	kg/s	0.686	Inlet mass flow rate	
T_{in}	°C	199.25	Inlet LBE temperature	
q_{tot}	kW	3.700	Total power to IW flow	
q''	kW/m^2	$f(z)$	Surface heat flux	From ANTEO+

Table 9.9: TIFONE input data for case 1.

iterations, after which the code automatically reduces the under-relaxation factor, thus leading to convergence in a few more iterations.

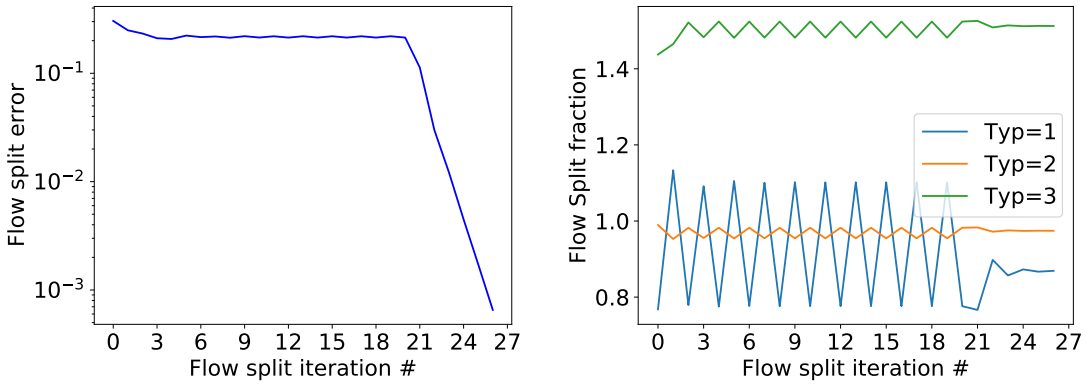

Figure 9.22: Convergence history for the flow split calculation, for case 1. After 20 iterations, the under-relaxation factor is halved, leading to the change in slope of the error curve. (left). Convergence of the flow split fraction for the three SC types occurring in the TIFONE calculations (right).

As far as the forced and mixed convection solutions are concerned, for case 1, the maximum value of Gr/Re^2 was $\sim 1.7 \cdot 10^{-3}$, which is slightly below $2 \cdot 10^{-3}$, the value suggested by Jackson for the onset of buoyancy effects, see section 9.8.5. Nevertheless, the stability of the forced convection solution was found to be severely limited in terms of maximum allowable Δz, a feature expected for the IW flow region also based on previous experience [12]. For this reason, the mixed convection solution - which was verified to be consistent to the forced convection solution for the limit of no buoyancy effects - was adopted. In the absence of the initialization provided by the forced convection calculation, the calculation was started from a linear axial temperature profile common to all SCs and computed based on energy conservation. The convergence of the mixed convection solution for four selected axial nodes (equally spaced along the axial length of the domain) is reported in Figure 9.23.

Figure 9.24 (left) shows the axial evolution of the Reynolds number for the three SC types considered in this simulation. Although the average Reynolds number

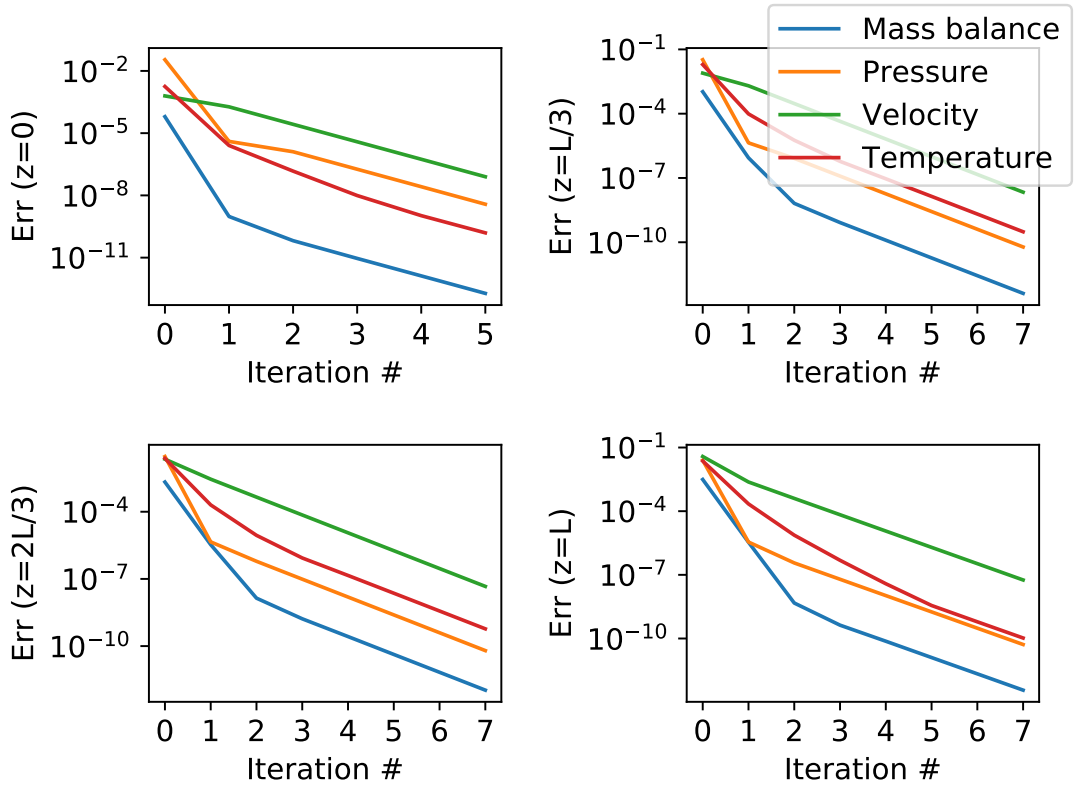

Figure 9.23: Convergence history for the mixed convection calculation, for case 1, at four axial locations. In the y axis label, L=700 mm indicates the total length of the test section.

is larger than 3200, the type 1 SC (i.e. the farthest SC from the center) falls within the transition range. Figure 9.24 (right) shows the axial evolution of the gap temperature. The discrepancy between computed and measured data could be associated to the lack of self-consistent coupling between ANTEO+ and TIFONE, but this should be addressed in more detail.

Since the main purpose of the TIFONE code is to determine the coolant and wall temperature distributions over the IW region, the availability of the outlet temperature profile measured via a movable Pitot probe is an important asset of the KALLA experimental dataset. Figure 9.25 shows the comparison between the computed and measured temperatures along the three wings. It should first be noticed that, due to the symmetric boundary conditions provided to the TIFONE code, the fact that the curve corresponding to the three wings are superimposed can be considered as a sanity check. As far as experimental data are concerned, the fine measurement of the temperature profile was only available along wing AB, whereas for wings AB and BC only three thermocouples were available. The comparison

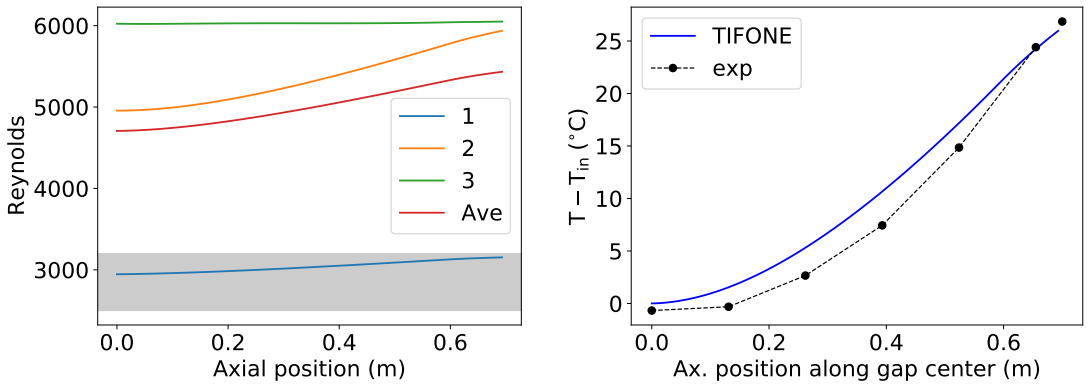

Figure 9.24: Axial evolution of the computed Reynolds number for the three SC types, for case 1. The average Reynolds number for the IW region is also plotted, and the grey area indicates the laminar-to-turbulent transition range (left). Computed and measured axial evolution of the temperature increase at the center of the IW region (right).

can be considered satisfactory, although a deviation in correspondence to the end of the gap (i.e. of the type 1 SC) is found.

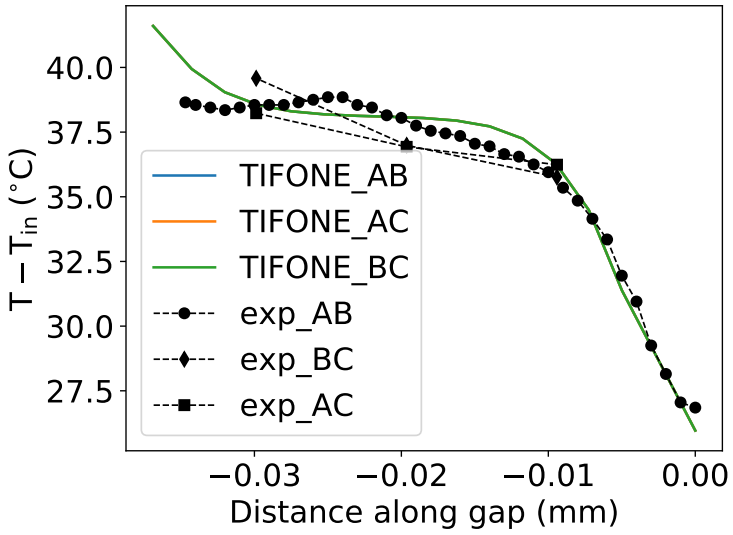

Figure 9.25: Measured and computed temperature profiles at gap outlet for case 1.

To investigate the origin of the deviation from the experimental behavior in correspondence of the type 1 SC, the computed and measured velocity profiles at the outlet section are compared in Figure 9.26. The plot shows good qualitative

agreement between the computed and measured velocity profiles along wing AB. The most noticeable deviations is the low computed velocity for the type 1 SC. It is supposed that the reason behind the larger than measured outlet temperature in the corresponding SC is indeed associated to that lower velocity. An improvement of the friction factor formulation adopted for the type 1 SC could improve the agreement. However, the impact of the friction factor correlation should be disentangled from other deviations which are associated to the local nature of the velocity measurement (whereas the SC method describes the axial evolution of the average temperature per SC. These further studies are left for future work.

Another observed deviation from the experimental behavior is the excessive velocity difference between the center of the IW region and the nearby SC. This calls for a review of the assumptions related to the eddy diffusivity, which for the sake of simplicity has been simply neglected here. This is also left for future work.

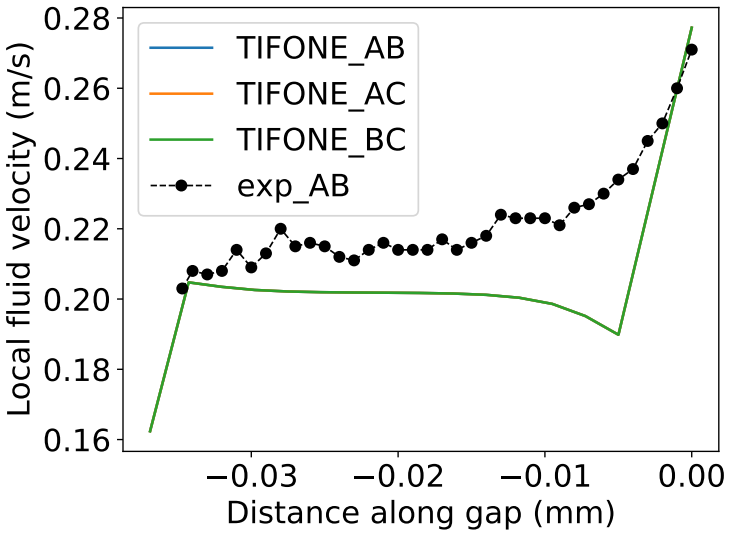

Figure 9.26: Measured and computed velocity profiles at gap outlet for case 2.

The available wrapper temperature measurements are compared to the computed values in Figure 9.27. In this respect, the agreement is satisfactory, although it can be noticed that the measured discrete temperatures are not symmetric, thus pointing out the presence of local effects, possibly related to the presence of wire spacers.

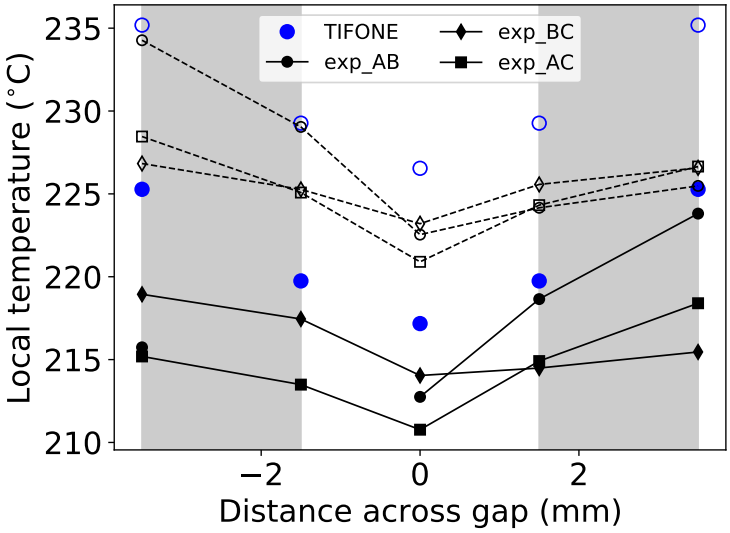

Figure 9.27: Measured and computed wrapper and coolant temperatures at locations indicated in Figure 9.21. Full symbols indicate the first measurement level ($z = 393$ mm), empty symbols indicate the second measurement level ($z = 524$ mm). For the sake of clarity, TIFONE results for the AB wing only are reported. Due to the symmetric simulation setup, the values computed for BC and AC are identical - within the imposed tolerance for the calculation.

9.18.3 Other symmetric cases

Case 4

Case 4 is symmetric, with a lower flowrate with respect to case 1 (see Table 9.10) yet still large enough to guarantee turbulent conditions in all SCs except the type 1 SCs, as shown in Figure 9.28 (left). In view of these characteristics, the results are expected to be similar to case 1 in terms of quality of the agreement. Indeed, the trend of the discrepancy between the computed and measured axial temperature profile along the gap shown in Figure 9.28 (right) is similar to the one shown in Figure 9.24, again being possibly associated to the not fully consistent axial shape of the heat flux provided to the code.

Similarly, Figure 9.29 shows a very good agreement of the computed outlet temperature profile, while the velocity profile is similar to the one shown in Figure 9.26.

Quantity	Unit	Value	Meaning	Notes
$\dot{m}$	kg/s	0.517	Inlet mass flow rate	
T_{in}	°C	199.2	Inlet LBE temperature	
q_{tot}	kW	3.010	Total power to IW flow	
q''	kW/m^2	$f(z)$	Surface heat flux	From ANTEO+

Table 9.10: TIFONE input data for case 4

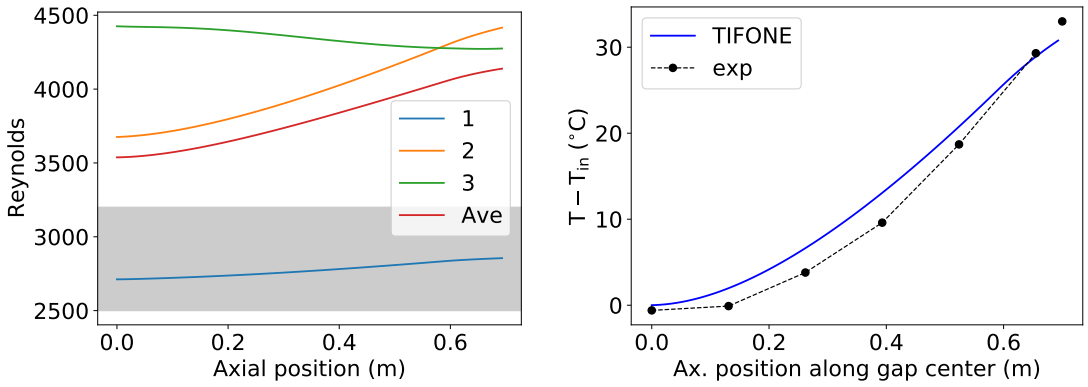

Figure 9.28: Axial evolution of the computed Reynolds number for the three SC types, for case 4. The average Reynolds number for the IW region is also plotted, and the grey area indicates the laminar-to-turbulent transition range (left). Computed and measured axial evolution of the temperature at the center of the IW region (right).

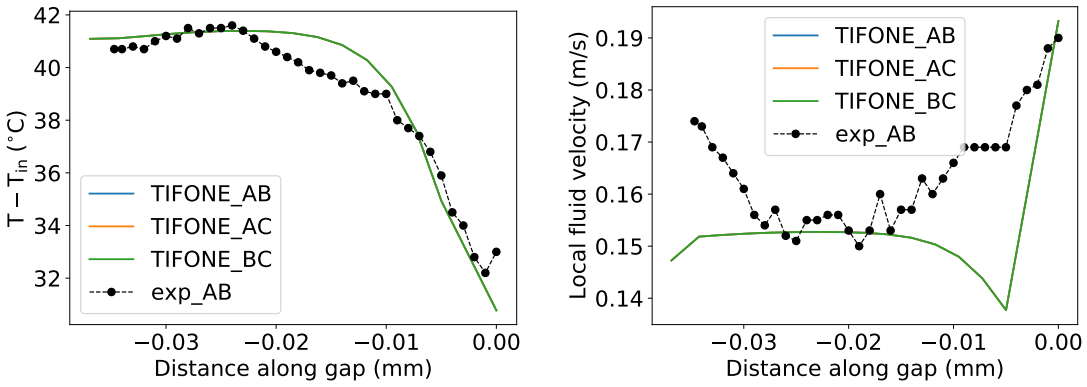

Figure 9.29: Measured and computed temperature (left) and velocity (right) profiles at gap outlet for case 4.

Case 6

Case 6 is again symmetric, with a lower flowrate with respect to case 4 (see Table 9.11), so that now the flow is laminar everywhere except in type 2 SCs, where it falls within the transition region, as shown in Figure 9.30 (left). It is therefore interesting to assess the code capabilities in this different flow regime, which is still relevant for the ALFRED IW region. The computed temperature profile along the gap shows again the expected discrepancy with respect to experimental data, possibly due to the approximations made concerning the heat flux entering the IW region.

It is interesting to notice that also in this case the agreement on the temperature profile is good, as is the one on the velocity profile, with the exception of type 1 SCs, see Figure 9.31.

Quantity	Unit	Value	Meaning	Notes
$\dot{m}$	kg/s	0.342	Inlet mass flow rate	
T_{in}	°C	199.1	Inlet LBE temperature	
q_{tot}	kW	2.160	Total power to IW flow	
q''	kW/m^2	$f(z)$	Surface heat flux	From ANTEO+

Table 9.11: TIFONE input data for case 6

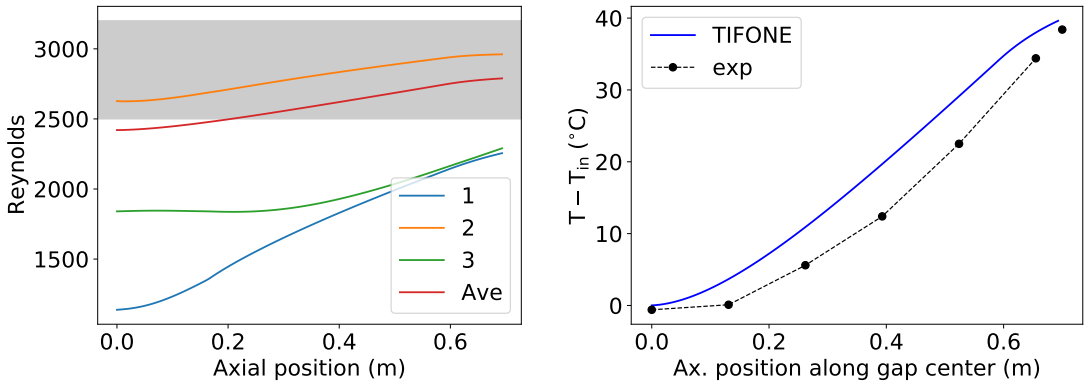

Figure 9.30: Axial evolution of the computed Reynolds number for the three SC types, for case 6. The average Reynolds number for the IW region is also plotted, and the grey area indicates the laminar-to-turbulent transition range (left). Computed and measured axial evolution of the temperature at the center of the IW region (right).

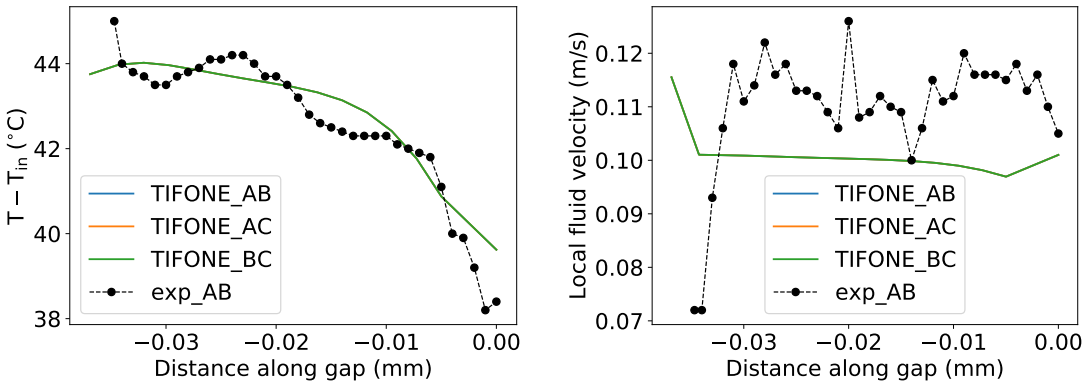

Figure 9.31: Measured and computed temperature (left) and velocity (right) profiles at gap outlet for case 6.

Case 8

Case 8 is again symmetric, with a lower flowrate with respect to case 6 (see Table 9.12), so that now the flow is laminar everywhere, as shown in Figure 9.30 (left). The computed temperature profile along the gap shows again the expected discrepancy with respect to experimental data, which however appears more significant with respect to the previous case. Again, it is postulated that this is due to the approximation made concerning the heat flux entering the IW region, but further investigations are envisaged in this respect.

For this latter case, the temperature profile is not well described, the slope being steeper for the experimental data with respect to the computed data, see Figure 9.33. Although this deserves further attention and study, it is believed that this could be associated to the onset of significant buoyancy-induced recirculation in the test section, which is plausible due to the very low flow rates here found. In this case, this validation case would fall outside of the anticipated validity domain of TIFONE. Velocity measurements along the AB wing were not available for this case and are therefore missing in Figure 9.33.

Quantity	Unit	Value	Meaning	Notes
$\dot{m}$	kg/s	0.17	Inlet mass flow rate	
T_{in}	°C	199.1	Inlet LBE temperature	
q_{tot}	kW	1.170	Total power to IW flow	
q''	kW/m^2	$f(z)$	Surface heat flux	From ANTEO+

Table 9.12: TIFONE input data for case 8

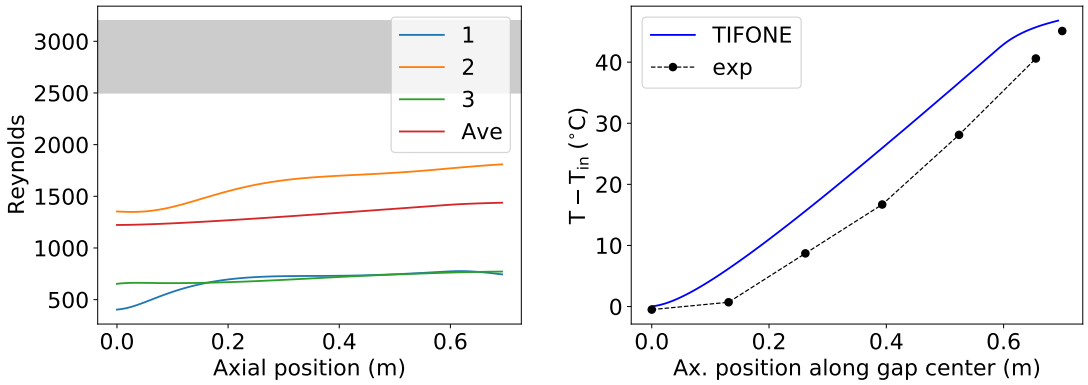

Figure 9.32: Axial evolution of the computed Reynolds number for the three SC types, for case 8. The average Reynolds number for the IW region is also plotted, and the grey area indicates the laminar-to-turbulent transition range (left). Computed and measured axial evolution of the temperature at the center of the IW region (right).

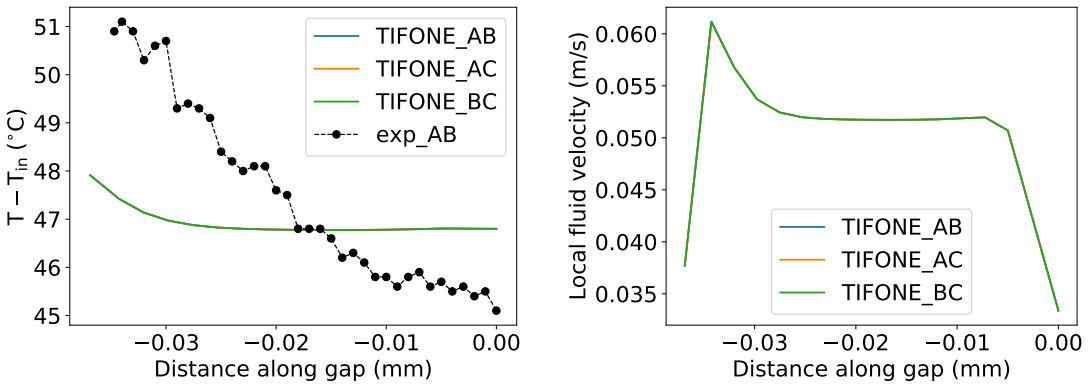

Figure 9.33: Measured and computed temperature (left) and velocity (right) profiles at gap outlet for case 8.

9.18.4 One asymmetric case

Case 93

Case 93 is the only asymmetric case (i.e. where the three neighboring SAs to the IW region do not share the same thermal-hydraulic inputs) for which detailed velocity and temperature measurements are available. In this case, for the sake of simplicity, the heat flux flowing from each side of the IW region is assumed to be uniformly distributed, with the specific values tuned in order to match the measured power repartition based on outlet temperature measurements. Indeed, ANTEO+ is currently only capable to handle a single FA with the surrounding gap region, which is considered adiabatic with respect to the surroundings. For this reason, it would not yield correct results if used for a physical setup where inter-SA heat transfer is significant, as it is the case for case 93.

The mass flow rate is the same as case 4, see Table 9.13, yielding a turbulent flow regime in all SCs with the exception of the ones of type 1, see Figure 9.34 (left). Somewhat surprisingly, notwithstanding the assumption of uniformly distributed heat flux, the temperature profile along the gap is retrieved correctly in this case. This could be associated to the fact that, for case 93, one of the SAs is not heated (i.e. is heated by the IW flow itself), which could compensate for the nonuniform heat flux expected along the heated SAs, see Figure 9.30 (right).

For this latter case, considering the uncertainties on the input data, the computed temperature profile can be said to be in good agreement with the measured one, see Figure 9.35 (left), with the relative magnitudes of the average temperatures for the three wings correctly retrieved. As far as the velocity profiles are concerned, it can be stated that the trend along wing AB is correctly retrieved, with uncertainties similar to the ones found in cases 1 and 4, see Figure 9.35 (right). Although measurements along the wings BC and AC are not available, the computed values are consistent with the expected acceleration of the fluid due to the larger density variation (which follows from the larger heat flux).

Quantity	Unit	Value	Meaning
$\dot{m}$	kg/s	0.516	Inlet mass flow rate
T_{in}	$°C$	198.98	Inlet LBE temperature
q_{tot}	kW	2.720	Total power to IW flow
q_{AB}	kW/m^2	10.11	Heat flux from SA A to gap AB
q_{BC}	kW/m^2	22.80	Heat flux from SA B to gap BC
q_{AC}	kW/m^2	21.01	Heat flux from SA A to gap AC
q_{BA}	kW/m^2	10.11	Heat flux from SA B to gap BA
q_{CB}	kW/m^2	22.80	Heat flux from SA C to gap CB
q_{CA}	kW/m^2	21.01	Heat flux from SA C to gap CA

Table 9.13: TIFONE input data for case 93

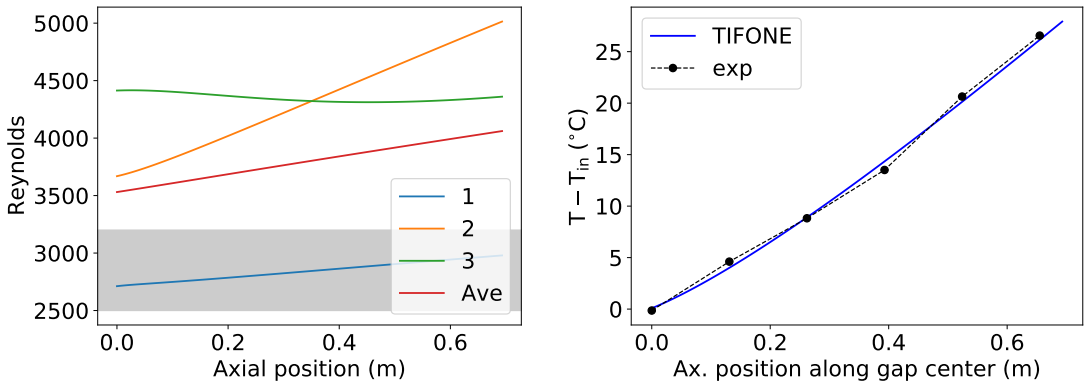

Figure 9.34: Axial evolution of the computed Reynolds number for the three SC types, for case 93. The average Reynolds number for the IW region is also plotted, and the grey area indicates the laminar-to-turbulent transition range (left). Computed and measured axial evolution of the temperature at the center of the IW region (right).

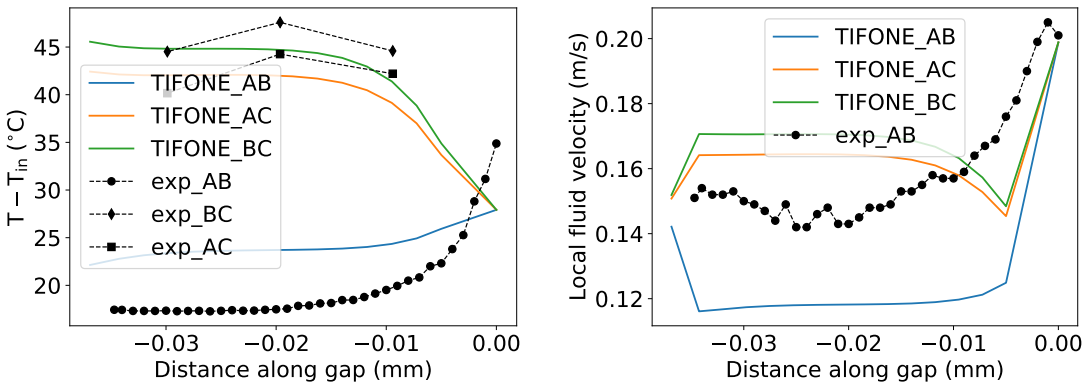

Figure 9.35: Measured and computed temperature (left) and velocity (right) profiles at gap outlet for case 93.

9.19 Conclusions and perspective

The design, development and preliminary validation of a new DOC, TIFONE code, was successfully carried out. The foregoing chapter not only described the models, methods and validation for the TIFONE code, but also reported a robust approach for the quality-compliant development of a DOC aimed at supporting the core design of HLMCRs.

While these results are encouraging, further work is necessary to extend the applicability of TIFONE and to validate its capabilities of reproducing experimental data within the specified validity range.

As far as the code extension is concerned, a version 1.1 of TIFONE is foreseen, which is capable of launching many instances of a SA code such as ANTEO+ (one for each SA in the core), obtaining in this way a full-core TH solution which can be effectively support core design.

As far as validation is concerned, two lines of activity are foreseen:

1. further analysis of the KALLA experimental dataset, including the retrieval of information for all the $\sim$ 100 experiments performed, is necessary. In this respect, the discrepancies found between measurements and calculations, especially in terms of the axial temperature profiles, should be further investigated. Moreover, further analysis of the velocity measurements, possibly driving a different choice of the friction factor correlations, is envisaged;
2. other available experimental datasets will be explored to extend the range of parameters for which the code performance are qualified.

Concerning point 2., opportunities to validate the TIFONE code could arise from at least two other experimental facilities where IW flow and heat transfer experiments have been performed. These experiments are briefly described below.

PLANDTL facility

Experiments to assess the effect of the IW flow and heat transfer on the core thermal-hydraulics have been performed in the PLANDTL facility [142]. The experimental layout consists in 7 SAs and of the corresponding IW region (including gaps between the SAs and the barrel, as discussed in section 9.9.3). The locations of the temperature sensors at the outlet of the test section are shown in Figure 9.36.

Experiments by Liang et al.

In [110] experimental data in support of the numerical investigation of the inter-wrapper flow characteristics in LMCRs are reported. The experimental setup is similar to the KALLA experiments. The working fluid is water and the range of Reynolds numbers investigated is $500 < Re < 7500$. This experimental and numerical study has led to the derivation of a novel formulation for the friction factor for the geometrical configuration relevant for IW flow. This friction factor

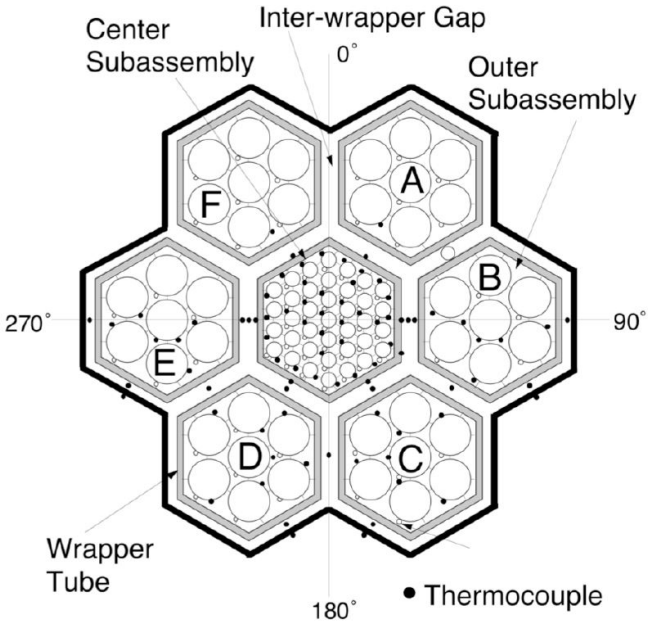

(a) Seven-Subassembly Core

Figure 9.36: Thermo-couple location at the outlet of the test section in PLANDTL facility, from

correlation has been included among the ones available for use in TIFONE, see section 9.8.2. The data included in [110] can be used for validating the hydraulic calculation in TIFONE.

Chapter 10

Benchmark of the FRENETIC code

A multi-physics (neutronic and thermal-hydraulic) code, Fast REactor NEutronics/ThermalhydraulICs (FRENETIC), was recently developed at Politecnico di Torino. The code implements simplified models for both neutronics and thermal-hydraulics: coarse mesh diffusion, and 1D advection-diffusion for each SA (coupled together via an estimated inter-SA thermal resistance), respectively. FRENETIC is aimed at the fast, multi-physics simulation of LFRs in both steady state and transient conditions. In view of the continuous application and qualification of this code, benchmarks against more detailed codes that can be considered as a reference are vital. However, multi-physics simulations performed with detailed codes (such as coupled CFD-Monte Carlo) still involve a prohibitive usage of computational resources. For this reason, a more easily accessible strategy consists in comparing the results of FRENETIC against results of single-physics codes. This requires a specific benchmark strategy to be devised, to separate the effects associated to the two physics, thus providing a fair comparison.

In this chapter, an approach for the multi-physics benchmark of the FRENETIC code is presented, as well as the corresponding results. After a brief introduction on the FRENETIC code provided in section 10.1, the original benchmark strategy here proposed is described in section 10.2. An overview concerning the generation of the cross-section libraries necessary for the coarse-mesh diffusion module of FRENETIC is provided in section 10.3. Finally, the neutronic and thermal-hydraulic part of the benchmark are described in sections 10.4 and 10.5, respectively, and conclusions and perspective for this activity and for the development of the FRENETIC code itself are proposed 10.6.

This chapter mostly derives from a rearrangement of preparatory material for the article [137] and for the presentation [79], and has been performed in collaboration with prof. Sandra Dulla, Ing. Nicolò Abrate and Ing. Domenico Valerio (PoliTo).

10.1 Introduction

10.1.1 Context and motivation

Within the framework of Italian activities aimed at deploying the LFR technology, during the last years Politecnico di Torino has been developing the FRENETIC code for the multiphysics analysis of liquid-metal cooled cores [18]. The code aims at the NE and TH coupled simulation of the steady state and transient behavior of the full core of LMCRs adopting a closed SA design. To achieve this ambitious goal while keeping the simulation time reasonably low, FRENETIC adopts simplified physical models, namely:

- a multigroup neutron diffusion model, spatially discretized with a coarse mesh nodal method at the assembly level;
- a 1D advection/diffusion model for the coolant flowing within each assembly, accounting for the inter-assembly heat transfer via a thermal resistance model to achieve a quasi-3D solution.

In the past years, the individual modules of the FRENETIC code have been benchmarked against other computational tools and validated against experimental data (e.g. TH validation against RELAP [218]). More recently, the multi-physics capabilities of the code have been validated against experimental data from the EBR-II SHRT-45R test in the frame of a Coordinated Research Project of the International Atomic Energy Agency [25]. That activity allowed to identify some necessary developments to be carried out in FRENETIC, such as the inclusion of a model for the photon and decay heat[1].

In view of the continuous testing and validation of FRENETIC, it is of interest to perform a steady-state benchmark against more detailed numerical codes that allow to obtain accurate solutions at the fuel pin level, and can therefore be regarded as a reference. Specifically, the following two codes have been selected:

- a full-core neutron transport code based on the Monte Carlo method (Serpent-2 [109]);
- a Computational Fluid Dynamics (CFD) code (OpenFOAM [206]).

Since the computational cost associated to a full-core coupled Serpent-OpenFOAM simulation remains prohibitive, even in steady state, a direct comparison of the FRENETIC results with a full-core solution from the detailed model remains prohibitive. For this reason, a benchmark strategy that circumvents this problem has been devised and will be presented in section 10.2.

[1] It is worth mentioning that the photon and decay heat model has been recently implemented in FRENETIC [24] and its validation is currently ongoing.

10.1.2 NE-TH coupling in FRENETIC

The NE-TH coupling in FRENETIC is achieved by exchanging, at time steps properly defined in accordance to the time scales of the phenomena at hand, information regarding the power distribution (NE information provided to the TH module) and the temperature distribution (TH information provided to the NE module). Such information is homogeneous at the level of the SA on the horizontal plane for different heights, consistently with the coarse mesh neutronic approach, and interpolations are performed if more spatially refined data are required. The temperature feedback on neutronics is evaluated by direct modification of the multi-group cross sections starting from a database at different temperatures for both fuel and coolant and performing multidimensional interpolations of the type:

$$\Sigma\left(T_f, T_c\right) = \Sigma\left(T_{f,0}, T_{c,0}\right) + \frac{\partial \Sigma}{\partial T_f}\left(T_f, T_{f,0}\right) + \frac{\partial \Sigma}{\partial T_c}\left(T_c - T_{c,0}\right) \tag{10.1}$$

where the derivatives are evaluated as incremental ratios on the existing temperature grid. The cross section values in the database are generated by means of Serpent runs at different temperatures.

10.2 Benchmark strategy

As discussed above, the Serpent-OpenFOAM coupling suffers from the fact that the neutronic calculation is carried out at the full-core level, with manageable CFD simulations within the time scale of the present thesis are limited to a single SA. Therefore, the temperature distribution obtained in OpenFOAM is not directly usable to provide the full-core temperature distribution to Serpent for a k_{eff} calculation. To compensate for this, the full-core temperature distribution can be provided by a FRENETIC run.

Considering the objectives of the benchmark activity, the required inputs for a FRENETIC run and the difficulties associated with a full-core Serpent-OpenFOAM simulation, the following strategy was proposed:

1. Serpent runs at different homogeneous temperatures are performed to generate the multigroup cross sections to be used in FRENETIC.
2. The nuclear data generated are used in FRENETIC to solve the full-core coupled problem, providing both the power map and the temperature distribution.
3. The temperature distribution is passed to Serpent, so that a NE reference simulation with the same temperatures as the FRENETIC run can be obtained. This choice allows to perform a consistent neutronic benchmark of FRENETIC.
4. The power distribution computed by Serpent for selected SAs is used as an input for OpenFOAM calculations. The radial boundary conditions to the selected SA are provided by the FRENETIC TH result.
5. The resulting CFD calculation is compared to the FRENETIC result for the selected SA, as a benchmark on the single SA performed assuming a fixed internal power source.

These five steps are graphically summarized in Figure 10.1.

To perform step 3, a further simplification is necessary. Indeed, if the full-core temperature distribution computed by FRENETIC was directly passed to Serpent, the latter would identify each single FRENETIC mesh as a separate universe, with its own temperature and composition, resulting in a prohibitive computer memory requirement. The proposed solution to this issue is to identify, radially, a set of concentric regions, each characterized by a single temperature value (verifying that the maximum temperature difference between SAs within the same radial region was below 1 K), as schematically shown in Figure 10.2. Axially, all the materials composing the regions below the active zone have been assumed to be at the inlet temperature). Similarly, regions above the active zone share the same temperature, which is equal to the average core outlet temperature. The active region of each SA has instead been subdivided into 10 axial segments, each characterized by the corresponding average temperature evaluated by FRENETIC. This approach allowed to

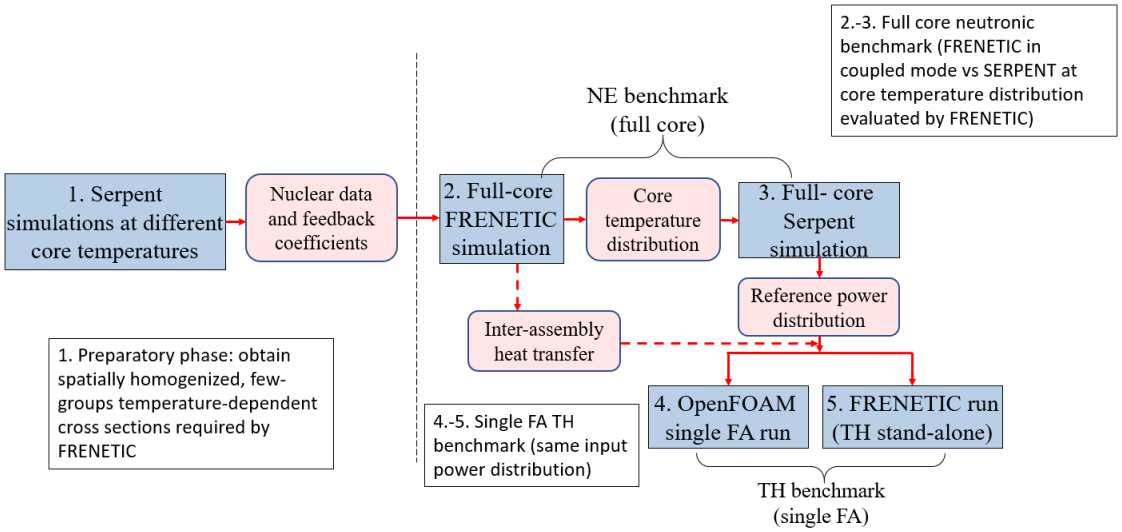

Figure 10.1: Schematic of the proposed benchmark strategy for FRENETIC vs. Serpent-OpenFOAM.

generate a more limited number of Serpent regions, thus enabling the k_{eff} calculation in Serpent with a physically significant temperature distribution. An example of a typical axial temperature distribution computed by FRENETIC for both the fuel and the coolant in three different core regions is shown in Figure 10.3. The step-like shape of the fuel temperature distributions derives from the coarse-mesh nodal method employed for the neutronic calculations, which computed a uniform temperature distribution for each NE axial node.

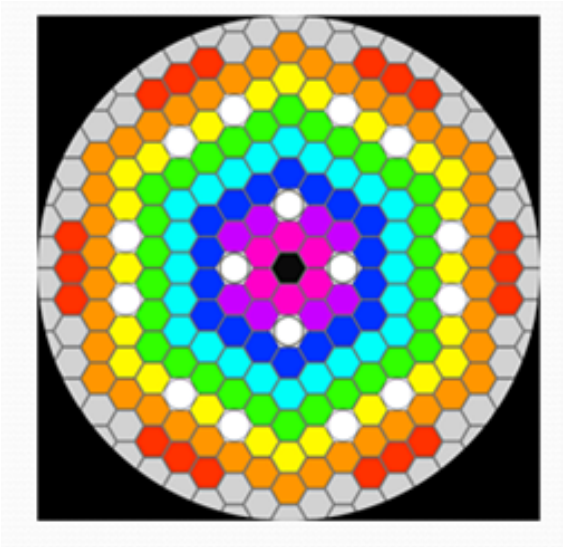

Figure 10.2: Example of the concentric regions assumed to be at the same temperature when performing the Serpent simulation.

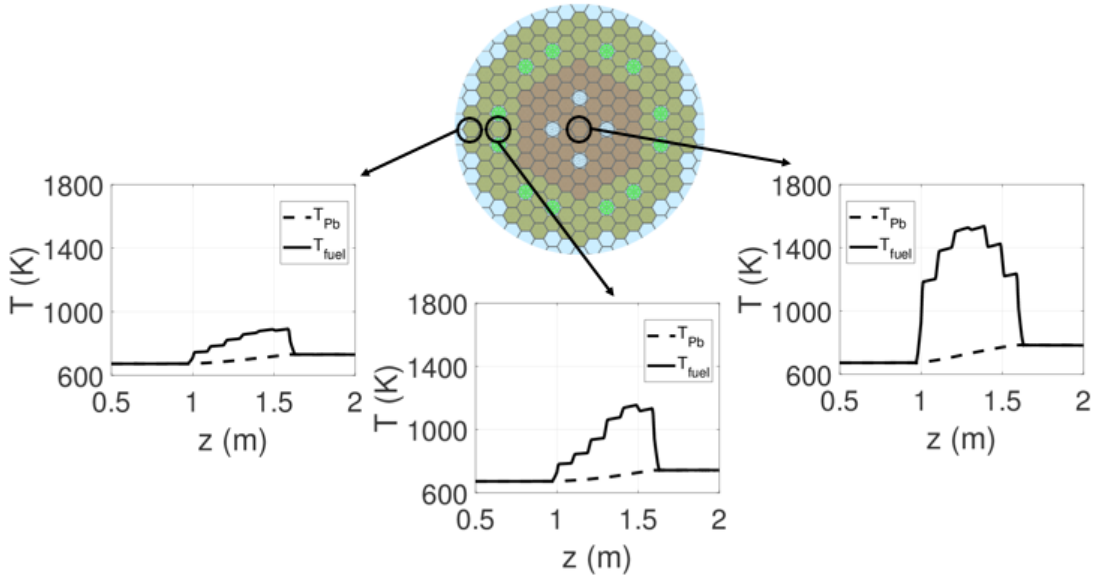

Figure 10.3: Axial temperature for fuel and coolant in three different SAs of the ALFRED core calculated with FRENETIC.

10.3 Generation of cross section library

The first step of the procedure consists in generating a library of cross sections at different temperatures, to be used in the FRENETIC multigroup diffusion calculation. In the following, the strategy adopted to generate the above-mentioned

library are summarized.

10.3.1 Serpent-2 model for multi-group nuclear data evaluation

As mentioned above, running the FRENETIC code requires to generate a consistent set of nuclear data [25]. In particular, few-group cross sections are needed for each of the materials present in the reactor. For this purpose, the Monte Carlo code Serpent-2 [109] is used to collapse the continuous energy data into six groups and to homogenize them over the reactor heterogeneous regions. The collapsing (in energy) and homogenization (in space) procedure is carried out (similarly to the previously descripted work) by means of a detailed 3D model of the ALFRED reactor, see Figure 10.4. The core geometry and material composition are consistent with the End Of Cycle (EOC) configuration (fully withdrawn control rods) provided by [72]. The correct implementation of the ALFRED geometry and material composition in the Serpent model has been assessed by means of a benchmark against a pre-existing ERANOS model.

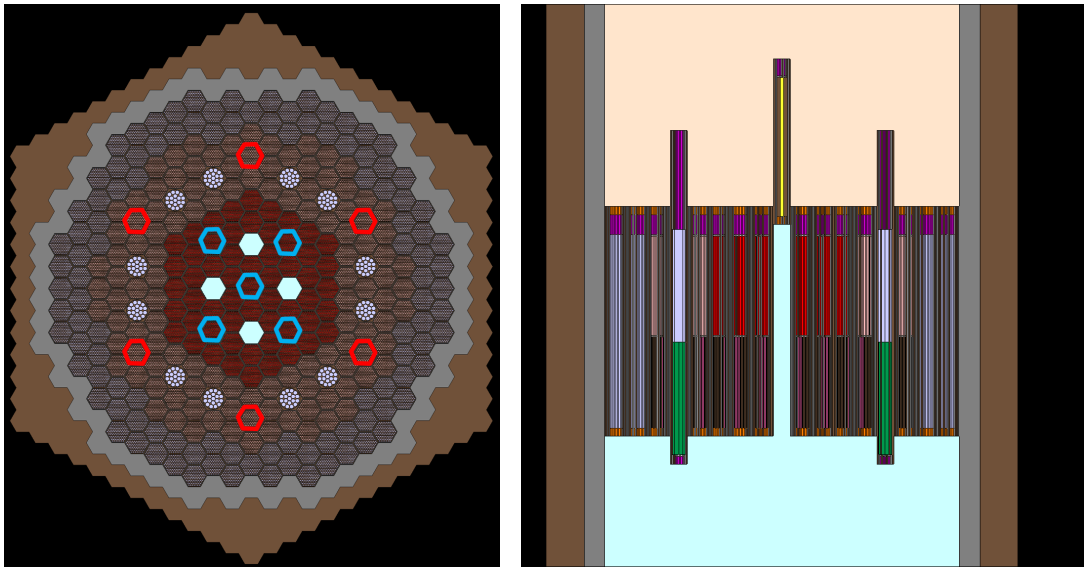

Figure 10.4: Radial (left) and axial (right) view of the ALFRED configuration simulated in Serpent.

As far as the statistical convergence of the simulation is concerned, input parameters have been tuned according to convergence studies. In particular, 500 inactive cycles and 1000 active cycles have been employed, with 10^6 particle histories per cycle. These simulation settings guarantee a good fission source convergence. The adopted indicators were implicit and explicit k_{eff} and Shannon entropy. After a Serpent simulation has correctly been set up, suitable tallies (both in energy and in

space) must be defined to generate the spatially homogenized and energy collapsed cross sections. The procedure is then repeated assuming different temperatures for coolant and fuel to reconstruct the cross section database required by FRENETIC.

10.3.2 Energy collapsing and spatial homogenization procedures in Serpent-2

Energy collapsing

As far as the energy collapsing is concerned, the calculation of effective cross sections, as well as other nuclear data, is carried out by means of an estimate of the required reaction rate on an energy interval and then dividing it by the flux average on the same interval. This ratio provides an effective cross section in that energy range that (for an infinite medium) exactly preserves the reaction rate. The choice of the boundary of such energy intervals is a delicate task which can be performed e.g. by observation of the neutron spectra in the various regions of the reactor core. Figure 10.5 reports such neutron spectra evaluated with the Serpent-2 run at 673 K. In the same figure, the flux subdivisions adopted for a previous work have been shown, allowing to highlight a relevant limit of that energy discretization: the fifth group, with upper energy bound at around 10^{-2} MeV, is able to describe the neutron behavior in the fuel regions, but it appears not adequate for the description of the outer regions. In fact, the presence of a larger portion of neutrons at thermal energies in the reflectors and dummy elements is completely disregarded if a single energy group is assumed down from 10^{-2} MeV.

To fix this issue an additional energy group has been added, considering that six groups are sufficient to approximate the behavior of the energy distribution within the various materials. The resulting energy group boundaries are reported in Table 10.1.

Energy group	Upper E bound (MeV)	Lower E bound (MeV)
1	20	1.353
2	1.353	$1.832 \cdot 10^{-1}$
3	$1.832 \cdot 10^{-1}$	$6.738 \cdot 10^{-2}$
4	$6.738 \cdot 10^{-2}$	$9.119 \cdot 10^{-4}$
5	$9.119 \cdot 10^{-4}$	$2 \cdot 10^{-5}$
6	$2 \cdot 10^{-5}$	$1 \cdot 10^{-11}$

Table 10.1: Six-group energy boundaries adopted to perform the macroscopic cross section energy collapsing.

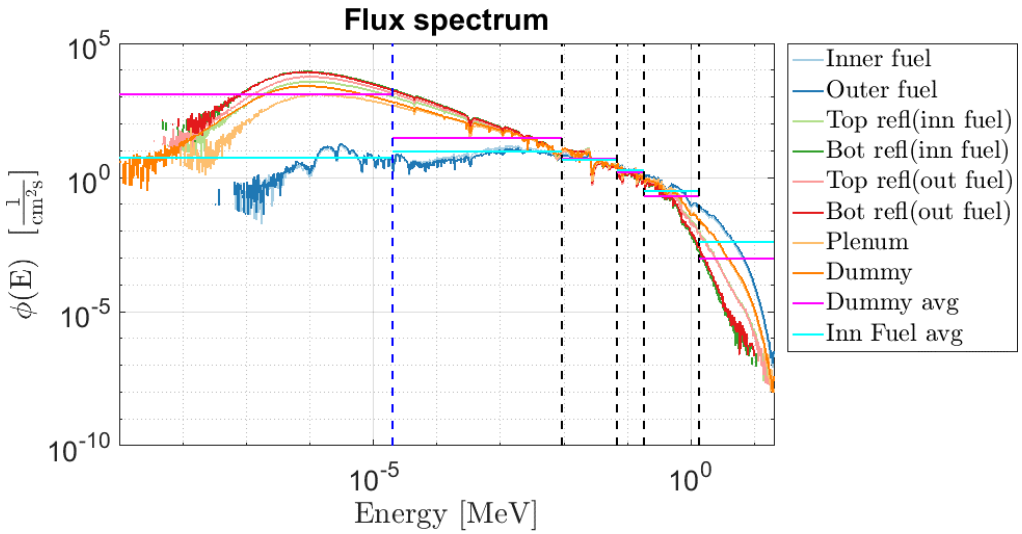

Figure 10.5: Neutron flux spectra computed by Serpent for selected regions of the core. Black dashed lines identify the 5-group energy subdivision originally adopted, while the blue dashed line identifies the additional group added to better account for the reflector spectrum. Reproduced from [137] with permission.

Spatial (axial and radial) homogenization

The energy collapsed cross sections need to be homogenized on spatial regions consistently with the structure of the FRENETIC code (i.e. homogeneous over each hexagonal SA and axially heterogeneous, according to the neutronic coarse meshing). Starting from the core modelling in Serpent as detailed in Figure 10.4, some regions (namely, the ones far from the fission source) have been merged in a single universe for the cross section tally, in order to achieve a better statistics. Specifically, the external lead (in brown in Figure 10.4), the barrel (in dark grey) and the dummy element region (in light grey), are each considered as a unique radial region. Moreover, the 12 control rods are grouped together as a single detector. The same choice has been made for the 4 safety rods. For the inner fuel, instead, it has been assumed that cross sections averaged on a subset of SAs (indicated in blue in Figure 10.4) could be representative of the entire zone. The same strategy has been adopted for the outer fuel region, for which the representative SAs are indicated in red. It should be noticed that SAs considered for the homogenization are the ones surrounded by SAs of the same type. This choice was based on a compromise between a homogenization over the whole inner and outer fuel rings and an assembly-wise homogenization, which would certainly provide a higher but probably unnecessary detail level.

The few-group cross sections evaluated by Serpent have been at first homogenized axially according to the finest achievable discretization, which takes into

account all the different regions, as shown in Figure 10.6. However, the axial discretization employed for the FRENETIC calculation is in general different - and coarser - with respect to the one introduced in the transport simulation. This is due to the requirement of avoiding excessively optically thin regions, which would hinder the convergence of the nodal method employed for the spatial solution of the diffusion problem in FRENETIC. Each of the coarse axial regions defined in the FRENETIC model requires a single spatial value for the multi-group cross sections, which should therefore be mapped to the ones computed by the transport model for the fine subdivisions composing that coarse axial region. This is performed by means of a suitable spatial homogenization procedure, which is carried out in such a way as to preserve the reaction rate for each material.

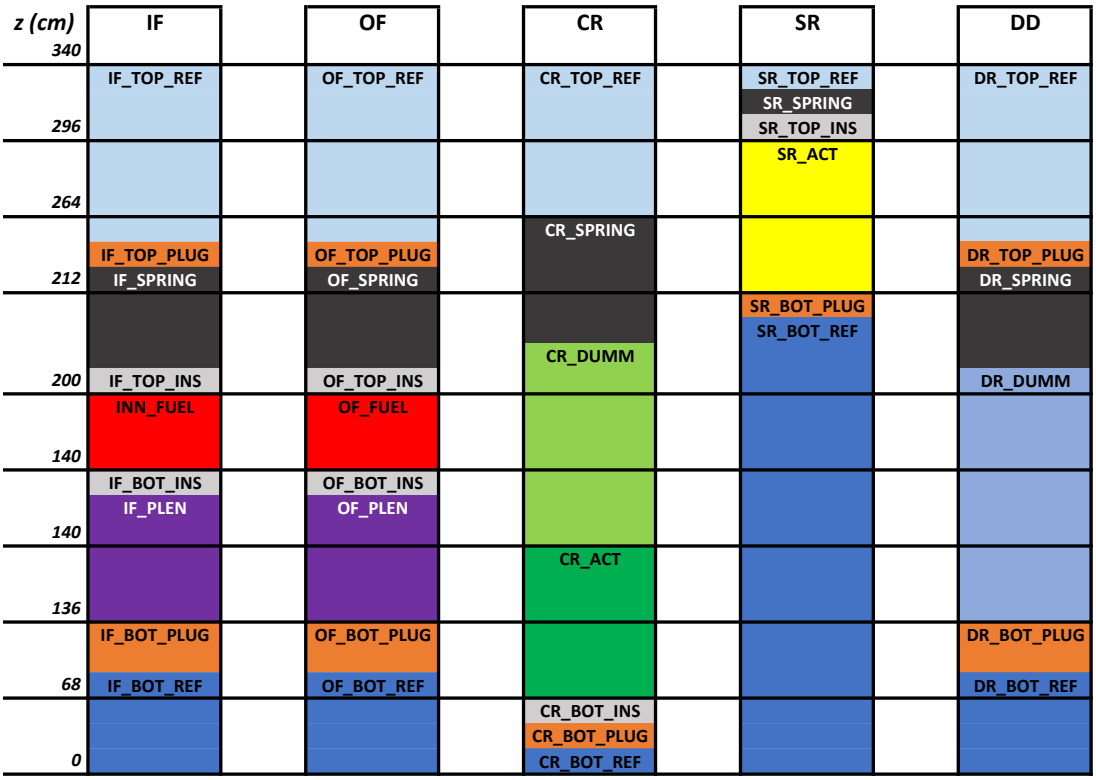

Figure 10.6: Axial discretization for the FRENETIC model (black lines) on top of fine Serpent axial discretization for each radial region.

This leads to the calculation of a new set of cross sections that are averaged on the flux of each material in the "macro-region", i.e. in the coarse axial mesh.

10.3.3 Temperature dependence of cross sections

A final remark concerns the evaluation of nuclear data at different temperatures. This is associated to the fact that the FRENETIC code evaluates the thermal feedback by interpolating nuclear cross sections between at least two temperatures according to the local temperature of the fuel and coolant. The fuel and coolant temperatures considered for the generation of this cross section library are listed in 10.2.

T_{fuel} (K) \ $T_{coolant}$ (K)	673	1073	1473
673	×		
1073	×	×	
1473	×	×	×

Table 10.2: Temperatures values adopted for the Serpent runs used to evaluate the few-group cross sections. The x indicate the runs actually performed.

The table lower triangular layout is due to the fact that the fuel temperature is always greater than the coolant one, at least for the intended applications of FRENETIC. The temperature of the structural materials is specified in Serpent according to the arithmetic average of the coolant and fuel temperatures.

10.4 Neutronic benchmark

10.4.1 FRENETIC simulation setup

The nuclear dataset obtained by means of the procedures outlined in the previous sections has been employed to feed the neutronic model of the FRENETIC code. The new dataset is distributed according to the radial "zoning" presented in Figure 10.7. The axial "macro-regions" indicated in Figure 10.6, which are each characterized by a single spatial value of the cross section, are then subdivided in a number of sub-nodes which is sufficient to ensure the grid independence of the NE solution.

The barrel and external lead have been simulated in FRENETIC by adding fictitious SAs corresponding to the latter two regions. In this way, the radial "zoning" of the core has been made fully consistent with the one employed in the Serpent model.

To verify the correct implementation of the ALFRED NE model in FRENETIC, the results obtained using the standalone NE module (setting the temperatures of all the materials in the core at 673 K) were compared to the corresponding Serpent calculations performed during the generation of the cross sections library. Although

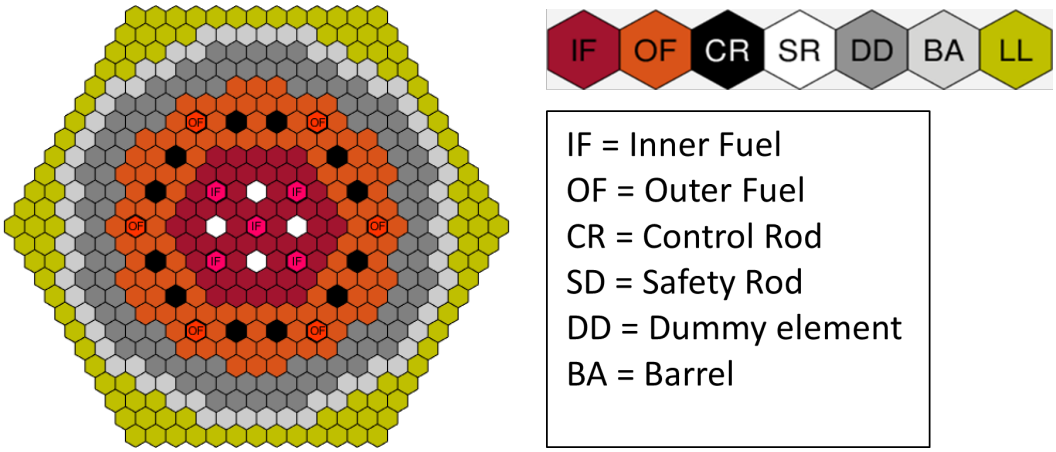

Figure 10.7: Radial scheme of the FRENETIC model of the ALFRED core.

a photon transport model is now available in FRENETIC, it has been turned off for the purpose of guaranteeing a fair comparison between the two simulations. This first, purely NE comparison was performed by imposing the same thermal power of 300 MW_{th} and corresponding boundary conditions for the two calculations (i.e. the transport calculation performed in Serpent and the coarse-mesh diffusion calculation performed in FRENETIC). The comparison between the effective multiplication eigenvalue computed by the two codes confirms the correct implementation of the model. Indeed, the value computed by FRENETIC (k_{eff}=1.08194) is in very good agreement (around 70 pcm difference) with the 1.08122±3 pcm evaluated by Serpent. The results of the NE FRENETIC run for the improved ALFRED model show a low relative error on the computed power, see Figure 10.8. The left plot shows a very good agreement for the axial distribution of the linear power along all the three selected SAs. The radial plot of the relative error on the right also shows a significant error reduction. The good quantitative agreement confirms that the FRENETIC code is able to reproduce the power distribution: for instance, for the EOC configuration here considered, the maximum value of the power per SA is not located at the core center, but at the beginning of the outer fuel zone, which is more enriched. This aspect is correctly recovered by FRENETIC as compared to Serpent.

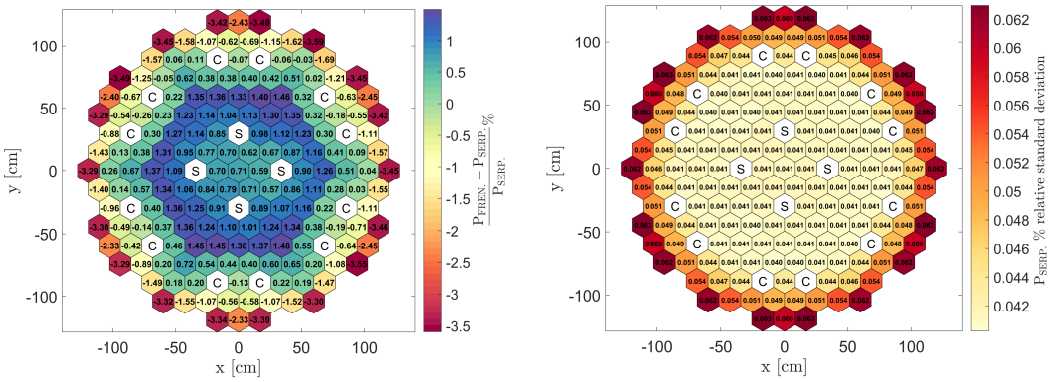

Figure 10.8: Percentage relative difference between the power per SA computed by Serpent and FRENETIC (left) and percentage relative standard deviation associated to the power computed by Serpent (right) in Hot Zero Power (HZP) conditions. Reproduced from [137] with permission.

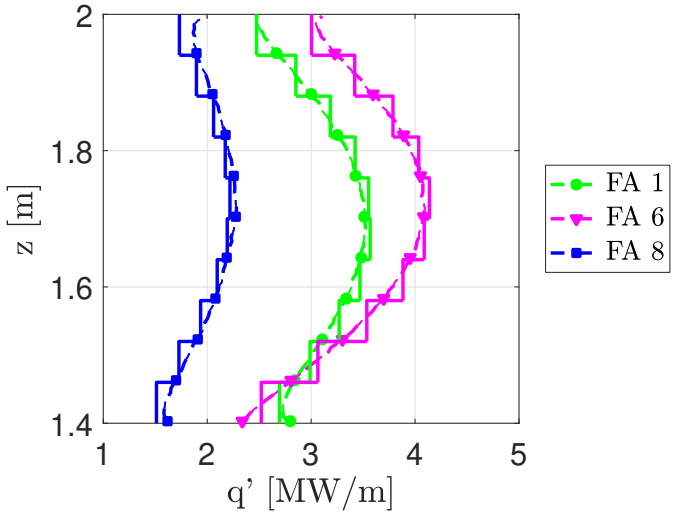

Figure 10.9: Comparison between the linear power calculated by Serpent and FRENETIC for three selected SAs in HZP conditions. Reproduced from [137] with permission.

10.4.2 NE benchmark at operational temperature

As foreseen by step 3 of the benchmark strategy, steady-state simulation in multi-physics mode, i.e. by taking into account the NE-TH coupling, has been performed. Since the FRENETIC TH module does not consider the temperature variation in the barrel and external lead, only the NE effects associated to these regions could be compared. Since these are the most relevant effects, this approximation is believed acceptable.

The resulting temperature distribution from the FRENETIC full-core coupled calculation was passed to Serpent following the procedure outlined in section 10.2, thus enabling a k_{eff} calculation in Serpent with a physically significant temperature distribution. In Figure 10.10 the radial concentric regions actually adopted are shown. The relative value of the eigenvalue computed by Serpent is 1.07848 ± 6 pcm, whereas 1.07902 is computed from the FRENETIC code, confirming the good results obtained in HZP conditions.

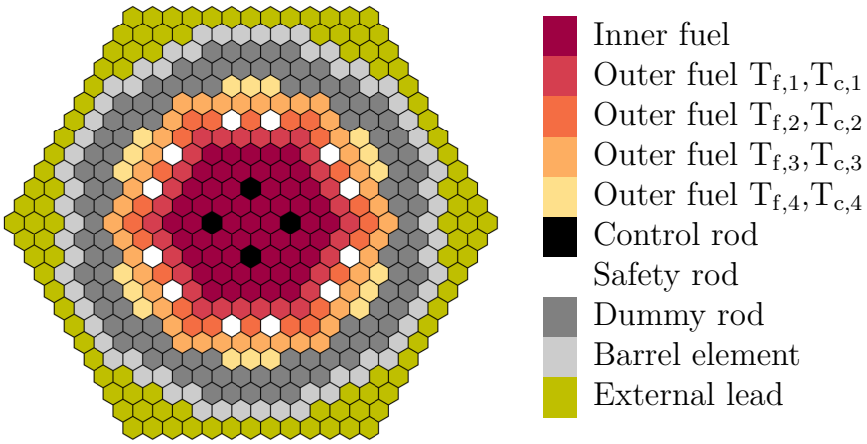

Figure 10.10: SERPENT model of the ALFRED core operating in Hot Full Power (HFP) conditions.

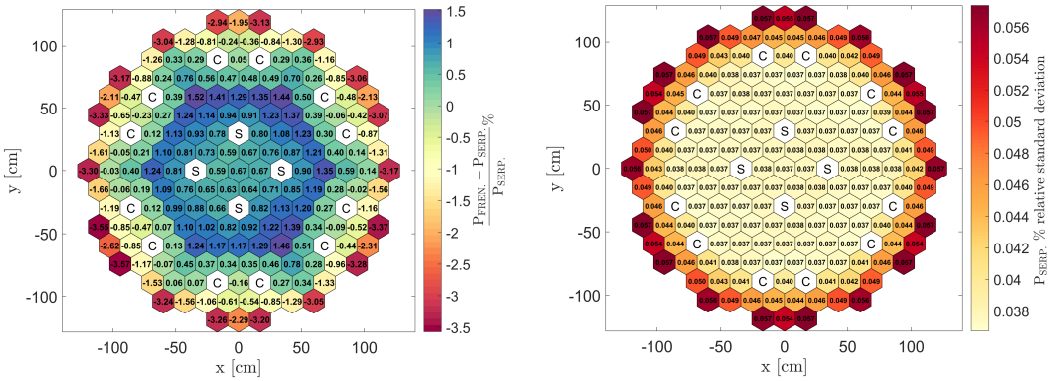

Figure 10.11: Percentage relative difference between the power per SA computed by Serpent and FRENETIC (left) and percentage relative standard deviation associated to the power computed by Serpent (right) in HFP conditions. Reproduced from [137] with permission.

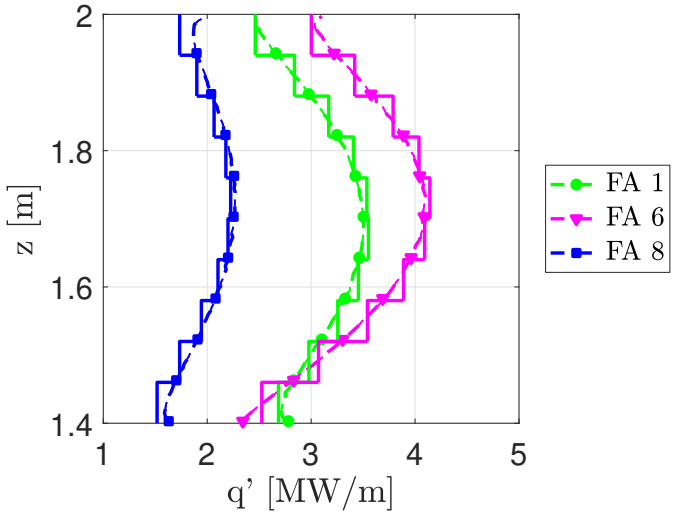

Figure 10.12: Comparison between the linear power calculated by Serpent and FRENETIC for three selected SAs in HFP conditions. Reproduced from [137] with permission.

10.5 Thermal-hydraulic benchmark

In the last phase of the benchmark activity, the TH results of FRENETIC have been tested against an OpenFOAM run performed with consistent boundary conditions on a single fuel assembly, keeping the same imposed internal power source. The comparison of the results in terms of pressure drop and temperatures is shown in the figures below. This study required first to setup correct CFD simulations, and in this respect the candidate has to acknowledge the contribution of J. Guadagni and E. Guadagni, two MSc students who decided to perform their master thesis on the subject of benchmarking multi-physics codes for HLMCRs [79, 80]. For this reason, and to avoid a long discussion which would be out of the scope of the present thesis, only the essential results shall here be very briefly presented.

From Figure 10.13, it can be seen that a good agreement between pressure losses is achieved. The comparison between the temperature profiles computed by TIFONE and OpenFOAM are shown in Figure 10.14. Both the axial profile of the average coolant temperature (left) and the axial profile of the centerline fuel temperature (right) are in good agreement.

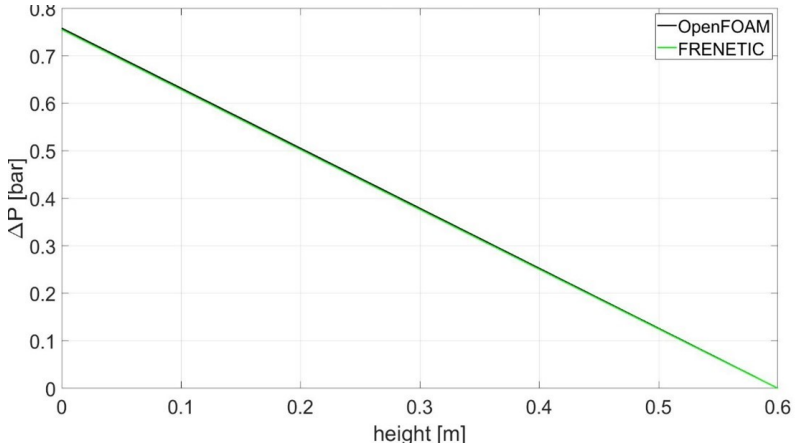

Figure 10.13: Pressure drop along the central SA calculated by FRENETIC and OpenFOAM. Reproduced from [80].

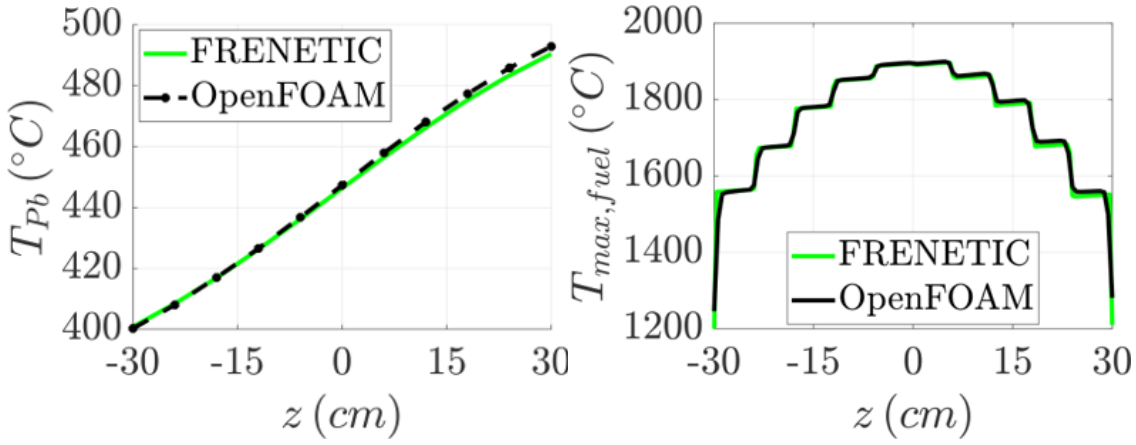

Figure 10.14: Comparison between the axial profile of the average coolant temperature calculated by FRENETIC and OpenFOAM for the central SA (left) and axial profile of the maximum fuel temperature computed by the same two codes (right).

10.6 Conclusions and perspective

The work here reported has allowed to move forward the development of the FRENETIC code, focusing the effort on the efficient and accurate simulation of the ALFRED core design, while proposing a strategy for benchmarking multiphysics codes based on simplified physical models against detailed codes which are used as a reference.

The benchmarking activity with the coupled Serpent-OpenFOAM model has allowed to assess the accuracy of FRENETIC full-core simulation, also highlighting some aspects requiring further R&D work.

Based on these results, some of the identified further developments are:

- Extension of the TH in order to allow the simulation of assemblies with stagnating lead in coupled NE-TH mode;
- Improvement of the energy group structure with more advanced methodologies, such as the one in [121];
- Improvement of the axial representation of the core, starting from the tally definition in Serpent.

Chapter 11

Conclusions and perspective for Part II

As for Part I, to conclude Part II of the present thesis, it is convenient to summarize here its content, including the introduction to the next-generation liquid metal cooled fast reactors, the original methodologies proposed to address the identified modelling needs and the obtained results, the relations among them and their relevance for the field, together with future perspective.

The motivations for pursuing the development of Generation IV of fission reactors, together with the international framework represented by the GIF initiative, were first presented. The role of ALFRED as a demonstrator for the LFR design was then introduced. To conclude the introduction to Part II of the thesis, the role of numerical tools in supporting the LFR core design was described, pointing out the relevance of design-oriented codes (as opposed to verification-oriented codes) in the design phase. Moreover, the multi-physics nature of the core design was highlighted.

To address the need for a DOC computing the inter-wrapper flow and heat transfer in an LFR, the TIFONE code was developed. The methodology devised to design the code in compliance with the ENEA Software Quality Assurance Requirements was clearly presented, with specific reference to the content of the Software Design and Implementation Document (i.e. the choice of the physico-mathematical model to solve the problem and the code design procedure) while clearly locating this document in the framework of the overall development activity. It can be stated that this methodology could represent a guideline for future developers of DOCs. Then, considering the need to benchmark the multiphysics (NE-TH) code FRENETIC, a step-wise benchmark methodology was presented and successfully applied. Again, this could represent a guideline for future benchmark activities of multi-physics codes.

As far as the results are concerned, the TIFONE code was preliminarily validated against experimental data from the inter-wrapper flow and heat transfer

experiments in the KALLA facility, confirming the ability of the code to reproduce experimental data in the anticipated application domain, while keeping a very low computational cost. The benchmark of FRENETIC against Serpent and OpenFOAM (which were used as reference codes) was also successful.

The conclusions and perspective for each of the two activities (TIFONE development and preliminary validation, and FRENETIC benchmark) were already presented in the respective sections. It shall here be convenient to suggest possible synergies between the two activities. First, TIFONE is a code for the inter-wrapper flow, and requires as an input the heat flux crossing the wrapper, which can be computed by codes for the SA thermal-hydraulics. Therefore, FRENETIC and TIFONE could be coupled to obtain a full-core solution. In this way, FRENETIC would benefit from a more detailed treatment of the inter-wrapper flow problem. The consistently computed axial distribution of the assembly-wise heat flux would also provide an input for TIFONE. It should be noticed, however, that the natural application of TIFONE will be represented by a coupling with multiple instances of DOCs for the single SAs such as ANTEO+. In terms of applicability of the various methodologies here presented, it can be stated that the code development procedure adopted for TIFONE is applicable to possible future extensions of the FRENETIC code (e.g. a TM module), while the benchmark procedure adopted for FRENETIC could be applied to TIFONE, once it has been coupled to other TH codes such as ANTEO+ and/or to other NE/TM codes.

Appendix A

Data used for SOLPS-ITER calculations

A.1 Lithum

Lithium:
Density (T in K, temperature range: 453.7-1700 K) [212]

$$\rho = 0.5584 - 1.01 \cdot 10^{-4} T \text{ [Mg/m}^3\text{]} \tag{A.1}$$

Viscosity (T in °C, temperature range: 180-1200°C)

$$\eta = 0.8836 - 1.248523 \cdot 10^{-3} T + 5.791460 \cdot 10^{-7} T^2 \text{ [mPa} \cdot \text{s]} \tag{A.2}$$

Thermal conductivity (T in °C, temperature range: 244-1140°C)

$$\lambda = 40.138 + 0.01908 T \text{ [W/m/K]} \tag{A.3}$$

Vapor pressure (T in K, temperature range: 180-1000 K)

$$p_v(T) = 10^{\left(A + \frac{B}{T}\right)} \text{ [Pa]} \tag{A.4}$$

with A=10.061, B=-8023.0 K^{-1} [5].
Enthalpy (T in K, temperature range: 453.7-1200 K) [37]

$$\Delta H = -7.519 \cdot 10^5 + 4169 T \text{ [J/kg]} \tag{A.5}$$

Specific heat (T in K, temperature range: 453.7-1200 K) (from the enthalpy equation)

$$c_p = 4169 \text{ [J/kg/C]} \tag{A.6}$$

Average heat of vaporization: 21.98MJ/kg

Surface tension (T in K, temperature range: 453.7-1700 K)

$$\sigma = 0.4738 - 1.627 \cdot 10^{-4} T \text{ [N/m]} \tag{A.7}$$

Data in adf11 format from ADAS database
Effective Recombination Coefficients: acd96_li.dat
Effective Ionisation Coefficients: scd96_li.dat
CX Cross Coupling Coefficients: ccd89_li.dat
Recombination and Bremsstrahlung: prb96_li.dat
Line emission from excitation: plt96_li.dat

A.2 Tin

Tin:
Density (T in K, temp. range: 506-1950 K) [10]

$$\rho = 6979 - 0.652 \cdot (T - 505.08) \text{ [kg/m}^3\text{]} \tag{A.8}$$

Viscosity (T in K, temp. range: 506-1280 K) [10]

$$\log_{10}\eta = -0.408 + \frac{343.4}{T} \text{ [mPa/s]} \tag{A.9}$$

Thermal Conductivity (T in K, temperature range: 506-1170 K): see table 3 of reference [175]
Vapor pressure (T in K, temperature range: 506-1850 K)

$$p_v(T) = 10^{\left(A + \frac{B}{T}\right)} \text{ [Pa]} \tag{A.10}$$

with A=10.268, B=-15332.0 K^{-1} [5].
Enthalpy (T in K) (ΔH wrt. enthalpy of solid Sn at 298 K [146])

$$\begin{aligned}\Delta H = {} & 9496.31 + 8.2590486T + 16.814429 \cdot 10^{-3}T^2 - 5.24626 \cdot 10^{-6}T^{-3} \\ & - 2162488T^{-1} \text{ [J/mol]} \ (505.078K < T < 800K)\end{aligned} \tag{A.11}$$

$$\Delta H = -1285.372 + 28.4512T \text{ [J/mol]} \ (800K < T < 3000K) \tag{A.12}$$

Specific heat (T in K, temperature range: 505.078K<T<800K) [146]

$$\begin{aligned}cp = {} & 8.2590486 + 33.628858 \cdot 10^{-3}T + 15.73878 \cdot 10^{-6}T^{-4} \\ & + 2162488T^{-2} \text{ [J/mol/K]}\end{aligned} \tag{A.13}$$

Atomic data: in adf11 format, not yet included in the ADAS database [34]
Effective Recombination Coefficients: acd89_sn.dat
Effective Ionisation Coefficients: scd89_sn.dat
Recombination and Bremsstrahlung: prb89_sn.dat
Line emission from excitation: plt89_sn.dat

Appendix B

Comparison of 0D vapor model with DSMC

To choose the appropriate tool to model the vapor transport, thus providing a reference for the adopted 0D model, a preliminary estimate of the expected flow regime is required. This is achieved by estimating an average Knudsen number (Kn) for each divertor chamber based on results from the 0D model. The Knudsen number is a dimensionless quantity giving the degree of rarefaction of a fluid and is defined as $Kn = \frac{\lambda}{L}$, where λ is the mean free path of a generic atom or molecule and L is a properly defined characteristic length. If $Kn \ll 1$, a vapor particle travels on average a distance much smaller than L between two collisions and the system can therefore be treated as a continuum. In this regime, conventional CFD codes are suitable for evaluating the flow field. If, instead, $Kn \gg 1$, collisions are rare events and free molecular flow occurs. In this regime, Molecular Dynamics (MD) simulations, which are able to describe the deterministic behavior of each particle in the system, are required. In between, there is the transition regime ($Kn \sim 1$) where the continuum assumption is no longer valid, but MD simulations would be unacceptably expensive. In this regime, which often occurs in differentially pumped systems [200] , statistical methods such as Direct Simulation Monte Carlo (DSMC) [14] provide the best performance. A sketch of the possible flow regimes and appropriate tools to treat them is provided in Figure B.1.

The DSMC simulation setup is reported in the appendix of [137] and therefore will not be repeated here. Only the selected domain is shown in Figure B.2. The red dots indicate surfaces that have been considered as condensing (case 1) or reflecting (case 2).

The key results are reported in Figure B.3 and Figure B.4.

In conclusion, it can be stated that a 2D vapor transport model based on the DSMC method has been set up and applied to a closed LM, pool-type divertor. The model was useful to assess the effect of reflecting walls on the distribution of thermodynamic variables for the vapor. The comparison with the 0D vapor

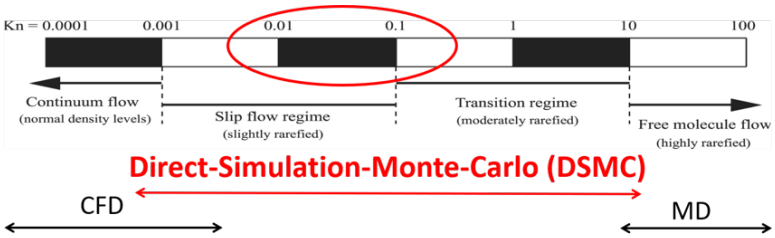

Figure B.1: Sketch of the flow regimes identified by the Knudsen number. Adapted from [210].

.

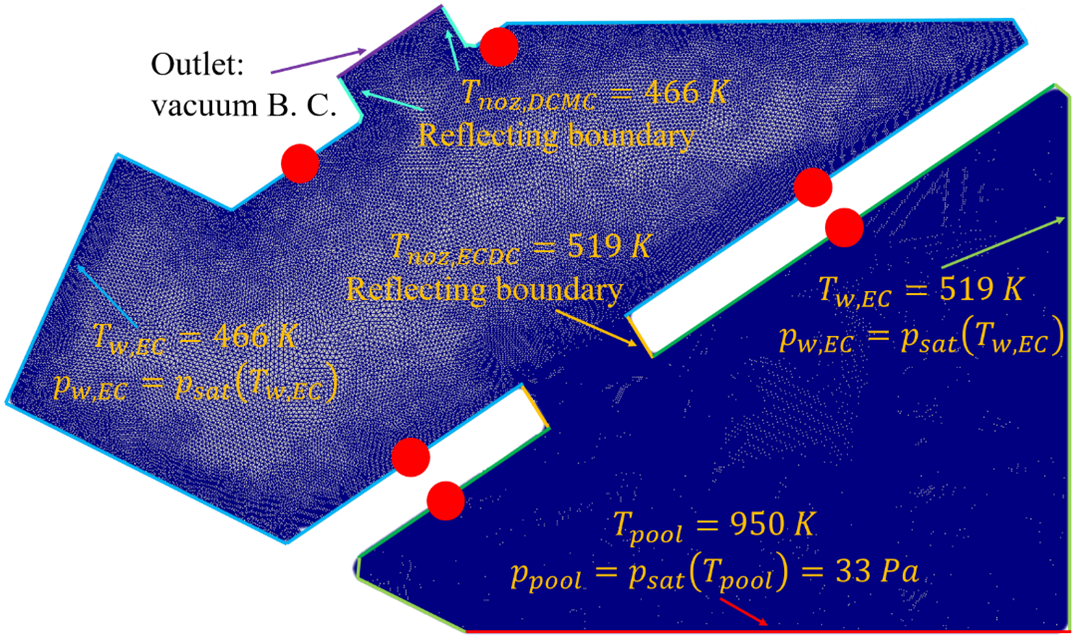

Figure B.2: Schematic of the simulation domain, including mesh and boundary conditions.

.

model shows that the 0D model conservatively overpredicts the temperature and underpredicts the density and, as such, it can be used for fast, order-of-magnitude estimates, while a more detailed 2D model is required if the detailed vapor density field is to be determined.

An example of the capabilities of the new model for the vapor has then been provided. In particular, the effectiveness of having reflecting rather than condensing surfaces, especially in the EC, has been studied. The model predicts an increase of a factor ~ 2 of the vapor density in the EC, at the expense of a ~ 1.3 increase of the leaked metal towards the MC.

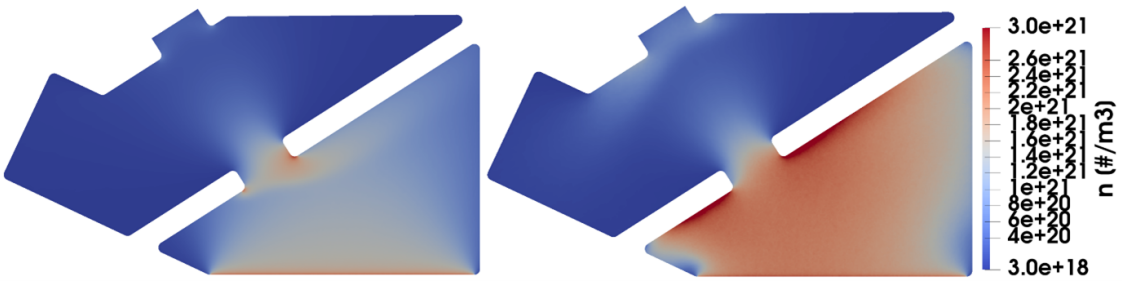

Figure B.3: Computed density for case 1- condensing (left) and case 2 - reflecting (right).

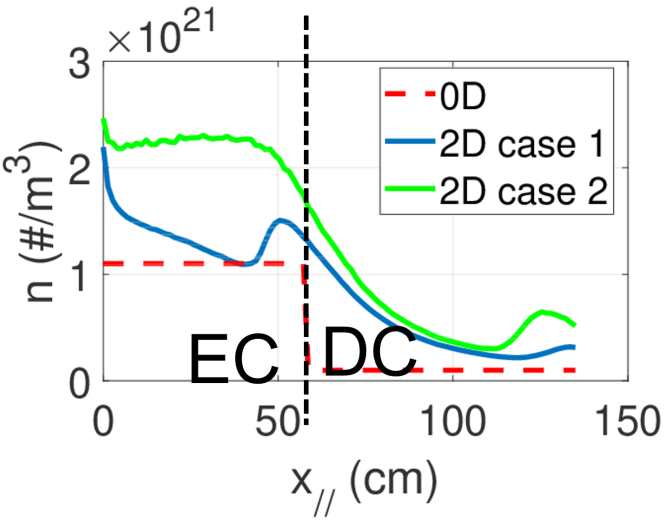

Figure B.4: Comparison between vapor density computed via DSMC and via the 0D model.

In conclusion, it is of interest to put this work in the context of the application of state-of the art plasma modelling tools, such as the one presented in 5. It can be stated that the need for models for vapor transport in the transition range, such as DSMC and Bhatnagar-Gross-Krook (BGK) [94], are not only required in a vapor box divertor (where the combination of evaporation and vapor expansion leads to the fluid working in the transition regime). Indeed, such models are also required in kinetic codes such as Eirene in the case of e.g. detached plasma, where the neutral density (in that case *fuel neutrals* are involved) is large.

Appendix C

Material properties used for TIFONE

TIFONE embeds the required material property libraries to solve the IW flow and heat transfer problem. Moreover, the user can include additional material libraries in TIFONE without the need to access the source code. For this purpose, a user-accessible module has been prepared, that shall be linked at compile time. The module can contain thermophysical properties for the coolant (i.e. density ρ, heat capacity c_p, thermal conductivity k and dynamic viscosity μ) and for the wrapper (i.e. thermal conductivity k_w) in functional or tabular form, as well as their temperature dependence. The module also allows to store the material name and the reference for the material properties (e.g. handbook, journal article). This information is echoed in output, so that a given simulation result can be traced back to the set of thermophysical properties correlations adopted therein. The user (as opposed to the developer/maintainer) has then only access to that module, whereas the rest of the code is compiled as a static library. This prevents source code modifications by the user, while allowing to possibly extend the code applicability to the simulation of problems employing different materials and/or to easily update the material property libraries.

Coolant properties TIFONE is specifically developed to support the design of LFRs, therefore it must at least contain lead properties which are valid for the foreseeable operational range of an LFR. However, due to the lack of significant experimental datasets using lead, code validation will rely on experiments performed with sodium and/or Lead-Bismuth Eutectic (LBE). For this reason, properties for these two latter materials are included in TIFONE as well. Selected coolant properties are listed in Table C.1.

Wrapper properties The wrapper materials to be embedded in the TIFONE property database include:

	Unit	Correlation	Validity range	Accuracy
Sodium [188]				
ρ	kg/m^3	$1011.8 - 0.22054 \cdot T - 1.9226 \times 10^{-5} \cdot T^2 + 5.6371 \times 10^{-9} \cdot T^3$	371-1644	±0.4%
c_p	J/(kg K)	$1629.1 - 0.83267 \cdot T + 4.6208 \times 10^{-4} \cdot T^2$	371-1155	±0.4%
k	W/(m K)	$106.69 - 6.4494 \times 10^{-2} \cdot T + 4.8696 \times 10^{-6} \cdot T^2$	371-1644	±7%
μ	kg/(m s)	$\exp\left(\frac{556.835}{T} - 0.3958 \ln T - 6.4406\right)$	371-1500	±4%
Lead [141]				
ρ	kg/m^3	$11441.0 - 1.2795 \cdot T$	600.6-2021	±1%
c_p	J/(kg K)	$175.1 - 4.961 \times 10^{-2} \cdot T + 1.985 \times 10^{-5} \cdot T^2 - 2.099 \times 10^{-9} \cdot T^3 - 1.524 \times 10^6 / T^2$	600.6-2000	±7%
k	W/(m K)	$9.2 + 1.1 \times 10^{-2} \cdot T$	600.6-1300	±15%
μ	kg/(m s)	$4.55 \times 10^{-4} \cdot \exp\left(\frac{1.069 \times 10^3}{T}\right)$	600.6-1473	±5%
LBE [141]				
ρ	kg/m^3	$11065 - 1.293 \cdot T$	398-1927	±0.8%
c_p	J/(kg K)	$164.8 - 3.94 \times 10^{-2} \cdot T + 1.25 \times 10^{-5} \cdot T^2 - 4.56 \times 10^5 / T^2$	400-1100	±5%
k	W/(m K)	$3.284 + 1.617 \times 10^{-2} \cdot T - 2.305 \times 10^{-6} \cdot T^2$	400-1100	±15%
μ	kg/(m s)	$4.94\text{x}10^{-4} \cdot \exp\left(\frac{7.541 \times 10^2}{T}\right)$	400-1173	±8%

Table C.1: Coolant properties to be embedded in TIFONE.

- AISI 316 austenitic steel;
- 15-15 Ti austenitic steel, adopted e.g. in PHENIX;
- T91 ferritic-martensitic steel, which is foreseen to be adopted in ALFRED.

Selected wrapper properties are listed in Table C.2.

	Unit	Correlation	Validity range	Accuracy
AISI 316 austenitic steel [84]				
k	W/(m K)	$9.106 + 1.502 \times 10^{-2} T$	293-1200	±5%
15-15 Ti austenitic steel [187]				
k	W/(m K)	$8.826 + 1.707 \times 10^{-2} \cdot T - 2.315 \times 10^{-6} \cdot T^2$	293-1273	±8%
T91 ferritic-martensitic steel [39]				
k	W/(m K)	$20.226 + 1.1363 \times 10^{-2} \cdot T - 4.82 \times 10^{-6} \cdot T^2$	293-873	N/A[1]

Table C.2: Steel properties to be embedded in TIFONE.

Acronyms

ADAS Atomic Data and Analysis Structure. 114
ALFRED Advanced Lead-cooled Fast Reactor European Demonstrator. 8, 134

BGK Bhatnagar-Gross-Krook. 261
BRC Bottom Ring Collector. 38, 40

CFD Computational Fluid Dynamics. 9, 11, 237, 238
CHF Critical Heat Flux. 5, 22, 60
CPS Capillary-Porous Structure. 3–5, 25, 26, 28–31, 33, 37, 39–41, 44, 59, 60, 63, 70, 71, 87, 89, 94, 98, 99, 102, 106
CX Charge eXchange. 45, 55, 113

DC Differential Chamber. 6, 94, 96, 98, 100–102, 104–106, 108, 120, 121, 123, 124
DFD Data Flow Diagram. 180, 193–200, 204, 205
DNS Direct Numerical Simulation. 171
DOC Design-Oriented Code. 8–11, 136–140, 143, 149, 154, 179, 235, 255, 256
DSMC Direct Simulation Monte Carlo. 126, 259, 261
DTT Divertor Tokamak Test. 3, 22, 23, 94

EC Evaporation Chamber. 6, 94, 98–102, 104–107, 114, 120, 123, 125, 260
ELM Edge-Localised Mode. 2, 3, 22, 25, 27, 86, 125, 128
EM Electro-Magnetic. 41
EOC End Of Cycle. 243, 248
ETB Edge Transport Barrier. 65

FALCON Fostering ALfred CONsortium. 8, 134
FEM Finite Element Modelling. 71, 72, 103, 105, 107, 109
FR Fast Reactor. 133
FRENETIC Fast REactor NEutronics/ThermalhydraulICs. 11, 237
FTU Frascati Tokamak Upgrade. 19, 30, 31
FW First Wall. 25, 27, 41, 62, 67, 85, 90, 98

GCR Gas-Cooled Reactor. 133
GIF Generation IV International Forum. 8, 131–133, 255

HFP Hot Full Power. 250, 251
HLMCR Heavy Liquid Metal Cooled Reactor. 1, 8, 133, 134, 137, 138, 235, 252
HZP Hot Zero Power. 249, 250

IDC Inboard Differential Chamber. 95, 97, 110
IEC Inboard Evaporation Chamber. 95, 97, 108, 109, 122, 123
IT Inboard Target. 75
IW Inter-Wrapper. 8–10, 138–144, 146–151, 155, 159, 170, 172, 176, 181, 182, 185, 189, 192, 197, 207, 219, 221–225, 229, 231, 233, 235, 263

KALLA Karlsruhe Liquid metal LAboratory. 138, 219

LBE Lead-Bismuth Eutectic. 134, 219, 263
LCMS Last Closed Magnetic Surface. 19
LFR Lead-cooled Fast Reactor. 8–10, 133–135, 138, 140, 149, 173, 182, 221, 237, 238, 255, 263
LiMIT Lithium Metal Infused Trenches. 35
LM Liquid Metal. 1, 3–7, 23, 25–33, 35, 37–42, 44, 47, 59, 60, 64, 70, 77, 79, 80, 85, 90, 93–96, 98, 99, 102, 103, 105–109, 114, 116, 119–125, 131, 133
LMCR Liquid Metal Cooled Reactor. 8, 11, 133, 140–142, 235, 238
LMD Liquid Metal Divertor. 1, 3–6, 22, 25–28, 31, 33, 36–39, 41, 47, 48, 54, 59, 60, 62–65, 74, 77, 80, 82, 83, 85, 87, 89–91, 98, 127
LPD Linear Plasma Device. 27, 29
LWR Light Water Reactor. 10, 133

MA Minor Actinide. 133
MARFE Multifaceted Asymmetric Radiation From the Edge. 22
MC Main plasma Chamber. 6, 93, 94, 96, 98, 100, 105, 106, 124, 125, 260
MC Monte Carlo. 11
MD Molecular Dynamics. 259
MHD MagnetoHydroDynamic. 17, 18, 29, 44
MSR Molten Salt Reactor. 133

NE NEutronic. 8–11, 136, 238–241, 247, 248, 250, 253, 255, 256
NSTX National Spherical Tokamak Experiment. 30

ODC Outboard Differential Chamber. 95, 97, 110
OEC Outboard Evaporation Chamber. 95, 97, 118, 122, 123
OMP Outboard Midplane. 19, 50, 65, 109, 111, 114
OT Outboard Target. 74–81, 86–89

PDE Partial Differential Equation. 54
PDL Program Design Language. 180, 204–207, 217
PEX Power EXhaust. 2, 15, 22, 60, 127

PFC Plasma-Facing Component. 2, 4, 19, 22, 25–28, 36, 41–43, 45, 63
PFS Plasma-Facing Surface. 3, 5, 15, 26, 28, 35, 37, 39, 41, 60, 63, 72, 106
PWI Plasma-Wall Interactions. 19, 29

SA sub-assembly. 8–11, 137, 138, 140, 141, 143, 146–151, 156, 173–178, 181–183, 185, 186, 188, 190, 219, 221, 233, 235, 237–240, 242, 245, 247–249, 251–253, 256
SC subchannel. 8, 10, 137, 138, 140–144, 146, 147, 149–156, 158–169, 171–173, 176–178, 182, 185, 186, 189, 192, 197, 207, 222–225, 227, 229, 233
SCWR SuperCritical-Water-cooled Reactor. 133
SDID Software Design and Implementation Document. 139, 179
SE Sheath Edge. 52
SFR Sodium-cooled Fast Reactor. 133, 134
SMR Small Modular Reactor. 8
SOL Scrape-Off Layer. 2–4, 19, 21, 25–27, 36, 37, 47, 49, 52, 54, 59–61, 64, 65, 78, 80, 81, 83, 86, 90, 93, 96, 97, 100, 102–105, 107–110, 114, 116, 122, 127
SQAP Software Quality Assurance Plan. 9, 139, 217
SRS Software Requirements Specification. 139, 140, 143, 179, 188, 217

TEMHD ThermoElectric MagnetoHydroDynamic. 35
TH Thermal-Hydraulic. 8–11, 136–138, 140, 143, 144, 149, 156, 221, 235, 238–240, 250, 252, 253, 255, 256
TIFONE Termo-Idraulica delle Fughe che Occorrono nel Nocciolo fra gli Elementi. 138
TM Thermo-Mechanic. 8, 9, 136, 138, 256
TRC Top Ring Collector. 38, 41

UML Unified Modeling Language. 193

VDE Vertical Displacement Event. 22, 27
VHTR Very-High-Temperature Reactor. 133
VOC Verification-Oriented Code. 8, 9, 11, 136
VT Vertical Target. 38
VV Vacuum Vessel. 37, 41

Bibliography

[1] T. Abrams. "Erosion and re-deposition of Lithium and Boron coatings under high-flux plasma bombardment". PhD thesis. Ph.D. thesis, Princeton University, 2015. URL: http://arks.princeton.edu/ark:/88435/dsp01jm214r372.

[2] T. Abrams et al. "Suppressed gross erosion of high-temperature lithium via rapid deuterium implantation". In: *Nuclear Fusion* 56.1 (2016), 16022 (10pp). ISSN: 17414326. DOI: 10.1088/0029-5515/56/1/016022. URL: http://dx.doi.org/10.1088/0029-5515/56/1/016022.

[3] R. Albanese. "DTT: a divertor tokamak test facility for the study of the power exhaust issues in view of DEMO". In: *Nuclear Fusion* 57.1 (2017), 016010 (13pp). ISSN: 0029-5515. DOI: 10.1088/0029-5515/57/1/016010. arXiv: /www.ingentaconnect.com.ezproxy.bangor.ac.uk/contentone/intellect/josc/2016/00000007/00000001/art00004 [http:]. URL: http://stacks.iop.org/0029-5515/57/i=1/a=016010?key=crossref.400ef38e911438010dc9700af78d62c9.

[4] R. Albanese, R. Ambrosino, and M. Mattei. "A procedure for the design of snowflake magnetic configurations in tokamaks". In: *Plasma Physics and Controlled Fusion* 56.3 (2014), 035008 (9pp). ISSN: 07413335. DOI: 10.1088/0741-3335/56/3/035008.

[5] C B Alcock, V P Itkin, and M K Horrigan. *VAPOUR PRESSURE EQUATIONS FOR THE METALLIC ELEMENTS: 298-2500K*. Tech. rep. 3. 1984, pp. 309–313.

[6] J. P. Allain and J. N. Brooks. "Lithium surface-response modelling for the NSTX liquid lithium divertor". In: *Nuclear Fusion* 51.2 (2011), 023002 (8pp). ISSN: 00295515. DOI: 10.1088/0029-5515/51/2/023002.

[7] J. P. Allain, M. D. Coventry, and D. N. Ruzic. "Collisional and thermal effects on liquid lithium sputtering". In: *Physical Review B - Condensed Matter and Materials Physics* 76.20 (2007), pp. 1–12. ISSN: 10980121. DOI: 10.1103/PhysRevB.76.205434.

[8] J. P. Allain and C. N. Taylor. "Lithium-based surfaces controlling fusion plasma behavior at the plasma-material interface". In: *Phys. Plasmas* 19 (2012), 56126 (9pp). DOI: 10.1063/1.4719688. URL: https://doi.org/10.1063/1.4719688.

[9] M. L. Apicella et al. "First experiments with lithium limiter on FTU". In: *Journal of Nuclear Materials* 363-365.1-3 (2007), pp. 1346–1351. ISSN: 00223115. DOI: 10.1016/j.jnucmat.2007.01.237.

[10] Marc J. Assael et al. "Reference data for the density and viscosity of liquid copper and liquid tin". In: *Journal of Physical and Chemical Reference Data* 39.3 (2010). ISSN: 00472689. DOI: 10.1063/1.3467496.

[11] M J Baldwin et al. "Deuterium retention in liquid lithium". In: *Nuclear Fusion* 42.11 (2002), pp. 1318–1323. ISSN: 0029-5515. DOI: 10.1088/0029-5515/42/11/305. URL: http://stacks.iop.org/0029-5515/42/i=11/a=305?key=crossref.9d6dd1f496ffc3a6e327b5297a6b2580.

[12] K. L. Basehore and N. E. Todreas. *SUPERENERGY-2: A Multiassembly, Steady- State Computer Code for LMFBR Core Thermal-Hydraulic Analysis*. Tech. rep. DOE, Richland, WA, 1980.

[13] *Binding energy per nucleon data*. https://web.archive.org/web/20060309210852/http://www.einstein-online.info/en/spotlights/binding_energy/binding_energy/index.txt. Accessed: 2021-06-21.

[14] G A Bird. *Molecular Gas Dynamics and the Direct Simulation of Gas Flows*. Oxford: Clarendon Press, 1994. ISBN: 978-981-287-211-1. DOI: 10.1007/978-981-287-212-8. URL: http://link.springer.com/10.1007/978-981-287-212-8.

[15] L Susan Blackford et al. "An updated set of basic linear algebra subprograms (BLAS)". In: *ACM Transactions on Mathematical Software* 28.2 (2002), pp. 135–151.

[16] P. R. H. Blasius. "Das aehnlichkeitsgesetz bei reibungsvorgangen in flussigk eiten". In: *Forschungsheft* 64 (1913), pp. 1–41. DOI: 10.1007/978-3-662-02239-9. URL: http://link.springer.com/10.1007/978-3-662-02239-9.

[17] Maarten Blommaert et al. "A spatially hybrid fluid-kinetic neutral model for SOLPS-ITER plasma edge simulations". In: *Nuclear Materials and Energy* 19 (May 2019), pp. 28–33. ISSN: 23521791. DOI: 10.1016/j.nme.2019.01.022. URL: https://linkinghub.elsevier.com/retrieve/pii/S235217911830228X.

[18] R. Bonifetto et al. "A full-core coupled neutronic/thermal-hydraulic code for the modeling of lead-cooled nuclear fast reactors". In: *Nuclear Engineering and Design* 261 (2013), pp. 85–94. ISSN: 00295493. DOI: 10.1016/j.nucengdes.2013.03.030. URL: http://dx.doi.org/10.1016/j.nucengdes.2013.03.030.

[19] Walter Borreani et al. "Design and selection of innovative primary circulation pumps for GEN-IV lead fast reactors". In: *Energies* 10.2 (2017). ISSN: 19961073. DOI: 10.3390/en10122079.

[20] S. I. Braginskii. *Transport processes in a plasma*. 1965. URL: http://people.hao.ucar.edu/judge/homepage/PHSX515/fall2012/Braginskii1965.pdf.

[21] S. Brezinsek et al. "Study of physical and chemical assisted physical sputtering of beryllium in the JET ITER-like wall". In: *Nuclear Fusion* 54 (2014), 103001 (11pp). ISSN: 17414326. DOI: 10.1088/0029-5515/54/10/103001.

[22] H. Bufferand et al. "Numerical modelling for divertor design of the WEST device with a focus on plasma–wall interactions". In: *Nuclear Fusion* 55.5 (Apr. 2015), p. 053025. DOI: 10.1088/0029-5515/55/5/053025. URL: https://doi.org/10.1088/0029-5515/55/5/053025.

[23] S Carli et al. "Effect of strike point displacements on the ITER tungsten divertor heat loads". In: *Nuclear Fusion* 58.12 (2018), 126022 (21pp). ISSN: 17414326. DOI: 10.1088/1741-4326/aae43f. URL: https://creativecommons.org/licences/by/3.0.

[24] D Caron. "Models and Methods for the Representation of Decay and Photon Heat in Spatial Kinetics Calculations". In: *PHYSOR 2016*. 2016, pp. 2416–2425. ISBN: 9781510825734.

[25] D. Caron et al. "Full-core coupled neutronic/thermal-hydraulic modelling of the EBR-II SHRT-45R transient". In: *International Journal of Energy Research* 42 (2018), pp. 134–150. ISSN: 1099114X. DOI: 10.1002/er.3571.

[26] M Carr and A Meakins. *cherab/core: Release v1.1.0*. Mar. 2019. DOI: 10.5281/zenodo.2585962. URL: https://doi.org/10.5281/zenodo.2585962.

[27] M Carr et al. *CHERAB's documentation*. 2018. URL: https://cherab.github.io/documentation/index.html.

[28] A. de Castro et al. "Lithium, a path to make fusion energy affordable". In: *Physics of Plasmas* 28.5 (May 2021), p. 050901. ISSN: 1070-664X. DOI: 10.1063/5.0042437. URL: https://aip.scitation.org/doi/10.1063/5.0042437.

[29] C. S. Chang et al. "Gyrokinetic projection of the divertor heat-flux width from present tokamaks to ITER". In: *Nuclear Fusion* 57.11 (2017), 116023 (15pp). ISSN: 17414326. DOI: 10.1088/1741-4326/aa7efb. arXiv: 1701.05507.

[30] A. V. Chankin, D. P. Coster, and R. Dux. "Monte Carlo simulations of tungsten redeposition at the divertor target". In: *Plasma Physics and Controlled Fusion* 56.2 (2014), 025003 (11pp). ISSN: 07413335. DOI: 10.1088/0741-3335/56/2/025003.

[31] Shih-kuei Chen. "Constitutive correlations for wire-wrapped subchannel analysis under forced and mixed convection conditions". Ph.D. thesis. Massachussets Institute of Technology, 1984, p. 543.

[32] *CMake build system*. https://cmake.org/. Accessed: 2020-01-09.

[33] C. F. Colebrook. "Turbulent Flow in Pipes, With Particular Reference To the Transition Region Between the Smooth and Rough Pipe Laws". In: *Journal of the Institution of Civil Engineers* 11.4 (1939), pp. 133–156. ISSN: 0368-2455. DOI: 10.1680/ijoti.1939.14509.

[34] D. Coster and M. O'Mullane. *Private communication*. 2019.

[35] D. P. Coster. "Reduced Physics Models in SOLPS for Reactor Scoping Studies". In: *Contributions to Plasma Physics* 56.6-8 (2016), pp. 790–795. ISSN: 15213986. DOI: 10.1002/ctpp.201610035.

[36] A. Cremona et al. "Deuterium retention and erosion in liquid Sn samples exposed to D2 and Ar plasmas in GyM device". In: *Nuclear Materials and Energy* 17.November (2018), pp. 253–258. ISSN: 23521791. DOI: 10.1016/j.nme.2018.11.010. URL: https://doi.org/10.1016/j.nme.2018.11.010.

[37] H. W. Davison. "Compilation of thermophysical properties of liquid lithium". In: *National Aeronautics and Space Administration* July 1968 (1968). URL: http://ntrs.nasa.gov/archive/nasa/casi.ntrs.nasa.gov/19680018893.pdf.

[38] R. Dejarnac et al. "Overview of power exhaust experiments in the COMPASS divertor with liquid metals". In: *Nuclear Materials and Energy* 25 (Dec. 2020). ISSN: 23521791. DOI: 10.1016/j.nme.2020.100801. URL: https://doi.org/10.1016/j.nme.2020.100801.

[39] *Design and Construction Rules for mechanical components of nuclear installations : high-temperature, research and fusion reactors*. 2018th ed. AFCEN.

[40] G Di Gironimo. *Private communication*. 2017.

[41] R. P. Doerner, S. I. Krasheninnikov, and K. Schmid. "Particle-induced erosion of materials at elevated temperature". In: *Journal of Applied Physics* 95.8 (Apr. 2004), pp. 4471–4475. ISSN: 00218979. DOI: 10.1063/1.1687038.

[42] A. J. Donné. *European Research Roadmap to the Realisation of Fusion Energy*. 2018. URL: https://www.euro-fusion.org/fileadmin/user_upload/EUROfusion/Documents/2018_Research_roadmap_long_version_01.pdf.

[43] *Doxygen documentation generator*. http://www.doxygen.nl. Accessed: 2020-01-09.

[44] Florent Duchaine et al. "Analysis of high performance conjugate heat transfer with the OpenPALM coupler". In: *Computational Science and Discovery* 8 (2015), 015003 (19pp). ISSN: 17494699. DOI: 10.1088/1749-4699/8/1/015003.

[45] L Duchatelle and L. Vautrey. "Determination des coefficients de convection d'un alliage NaK en ecoulement turbulent entre plaques planes paralleles". In: *International Journal of Heat and Mass Transfer* 7 (1964), pp. 1017–1031. ISSN: 00092347. DOI: 10.1021/cen-v035n051.p050a.

[46] F E Dunn, D J Malloy, and D Mohr. "Liquid-metal-cooled reactor thermal-hydraulic calculations in the United States". In: *Nuclear Science and Engineering* 100.4 (1988), pp. 558–563. ISSN: 00295639. DOI: 10.13182/NSE88-A23588.

[47] O. E. Dwyer. "Heat Transfer to Liquid Metals Flowing Turbulently Between Parallel Plates". In: *Nuclear Science and Engineering* 21.1 (1965), pp. 79–89. ISSN: 0029-5639. DOI: 10.13182/nse65-a21017.

[48] T. Eich et al. "Inter-ELM power decay length for JET and ASDEX Upgrade: Measurement and comparison with heuristic drift-based model". In: *Physical Review Letters* 107.21 (2011), pp. 1–4. ISSN: 00319007. DOI: 10.1103/PhysRevLett.107.215001.

[49] T. Eich et al. "Scaling of the tokamak near the scrape-off layer H-mode power width and implications for ITER". In: *Nuclear Fusion* 53.9 (2013), 093031 (7pp). ISSN: 00295515. DOI: 10.1088/0029-5515/53/9/093031.

[50] E. D. Emdee et al. "A simplified lithium vapor box divertor". In: *Nuclear Fusion* 59.8 (2019). ISSN: 17414326. DOI: 10.1088/1741-4326/ab2825.

[51] E. D. Emdee et al. "Predictive modeling of a lithium vapor box divertor in NSTX-U using SOLPS-ITER". In: *Nuclear Materials and Energy* 27 (2021), 101004 (6 pp). ISSN: 23521791. DOI: 10.1016/j.nme.2021.101004. URL: https://doi.org/10.1016/j.nme.2021.101004.

[52] ENEA. *Divertor Tokamak Test facility Project Proposal*. 2015. ISBN: 9788882863180.

[53] ENEA. *DTT Divertor Tokamak Test Facility Interim Design Report (green book)*. Ed. by A. Pizzuto. Frascati (Roma), Italy: ENEA, 2019, p. 278. ISBN: 978-88-8286-378-4. URL: https://www.dtt-project.enea.it/downloads/DTT_IDR_2019_WEB.pdf.

[54] S. K. Erents, G. M. McCracken, and P. Goldsmith. "Trapping of keV deuterons in lithium". In: *Journal of Physics D: Applied Physics* 4.5 (1971), pp. 672–676. ISSN: 00223727. DOI: 10.1088/0022-3727/4/5/305.

[55] V. A. Evtikhin et al. "Calculation and experimental investigation of fusion reactor divertor plate and first wall protection by capillary-pore systems with lithium". In: *Journal of Nuclear Materials* 271-272 (1999), pp. 396–400. ISSN: 00223115. DOI: 10.1016/S0022-3115(98)00793-4.

[56] V. A. Evtikhin et al. "Research of lithium capillary-pore systems for fusion reactor plasma facing components". In: *Journal of Nuclear Materials* 307-311.2 SUPPL. (2002), pp. 1664–1669. ISSN: 00223115. DOI: 10.1016/S0022-3115(02)01132-7.

[57] Amir Faghri. "Heat Pipes: Review, Opportunities and Challenges". In: *Frontiers in Heat Pipes* 5.1 (2014). ISSN: 2155-658X. DOI: 10.5098/fhp.5.1. URL: http://thermalfluidscentral.org/journals/index.php/Heat_Pipes/article/view/360.

[58] Simon Fear. *Publication quality tables in LATEX*. 2005.

[59] T. Fei, A. Mohamed, and T. K. Kim. *Neutronic benchmark specifications for EBR-II Shutdown Heat Removal Test SHRT-45R - Revision 1*. Tech. rep. Argonne National Laboratory, 2013.

[60] Y Feng et al. "Transport in island divertors: physics, 3D modelling and comparison to first experiments on W7-AS". In: *Plasma Physics and Controlled Fusion* 44.5 (May 2002), pp. 611–625. DOI: 10.1088/0741-3335/44/5/308. URL: https://doi.org/10.1088/0741-3335/44/5/308.

[61] Giulio Fiorita. "Analisi numerica delle interazioni plasma-parete in presenza di un divertore a metallo liquido". Bachelor. Politecnico di Torino, 2020, p. 34.

[62] Jeffrey P. Freidberg. *Plasma physics and fusion energy*. Cambridge: Cambridge University Press, 2007, p. 690. ISBN: 9780511755705. DOI: 10.1017/CBO9780511755705. arXiv: arXiv:1011.1669v3. URL: www.cambridge.org/9780521851077%0Ahttp://ebooks.cambridge.org/ref/id/CBO9780511755705.

[63] T. L. George, K. L. Basehore, and W. A. Prather. *Cobra-WC model and predictions for afast-reactor natural-circulation transient*. Tech. rep. Richland, WA, 1980.

[64] R. J. Goldston. "Heuristic drift-based model of the power scrape-off width in low-gas-puff H-mode tokamaks". In: *Nuclear Fusion* 52.1 (2012), 013009 (7 pp). ISSN: 00295515. DOI: 10.1088/0029-5515/52/1/013009.

[65] R. J. Goldston, R. Myers, and J. Schwartz. "The lithium vapor box divertor". In: *Physica Scripta* T167 (2016), 14017 (6pp). ISSN: 02811847. DOI: 10.1088/0031-8949/T167/1/014017. URL: http://dx.doi.org/10.1088/0031-8949/T167/1/014017.

[66] R. J. Goldston, M. L. Reinke, and J. A. Schwartz. "A new scaling for divertor detachment". In: *Plasma Physics and Controlled Fusion* 59 (2017), 055015 (7pp). ISSN: 13616587. DOI: 10.1088/1361-6587/aa5e6e.

[67] R.J. Goldston et al. "Recent advances towards a lithium vapor box divertor". In: *Nuclear Materials and Energy* 12 (Aug. 2017), pp. 1118–1121. ISSN: 23521791. DOI: 10.1016/j.nme.2017.03.020. URL: https://linkinghub.elsevier.com/retrieve/pii/S235217911630103X.

[68] L G Golubchikov et al. "Development of a liquid-metal fusion reactor divertor with a capillary-pore system". In: *Journal of Nuclear Materials* 233 (1996), pp. 667–672. URL: https://ac.els-cdn.com/S0022311596000104/1-s2.0-S0022311596000104-main.pdf?_tid=4e71c53e-0f3b-4f6a-8c1d-54fd6b962f3d&acdnat=1546848861_406024af873ed48156978dee34bcf49c.

[69] G Grasso et al. "The core design of ALFRED, a demonstrator for the European lead-cooled reactors". In: *Nuclear Engineering and Design* 278 (2014), pp. 287–301. DOI: 10.1016/j.nucengdes.2014.07.032. URL: http://dx.doi.org/10.1016/j.nucengdes.2014.07.0320029-5493/.

[70] G. Grasso. *Modeling and simulation needs for core design: vision paper. Technical Report SICNUC-P000-###*. Tech. rep. ENEA, Bologna, IT, 2020.

[71] G. Grasso. *Specifiche tecniche per la progettazione di un nuovo strumento di analisi numerica per lo studio della termoidraulica delle portate interstiziali (y- pass) fra gli elementi di combustibile del nocciolo di un reattore veloce refrigerato a metallo liquido*. Tech. rep. ENEA Bologna, 2017.

[72] G. Grasso. "The core design of ALFRED, a demonstrator for the European lead-cooled reactors". In: *Nuclear Engineering and Design* 278 (2014), pp. 2040–2053.

[73] G. Grasso and F. Lodi. *Software Quality Assurance: Procedures and Guidelines for software development. Technical Report SICNUC-P000-###*. Tech. rep. ENEA, Bologna, IT, 2020.

[74] G. Grasso and F. Lodi. *Software quality assurance: Program and Guidelines*. Tech. rep. ENEA Bologna, 2017.

[75] G. Grasso and F. Lodi. *Software Quality Assurance: Quality Manual. Technical Report SICNUC-P000-###*. Tech. rep. ENEA, Bologna, IT, 2020.

[76] G. Grasso and F. Lodi. *Software Requirements Specification for TIFONE*. Tech. rep. ENEA, Bologna, IT, 2019.

[77] G. Grasso and F. Lodi. *TIFONE Project Plan. Technical Report SICNUC-P000-###*. Tech. rep. ENEA, Bologna, IT, 2020.

[78] G. Grasso and F. Lodi. *TIFONE Software Quality Assurance Plan. Technical Report SICNUC-P000-###*. Tech. rep. ENEA, Bologna, IT, 2020.

[79] Ettore Guadagni et al. *Numerical benchmark of the FRENETIC multiphysics code, presented at ICONE conference, London, UK, Jul. 22-26, 2018.*

[80] J. Guadagni. "Innovative Simulation Tools for Lead Fast Reactor Subchannel Analysis". Master's Thesis. Politecnico di Milano - Politecnico di Torino. URL: https://www.politesi.polimi.it/handle/10589/150832.

[81] S. E. Haaland. "Simple and explicit formulas for the i friction factor in turbulent pipe flow". In: *Journal of Fluids Engineering, Transactions of the ASME* 105 (1983), pp. 89–90. ISSN: 1528901X. DOI: 10.1115/1.3240975.

[82] F. Hecht. "New development in freefem++". In: *Journal of Numerical Mathematics* 20.3-4 (Jan. 2012), pp. 251–266. ISSN: 1569-3953. DOI: 10.1515/jnum-2012-0013. URL: https://www.degruyter.com/view/j/jnma.2012.20.issue-3-4/jnum-2012-0013/jnum-2012-0013.xml.

[83] Peter Hertel. "Writing Articles with LATEX". In: (2010).

[84] C. Y. Ho and T. K. Chu. *Electrical Resistivity and Thermal Conductivity of nine selected AISI Stainless Steels*. Tech. rep. Report 45. CINDAS, 1977.

[85] J D Huba. *NRL PLASMA FORMULARY*. Tech. rep. NRL, 2013, p. 71. DOI: 10.1109/MEI.2003.1178121. URL: http://wwwppd.nrl.navy.mil/nrlformulary/.

[86] Matteo Iafrati. "Phenomenology of plasma-wall interaction using liquid metals in tokamak devices". PhD thesis. Ph.D. thesis, Università degli studi di Padova, 2018, p. 209. URL: http://paduaresearch.cab.unipd.it/11904/.

[87] I. E. Idelchik. *Handbook of hydraulic resistance*. 4th Editio. Redding: Begell House, 2007, p. 914. ISBN: 978-1-56700-251-5.

[88] Frank P Incropera et al. *Introduction to Conduction*. 2007. DOI: 10.1016/j.applthermaleng.2011.03.022. arXiv: 1105-.

[89] ISO. *Information technology – Programming languages – Fortran – Part 1: Base Language*. Standard ISO/IEC 1539-1:2018. Geneva, CH: International Organization for Standardization, Nov. 2018.

[90] J. D. Jackson. "Turbulent mixed convection heat transfer to liquid sodium". In: *International Journal of Heat and Fluid Flow* 4.2 (1983), pp. 107–111. ISSN: 0142727X. DOI: 10.1016/0142-727X(83)90011-5.

[91] M. A. Jaworski, N. B. Morley, and D. N. Ruzic. "Thermocapillary and thermoelectric effects in liquid lithium plasma facing components". In: *Journal of Nuclear Materials* 390-391.1 (2009), pp. 1055–1058. ISSN: 00223115. DOI: 10.1016/j.jnucmat.2009.01.255. URL: http://dx.doi.org/10.1016/j.jnucmat.2009.01.255.

[92] M. A. Jaworski et al. "Liquid lithium divertor characteristics and plasma-material interactions in NSTX high-performance plasmas". In: *Nuclear Fusion* 53.8 (2013), 083032 (9pp). ISSN: 00295515. DOI: 10.1088/0029-5515/53/8/083032.

[93] M. A. Jaworski et al. "Upgrades toward high-heat flux, liquid lithium plasma-facing components in the NSTX-U". In: *Fusion Engineering and Design* 112 (2016), pp. 93–101. ISSN: 09203796. DOI: 10.1016/j.fusengdes.2016.07.009. URL: http://dx.doi.org/10.1016/j.fusengdes.2016.07.009.

[94] Jonathan Josyula, Eswar and Burt. "Review of Rarefied Gas Effects in Hypersonic Applications". In: *Rto-En-Avt-194* (2011). ISSN: 14709325.

[95] R. Kaita et al. "Hydrogen retention in lithium on metallic walls from "in vacuo" analysis in LTX and implications for high-Z plasma-facing components in NSTX-U". In: *Fusion Engineering and Design* 117 (2017), pp. 135–139. ISSN: 09203796. DOI: 10.1016/j.fusengdes.2016.06.056. URL: http://dx.doi.org/10.1016/j.fusengdes.2016.06.056.

[96] Robert Kaita et al. "Experiments with liquid metal walls: Status of the lithium tokamak experiment". In: *Fusion Engineering and Design* 85.6 (2010), pp. 874–881. ISSN: 09203796. DOI: 10.1016/j.fusengdes.2010.04.005. URL: http://dx.doi.org/10.1016/j.fusengdes.2010.04.005.

[97] A. Kallenbach et al. "Analytical calculations for impurity seeded partially detached divertor conditions". In: *Plasma Physics and Controlled Fusion* 58.4 (2016), 45013 (9pp). ISSN: 13616587. DOI: 10.1088/0741-3335/58/4/045013. URL: http://dx.doi.org/10.1088/0741-3335/58/4/045013.

[98] H Kamide, K Hayashi, and S Toda. "An experimental study of inter-subassembly heat transfer during natural circulation decay heat removal in fast breeder reactors". In: *Nuclear Engineering and Design* 183 (1998), pp. 97–106. ISSN: 00295493. DOI: 10.1016/S0029-5493(98)00169-1.

[99] E. Kaveeva et al. "SOLPS-ITER modelling of ITER edge plasma with drifts and currents". In: *Nuclear Fusion* 60.4 (2020), 046019 (14pp). ISSN: 17414326. DOI: 10.1088/1741-4326/ab73c1.

[100] Hiroshi Kawamura et al. "DNS of turbulent heat transfer in channel flow with low to medium-high Prandtl number fluid". In: *International Journal of Heat and Fluid Flow* 19 (1998), pp. 482–491.

[101] W. M. Kays and E. Y. Leung. "Heat transfer in annular passages - hydrodynamically developed laminar flow with arbitrarily prescribed wall temperatures or heat fluxes". In: *International Journal of Heat and Mass Transfer* 6 (1963), pp. 537–557. ISSN: 00179310. DOI: 10.1016/0017-9310(63)90124-8.

[102] C. E. Kessel et al. "Critical Exploration of Liquid Metal Plasma-Facing Components in a Fusion Nuclear Science Facility". In: *Fusion Science and Technology* 00.00 (2019), pp. 1–32. ISSN: 19437641. DOI: 10.1080/15361055.2019.1610685. URL: https://doi.org/10.1080/15361055.2019.1610685.

[103] J. Knaster, T. Kanemura, and K. Kondo. "An assessment of the evaporation and condensation phenomena of lithium during the operation of a Li(d,xn) fusion relevant neutron source". In: *Heliyon* 2.12 (2016), pp. 1–23. ISSN: 24058440. DOI: 10.1016/j.heliyon.2016.e00199. URL: http://dx.doi.org/10.1016/j.heliyon.2016.e00199.

[104] Boštjan Končar et al. "Initial optimization of DEMO fusion reactor thermal shields by thermal analysis of its integrated systems". In: *Fusion Engineering and Design* 125.July (2017), pp. 38–49. ISSN: 09203796. DOI: 10.1016/j.fusengdes.2017.10.017.

[105] H. W. Kugel et al. "NSTX plasma operation with a Liquid Lithium Divertor". In: *Fusion Engineering and Design* 87.10 (2012), pp. 1724–1731. ISSN: 09203796. DOI: 10.1016/j.fusengdes.2011.07.010. URL: http://dx.doi.org/10.1016/j.fusengdes.2011.07.010.

[106] Leslie Lamport. *Latex*. Addison-Wesley, 1994.

[107] A. W. Leonard. "Plasma detachment in divertor tokamaks". In: *Plasma Physics and Controlled Fusion* 60.4 (2018), 04401 (24pp). ISSN: 13616587. DOI: 10.1088/1361-6587/aaa7a9.

[108] Jaakko Leppänen. *Development of a new Monte Carlo reactor physics code*. Espoo: VTT Technical Research Centre of Finland, 2007.

[109] Jaakko Leppänen et al. "The Serpent Monte Carlo code: Status, development and applications in 2013". In: *Annals of Nuclear Energy* 82 (2015). Joint International Conference on Supercomputing in Nuclear Applications and Monte Carlo 2013, SNA + MC 2013. Pluri- and Trans-disciplinarity, Towards New Modeling and Numerical Simulation Paradigms, pp. 142–150. ISSN: 0306-4549. DOI: https://doi.org/10.1016/j.anucene.2014.08.024. URL: http://www.sciencedirect.com/science/article/pii/S0306454914004095.

[110] Yu Liang et al. "Experimental and numerical investigation on flow characteristics of inter-wrapper channel in LMFBR". In: *Annals of Nuclear Energy* 151 (2021). ISSN: 18732100. DOI: 10.1016/j.anucene.2020.107918.

[111] F Lodi and G Grasso. "Stress-testing the ALFRED design - Part III: Safety margins evaluation". eng. In: *Progress in nuclear energy (New series)* 106 (2018), pp. 433–439. ISSN: 0149-1970.

[112] F. Lodi and G. Grasso. "Extension of the sub-channel code ANTEO+ to the mixed convection regime". In: *Nuclear Engineering and Design* 322.September (2017), pp. 368–378. ISSN: 00295493. DOI: 10.1016/j.nucengdes.2017.07.018. URL: http://dx.doi.org/10.1016/j.nucengdes.2017.07.018.

[113] Francesco Lodi. "Development of Core Design Methods and Tools for Gen-IV Heavy Liquid Metal Cooled Reactors". Ph.D. thesis. Alma Mater Studiorum Universit'a di Bologna, 2017, pp. xlii–324.

[114] Francesco Lodi and Giacomo Grasso. "ANTEO+: a subchannel code for thermal-hydraulic analysis of liquid-metal cooled systems". In: *Nuclear Engineering and Design* 301 (2016), pp. 128–152.

[115] J. P.S. Loureiro et al. "Deuterium retention in tin (Sn) and lithium–tin (Li–Sn) samples exposed to ISTTOK plasmas". In: *Nuclear Materials and Energy* 12 (2017), pp. 709–713. ISSN: 23521791. DOI: 10.1016/j.nme.2016.12.026.

[116] R E Macfarlane et al. *The NJOY Nuclear Data Processing System, Version 2016*. Tech. rep. 2018.

[117] A. Manhard et al. "Deuterium retention in solid and liquid tin after low-temperature plasma exposure". In: *Nuclear Fusion* 60 (2020), 106007 (22pp). ISSN: 17414326. DOI: 10.1088/1741-4326/aba801.

[118] E D Marenkov and A.A. Pshenov. "Vapor shielding of liquid lithium divertor target during steady-state and transient events". In: *Nucl. Fus.* 60 (2020), 026011 (12pp). DOI: https://doi.org/10.1088/1741-4326/ab5eb5.

[119] E. D. Marenkov, A. S. Kukushkin, and A. A. Pshenov. "Modeling the vapor shielding of a liquid lithium divertor target using SOLPS 4.3 code". In: *Nuclear Fusion* 61.3 (2021), 034001 (7pp). ISSN: 17414326. DOI: 10.1088/1741-4326/abd642.

[120] Y. R. Martin and T. Takizuka. "Power requirement for accessing the H-mode in ITER". In: *Journal of Physics: Conference Series* 123 (2008), 012033 (11pp). ISSN: 17426596. DOI: 10.1088/1742-6596/123/1/012033.

[121] Mattia Massone. "Cross-Sections for Transient Analyses: Development of a Genetic Algorithm for the Energy Meshing". Ph.D. thesis. Karlsruher Instituts fur Technologie (KIT), 2018, p. 134. DOI: 10.5445/IR/1000083680.

[122] Akihiro MATSUBARA et al. "Plasma Plugging in Gas Divertor". In: *Journal of Nuclear Science and Technology* 36.1 (1999), pp. 114–115. ISSN: 0022-3131. DOI: 10.1080/18811248.1999.9726188. URL: https://www.tandfonline.com/doi/full/10.1080/18811248.1999.9726188.

[123] G. Mazzitelli et al. "Experiments on FTU with an actively water cooled liquid lithium limiter". In: *Journal of Nuclear Materials* 463 (2015), pp. 1152–1155. ISSN: 00223115. DOI: 10.1016/j.jnucmat.2014.12.050. URL: http://dx.doi.org/10.1016/j.jnucmat.2014.12.050.

[124] G. Mazzitelli et al. "Experiments on the Frascati Tokamak Upgrade with a liquid tin limiter". In: *Nuclear Fusion* 59.9 (2019), 096004 (8pp). ISSN: 17414326. DOI: 10.1088/1741-4326/ab1d70.

[125] Matthew Memmott, Jacopo Buongiorno, and Pavel Hejzlar. "On the use of RELAP5-3D as a subchannel analysis code". In: *Nuclear Engineering and Design* 240.4 (2010), pp. 807–815. ISSN: 0029-5493. DOI: 10.1016/j.nucengdes.2009.11.006. URL: http://dx.doi.org/10.1016/j.nucengdes.2009.11.006.

[126] B. Meszaros. *EU DEMO1 2015 - DEMO TOKAMAK COMPLEX*. Tech. rep. EUROfusion, 2015. URL: http://idm.euro-fusion.org/?uid=2D3FBF.

[127] S V Mirnov, V N Dem'yanenko, and E V Murav'ev. "Liquid-metal tokamak divertors". In: *Journal of Nuclear Materials* 196-198 (1992), pp. 45–49. URL: https://ac.els-cdn.com/S0022311506800103/1-s2.0-S0022311506800103-main.pdf?_tid=69737c2a-bc58-4d7f-b85f-173f66519711&acdnat=1546597465_db2f979d25888864e30b8d2f740aba66.

[128] S V Mirnov et al. "Experiments with lithium limiter on T-11M tokamak and applications of the lithium capillary-pore system in future fusion reactor devices". In: *Plasma Physics and Controlled Fusion* 48.6 (2006), pp. 821–837. ISSN: 07413335. DOI: 10.1088/0741-3335/48/6/009. URL: http://iopscience.iop.org/article/10.1088/0741-3335/48/6/009/pdf.

[129] S. Mirnov. "Plasma-wall interactions and plasma behaviour in fusion devices with liquid lithium plasma facing components". In: *Journal of Nuclear Materials* 390-391.1 (2009), pp. 876–885. ISSN: 00223115. DOI: 10.1016/j.jnucmat.2009.01.228. URL: http://dx.doi.org/10.1016/j.jnucmat.2009.01.228.

[130] S. V. Mirnov et al. "Experimental test of the system of vertical and longitudinal lithium limiters on T-11M tokamak as a prototype of plasma facing components of a steady-state fusion neutron source". In: *Nuclear Fusion* 55.12 (2015), 123015 (8pp). ISSN: 17414326. DOI: 10.1088/0029-5515/55/12/123015. URL: http://dx.doi.org/10.1088/0029-5515/55/12/123015.

[131] H. Mochizuki. "Inter-subassembly heat transfer of sodium-cooled fast reactors: validation of the NETFLOW code". In: *Nuclear Engineering and Design* 42 (2007), pp. 2040–2053.

[132] T. W. Morgan et al. "Liquid metals as a divertor plasma-facing material explored using the Pilot-PSI and Magnum-PSI linear devices". In: *Plasma Physics and Controlled Fusion* 60.1 (2018), 14025 (11 pp). ISSN: 13616587. DOI: 10.1088/1361-6587/aa86cd. URL: http://dx.doi.org/10.1088/1361-6587/aa86cd.

[133] T. W. Morgan et al. "Power handling of a liquid-metal based CPS structure under high steady-state heat and particle fluxes". In: *Nuclear Materials and Energy* 12 (2017), pp. 210–215. ISSN: 23521791. DOI: 10.1016/j.nme.2017.01.017.

[134] M. Moscheni et al. "Radiative Heat Load Distribution on the EU-DEMO First Wall Due to Mitigated Disruptions". In: *Nuclear Materials and Energy* 25 (2020), 100824 (6pp). DOI: https://doi.org/10.1016/j.nme.2020.100824.

[135] R. Myers. "A Lithium Vapor-Box Divertor for Tokamak Applications". Bachelor's Thesis. Princeton University. URL: http://arks.princeton.edu/ark:/88435/dsp013484zk27j.

[136] Yoshio Nagayama. "Liquid lithium divertor system for fusion reactor". In: *Fusion Engineering and Design* 84.7-11 (2009), pp. 1380–1383. ISSN: 09203796. DOI: 10.1016/j.fusengdes.2009.02.002.

[137] G F Nallo et al. "Neutronic benchmark of the FRENETIC code for the multiphysics analysis of lead fast reactors". In: *European Physical Journal Plus* 135.2 (2020). ISSN: 21905444. DOI: 10.1140/epjp/s13360-020-00171-8. URL: https://doi.org/10.1140/epjp/s13360-020-00171-8.

[138] G. F. Nallo et al. "Self-consistent modelling of a liquid metal box-type divertor with application to the divertor tokamak test facility: Li versus Sn". In: *Nuclear Fusion* 59.6 (2019), 066020 (17pp). ISSN: 17414326. DOI: 10.1088/1741-4326/ab145b.

[139] G.F. Nallo et al. "Modeling the lithium loop in a liquid metal pool-type divertor". In: *Fusion Engineering and Design* 125 (Dec. 2017), pp. 206–215. ISSN: 09203796. DOI: 10.1016/j.fusengdes.2017.07.004. URL: https://linkinghub.elsevier.com/retrieve/pii/S0920379617307445.

[140] G.F. Nallo et al. "Modeling the lithium loop in a liquid metal pool-type divertor". In: *Fusion Engineering and Design* 125 (Dec. 2017), pp. 206–215. ISSN: 09203796. DOI: 10.1016/j.fusengdes.2017.07.004. URL: https://linkinghub.elsevier.com/retrieve/pii/S0920379617307445.

[141] NEA. *Handbook on Lead-bismuth Eutectic Alloy and Lead Properties , Materials Compatibility , Thermal- hydraulics and Technologies, 2015 Edition*. NEA, 2015, p. 950.

[142] M. Nishimura et al. "Transient experiments on fast reactor core thermal-hydraulics and its numerical analysis. Inter-subassembly heat transfer and inter-wrapper flow under natural circulation conditions". In: *Nuclear Engineering and Design* 200 (2000), pp. 157–175.

[143] R. E. Nygren and F. L. Tabares. "Liquid surfaces for fusion plasma facing components—A critical review. Part I: Physics and PSI". In: *Nuclear Materials and Energy* 9 (2016), pp. 6–21. ISSN: 23521791. DOI: 10.1016/j.nme.2016.08.008. URL: http://dx.doi.org/10.1016/j.nme.2016.08.008.

[144] OECD. *A Technology Roadmap for Generation IV Nuclear Energy Systems*. 2002. URL: https://www.gen-4.org/gif/jcms/c_40481/technology-roadmap.

[145] OECD. *Technology Roadmap Update for Generation IV Nuclear Energy Systems*. 2013. URL: https://www.gen-4.org/gif/jcms/c_60729/technology-roadmap-update-2013.

[146] K. I. Oleinik, A. S. Bykov, and E. A. Pastukhov. "Refinement of the Thermophysical Properties of Liquid Tin at High Temperatures". In: *Russian Metallurgy (Metally)* 2018.2 (2018), pp. 110–113. ISSN: 15556255. DOI: 10.1134/S0036029518020143.

[147] M. Ono et al. "Active radiative liquid lithium divertor concept". In: *Fusion Engineering and Design* 89.12 (2014), pp. 2838–2844. ISSN: 09203796. DOI: 10.1016/j.fusengdes.2014.05.008. URL: http://dx.doi.org/10.1016/j.fusengdes.2014.05.008.

[148] Masayuki Ono. "Lithium As Plasma Facing Component for Magnetic Fusion Research". In: (2012). DOI: 10.2172/1056493.

[149] W. Ou et al. "Deuterium retention in Sn-filled samples exposed to fusion-relevant flux plasmas". In: *Nuclear Fusion* 60 (2020), 026008 (16pp). ISSN: 17414326. DOI: 10.1088/1741-4326/ab5cd4.

[150] J. Pacio et al. "Experimental study of the influence of inter-wrapper flow on liquid-metal cooled fuel assemblies". In: *Nuclear Engineering and Design* 352.April (2019), p. 110145. ISSN: 00295493. DOI: 10.1016/j.nucengdes.2019.06.007. URL: https://doi.org/10.1016/j.nucengdes.2019.06.007.

[151] Julio Pacio et al. *D2.12 - KALLA Inter-wrapper flow experiments*. Tech. rep. KIT, 2018, p. 120.

[152] Julio Pacio et al. “INTER-WRAPPER FLOW: LBE EXPERIMENTS AND SIMULATIONS”. In: *NURETH-18, Portland, OR, August 18-22, 2019*. Portland, OR, 2019, pp. 796–809.

[153] Vincenzo Pericoli Ridolfini. *Final Report on Deliverable DTT1-LMD.P2-T003, EUROfusion report EFDA_D_2NJWW3*. Tech. rep. 2020.

[154] Vincenzo Pericoli Ridolfini et al. “Perspectives for the Liquid Lithium and Tin Targets in the I-DTT Divertor”. In: *Nuclear Fusion* 59 (2019), 126008 (15pp). ISSN: 0029-5515. DOI: 10.1088/1741-4326/ab3969.

[155] R.A. Pitts et al. “Physics basis for the first ITER tungsten divertor”. In: *Nuclear Materials and Energy* 20 (2019), 100696 (25pp). ISSN: 23521791. DOI: 10.1016/j.nme.2019.100696. URL: https://doi.org/10.1016/j.nme.2019.100696.

[156] M Poradzinski et al. “Integrated core-SOL-divertor modelling for DEMO with tin divertor”. In: *Fusion Engineering and Design* 124 (2017), pp. 248–251. DOI: 10.1016/j.fusengdes.2017.04.131. URL: http://dx.doi.org/10.1016/j.fusengdes.2017.04.131.

[157] M. Poradziński et al. “Integrated core-SOL-divertor modelling for DEMO with tin divertor”. In: *Fusion Engineering and Design* 124 (2017), pp. 248–251. ISSN: 09203796. DOI: 10.1016/j.fusengdes.2017.04.131.

[158] Roger S. Pressman. *Software Engineering: a Practitioner’s approach*. McGraw-Hill, 2001. ISBN: 0073655783.

[159] A. A. Pshenov, A. S. Kukushkin, and S. I. Krasheninnikov. “Energy balance in plasma detachment”. In: *Nuclear Materials and Energy* 12 (2017), pp. 948–952. ISSN: 23521791. DOI: 10.1016/j.nme.2017.03.019. URL: http://dx.doi.org/10.1016/j.nme.2017.03.019.

[160] T. Putterich et al. “Impurity limits in a reactor grade fusion device”. In: *42nd European Physical Society Conference on Plasma Physics, EPS 2015, paper n. 4.111*. 2015. URL: http://ocs.ciemat.es/EPS2015PAP/pdf/P4.111.pdf.

[161] T Pütterich et al. “Determination of the tolerable impurity concentrations in a fusion reactor using a consistent set of cooling factors”. In: *Nuclear Fusion* 59.5 (2019), 056013 (28pp). ISSN: 17414326. DOI: 10.1088/1741-4326/ab0384. URL: https://doi.org/10.1088/1741-4326/ab0384.

[162] D. Reiter. “The EIRENE Code User Manual Manual version : May 16, 2019”. In: (2019), p. 304. URL: http://eirene.de/.

[163] Detlev Reiter. *The physics and technology of power flux handling in tokamaks*. 10th ITER international school 2019. 2019. URL: https://www.iter.org/education/iis.

[164] M. E. Rensink, T. D. Rognlien, and C. E. Kessel. "Modeling the Edge-Plasma Interface for Liquid-Lithium Walls in FNSF". In: *Fusion Science and Technology* 75.8 (2019), pp. 959–972. ISSN: 1536-1055. DOI: 10.1080/15361055.2019.1643686. URL: https://doi.org/10.1080/15361055.2019.1643686.

[165] P. Rindt et al. "Power handling limit of liquid lithium divertor targets". In: *Nuclear Fusion* 58.10 (2018), 104002 (5pp). ISSN: 17414326. DOI: 10.1088/1741-4326/aad290. URL: https://doi.org/10.1088/1741-4326/aad290.

[166] Peter Rindt. "The potential of liquid-metal 3D-printed heat shields for fusion reactors". Ph.D. thesis. Technische Universiteit Eindhoven, 2019. ISBN: 9789038648101. URL: https://research.tue.nl/files/129598079/20190701_CO_Rindt.pdf.

[167] S. Roccella et al. "CPS Based Liquid Metal Divertor Target for EU-DEMO". In: *Journal of Fusion Energy* (2020), (7pp). ISSN: 1572-9591. DOI: 10.1007/s10894-020-00263-4. URL: https://doi.org/10.1007/s10894-020-00263-4.

[168] F. Roelofs. *Advanced Thermal-Hydraulics for Liquid-Metal Reactors: Beyond State-of-the-art Methods, Techniques and Experiments*. 2016.

[169] T.D. Rognlien, M.E. Rensink, and D.P. Stotler. "Scrape-off layer plasma and neutral characteristics and their interactions with walls for FNSF". In: *Fusion Engineering and Design* 135 (Oct. 2018), pp. 380–393. ISSN: 09203796. DOI: 10.1016/j.fusengdes.2017.07.024. URL: https://linkinghub.elsevier.com/retrieve/pii/S0920379617307652.

[170] T.D. Rognlien et al. "A fully implicit, time dependent 2-D fluid code for modeling tokamak edge plasmas". In: *Journal of Nuclear Materials* 196-198 (1992). Plasma-Surface Interactions in Controlled Fusion Devices, pp. 347–351. ISSN: 0022-3115. DOI: https://doi.org/10.1016/S0022-3115(06)80058-9. URL: https://www.sciencedirect.com/science/article/pii/S0022311506800589.

[171] D. N. Ruzic et al. "Lithium-metal infused trenches (LiMIT) for heat removal in fusion devices". In: *Nuclear Fusion* 51.10 (2011). ISSN: 00295515. DOI: 10.1088/0029-5515/51/10/102002.

[172] D.N. Ruzic et al. "Flowing liquid lithium plasma-facing components – Physics, technology and system analysis of the LiMIT system". In: *Nuclear Materials and Energy* 12 (Aug. 2017), pp. 1324–1329. ISSN: 23521791. DOI: 10.1016/j.nme.2017.06.001. URL: https://linkinghub.elsevier.com/retrieve/pii/S2352179116302186.

[173] M. Sadatomi, Y. Sato, and S. Saruwatari. "Two-phase flow in vertical noncircular channels". In: *International Journal of Multiphase Flow* 8.6 (1982), pp. 641–655. ISSN: 03019322. DOI: 10.1016/0301-9322(82)90068-4.

[174] Jafar Safarian and Thorvald A. Engh. "Vacuum Evaporation of Pure Metals". In: *Metallurgical and Materials Transactions A* 44.2 (2013), pp. 747–753. ISSN: 1073-5623. DOI: 10.1007/s11661-012-1464-2. URL: http://link.springer.com/10.1007/s11661-012-1464-2.

[175] I. V. Savchenko, S. V. Stankus, and A. H. Agadjanov. "Measurement of liquid tin heat transfer coefficients within the temperature range of 506-1170 K". In: *High Temperature* 49.4 (2011), pp. 506–511. ISSN: 0018151X. DOI: 10.1134/S0018151X11040171.

[176] Jacob A. Schwartz et al. "Physics design for a lithium vapor box divertor experiment on magnum PSI". In: *Nuclear Materials and Energy* 18 (Jan. 2019), pp. 350–355. ISSN: 23521791. DOI: 10.1016/j.nme.2019.01.024. URL: https://linkinghub.elsevier.com/retrieve/pii/S2352179118302618.

[177] Jacob Alexander Schwartz. "Experimental and modeling studies for the development of the lithium vapor-box divertor". PhD thesis. Princeton University, 2020. URL: http://arks.princeton.edu/ark:/88435/dsp01jq085p04m.

[178] I. Yu Senichenkov et al. "Integrated modeling of H-mode tokamak discharges with ASTRA and B2SOLPS numerical codes". In: *Plasma Physics and Controlled Fusion* 56.5 (2014), 055002 (12pp). ISSN: 13616587. DOI: 10.1088/0741-3335/56/5/055002.

[179] I. Yu Senichenkov et al. "Integrated modelling of the Globus-M tokamak plasma and a comparison with SOL width scaling". In: *Nuclear Fusion* 55.5 (2015), 053012 (7pp). ISSN: 17414326. DOI: 10.1088/0029-5515/55/5/053012.

[180] A. Simonič. "A Construction of Lomonosov Functions and Applications to the Invariant Subspace Problem". In: *Pacific J. Math.* 175 (1996), pp. 257–270.

[181] A. Simonič. "An Extension of Lomonosov's Techniques to Non-Compact Operators". PhD thesis. Dalhousie University, Department of Mathematics, Statistics, & Computing Science, 1994.

[182] A. Simonič. "Grupe Operatorjev s Pozitivnim Spektrom". MA thesis. Univerza v Ljubljani, FNT, Oddelek za Matematiko, 1990.

[183] A. Simonič. "Matrix Groups with Positive Spectra". In: *Linear Algebra Appl.* 173 (1992), pp. 57–76.

[184] A. Simonič. "Notes on Subharmonic Functions". Lecture Notes, Dalhousie University, Department of Mathematics, Statistics, & Computing Science. 1991.

[185] R Simonini et al. "Models and Numerics in the Multi-Fluid 2-D Edge Plasma Code EDGE2D/U". In: *Contributions to Plasma Physics* 34.2-3 (1994), pp. 368–373. DOI: https://doi.org/10.1002/ctpp.2150340242. eprint: https://onlinelibrary.wiley.com/doi/pdf/10.1002/ctpp.2150340242. URL: https://onlinelibrary.wiley.com/doi/abs/10.1002/ctpp.2150340242.

[186] C. A. Sleicher and M. W. Rouse. "A convenient correlation for heat transfer to constant and variable property fluids in turbulent pipe flow". In: *International Journal of Heat and Mass Transfer* 18.5 (1975), pp. 677–683. ISSN: 00179310. DOI: 10.1016/0017-9310(75)90279-3.

[187] V. Sobolev. *Preliminary recommendations for thermal and mechanical properties of unirradiated stainless steel 15-15Ti*. Tech. rep. I-198. SCK-CEN, 2011.

[188] Vitaly Sobolev. *Database of thermophysical properties of liquid metal coolants for GEN-IV*. Tech. rep. SCK • CEN, 2011. URL: http://www.iaea.org/inis/collection/NCLCollectionStore/%7B%5C_%7DPublic/43/095/43095088.pdf.

[189] E. Sobrero. *Impostazione dell'analisi del regime fluidodinamico della portata di fuga che fluisce fra gli elementi di combustibile*. Tech. rep. ENEA Bologna, 1977, p. 48.

[190] P.C. Stangeby. *The Plasma Boundary of Magnetic Fusion Devices*. Ed. by Simon Laurenson. London: Institute of Physics Publishing, 2001, p. 715. ISBN: 978-0-7503-0559-4. DOI: 10.1088/0741-3335/43/2/702. URL: http://stacks.iop.org/0741-3335/43/i=2/a=702?key=crossref.697b1e31667aa5230930cad92b5e0e4f.

[191] Fabio Subba. *SOLPS Calculations for DEMO, EUROfusion report EFDA_D_2N3L2S*. Tech. rep. EUROfusion, 2020.

[192] Fabio Subba et al. "Modelling of mitigation of the power divertor loading for the EU DEMO through Ar injection". In: *Plasma Physics and Controlled Fusion* 60.3 (2018), 035013 (9pp). ISSN: 13616587. DOI: 10.1088/1361-6587/aaa508.

[193] H P Summers. *The ADAS User Manual, version 2.6*. Tech. rep. 2004. URL: http://www.adas.ac.uk/man/contents.pdf.

[194] E. Sytova et al. "Impact of a new general form of friction and thermal forces on SOLPS-ITER modelling results". In: *Contributions to Plasma Physics* 58.6-8 (2018), pp. 622–628. ISSN: 15213986. DOI: 10.1002/ctpp.201700135.

[195] The HDF Group. *HDF5 User ' s Guide*. 2019. URL: https://portal.hdfgroup.org/display/HDF5/HDF5+User+Guides.

[196] Neil E. Todreas and Mujid S. Kazimi. *Nuclear Systems II - Elements of Thermal Hydraulic Design*. Corporation, Hemisphere Publishing, 1990, p. 506.

[197] D Tskhakaya, M Groth, and J E T Efda. "Modelling of tungsten re-deposition coefficient". In: *Journal of Nuclear Materials* 463 (2015), pp. 624–628. ISSN: 0022-3115. DOI: 10.1016/j.jnucmat.2014.10.086. URL: http://dx.doi.org/10.1016/j.jnucmat.2014.10.086.

[198] Riku Tuominen, Ville Valtavirta, and Jaakko Leppänen. "New energy deposition treatment in the Serpent 2 Monte Carlo transport code". In: *Annals of Nuclear Energy* 129 (2019), pp. 224–232. ISSN: 18732100. DOI: 10.1016/j.anucene.2019.02.003. URL: https://doi.org/10.1016/j.anucene.2019.02.003.

[199] H. J. Uitslag-Doolaard et al. "Experiment design to assess the inter-wrapper heat transfer in LMFR". In: *Nuclear Engineering and Design* 341.June 2018 (2019), pp. 297–305. ISSN: 00295493. DOI: 10.1016/j.nucengdes.2018.11.019. URL: https://doi.org/10.1016/j.nucengdes.2018.11.019.

[200] H. J.N. Van Eck et al. "Modeling and experiments on differential pumping in linear plasma generators operating at high gas flows". In: *Journal of Applied Physics* 105.6 (2009), pp. 1–11. ISSN: 00218979. DOI: 10.1063/1.3086622.

[201] G. G. Van Eden et al. "Oscillatory vapour shielding of liquid metal walls in nuclear fusion devices". In: *Nature Communications* 8 (2017), 192 (10pp). ISSN: 20411723. DOI: 10.1038/s41467-017-00288-y. URL: http://dx.doi.org/10.1038/s41467-017-00288-y.

[202] A Vertkov et al. "The concept of lithium based plasma facing elements for steady state fusion tokamak-reactor and its experimental validation". In: *2018 IAEA Fusion Energy Conference - EX/P1-12*. Gandhinagar, 2018. URL: https://nucleus.iaea.org/sites/fusionportal/Shared%20Documents/FEC%202018/FEC2018_ConfMat_Online.pdf.

[203] A. Vertkov et al. "Technological aspects of liquid lithium limiter experiment on FTU tokamak". In: *Fusion Engineering and Design* 82.15-24 (2007), pp. 1627–1633. ISSN: 09203796. DOI: 10.1016/j.fusengdes.2007.05.009.

[204] A. V. Vertkov et al. "Behavior of Capillary-Porous Systems with Liquid Lithium under Influence of Pulsed Deuterium Plasma". In: *Inorganic Materials: Applied Research* 10.2 (2019), pp. 326–332. ISSN: 2075115X. DOI: 10.1134/S2075113319020382.

[205] Manoj Warrier, Ralf Schneider, and Xavier Bonnin. "Subroutines for some plasma surface interaction processes: Physical sputtering, chemical erosion, radiation enhanced sublimation, backscattering and thermal evaporation". In: *Computer Physics Communications* 160.1 (2004), pp. 46–68. ISSN: 00104655. DOI: 10.1016/j.cpc.2004.02.011.

[206] H G Weller et al. “A tensorial approach to computational continuum mechanics using object-oriented techniques”. In: *Comput. Phys.* 12.6 (1998), pp. 620–631. ISSN: 08941866. DOI: 10.1063/1.168744. URL: https://foam-extend.fsb.hr/wp-content/uploads/2018/04/Weller_Tabor_Jasak_Fureby_A_tensorial_approach_to_computational_continuum_mechanics_using_object-oriented_techniques_1998.pdf.

[207] R Wenninger et al. “DEMO divertor limitations during and in between ELMs”. In: *Nucl. Fusion* 54 (2014), 114003 (8pp). DOI: 10.1088/0029-5515/54/11/114003. URL: https://iopscience.iop.org/article/10.1088/0029-5515/54/11/114003/pdf.

[208] R. Wenninger. “DEMO1 Reference Design - 2017 April ("EU DEMO1 2017") - SOF and EOF equilibria”. 2017.

[209] J. Wesson. *Tokamaks*. Fourth. New York: Oxford University Press, 2011.

[210] C. White et al. “DsmcFoam+: An OpenFOAM based direct simulation Monte Carlo solver”. In: *Computer Physics Communications* 224 (2017), pp. 22–43. ISSN: 00104655. DOI: 10.1016/j.cpc.2017.09.030. URL: https://doi.org/10.1016/j.cpc.2017.09.030.

[211] S. Wiesen et al. “The new SOLPS-ITER code package”. In: *Journal of Nuclear Materials* 463 (2015), pp. 480–484. ISSN: 00223115. DOI: 10.1016/j.jnucmat.2014.10.012.

[212] R. K. Williams, G. L. Coleman, and D. W. Yarbrough. “An Evaluation of some Thermodynamic and Transport Properties of solid and liquid lithium over the Temperature Range 200-1700 K”. In: (1988), p. 40. ISSN: 1098-6596. DOI: 10.1017/CBO9781107415324.004. arXiv: arXiv:1011.1669v3. URL: http://web.ornl.gov/info/reports/1988/3445602747393.pdf.

[213] Zongbiao Ye et al. “The investigation of plasma-induced wettability of liquid tin-capillary porous system”. In: *Nuclear Materials and Energy* 20 (Aug. 2019), p. 100694. ISSN: 23521791. DOI: 10.1016/j.nme.2019.100694.

[214] J. H. You et al. “European divertor target concepts for DEMO: Design rationales and high heat flux performance”. In: *Nuclear Materials and Energy* 16.April (2018), pp. 1–11. ISSN: 23521791. DOI: 10.1016/j.nme.2018.05.012.

[215] R Zagorski and H Gerhauser. “Numerical Modelling of Marfe Phenomena in TEXTOR Tokamak”. In: *Physica Scripta* 70.2-3 (Jan. 2004), pp. 173–186. DOI: 10.1088/0031-8949/70/2-3/017. URL: https://doi.org/10.1088/0031-8949/70/2-3/017.

[216] R. Zagórski et al. “The DTT device: Power and particle exhaust”. In: *Fusion Engineering and Design* 122 (2017), pp. 313–321. ISSN: 09203796. DOI: 10.1016/j.fusengdes.2017.05.114. URL: https://doi.org/10.1016/j.fusengdes.2017.05.114.

[217] Leonid E. Zakharov. “On a burning plasma low recycling regime with P DT = 23-26 MW, Q DT = 5-7 in a JET-like tokamak”. In: *Nuclear Fusion* 59.9 (2019), 096008 (22pp). ISSN: 17414326. DOI: 10.1088/1741-4326/ab246b.

[218] R. Zanino et al. “Benchmark and preliminary validation of the thermal-hydraulic module of the FRENETIC code against EBR-II data”. In: *Embedded Topical Meeting on Advances in Thermal Hydraulics, ATH 2014, Held at the American Nuclear Society 2014 Annual Meeting* (2014), pp. 173–187.

[219] V. Zhdanov. *Transport processes in multicomponent plasmas*. New York and London: Taylor and Francis, 2002.

[220] H. Zohm et al. “The EU strategy for solving the DEMO exhaust problem”. In: *Fusion Engineering and Design* 166.January (2021), 112307 (8pp). ISSN: 09203796. DOI: 10.1016/j.fusengdes.2021.112307. URL: https://doi.org/10.1016/j.fusengdes.2021.112307.

This Ph.D. thesis has been typeset by means of the TEX-system facilities. The typesetting engine was pdfLATEX. The document class was `toptesi`, by Claudio Beccari, with option `tipotesi=scudo`. This class is available in every up-to-date and complete TEX-system installation.